INVESTIGATING THE EFFECTS OF AGE AND EXERCISE ON BONE COMPOSITION AND THE IMPACT OF COMPOSITION ON MECHANICAL INTEGRITY

by

Nadder David Sahar

A dissertation submitted in partial fulfillment
of the requirements for the degree of
Doctor of Philosophy
(Biomedical Engineering)
in The University of Michigan
2009

Doctoral Committee:

Professor David H. Kohn, Chair
Professor Steven A. Goldstein
Professor Michael D. Morris
Professor Peter D. Washabaugh

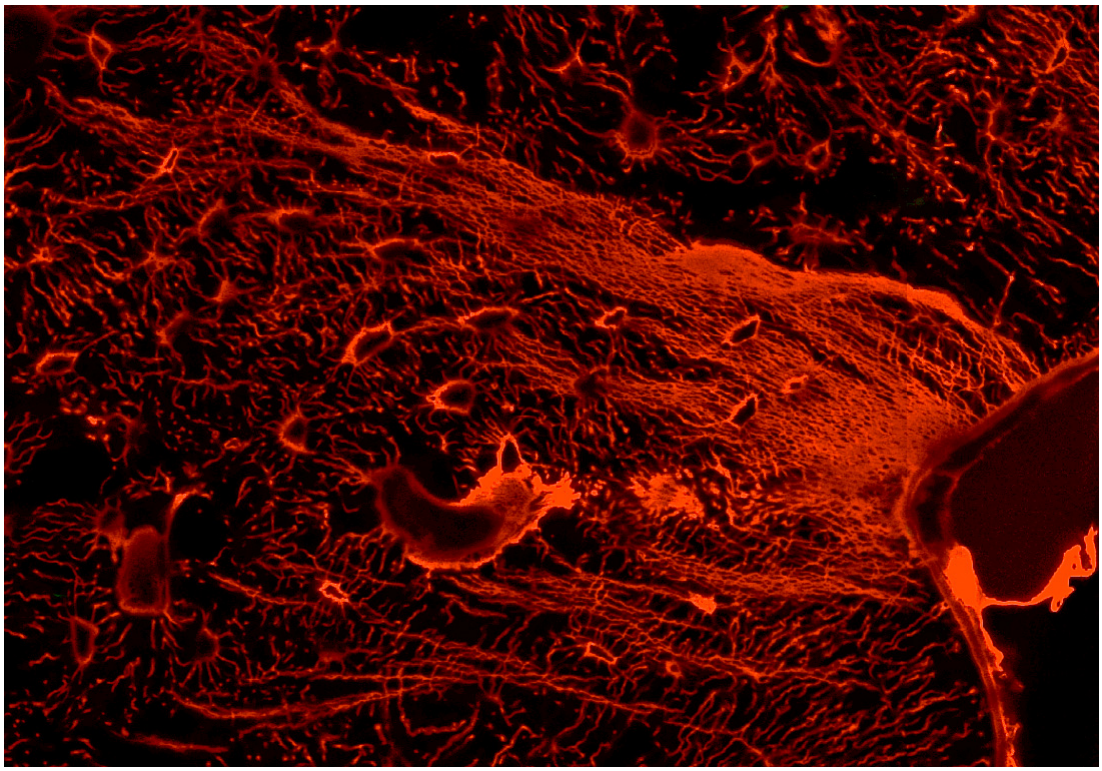

“Success is the ability to go from one failure to another with no loss of enthusiasm.”

- Winston Churchill

Dedicated with great gratitude to my parents
and brother for their boundless support and to
my grandparents for making this possible

ACKNOWLEDGEMENTS

I owe most of my growth in scientific research to the mentoring of Dave Kohn. I am grateful for the freedom he gave me to develop and explore my own ideas, to work in my own style, and to learn from my mistakes. His ability to challenge me made me a better writer and researcher. I always valued his input and perspective.

I would like to thank my committee members Mike Morris, Steve Goldstein, and Pete Washabaugh, for their invaluable insight. Their advice helped shape my research and provided new perspectives for interpretation of my data. I am also grateful for a long and fruitful collaboration with Mike's group, in particular Kurtulus Golcuk and Mekhala Raghavan for their help in spectroscopic characterization of bone. The last aim of this thesis would not have been possible without the intensely cooperative and thoughtful effort from Mekhala.

Mike Ron, Steve Obreiter, and Lisa Winkel all contributed significantly to the work in this thesis. I am grateful for their help and for the chance to know them personally. I also thank Jeff Meganck and Jaclynn Kreider for training me on micro-CT scanning and analysis, and for never seeming to mind when I pestered them with questions.

I was fortunate to be in a lab full of fun and intelligent people, including Erin Gatenby, Sun Ig Hong, Shan Lee, Joey Wallace, Ho Jun Song, Linh Luong, Ricardo Rossello, Sharon Miller (Segvich), Kyungsup Shin, and Hayes Smith. I enjoyed our happy hours, field trips, softball seasons, and camaraderie in lab. To the folks at the dental stores, in particular Teresa Paterson, Eugene Carter and Tim Deventer, thanks for making spending

many years in the basement of the dental school more tolerable. Finally, thanks to Elizabeth Rodriguez and Maria Steele for keeping our departments running smoothly.

The best part of my time at Michigan has been making lifelong friends. Going to football games, traveling, playing sports, or just hanging out with Joey, Ricky, Marwa, Jesse, Hugh, Kiran, Jen, and many others always revived my spirit. I can't image my experience at Michigan without them. I also established great friendships playing hockey, particularly with Mark and Karin, with whom I've also shared many great memories outside the rink. After years of playing hockey with my team, I still looked forward to every game. Thanks also to the Arena Bar and Grill, because sometimes you want to go where everyone knows your name.

Although I have been away from my childhood friends Jeff and Bob for the majority of the last 12 years, our friendship has only grown stronger. I look forward to seeing them more regularly very soon. Scott and Sharon, thank you for inviting me into your home and helping me after my surgery. More importantly thank you for always treating me like family and never making me feel like a fifth wheel. Sharon, thank you also for being my constant companion in lab. It will be a hard adjustment not to see you on a daily basis. Andrea, you were a great roommate and an even better friend. You are generous and loyal and you have a natural ability to make me happy. Even though you left Ann Arbor, the ridiculousness of our friendship continues.

Most importantly, I thank my family for their love, support, and encouragement throughout my life. Along with my parents and brother, my entire extended family has shaped my life and instilled values in me that I am still proud to hold. I was fortunate to grow up with all of my family around me. My cousins were my best friends and my aunts and uncles often acted as parents to me. My brother has always been my best friend and someone that I can count on. The sacrifices that my parents and grandparents made throughout their lives have made my current life and education possible. I cannot thank them enough for that. It has been difficult to be away from my family for so long, but they were in my thoughts every day.

TABLE OF CONTENTS

LIST OF FIGURES

CHAPTER FOUR: AGING DECREASED MECHANICAL PROPERTIES OF BONE BY COMPROMISING TISSUE QUALITY, NOT QUANTITY, IN MURINE TIBIAE

CHAPTER FIVE: COMPOSITIONAL CHANGES OF BONE MINERAL AND MATRIX HAVE ASSOCIATIONS WITH MECHANICAL PROPERTIES THAT MAY DEPEND ON BONE AGE AND INITIAL COMPOSITION

APPENDIX A: MICRO- AND NANO-STRUCTURAL ANALYSES OF DAMAGE IN BONE

APPEDNIX B: VALIDATION OF A PORTABLE DEVICE FOR INSTRUMENTED INDENTATION

APPENDIX C: PROTOCOL FOR MECHANICAL TESTING OF TIBIAE

APPENDIX E: RAMAN - NANOINDENTATION PROTOCOL

LIST OF TABLES

CHAPTER FIVE: COMPOSITIONAL CHANGES OF BONE MINERAL AND MATRIX HAVE ASSOCIATIONS WITH MECHANICAL PROPERTIES THAT MAY DEPEND ON BONE AGE AND INITIAL COMPOSITION

APPENDIX A: MICRO- AND NANO-STRUCTURAL ANALYSES OF DAMAGE IN BONE

APPEDNIX B: VALIDATION OF A PORTABLE DEVICE FOR INSTRUMENTED INDENTATION

LIST OF APPENDICES

ABSTRACT

Fractures are the most frequent health problem associated with bone and represent a significant clinical and economic burden. Clinically, fracture risk is diagnosed by low bone mass and interventions to reduce fracture risk are designed to increase mass. However, aging and interventions, like exercise, influence fracture risk by more than what changes in mass predict, indicating that exercise and aging alter skeletal integrity by altering tissue quality, not just quantity. Currently, there is no clear understanding of how tissue quality contributes to skeletal integrity or how it can be altered by external influences. Therefore, this study examined the hypothesis that exercise and aging in adult mice would alter bone composition leading to altered mechanical competence, even when adjusting for changes to bone size and shape.

Exercise significantly improved strength and resistance to fatigue-induced damage in young mice, but had no measured benefit in old mice. In young mice, exercise also increased mineralization and decreased carbonate substitution. Aging significantly reduced structural and tissue-level mechanical properties and increased mineral crystal size, carbonate substitution, and microcracking. Compositional changes with exercise and aging occurred in pre-existing bone (determined by micro-CT and calcein labeling) and mechanical improvements were observed without significant increases in bone size, demonstrating that bone can adapt to external stimuli by altering tissue quality without requiring modeling or remodeling. Further, colocalization of compositional and mechanical measurements by Raman microspectroscopy and nanoindentation provided corroborative evidence that the observed compositional changes contributed significantly to the observed changes in mechanical competence, but in an age dependent manner.

This work challenges conventional theories about bone adaptation and the influence of bone composition on mechanical integrity. It was demonstrated for the first time that exercise and aging can modulate bone composition, and therefore tissue-level mechanical properties, even in the absence of bone formation or remodeling. Therefore, changes in tissue quality may often be overlooked because they may occur without significant changes in bone mass. This work also illustrates the potential utility of using compositional markers in diagnosing skeletal fragility but warns against making sweeping conclusions about the consequences of compositional changes in bone.

CHAPTER ONE

INTRODUCTION

FRAGILITY FRACTURES: DIAGNOSIS AND THE INFLUENCE OF AGE AND EXERCISE

Fractures are the most frequent and significant health problem associated with bone. The most troublesome and potentially avoidable of these injuries are fragility fractures, which can occur in the absence of any traumatic event. Osteoporotic fractures are one such injury with an incidence of 1.5 million per year in the United States resulting in 12-18 billion dollars in direct health care costs [1]. Osteoporosis, the disease associated with these fractures, may be responsible for 80-95 percent of all hip and spine fractures in women older than 45 years [2] and is becoming a greater problem because of the aging population in the United States. By 2010, an estimated 12 million people will have osteoporosis [3]. Although osteoporotic fractures generally occur in older individuals, stress fractures and spontaneous fractures are two examples of injuries that affect young individuals and can also occur in the absence of a traumatic event. In the United States alone, nearly half a million runners will suffer a stress fracture each year [4].

The risk factors for these types of injury are unclear though many consider bone mass to be the most important factor. Bone mass is a generic term that refers to the amount of bone tissue present at specific anatomical sites, such as the proximal femur, wrist or vertebra. Most often bone mass is measured by dual energy X-ray absorptiometry (DXA) which measures mass in terms of areal bone mineral density (aBMD), the amount of bone mineral divided by the scanned area. The calculation of aBMD ignores the depth of bone

being scanned because it cannot be determined by traditional X-ray techniques. This limitation also prevents any inference about bone shape, geometric distribution or trabecular architecture. Therefore, bone mass scans cannot discriminate the relative contributions of bone depth, bone volume fraction, or tissue volumetric mineral density to aBMD. As a result, bone mass measured in the clinic does not directly correspond to the better defined measurements of bone geometry and volumetric density used in most laboratory experiments. Bone mass is presumed to be most closely related to total tissue volume at the scan site because changes in aBMD are primarily attributed to alterations in bone tissue volume, not tissue volumetric mineral density.

Currently, DXA scans are used to diagnose osteoporosis and evaluate interventions to the disease. Similarly, attempts have been made to use bone mass in risk assessment of stress fractures. However, there is growing evidence that "tissue quality" and not just quantity plays a significant role in determining the mechanical competence of bone and risk of fracture. Changes to bone mass and risk of falling inadequately predict increased risk of fracture in the elderly and therefore point to reductions in the material properties of bone with age [5-10]. Similarly, stress fractures and spontaneous fractures in non-elderly individuals often have no clear association with bone mass [4, 11]. There is also concern that interventions like antiresorptive drug treatments may compromise tissue quality by suppressing bone's repair mechanism, despite increasing bone mass, and eventually lead to increased fracture risk [12-14].

The shortcoming of bone scans is that they indicate how much bone tissue is present but provide little information about the quality of that tissue. There are many properties besides bone mass that may influence skeletal integrity, such as material distribution, mineralization, chemical composition, microscopic and macroscopic architecture, tissue-level mechanical properties, microdamage, remodeling health, and fatigue resistance. However, clinical diagnosis of bone health is still conducted primarily through the use of bone mass scans. Further, the effects of external influences on skeletal integrity – such as exercise, nutrition and drug treatments – have been largely judged through their effect on

bone mass [7]. As a result, there is an incomplete understanding of how external influences may contribute to fracture risk.

Exercise is one such external influence that may impact skeletal integrity and has been recommended by the United States Office of the Surgeon General as a potentially effective treatment against fragility fractures [1]. Traditional thought is that the primary benefit of exercise is increased bone mass because the mechanical loading associated with exercise can create an osteogenic response [15-19]. However, changes in bone mass alone do not explain the decreased incidence of fracture in individuals who exercise. For example, fracture risk in elderly women decreases with physical activity even when risk is adjusted for bone mineral density or number of falls [20]. Despite this evidence, the Surgeon General attributes the benefits of exercise completely to changes in bone mass and fall risk and have not considered improvements to tissue quality as a potential benefit of exercise.

The diagnosis and treatment of bone fragility could be improved through a better understanding what contributes to "tissue quality" and how it affects overall affects skeletal integrity. Additionally, it is important to understand how tissue quality can be altered by external influences under patient control, such as exercise.

THE CONTRIBUTION OF TISSUE QUALITY TO SKELETAL INTEGRITY

Despite its shortcomings as a solitary diagnostic for skeletal fragility, there are currently few alternatives to replace or supplement bone scans in the clinical evaluation of bone. There, however, have been recent and ongoing efforts to develop new techniques for *in vivo* monitoring of bone compositional and mechanical properties [21-27]. If these techniques are successfully developed, their clinical utility will not be realized until there is a clearer understanding of how the properties they measure contribute to skeletal fragility.

Many investigations have implicated tissue properties in contributing to bone's mechanical competence, but the findings of these studies are often conflicting. For instance, mineral and matrix composition are believed to be important determinants of tissue quality but clear associations between composition and tissue quality have not been established. Increasing levels of mineralization, carbonate substitution, mineral crystallinity, and collagen cross-linking have been both positively and negatively associated with mechanical properties and fracture risk [28-35]. Similarly, formation of microdamage has been associated with both increased and decreased toughness of bone [36-44]. However, bone's ability to resist excessive accumulation of microdamage may be an important determinant of fracture risk. Accumulation and coalescence of microdamage into larger cracks is a likely mechanism for repetitive loading injuries, like stress and osteoporotic fractures. Moreover, resorptive cavities associated with the targeted remodeling of microdamage may further weaken the bone and create a positive feedback cycle of damage formation and bone resorption [6, 7, 44].

It is unclear how tissue properties contribute to overall mechanical competence of bone and fracture risk. There is even less understanding of what influences age and exercise may have on tissue properties and their relation to fracture risk. Because fracture risk cannot be measured in many experimental designs, whole-bone mechanical properties of bone are often used as a corollary to fracture risk. In the same way, tissue-level mechanical properties may be a suitable metric for tissue quality. Tissue-level mechanical properties are likely a significant determinant of skeletal integrity because overall mechanical competence of any material is the aggregate of size, shape, and material properties. By using bone's material properties as an outcome metric for tissue quality, the contributions of composition and microdamage on skeletal integrity can be evaluated.

AIMS & HYPOTHESES

Increased risk of skeletal fracture in older individuals has been primarily attributed to decreased bone mass. However, clinical and experimental evidence suggests that

reductions of tissue quality also play an important role in age-related skeletal fragility. Similarly, while the benefits of exercise are primarily believed to be increased bone mass, exercise decreases fracture risk more than what changes to bone mass would predict. Therefore, this study investigated how age and exercise induced changes to bone tissue quality, in addition to bone quantity, could influence skeletal integrity.

> ***Global Hypothesis:*** *Age and exercise in a murine model will alter bone mineral and matrix composition, thereby affecting tissue-level mechanical properties and overall skeletal integrity.*

The global hypothesis was subdivided into three separate hypotheses that were tested in separate sets of experiments.

Hypothesis 1 – Exercise may not only influence bone size, but also bone composition and tissue-level strength and fatigue resistance.

> Aim 1: To test this hypothesis, we employed 16 week old male C57Bl/6 mice in a short-term exercise model that consisted of running on a treadmill, 30 minutes a day for 21 consecutive days. After sacrifice, a randomly selected tibia from each mouse was fatigued *ex vivo* while the contralateral tibia remained nonfatigued. Interactive effects of fatigue and exercise were assessed on mechanical properties (by four point bending), composition (by Raman microspectroscopy), and microdamage (by fuchsin staining and histomorphometry). A baseline group, sacrificed on day 1, was included to evaluate growth effects on bone size and shape (by micro-computed tomography) and mechanical properties.

Hypothesis 2 – Aging results in decreased skeletal integrity not only through reduced bone size, but also through altered composition, increased microdamage, decreased material properties, and decreased adaptation to mechanical loading.

Aim 2: A murine aging model was used, examining the tibiae of young, but skeletally mature, male mice (5 month old) and old male mice (19 months old). The effects of aging were assessed on whole-bone and tissue-level mechanical properties (by four point bending), composition (by Raman microspectroscopy), microdamage (by fuchsin staining and histomorphometry), and bone geometric properties (by micro-computed tomography). Additionally, the ability of exercise to modulate those properties was examined in each age group, by subjecting weight and age-matched groups of mice to a short-term exercise program and then conducting the same assays.

Hypothesis 3 – Tissue-level mechanical properties are related to composition and size of bone mineral crystals as well as maturity of collagen cross-links.

Aim 3: Femora from mice used in Aims 1 and 2 were used to establish correlations between composition and mechanical properties. A 60 μm marker system was used to ensure that compositional measurements (by Raman microspectroscopy) and mechanical measurements (by nanoindentation) were taken at the same location in each bone. Multivariate regression analyses were conducted using Raman metrics as covariates and nanoindentation metrics as dependent variables. The influence of mouse age group on the regressions was also investigated.

Aim 1 is addressed in Chapter 2. In young mice, exercise resulted in improved tissue-level strength over baseline and control tibiae, without significant bone formation. Exercise also significantly increased resistance to microdamage formation and cross-link reduction by *ex vivo* fatigue. The improvements in tissue-strength and fatigue resistance by exercise were accompanied by a ubiquitous increase in mineralization and decrease in carbonate substitution throughout the mid-diaphysis. Because compositional changes took place in pre-existing bone and mechanical improvements were observed without significant increases in bone size, it is concluded that bone can adapt to external stimuli by altering tissue quality, even in the absence of a formation or remodeling response.

In Chapter 3, this work is expanded to address Aim 2 by adding exercised and non-exercised groups of old mice. Compared to young mice, old mice had significantly reduced structural and tissue-level mechanical properties, larger mineral crystals with increased carbonate substitution, and significantly increased microcracking. There were no changes to bone size or shape with aging that would account for the reductions in whole-bone mechanical properties, indicating that the changes in composition, damage, and material properties were the primary source of reduced skeletal integrity. Finally, whereas the exercise program significantly improved tissue strength and fatigue resistance in young mice, it provided no measured benefit in old mice. The data presented in this chapter demonstrates that changes to tissue quality with aging can occur in the absence of changes to bone size and can significantly impact the mechanical competence of bones.

Because the assays used in Chapters 2 and 3 required destruction of tibiae, direct associations could not be made between composition and mechanical properties. Therefore the work presented in Chapter 4 attempted to establish direct correlations between composition and mechanical properties (Aim 3) by using nondestructive sample preparation techniques and Raman microspectroscopy, which is also nondestructive, followed by nanoindentation. Significant correlations were found between bone composition and mechanical properties. However, the mechanical consequence of compositional changes in bone may depend on the age and initial compositional state of the bone. These results highlight the potential utility of using bone compositional measurements in diagnosing skeletal fragility but also show the difficulty in making sweeping conclusions about the effects of compositional changes in bone.

Collectively, this work demonstrates for the first time that external stimuli and aging modulate bone composition, and therefore tissue-level mechanical properties, even in the absence of bone formation or remodeling. These findings make evident the importance of including measures of tissue quality in diagnosing fracture risk and evaluating interventions designed to decrease skeletal fragility. The results also demonstrate that

currently changes to tissue quality can easily be overlooked because they may not always be accompanied with detectable changes in bone mass. There is therefore great potential for improving diagnosis and treatment of skeletal fragility by inclusion of markers for tissue quality. However, much work remains before markers for tissue quality can be used in clinical evaluations with confidence.

REFERENCES

1. United States. Public Health Service. Office of the Surgeon General. Bone health and osteoporosis. (2004).
2. Melton, L. J.,3rd *et al*. Fractures attributable to osteoporosis: report from the National Osteoporosis Foundation. *J. Bone Miner. Res.* 12(1): 16-23 (1997).
3. National Osteoporosis Foundation. America's bone health: The state of osteoporosis and low bone mass in our nation. (2002).
4. Burr, D. B. & Milgrom, C. *Musculoskeletal Fatigue and Stress Fractures*. (2001).
5. Allolio, B. Risk factors for hip fracture not related to bone mass and their therapeutic implications. *Osteoporos. Int.* 9 Suppl 2: S9-S16 (1999).
6. Burr, D. B. *et al*. Bone microdamage and skeletal fragility in osteoporotic and stress fractures. *J. Bone Miner. Res.* 12(1): 6-15 (1997).
7. Heaney, R. P. Is the paradigm shifting? *Bone* 33(4): 457-465 (2003).
8. Marshall, D., Johnell, O. & Wedel, H. Meta-analysis of how well measures of bone mineral density predict occurrence of osteoporotic fractures. *BMJ* 312(7041): 1254-1259 (1996).
9. McCreadie, B. R. & Goldstein, S. A. Biomechanics of fracture: is bone mineral density sufficient to assess risk? *J. Bone Miner. Res.* 15(12): 2305-2308 (2000).
10. Sandor, T., Felsenberg, D. & Brown, E. Comments on the hypotheses underlying fracture risk assessment in osteoporosis as proposed by the World Health Organization. *Calcif. Tissue Int.* 64(3): 267-270 (1999).
11. Paschalis, E. P. *et al*. Bone fragility and collagen cross-links. *J. Bone Miner. Res.* 19(12): 2000-2004 (2004).
12. Grynpas, M. Age and disease-related changes in the mineral of bone. *Calcif. Tissue Int.* 53 Suppl 1: S57-64 (1993).
13. Mashiba, T. *et al*. Suppressed bone turnover by bisphosphonates increases microdamage accumulation and reduces some biomechanical properties in dog rib. *J. Bone Miner. Res.* 15(4): 613-620 (2000).
14. Mashiba, T. *et al*. Effects of suppressed bone turnover by bisphosphonates on microdamage accumulation and biomechanical properties in clinically relevant skeletal sites in beagles. *Bone* 28(5): 524-531 (2001).
15. Gordon, K. R., Perl, M. & Levy, C. Structural alterations and breaking strength of mouse femora exposed to three activity regimens. *Bone* 10(4): 303-312 (1989).
16. Hoshi, A., Watanabe, H., Chiba, M. & Inaba, Y. Bone density and mechanical properties in femoral bone of swim loaded aged mice. *Biomed. Environ. Sci.* 11(3): 243-250 (1998).

17. Mosley, J. R. & Lanyon, L. E. Strain rate as a controlling influence on adaptive modeling in response to dynamic loading of the ulna in growing male rats. *Bone* 23(4): 313-318 (1998).

18. Umemura, Y., Baylink, D. J., Wergedal, J. E., Mohan, S. & Srivastava, A. K. A time course of bone response to jump exercise in C57BL/6J mice. *J. Bone Miner. Metab.* 20(4): 209-215 (2002).

19. Warden, S. J. *et al*. Bone adaptation to a mechanical loading program significantly increases skeletal fatigue resistance. *J. Bone Miner. Res.* 20(5): 809-816 (2005).

20. Gregg, E. W., Cauley, J. A., Seeley, D. G., Ensrud, K. E. & Bauer, D. C. Physical activity and osteoporotic fracture risk in older women. Study of Osteoporotic Fractures Research Group. *Ann. Intern. Med.* 129(2): 81-88 (1998).

21. Hansma, P. K., Turner, P. J. & Fantner, G. E. Bone diagnostic instrument. *Rev. Sci. Instrum.* 77(7): 075105 (2006).

22. Hansma, P. *et al*. The bone diagnostic instrument II: Indentation distance increase. *Rev. Sci. Instrum.* 79(6): 064303 (2008).

23. Schulmerich, M. V., Dooley, K. A., Morris, M. D., Vanasse, T. M. & Goldstein, S. A. Transcutaneous fiber optic Raman spectroscopy of bone using annular illumination and a circular array of collection fibers. *J. Biomed. Opt.* 11(6): 060502 (2006).

24. Schulmerich, M. V. *et al*. Noninvasive Raman tomographic imaging of canine bone tissue. *J. Biomed. Opt.* 13(2): 020506 (2008).

25. Wang, X. *et al*. Detection of trabecular bone microdamage by micro-computed tomography. *J. Biomech.* 40(15): 3397-3403 (2007).

26. Gluer, C. C. Quantitative Ultrasound--it is time to focus research efforts. *Bone* 40(1): 9-13 (2007).

27. Marin, F., Gonzalez-Macias, J., Diez-Perez, A., Palma, S. & Delgado-Rodriguez, M. Relationship between bone quantitative ultrasound and fractures: a meta-analysis. *J. Bone Miner. Res.* 21(7): 1126-1135 (2006).

28. Akkus, O., Adar, F. & Schaffler, M. B. Age-related changes in physicochemical properties of mineral crystals are related to impaired mechanical function of cortical bone. *Bone* 34(3): 443-453 (2004).

29. Paschalis, E. P. *et al*. Spectroscopic characterization of collagen cross-links in bone. *J. Bone Miner. Res.* 16(10): 1821-1828 (2001).

30. Zioupos, P., Currey, J. D. & Hamer, A. J. The role of collagen in the declining mechanical properties of aging human cortical bone. *J. Biomed. Mater. Res.* 45(2): 108-116 (1999).

31. Ager, J. W., Nalla, R. K., Breeden, K. L. & Ritchie, R. O. Deep-ultraviolet Raman spectroscopy study of the effect of aging on human cortical bone. *J. Biomed. Opt.* 10(3): 034012 (2005 May-Jun).

32. Gordon, K. R., Burns, P. & Keller, G. Experimental changes in mineral content of juvenile mouse femora. *Calcif. Tissue Int.* 51(3): 229-232 (1992).

33. Camacho, N. P. *et al*. The material basis for reduced mechanical properties in oim mice bones. *J. Bone Miner. Res.* 14(2): 264-272 (1999).

34. Burr, D. B. The contribution of the organic matrix to bone's material properties. *Bone* 31(1): 8-11 (2002).

35. Viguet-Carrin, S., Garnero, P. & Delmas, P. D. The role of collagen in bone strength. *Osteoporos. Int.* 17(3): 319-336 (2006).

36. Carter, D. R. & Hayes, W. C. Compact bone fatigue damage--I. Residual strength and stiffness. *J. Biomech.* 10(5-6): 325-337 (1977).

37. Norman, T. L., Yeni, Y. N., Brown, C. U. & Wang, Z. Influence of microdamage on fracture toughness of the human femur and tibia. *Bone* 23(3): 303-306 (1998).

38. Reilly, G. C. & Currey, J. D. The effects of damage and microcracking on the impact strength of bone. *J. Biomech.* 33(3): 337-343 (2000).

39. Danova, N. A. *et al*. Degradation of bone structural properties by accumulation and coalescence of microcracks. *Bone* 33(2): 197-205 (2003).

40. Schaffler, M. B., Choi, K. & Milgrom, C. Aging and matrix microdamage accumulation in human compact bone. *Bone* 17(6): 521-525 (1995).

41. Sobelman, O. S. *et al*. Do microcracks decrease or increase fatigue resistance in cortical bone? *J. Biomech.* 37(9): 1295-1303 (2004).

42. Vashishth, D., Behiri, J. C. & Bonfield, W. Crack growth resistance in cortical bone: concept of microcrack toughening. *J. Biomech.* 30(8): 763-769 (1997).

43. Vashishth, D., Tanner, K. E. & Bonfield, W. Experimental validation of a microcracking-based toughening mechanism for cortical bone. *J. Biomech.* 36(1): 121-124 (2003).

44. Sahar, N. D., Hong, S. I. & Kohn, D. H. Micro- and nano-structural analyses of damage in bone. *Micron* 36(7-8): 617-629 (2005).

CHAPTER TWO

EXERCISE IMPROVED STRENGTH, FATIGUE RESISTANCE AND MINERAL COMPOSITION OF PRE-EXISTING TISSUE IN MURINE TIBIAE

ABSTRACT

This chapter examined the hypothesis that exercise could improve tissue quality by altering bone composition and improving fatigue resistance and mechanical properties, even when adjusting for changes to bone size and shape. To test this hypothesis, 16 week old male C57Bl/6 mice were employed in a short-term exercise model that consisted of running on a treadmill, 30 minutes a day for 21 consecutive days. After sacrifice, a randomly selected tibia from each mouse was fatigued *ex vivo* while the contralateral tibia remained nonfatigued. Interactive effects of fatigue and exercise were assessed on mechanical properties (by four point bending), composition (by Raman microspectroscopy), and microdamage (by fuchsin staining and histomorphometry). A baseline group, sacrificed on day 1, was included to evaluate growth effects on bone size and shape (by micro-computed tomography) and mechanical properties. Exercise resulted in improved tissue-level strength over baseline and control bones, without significant bone formation. Exercise also significantly increased resistance to microdamage formation and cross-link reduction by *ex vivo* fatigue. The improvements in tissue-strength and fatigue resistance by exercise were accompanied by a ubiquitous increase in mineralization and decrease in carbonate substitution throughout the mid-diaphysis. Because compositional changes took place in pre-existing bone and mechanical improvements were observed without significant increases in bone size, it is

concluded that bone can adapt to external stimuli by altering tissue quality, even in the absence of a formation or remodeling response.

INTRODUCTION

Fractures are the most frequent and significant health problem associated with bone. While some fractures occur by a single traumatic overloading of bone, many fractures, such as osteoporotic and stress fractures, can occur in the absence of any trauma. These non-traumatic fractures present a significant clinical and economic burden. In the United States alone, nearly half a million runners will suffer a stress fracture each year [1] and osteoporosis may be responsible for 80-95 percent of all hip and spine fractures in women older than 45 years [2]. These non-traumatic injuries are indicative of compromised bone health, a combination of bone quality and quantity, as healthy bone should not fail from physiological loading.

In the clinic, there has been little focus on bone quality and almost all attention has been given to bone quantity, or mass, as the primary parameter defining skeletal integrity. Bone mass scans are used to diagnose osteoporosis and evaluate interventions to the disease, but mass alone is insufficient to predict fracture risk [3-8]. For instance, fracture risk increases with age even when risk is adjusted for bone mass [9]. There is also concern that interventions like antiresorptive drug treatments may compromise tissue quality, despite increasing bone mass, and eventually lead to increased fracture risk [10-12].

While it has been generally accepted that tissue-level factors such as material properties and composition affect skeletal integrity, clinically their contributions have been considered peripheral compared to bone mass [8]. Further, the effects of external influences on skeletal integrity – such as exercise, nutrition and drug treatments – have been largely judged through their effect on bone mass [8]. Therefore, there is little knowledge of what effect these external factors have on material properties or composition. Diagnosis and treatment of bone fragility could be improved through a

better understanding of how tissue quality affects skeletal integrity and how tissue quality is altered by external influences.

Exercise is one such external influence that may impact skeletal integrity and has been recommended by the United States Office of the Surgeon General as a potentially effective treatment against fragility fractures [13]. Traditional thought is that the primary benefit of exercise is increased bone mass because the mechanical loading associated with exercise can create an osteogenic response [14-18]. However, changes in bone mass alone do not explain the decreased incidence of fracture in individuals who exercise. For example, fracture risk in elderly women decreases with physical activity even when risk is adjusted for bone mineral density or number of falls [19]. Despite this evidence, the Surgeon General attributes the benefits of exercise completely to changes in bone mass and fall risk and has not considered improvements to tissue quality as a potential benefit of exercise.

Tissue-level properties that may be important to mechanical competence of bone are tissue strength, mineral and matrix composition, and resistance to damage accumulation by fatigue. Tissue strength is important because overall strength of any material is the aggregate of size, shape, and material-level strength. Bone composition is also a likely determinant of skeletal competence as changes to mineralization, carbonate substitution, and collagen cross-linking have all been associated with changes to mechanical integrity [20-23]. Bone's ability to resist excessive accumulation of microdamage may also be an important determinant of skeletal integrity as excessive microdamage reduces elastic modulus, strength, and toughness [24-28]. Accumulation and coalescence of microdamage into larger cracks is a likely mechanism for repetitive loading injuries, like stress and osteoporotic fractures. Moreover, resorptive cavities associated with the targeted remodeling of microdamage may further weaken the bone and create a positive feedback cycle of damage formation and bone resorption [4, 8, 29].

This study examined bone adaptation to exercise, focusing on alterations to tissue quality. The hypothesis was that exercise could improve tissue quality by altering bone

composition and improving fatigue resistance and mechanical properties, even when adjusting for changes to bone size and shape. A short-term murine exercise model was employed that is capable of altering tissue-level mechanical properties in the tibia [30]. The effects of exercise on mineral and matrix composition, tissue-level mechanical properties, and resistance to fatigue-induced damage were evaluated.

MATERIALS AND METHODS

Experimental Design

Sixteen week old C57BL/6 male mice were approved for use in this study by the University of Michigan Committee on Use and Care of Animals (protocol # 8518). At this age, mice are nearing skeletal maturity [31-34]. Mice were divided into two groups, control and exercise, with 30 animals in each group. This group size was chosen through a power analysis with expected variances based on previous experiments [30]. Control mice remained in their cages for the duration of the experiment while exercise mice were run on a treadmill (12 m/min, 5 degree incline) 30 minutes a day for 21 consecutive days [30]. Calcein injections were given on day 3 and day 17 to mark bone deposition and resorption. All mice were sacrificed on the 22nd day and left and right tibiae were harvested, stripped of soft tissue, and stored in calcium buffered saline (-80 °C). A baseline group (N=16, sacrificed on day 1) was also included to evaluate growth effects. All mice had access to food and water ad libitum throughout the experiment.

All tibiae were first analyzed by micro-computed tomography (micro-CT) to determine cross-sectional geometric properties. Bones from half of the mice in control and exercise groups were then designated for mechanical testing while bones from the other half were designated for quantification of microdamage. Bones used for microdamage analysis were also used for compositional analysis via Raman microspectroscopy. Within each mouse, a randomly selected tibia was mechanically fatigued *ex vivo* while the contralateral tibia in each mouse was used as a nonfatigued control. Thus, mechanical properties from nonfatigued and fatigued bones were determined in each mouse of the

first subset (N=15 mice per control and exercise groups) while microdamage and Raman spectra from nonfatigued and fatigued bones were quantified for each mouse of the second subset (N=15 mice per control and exercise groups). Baseline bones were not fatigued and only evaluated by micro-CT and mechanical testing.

Micro-Computed Tomography

Whole tibiae were scanned with a voxel size of 25 μm using a GE/EVS MS-8 specimen scanner and then analyzed with MicroView software (General Electric Health Care) and custom written scripts [35, 36]. A 125 μm thick transverse section from a standard location (22% of distance from the tibio-fibular junction to the tibial plateau) was selected for analysis. This mid-diaphyseal site lies in the center of the mechanical testing region and is the same location used for microdamage analysis (see below).

Fatigue Protocol

Tibiae were fatigued by cyclic four-point bending (9 mm outer span, 3 mm inner span), using a material testing machine (Admet eXpert 450 Universal Testing Machine). The loading fixture was custom designed to meet ASTM Standard D6272-02 [37] for four point bending. Additionally, the loading fixture was mounted on a pivot and had cylindrical rollers as loading points to minimize testing errors [38].

Fatigue loading was normalized for each specimen to generate a peak load in each cycle that would produce a peak stress of 95 MPa at the medial surface (the side of tension). The load required to produce 95 MPa was calculated by beam bending theory using the average geometry from the 3mm region between the inner loading points, determined by micro-CT. Fatigue loading was then conducted under load control using a 2Hz haversine waveform for 21,600 cycles. Specimens were kept in a calcium buffered saline bath during testing to avoid dehydration and loss of mineral [39].

Mechanical Testing

Mechanical properties were determined by monotonic loading of tibiae to failure under four point bending, using the same testing machine and loading fixture as in the fatigue protocol. Tests were conducted with the medial side of the mid-diaphysis in tension and under position control with a crosshead displacement of 0.025 mm/s until failure. Force and displacement data were recorded and converted to stress and strain using beam bending theory and geometric measurements taken by micro-CT at the fracture site. A MatLab program (The MathWorks, Inc.) was created to perform this transformation and calculate all bone-level mechanical properties and estimated pre-yield tissue-level mechanical properties. Post-yield properties were not transformed to the stress-strain domain because conventional beam bending theory is invalid after yield.

Quantification of Microdamage

Bones were stained *en bloc* with 1% basic fuchsin in a graded series of ethanol solutions, allowing thorough penetration of stain and dehydration of the bones [40-42]. Staining the whole bone before sectioning ensured that damage produced during processing would not be stained and would therefore be excluded from damage quantification. After staining, the tibiae were embedded in Koldmount (Vernon-Benshoff Company), a low temperature curing acrylic. A transverse cross section was removed from the mid-diaphysis of each bone using a low-speed sectioning saw (South Bay Technology), and polished to a final thickness of 125 μm. The location of this section matched the location used for geometric analysis and lies in the center of the fatigue testing region.

Sections were imaged using a Bio-Rad MRC-600 laser scanning confocal microscope with a Nikon 60X oil immersion objective and LaserSharp 2000 acquisition software. Confocal microscopy allowed panning through the depth of the specimen to distinguish damage from native bone structures such as blood vessels, lacunae, and canaliculi [29, 43]. Two types of damage were observed: microcracks and diffuse damage. Microcracks were clear, individually distinguishable, linear cracks, while diffuse damage appeared as a dense collection of indistinguishable tiny cracks (Figure A.2). Therefore,

microcracks were quantified by number of cracks and cumulative length per section while diffuse damage was quantified by total area in each section. These metrics were divided by cross-sectional area to obtain a normalized measure of damage per unit area.

Raman Microspectroscopy

After sections were examined for microdamage, the same sections were analyzed by Raman microspectroscopy. A line-focused 785 nm laser (Invictus, Kaiser Optical Systems, Inc.) was focused on the specimens through a NIR-optimized 20 × 0.75 NA objective (Fluar Series, Carl Zeiss, Inc.), producing incident laser power of 98 mW distributed over a 100 μm long line. Raman scatter was collected with a 5 min integration time through the objective and focused into an axial-transmissive spectrograph (HoloSpec f/1.8I, Kaiser Optical Systems Inc.) equipped with a 25-μm slit, providing a maximum spectral resolution of 3-4 cm^{-1} [44]. Spectral data analysis was performed with Matlab (Math Works, Inc.) and GRAMS/32 (Galactic Industries). All spectra were preprocessed by removing detector-generated artifacts (spikes) and subtracting the detector dark current. The extraction of Raman spectra was performed by band target entropy minimization (BTEM) [45].

Band areas were determined for select Raman peaks representing specific components of bone mineral (phosphate, 958 cm^{-1}; carbonate, 1070 cm^{-1}) and bone matrix (hydroxyproline, 851 and 873 cm^{-1}; proline, 917 cm^{-1}; amide-I, 1660 cm^{-1}). The following band area ratios were used to characterize the chemical composition of the bone samples: mineral/matrix ratio (958 / [851+873+917]), carbonate/phosphate ratio (1070 / 958), and collagen cross-linking ratio (1660 / 1690) [21, 46-49]. Mineral/matrix ratio is often defined as the band area ratio of 958/1660 but here the matrix is represented by the summed band areas of the hydroxyproline and proline peaks because the amide-I band area could be altered by changes in cross-linking even if the amount of collagen is unchanged.

Mineral/matrix gives insight into the degree of bone mineralization and carbonate/phosphate ratio is related to the level of carbonate substitution in the apatite lattice [50]. The two peaks at 1660 and 1690 cm^{-1} underlie the amide I band are indicative of changes in collagen cross-linking, with the area ratio between them corresponding to the non-reducible/reducible cross-link ratio [21]. Therefore, the collagen cross-linking ratio increases with increasing number of stable cross-links.

Sixteen spectral lines were collected from each sample. Four circumferentially-oriented lines incrementing radially through the cortical thickness were collected at each of the four quadrants (anterior, posterior, lateral, medial). No significant effect of location was found for any Raman metric, so for each metric the band area ratios were averaged from all sixteen locations to obtain an overall measurement for each specimen.

Statistical Analysis

Statistical analyses were performed using Sigma Stat 3.1 (Systat Software, Inc.). Data from Raman microspectroscopy, mechanical testing, and microdamage quantification were analyzed for effects of exercise and fatigue using two-way analyses of variance (ANOVA) with Student-Newman-Keuls post-hoc tests. When the sample distributions were not normal or had unequal variances, a Mann-Whitney U test was used. For cases where there was no fatigue group (geometric data, baseline comparisons), Student t-tests were used to determine the effects of exercise. For all statistical tests, differences were considered significant for p values less than 0.05.

RESULTS

Microdamage

There were no significant differences in any damage metric between nonfatigued exercise and control bones (Figure 2.1), indicating that the exercise program did not produce microdamage in the tibiae. *Ex vivo* fatigue of bones from control animals significantly

increased the number of cracks, cumulative crack length, and diffuse damage area, per unit area (Figure 2.1, $p = 0.002$, 0.034, and 0.015, respectively). In contrast, fatigue did not significantly increase any damage metric in bones from exercise animals. As a result, fatigued exercise bones had significantly decreased number of cracks, cumulative crack length, and diffuse damage area, per unit area, than fatigued control bones ($p = 0.006$, 0.040, and 0.009, respectively). This data indicates that tibiae from mice subjected to the short-term, moderate intensity exercise program in this investigation were more resistant to fatigue-induced microdamage formation than tibiae from control mice. Average crack length was not significantly altered by fatigue or exercise (Figure 2.1C), indicating that exercise affected resistance to crack initiation more than crack propagation.

Mechanical Properties

In nonfatigued tibiae, exercise led to significantly greater yield strength, ultimate strength, and resilience (energy required to yield the bone) compared to baseline tibiae ($p = 0.013$, 0.016 and 0.09, respectively), whereas control tibiae had no significant improvement in these properties compared to baseline (Figure 2.2). Deformation to failure was significantly reduced in control bones compared to baseline ($p = 0.014$) but not in exercised bones. Ultimate strength in exercised bones was significantly greater than in control bones ($p = 0.050$, Figure 2.3).

Ex vivo fatigue significantly increased ultimate strength in control bones ($p = 0.038$) but not in exercised bones (Figure 2.3). No other mechanical properties were significantly reduced by fatigue loading in control or exercise groups.

Chemical Composition

Exercise significantly increased mineral/matrix ratio ($p = 0.027$) and significantly decreased carbonate/phosphate ratio ($p = 0.023$ by two-way ANOVA, not significant by individual group post hoc test), but had no significant effect on collagen cross-linking ratio (Figure 2.4). Compositional differences between groups were not dependent on

radial location or anatomical quadrant, indicating that differences between groups were due to ubiquitous changes throughout the transverse cross-section.

Fatigue loading of control tibiae significantly decreased mineral/matrix ratio and collagen cross-linking ratio ($p = 0.024$ and 0.003, respectively), but did not significantly alter these properties in exercised bones. As a result, fatigued exercised bones had significantly greater mineral/matrix and cross-linking ratios than fatigued controls ($p = 0.002$ and 0.023, respectively). This pattern of fatigue significantly altering properties in control bones but not exercised bones parallels the effects of fatigue on microdamage (Figure 2.1).

Bone Size and Shape

Between 16 and 19 weeks of age, control bones showed significant periosteal expansion and endocortical resorption in almost all directions (Figure 2.5). This growth led to significantly increased cortical area, average cortical thickness, and second moment of area (I) across both the anterior-posterior (A-P) axis and medial-lateral (M-L) axis (Table 2.2). Because radial expansion occurred in every direction, control tibiae had a similar cross-sectional shape as baseline tibiae, as indicated by the lack of difference in the ratio of M-L to A-P diameters (ML/AP Ratio). There was also significant lengthening of control bones.

In contrast, exercised bones showed significant periosteal expansion on only the medial and lateral surfaces and periosteal resorption on the posterior surface (Figure 2.5). These areas of periosteal expansion and resorption were paired with significant endocortical resorption and expansion, respectively, resulting in a change of shape, indicated by a significantly increased ML/AP ratio compared to baseline (Table 2.2). Second moment of area across the A-P axis was also significantly increased.

Control bones were significantly larger than exercise bones for all geometric properties except ML/AP ratio, for which exercised bones were significantly greater than control

bones. Calcein labeling was not analyzed quantitatively (because there was limited double labeling), but qualitatively showed the same growth patterns observed by micro-CT in control and exercised tibiae. Also, the labeling showed no case of intracortical remodeling in any of the bones. One week before sacrifice, control mice weighed significantly more than exercised mice, but both groups were significantly heavier than baseline mice (Table 2.2).

DISCUSSION

This experiment provides some of the first direct evidence that exercise can improve skeletal fatigue resistance, as indicated by increased resistance to both microdamage accumulation (Figure 2.1) and collagen cross-link reduction (Figure 2.4). Nonfatigued exercised and control bones had similar levels of microdamage, denoting that exercise did not increase microdamage. However, after *ex vivo* fatigue, control bones had 2.2 times greater crack density and 5.2 times greater diffuse damage density than exercised bones (Figure 2.1). In control bones, the fatigue protocol significantly increased number of cracks, cumulative crack length and diffuse damage area. Yet the same fatigue protocol, which is normalized by bone geometry to produce the same peak stress in each bone, did not significantly alter any damage metric in exercised bones. There were no significant differences in average crack length (Figure 2.1C) between any groups, indicating that crack growth was self limiting in all groups. Therefore, the exercise-induced improvement to damage resistance is likely due to an improved resistance to crack initiation. This idea is supported by the increased diffuse damage area in controls, which reflects the formation of many new, tiny cracks.

Paralleling the microdamage data, albeit on a smaller scale, fatigue significantly reduced collagen cross-linking ratio in bones from control mice but not bones from exercised mice (Figure 2.4C). The reduced cross-linking ratio observed in fatigued control bones is indicative of ruptured collagen cross-links [21, 51], suggesting that perhaps increased integrity of cross-links in exercised bones contributed to improved fatigue resistance. However, it is unlikely that exercise directly affected cross-linking because the cross-

linking ratio was similar in nonfatigued control and exercised bones. A more likely explanation for improved fatigue resistance in exercised bones is that improved tissue quality in those bones, for instance improved tissue strength, protected cross-links from being reduced, just as it may have prevented formation of microdamage. While mineral/matrix ratio was also reduced by fatigue in control bones (Figure 2.4A), this was likely artifact of crack formation releasing mineral into the hydrating buffer.

It has long been hypothesized that bone adaptations can improve tissue quality leading to improved fatigue resistance, but until now there has been no direct evidence. Warden et al. observed that bone adaptation to *in vivo* mechanical loading significantly increased *ex vivo* skeletal fatigue resistance [18]. However, improved fatigue resistance was a result of increased bone size and no improvement in fatigue resistance was seen when loading was normalized to bone size. In our study, fatigue loading was normalized to produce the same peak stress in each bone, meaning that improvements to fatigue resistance were due to improvements in tissue quality and not shape or size. Further, peak strains during fatigue should have also been similar between control and exercised bones because elastic moduli were similar between these groups (Figure 2.3B). It can therefore be inferred that improvements to fatigue resistance by exercise occurred at the tissue level.

A possible explanation for enhanced fatigue resistance in exercised mice is that their tibiae had significantly improved tissue-level strength relative to tibiae from control mice (Figure 2.3A). Exercise-induced improvements to tissue quality were also exhibited by significant improvements in yield strength, ultimate strength, and resilience over baseline in exercised bones but not control bones (Figure 2.2). Also, control bones had significantly decreased deformation to failure compared to baseline bones, but exercised bones did not. Therefore, this exercise model increased the gains in pre-yield mechanical properties and decreased the loss of ductility that occurred with normal growth.

Alterations to bone composition by exercise may have been the source of improved tissue-level mechanical properties. Specifically, exercised bones had significantly increased mineral/matrix ratio and significantly decreased carbonate/phosphate ratio

compared to control bones (Figure 2.4), indicating increased mineralization and decreased type B carbonate substitution, respectively [50]. These changes point to secondary mineralization, in which average carbonate substitution can be decreased as a less substituted mineral apatite is deposited onto existing mineral [52-54]. Both increased mineralization [55-57] and decreased carbonate substitution [20] have been associated with increased bone tissue strength.

Exercise-induced changes in composition occurred ubiquitously throughout the mid-diaphyseal cross-section of the tibiae, as there was no significant location dependence on group differences. Furthermore, compositional and mechanical changes occurred with little bone formation or resorption (Figure 2.5, Table 2.2) and no intracortical remodeling found by calcein labeling. For instance, exercised bones compared to baseline bones had a non-significant 3% increase in cortical area, but had significant improvements in mechanical properties, with some properties increasing by as much as 40% (Figure 2.2). Moreover, the assays determined average tissue-level properties, which are independent of bone size. Mechanical properties, fatigue loading and damage metrics were all adjusted for bone size and Raman metrics were spatially averaged in each cross-section. We therefore conclude that exercise induced an adaptation in bone, independent of modeling or remodeling, which improved tissue quality of pre-existing bone.

This adaptation may be in part a physical-chemical response. Exercise increases serum concentration of calcium and phosphorous ions [58, 59] and fluid flow through bone [60, 61], which may alter the chemical environment around mineral crystals and maturation of those crystals. Alternatively, the response may have been controlled by the vast osteocyte network, which is involved in mechanotransduction [62] and covers approximately 100 times more bone surface area than any other cell type [63]. It is possible that osteocytes sense mechanical loading and increase transport of calcium and phosphate to the bone mineral [64, 65] or release factors such as dentin matrix protein 1 (DMP1) [66] to guide mineral formation and homeostasis [67, 68].

The response to exercise observed in these mice implies that tissue quality can be altered by external influences without requiring addition of new bone. This implication may partially explain why exercise decreases fracture risk in the elderly even though it often does not increase bone mass [13, 19, 69]. Studies of bone adaptation to exercise or direct loading most often attibute improvements in mechanical competence to periosteal expansion. In those studies, improvements to the quality of existing bone tissue may still play a signifcant, yet overlooked, role. Bone adapation therefore must be considered in a new context where lack of bone formation in response to an external stimulus does not imply that the stimulus had no effect.

Although it is unlikely that bone growth contributed to altered tissue quality, control and exercise mice did exhibit different cross-sectional growth patterns. Exercised bones grew only in the medial and lateral directions (Figure 2.5), which significantly increased the ML/AP ratio relative to baseline and control bones (Table 2.2). This reshaping would preferentially improve resistance to bending in the medial-lateral direction and was likely an adaptation to medial-lateral bending caused by running on a treadmill. During running, the tibia of a mouse is not perpendicular to the ground but rather extends laterally from the body, potentially creating a medial-lateral bending moment from the ground reaction force. Similar effects of exercise on bone growth patterns were previously observed in 8 week old, C57BL6/129 male mice [30].

Despite having improved tissue-level properties, exercised bones were smaller than controls (Figure 2.5, Table 2.2). Exercise is often thought to be osteogenic [13, 14, 16], but may have temporarily reduced bone growth in this study because of mouse age, short experiment duration, diet, and body weight. Mice were approaching skeletal maturity when exercise was initiated, [31-34] which may have decreased their ability to add bone mass in response to mechanical loading [70]. Body weight, which may influence bone size as much or more than exercise [71], was significantly reduced by exercise (Table 2.2). In addition, the sudden metabolic costs of exercise may have resulted in temporarily blocked support for growth, particularly if there was a chronic shortage of nutrient or energy supply [72]. Indeed, insufficient energy and nutrient supply may have

been a problem for exercised mice as they had no days of rest and were fed a standard lab diet. A high protein diet may be necessary to elicit the osteogenic benefits of exercise in rodents [73]. Further, deposition of new tissue may have been competitively slowed to make more ions and metabolic resources available for improving material properties of existing tissue. Finally, exercise transiently increases corticosterone expression, which can inhibit growth [74-77]. Corticosterone levels may return to normal after 4 weeks [76], which may explain why exercise-induced bone formation in rodents may not be exhibited until after four weeks of exercise [78]. Once the sources of slowed growth are removed, bones will often exhibit a period of accelerated growth to compensate for the lost growth. This catch-up growth may have taken place if exercise subsided, if corticosterone expression returned to normal levels, or if the mice adequately adapted to the demand of exercise [72, 77, 79]. The duration of this experiment was too short to observe catch-up growth or restoration of normal growth. Regardless of the cause, bone tissue quality was improved despite the slowed growth pattern.

The fatigue-induced increase in ultimate strength in control bones (Figure 2.3) could be explained by strain hardening, which can strengthen materials and has been observed in many tissues, including bone [80, 81]. Exercised bones may have been unaffected by strain hardening because they were already precycled by the loading of exercise or because the altered mineral state in exercised bones made them less susceptible to hardening. Although fatigue loading significantly increased microdamage in control bones, it did not negatively impact mechanical properties in either control or exercise groups. It is therefore reasonable to question whether the exercised bones' ability to resist damage accumulation by fatigue is beneficial. There are two considerations. First, the fatigue protocol was short (21,600 cycles), but normal physiological loading would produce two orders of magnitude more cycles per year, which could grow and coalesce cracks. Moderate amounts of microdamage are well tolerated in bone [82-84], but additional microdamage can significantly compromise mechanical integrity [24-27]. Second, microdamage in healthy adults would trigger remodeling, creating temporary resorptive cavities which reduce the continuity of bone and produce stress concentrations. New microdamage may form because of increased strain near resorptive cavities, which

would trigger further remodeling. This positive feedback cycle may play a central role in bone fragility [4, 8, 29]. The damage/remodeling loop combined with the millions of loading cycles associated with normal activity explain why resistance to microdamage formation may be vital to long-term skeletal integrity.

Conclusions

In the tibial mid-diaphysis, this short-term murine exercise model resulted in spatially ubiquitous increases in mineralization and decreases in carbonate substitution, along with increased tissue strength and increased resistance to fatigue-induced microdamage formation and collagen cross-link reduction. These changes reflect an improvement in bone quality at the tissue level, with implications for decreased risk of traumatic fracture (through increased strength) and fragility fracture (through increased fatigue resistance). Compositional changes took place in pre-existing bone and mechanical improvements were observed without significant increases in bone size. These findings challenge traditional views of bone adaptation and suggest that bone may adapt to external stimuli by altering tissue quality, even in the absence of a formation or remodeling response.

Acknowledgements

I would like to thank the co-authors of this work, Kurtulus Golcuk, Michael D. Morris, Steven R. Obreiter, Michael S. Ron and David H. Kohn. I would also like to thank Lisa Winkel and Jaclynn Kreider for their assistance on this project. This study was funded by DoD/US Army DAMD17-03-1-0556, The University of Michigan Regenerative Sciences Training Grant R90-DK071506, NIH P30-AR46024, NIDCR Training Grant DE007057, an American Association for Dental Research Fellowship, and The University of Michigan School of Dentistry.

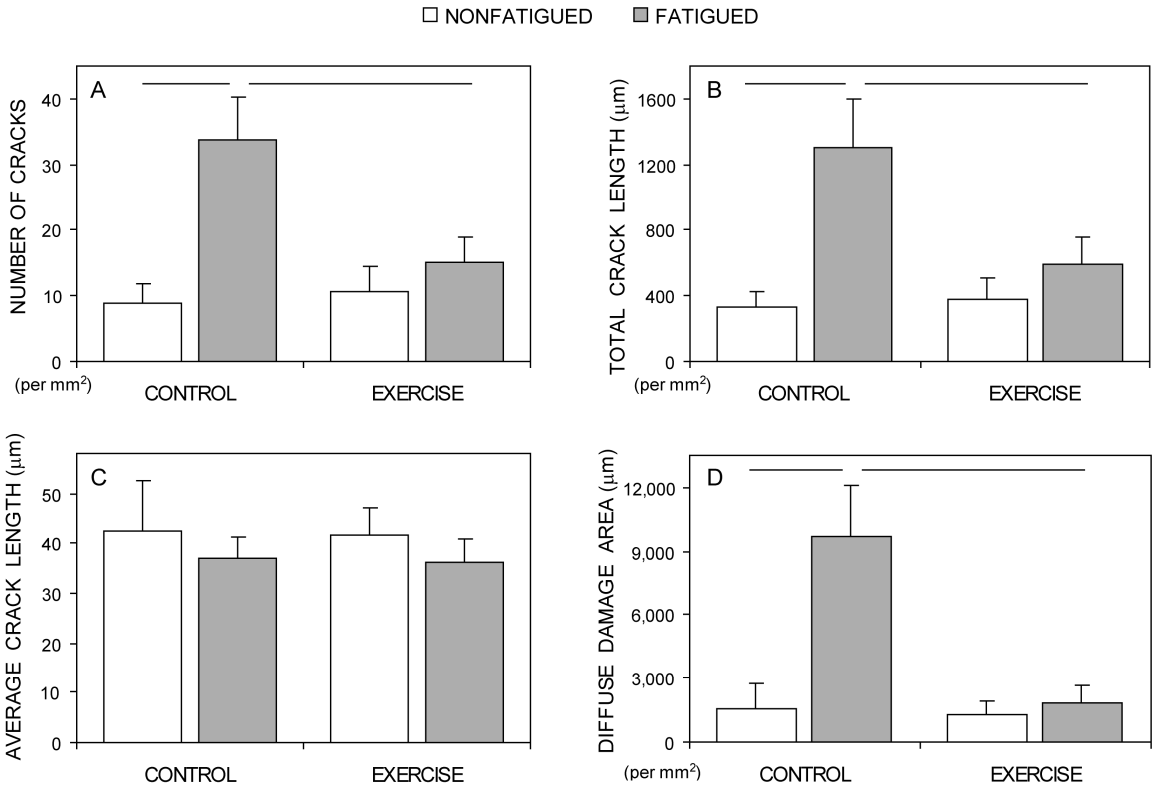

Figure 2.1. Microdamage in transverse cross-sections of tibiae (mean ± SEM). *Ex vivo* fatigue significantly increased the number of cracks (A), the total crack length (B), and diffuse damage area (D), per unit area in tibiae of control mice but not exercised mice. As a result, fatigued exercised bones had significantly less damage than fatigued control bones. C. There were no significant differences in average crack length with fatigue. Exercise did not significantly increase any metric of microdamage. Bars indicate significant differences determined by two-way ANOVA post-hoc tests.

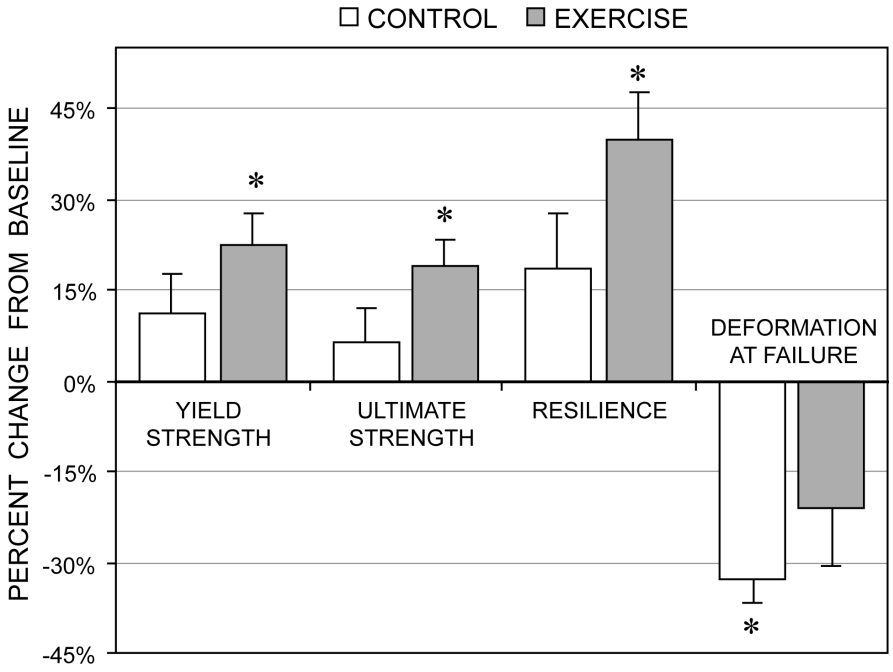

Figure 2.2. Mechanical properties of nonfatigued bones relative to baseline (mean ± SEM). Exercised bones had significant improvements in tissue-level properties (yield strength, ultimate strength, and resilience) over baseline but control bones did not. Deformation to failure was significantly reduced in control bones but not in exercised bones. The baseline values used to normalize control and exercise data are shown in Table 2.1. ∗ indicates significant difference from baseline.

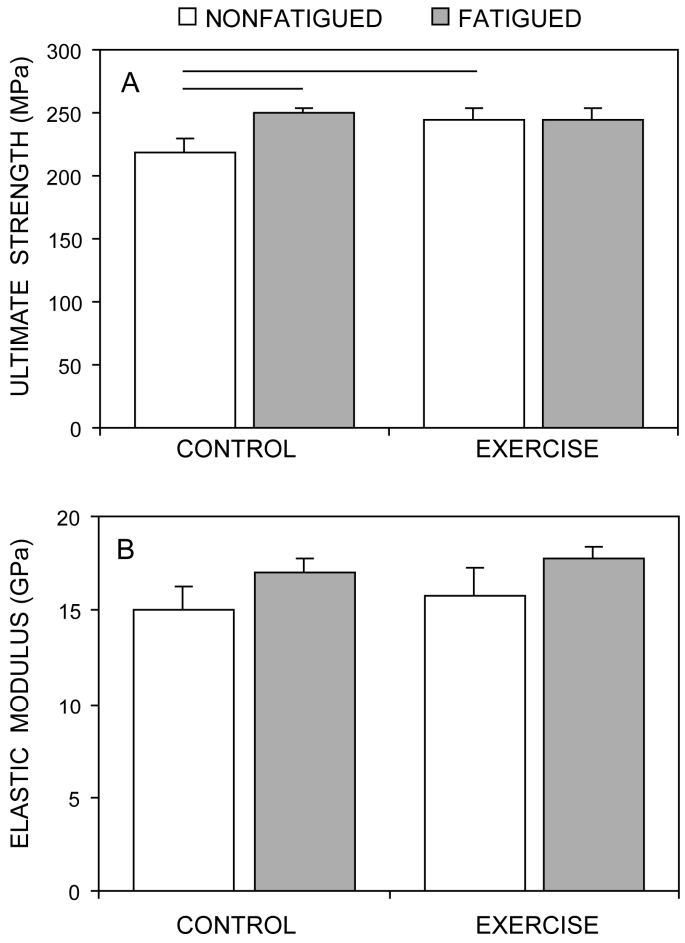

Figure 2.3. Effects of exercise and *ex vivo* fatigue on tissue-level mechanical properties (mean ± SEM). A. Nonfatigued exercised bones had significantly greater ultimate strength than nonfatigued control bones. *Ex vivo* fatigue significantly increased ultimate strength in control bones but not exercised bones. B. There was no significant effect of exercise or fatigue on elastic modulus. Bars indicate significant differences determined by two-way ANOVA post-hoc tests.

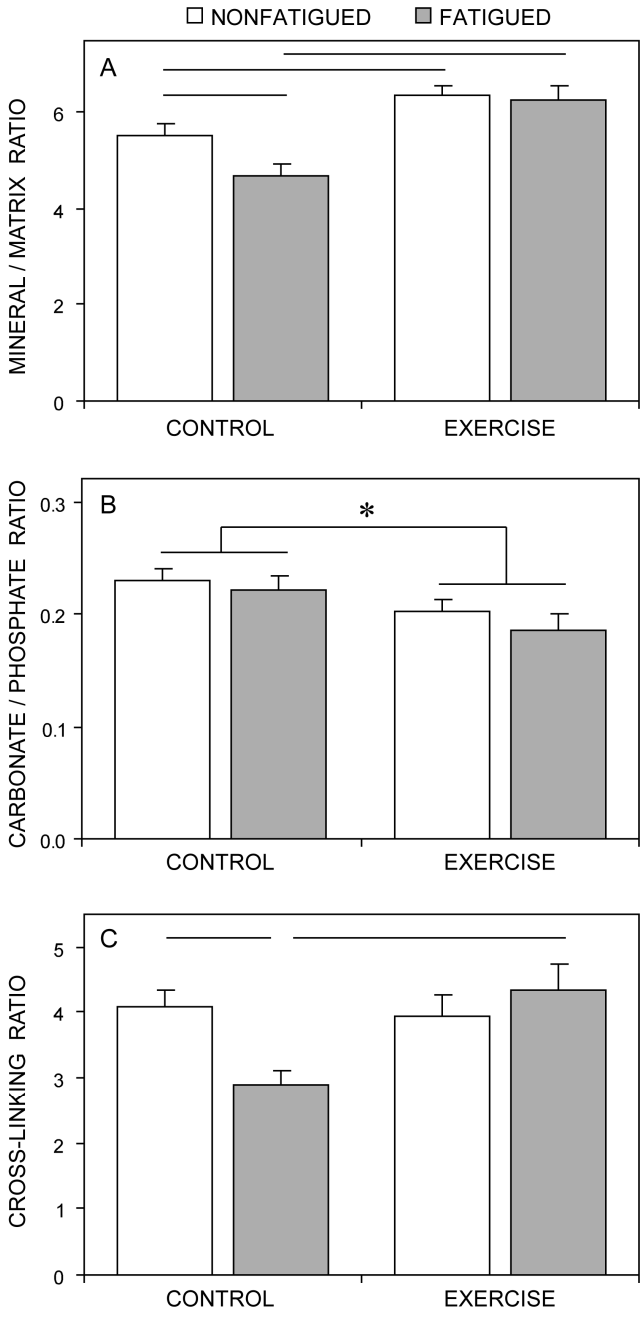

Figure 2.4. Bone composition as measured by Raman microspectroscopy (mean ± SEM). Exercise significantly increased mineral/matrix ratio (A) and decreased carbonate/phosphate ratio (B), but had no significant effect on collagen cross-linking ratio (C). *Ex vivo* fatigue significantly decreased mineral/matrix ratio and cross-linking ratio in control bones but not exercised bones, resulting in significantly lower ratios in fatigued control bones vs. fatigued exercised bones. Bars indicate significant differences determined by two-way ANOVA post-hoc tests. ∗ indicates significant effect of fatigue across control and exercise groups by two-way ANOVA (no significance within groups by post hoc test).

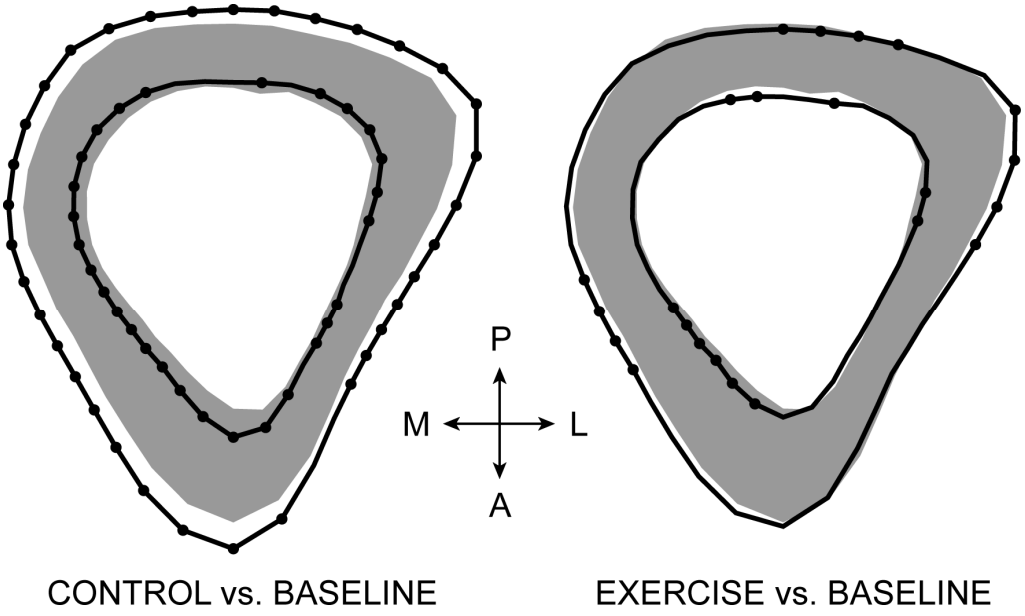

Figure 2.5. Average geometric traces from micro-CT measurements of transverse tibial mid-diaphysis cross-sections. The grey areas are identical and represent the original size and shape of the tibiae as determined from baseline bones. The black lines show the final size of control and exercised bones (three weeks older than baseline). Black dots represent locations (at 10˚ increments) where radii from the centroid are significantly different than baseline ($p < 0.05$). Control bones expanded radially in almost all directions. Periosteal expansion of exercise bones was limited to the medial and lateral directions with periosteal resorption in the posterior direction.

Table 2.1. Mechanical properties of tibiae from baseline mice, shown as mean (standard deviation).

Yield Strength (MPa)	186.2 (9.1)
Ultimate Strength (MPa)	205.4 (9.1)
Resilience (MPa)	1.585 (0.103)
Deformation at Failure (microns)	503.4 (53.7)

Baseline means were used to normalize control and exercise values shown in Figure 2.2.

Table 2.2. Effects of growth and exercise on tibia geometric properties and mouse weights, shown as mean (standard deviation).

	Baseline	Control	Exercise
Cortical Area (mm^2)	0.598 (0.043)	**0.691*** (0.068)	0.618 (0.066)
Cortical Thickness (mm)	0.191 (0.011)	**0.204 *** (0.015)	0.195 (0.014)
I_{AP} (mm^4)	0.066 (0.007)	**0.091 *** (0.015)	**0.074** (0.015)
I_{ML} (mm^4)	0.098 (0.015)	**0.131 *** (0.024)	0.101 (0.025)
ML/AP Ratio	0.802 (0.045)	0.805 (0.034)	**0.837 *** **(0.043)**
Tibia Length (mm)	17.21 (0.23)	**17.60 *** (0.23)	17.30 (0.34)
Mouse Weight (g)	26.8 (1.2)	**30.6 *** (2.3)	**28.2** (2.1)

Values shown in **bold** are significantly greater than baseline.
* indicates control and exercise values are significantly different.

REFERENCES

1. Burr, D. B. & Milgrom, C. *Musculoskeletal Fatigue and Stress Fractures*. (2001).
2. Melton, L. J.,3rd *et al*. Fractures attributable to osteoporosis: report from the National Osteoporosis Foundation. *J. Bone Miner. Res.* 12(1): 16-23 (1997).
3. Allolio, B. Risk factors for hip fracture not related to bone mass and their therapeutic implications. *Osteoporos. Int.* 9 Suppl 2: S9-S16 (1999).
4. Burr, D. B. *et al*. Bone microdamage and skeletal fragility in osteoporotic and stress fractures. *J. Bone Miner. Res.* 12(1): 6-15 (1997).
5. Marshall, D., Johnell, O. & Wedel, H. Meta-analysis of how well measures of bone mineral density predict occurrence of osteoporotic fractures. *BMJ* 312(7041): 1254-1259 (1996).
6. McCreadie, B. R. & Goldstein, S. A. Biomechanics of fracture: is bone mineral density sufficient to assess risk? *J. Bone Miner. Res.* 15(12): 2305-2308 (2000).
7. Sandor, T., Felsenberg, D. & Brown, E. Comments on the hypotheses underlying fracture risk assessment in osteoporosis as proposed by the World Health Organization. *Calcif. Tissue Int.* 64(3): 267-270 (1999).
8. Heaney, R. P. Is the paradigm shifting? *Bone* 33(4): 457-465 (2003).
9. Hui, S. L., Slemenda, C. W. & Johnston, C. C.,Jr. Age and bone mass as predictors of fracture in a prospective study. *J. Clin. Invest.* 81(6): 1804-1809 (1988).
10. Grynpas, M. Age and disease-related changes in the mineral of bone. *Calcif. Tissue Int.* 53 Suppl 1: S57-64 (1993).
11. Mashiba, T. *et al*. Suppressed bone turnover by bisphosphonates increases microdamage accumulation and reduces some biomechanical properties in dog rib. *J. Bone Miner. Res.* 15(4): 613-620 (2000).
12. Mashiba, T. *et al*. Effects of suppressed bone turnover by bisphosphonates on microdamage accumulation and biomechanical properties in clinically relevant skeletal sites in beagles. *Bone* 28(5): 524-531 (2001).
13. United States. Public Health Service. Office of the Surgeon General. Bone health and osteoporosis. (2004).
14. Gordon, K. R., Perl, M. & Levy, C. Structural alterations and breaking strength of mouse femora exposed to three activity regimens. *Bone* 10(4): 303-312 (1989).
15. Hoshi, A., Watanabe, H., Chiba, M. & Inaba, Y. Bone density and mechanical properties in femoral bone of swim loaded aged mice. *Biomed. Environ. Sci.* 11(3): 243-250 (1998).

16. Mosley, J. R. & Lanyon, L. E. Strain rate as a controlling influence on adaptive modeling in response to dynamic loading of the ulna in growing male rats. *Bone* 23(4): 313-318 (1998).

17. Umemura, Y., Baylink, D. J., Wergedal, J. E., Mohan, S. & Srivastava, A. K. A time course of bone response to jump exercise in C57BL/6J mice. *J. Bone Miner. Metab.* 20(4): 209-215 (2002).

18. Warden, S. J. *et al*. Bone adaptation to a mechanical loading program significantly increases skeletal fatigue resistance. *J. Bone Miner. Res.* 20(5): 809-816 (2005).

19. Gregg, E. W., Cauley, J. A., Seeley, D. G., Ensrud, K. E. & Bauer, D. C. Physical activity and osteoporotic fracture risk in older women. Study of Osteoporotic Fractures Research Group. *Ann. Intern. Med.* 129(2): 81-88 (1998).

20. Akkus, O., Adar, F. & Schaffler, M. B. Age-related changes in physicochemical properties of mineral crystals are related to impaired mechanical function of cortical bone. *Bone* 34(3): 443-453 (2004).

21. Paschalis, E. P. *et al*. Spectroscopic characterization of collagen cross-links in bone. *J. Bone Miner. Res.* 16(10): 1821-1828 (2001).

22. Zioupos, P., Currey, J. D. & Hamer, A. J. The role of collagen in the declining mechanical properties of aging human cortical bone. *J. Biomed. Mater. Res.* 45(2): 108-116 (1999).

23. Ager, J. W., Nalla, R. K., Breeden, K. L. & Ritchie, R. O. Deep-ultraviolet Raman spectroscopy study of the effect of aging on human cortical bone. *J. Biomed. Opt.* 10(3): 034012 (2005 May-Jun).

24. Carter, D. R. & Hayes, W. C. Compact bone fatigue damage--I. Residual strength and stiffness. *J. Biomech.* 10(5-6): 325-337 (1977).

25. Norman, T. L., Yeni, Y. N., Brown, C. U. & Wang, Z. Influence of microdamage on fracture toughness of the human femur and tibia. *Bone* 23(3): 303-306 (1998).

26. Reilly, G. C. & Currey, J. D. The effects of damage and microcracking on the impact strength of bone. *J. Biomech.* 33(3): 337-343 (2000).

27. Danova, N. A. *et al*. Degradation of bone structural properties by accumulation and coalescence of microcracks. *Bone* 33(2): 197-205 (2003).

28. Schaffler, M. B., Choi, K. & Milgrom, C. Aging and matrix microdamage accumulation in human compact bone. *Bone* 17(6): 521-525 (1995).

29. Sahar, N. D., Hong, S. I. & Kohn, D. H. Micro- and nano-structural analyses of damage in bone. *Micron* 36(7-8): 617-629 (2005).

30. Wallace, J. M. *et al*. Exercise-induced changes in the cortical bone of growing mice are bone- and gender-specific. *Bone* 40(4): 1120-1127 (2007).

31. Ferguson, V. L., Ayers, R. A., Bateman, T. A. & Simske, S. J. Bone development and age-related bone loss in male C57BL/6J mice. *Bone* 33(3): 387-398 (2003).

32. Somerville, J. M., Aspden, R. M., Armour, K. E., Armour, K. J. & Reid, D. M. Growth of C57BL/6 mice and the material and mechanical properties of cortical bone from the tibia. *Calcif. Tissue Int.* 74(5): 469-475 (2004).

33. Brodt, M. D., Ellis, C. B. & Silva, M. J. Growing C57Bl/6 mice increase whole bone mechanical properties by increasing geometric and material properties. *J. Bone Miner. Res.* 14(12): 2159-2166 (1999).

34. Favus, M. J. *Primer on the Metabolic Bone Diseases and Disorders of Mineral Metabolism, 4th Edition*. (1999).

35. Feldkamp, L. A., Goldstein, S. A., Parfitt, A. M., Jesion, G. & Kleerekoper, M. The direct examination of three-dimensional bone architecture in vitro by computed tomography. *J. Bone Miner. Res.* 4(1): 3-11 (1989).

36. Kuhn, J. L., Goldstein, S. A., Feldkamp, L. A., Goulet, R. W. & Jesion, G. Evaluation of a microcomputed tomography system to study trabecular bone structure. *J. Orthop. Res.* 8(6): 833-842 (1990).

37. ASTM International. Standard Test Method for Flexural Properties of Unreinforced and Reinforced Plastics and Electrical Insulating Materials by Four-Point Bending. *D 6272-02* (2002).

38. Hoagland, R. G., Marschall, C. W. & Duckworth, W. H. Reduction of Errors in Ceramic Bend Tests. *J Am Ceram Soc* 59(5-6): 189-192 (1976).

39. Gustafson, M. B. *et al*. Calcium buffering is required to maintain bone stiffness in saline solution. *J. Biomech.* 29(9): 1191-1194 (1996).

40. Frost, H. M. Presence of microscopic cracks *in vivo* in bone. *Bulletin of the Henry Ford Hospital* 8: 25-35 (1960).

41. Burr, D. B. & Stafford, T. Validity of the bulk-staining technique to separate artifactual from in vivo bone microdamage. *Clin. Orthop. Relat. Res.* (260)(260): 305-308 (1990).

42. Burr, D. B. & Hooser, M. Alterations to the en bloc basic fuchsin staining protocol for the demonstration of microdamage produced in vivo. *Bone* 17(4): 431-433 (1995).

43. Zioupos, P., Currey, J. D. & Sedman, A. J. An examination of the micromechanics of failure of bone and antler by acoustic emission tests and Laser Scanning Confocal Microscopy. *Med. Eng. Phys.* 16(3): 203-212 (1994).

44. Crane, N. J., Popescu, V., Morris, M. D., Steenhuis, P. & Ignelzi, M. A.,Jr. Raman spectroscopic evidence for octacalcium phosphate and other transient mineral species deposited during intramembranous mineralization. *Bone* 39(3): 434-442 (2006).

45. Widjaja, E. *et al*. Band-target entropy minimization (BTEM) applied to hyperspectral Raman image data. *Appl. Spectrosc.* 57(11): 1353-1362 (2003).

46. Timlin, J. A., Carden, A., Morris, M. D., Rajachar, R. M. & Kohn, D. H. Raman spectroscopic imaging markers for fatigue-related microdamage in bovine bone. *Anal. Chem.* 72(10): 2229-2236 (2000).

47. Rajachar, R. M. Effects of age-related ultra-structural level changes in bone on microdamage mechanisms, Ph.D. Dissertation. (2003).

48. Golcuk, K. *et al*. Is photobleaching necessary for Raman imaging of bone tissue using a green laser? *Biochim. Biophys. Acta* (2006).

49. Carden, A., Rajachar, R. M., Morris, M. D. & Kohn, D. H. Ultrastructural changes accompanying the mechanical deformation of bone tissue: a Raman imaging study. *Calcif. Tissue Int.* 72(2): 166-175 (2003).

50. Awonusi, A., Morris, M. D. & Tecklenburg, M. M. Carbonate assignment and calibration in the Raman spectrum of apatite. *Calcif. Tissue Int.* 81(1): 46-52 (2007).

51. Ruppel, M. E., Burr, D. B. & Miller, L. M. Chemical makeup of microdamaged bone differs from undamaged bone. *Bone* 39(2): 318-324 (2006).

52. Paschalis, E. P. *et al*. FTIR microspectroscopic analysis of human osteonal bone. *Calcif. Tissue Int.* 59(6): 480-487 (1996).

53. Akkus, O., Polyakova-Akkus, A., Adar, F. & Schaffler, M. B. Aging of microstructural compartments in human compact bone. *J. Bone Miner. Res.* 18(6): 1012-1019 (2003).

54. Marotti, G., Favia, A. & Zallone, A. Z. Quantitative analysis on the rate of secondary bone mineralization. *Calcif. Tissue Res.* 10(1): 67-81 (1972).

55. Vose, G. P. & Kubala, A. L. Bone strength—its relationship to x-ray determined ash content. *Human Biology* 31: 261-270 (1959).

56. Hernandez, C. J., Beaupre, G. S., Keller, T. S. & Carter, D. R. The influence of bone volume fraction and ash fraction on bone strength and modulus. *Bone* 29(1): 74-78 (2001).

57. Akhter, M. P. *et al*. Genetic variations in bone density, histomorphometry, and strength in mice. *Calcif. Tissue Int.* 67(4): 337-344 (2000).

58. Yeh, J. K., Aloia, J. F. & Yasumura, S. Effect of physical activity on calcium and phosphorus metabolism in the rat. *Am. J. Physiol.* 256(1 Pt 1): E1-6 (1989).

59. Yeh, J. K. & Aloia, J. F. Effect of physical activity on calciotropic hormones and calcium balance in rats. *Am. J. Physiol.* 258(2 Pt 1): E263-8 (1990).

60. Duncan, R. L. & Turner, C. H. Mechanotransduction and the functional response of bone to mechanical strain. *Calcif. Tissue Int.* 57(5): 344-358 (1995).

61. Burger, E. H. & Klein-Nulend, J. Mechanotransduction in bone--role of the lacuno-canalicular network. *FASEB J.* 13 Suppl: S101-12 (1999).

62. Burger, E. H. & Klein-Nulend, J. Mechanotransduction in bone--role of the lacuno-canalicular network. *FASEB J.* 13 Suppl: S101-12 (1999).

63. Johnson, L. C. The kinetics of skeletal remodeling in structural organization of the skeleton. *Birth Defects* 11: 66-142 (1966).

64. Aarden, E. M., Burger, E. H. & Nijweide, P. J. Function of osteocytes in bone. *J. Cell. Biochem.* 55(3): 287-299 (1994).

65. Cullinane, D. M. The role of osteocytes in bone regulation: mineral homeostasis versus mechanoreception. *J. Musculoskelet. Neuronal Interact.* 2(3): 242-244 (2002).

66. Gluhak-Heinrich, J. *et al*. Mechanical loading stimulates dentin matrix protein 1 (DMP1) expression in osteocytes in vivo. *J. Bone Miner. Res.* 18(5): 807-817 (2003).

67. Feng, J. Q. *et al*. Loss of DMP1 causes rickets and osteomalacia and identifies a role for osteocytes in mineral metabolism. *Nat. Genet.* 38(11): 1310-1315 (2006).

68. Ling, Y. *et al*. DMP1 depletion decreases bone mineralization in vivo: an FTIR imaging analysis. *J. Bone Miner. Res.* 20(12): 2169-2177 (2005).

69. Haapasalo, H. *et al*. Dimensions and estimated mechanical characteristics of the humerus after long-term tennis loading. *J. Bone Miner. Res.* 11(6): 864-872 (1996).

70. Hoshi, A., Watanabe, H., Chiba, M. & Inaba, Y. Effects of exercise at different ages on bone density and mechanical properties of femoral bone of aged mice. *Tohoku J. Exp. Med.* 185(1): 15-24 (1998).

71. van der Wiel, H. E. *et al*. Additional weight-bearing during exercise is more important than duration of exercise for anabolic stimulus of bone: a study of running exercise in female rats. *Bone* 16(1): 73-80 (1995).

72. Borer, K. T. The effects of exercise on growth. *Sports Med.* 20(6): 375-397 (1995).

73. Zernicke, R. F. *et al*. Adaptations of immature trabecular bone to exercise and augmented dietary protein. *Med. Sci. Sports Exerc.* 27(11): 1486-1493 (1995).

74. Coleman, M. A. *et al*. Glucocorticoid response to forced exercise in laboratory house mice (Mus domesticus). *Physiol. Behav.* 63(2): 279-285 (1998).

75. Girard, I. & Garland, T.,Jr. Plasma corticosterone response to acute and chronic voluntary exercise in female house mice. *J. Appl. Physiol.* 92(4): 1553-1561 (2002).

76. Fediuc, S., Campbell, J. E. & Riddell, M. C. Effect of voluntary wheel running on circadian corticosterone release and on HPA axis responsiveness to restraint stress in Sprague-Dawley rats. *J. Appl. Physiol.* 100(6): 1867-1875 (2006).

77. Boersma, B. & Wit, J. M. Catch-up growth. *Endocr. Rev.* 18(5): 646-661 (1997).

78. Iwamoto, J., Takeda, T. & Ichimura, S. Effects of exercise on bone mineral density in mature osteopenic rats. *J. Bone Miner. Res.* 13(8): 1308-1317 (1998).

79. Conn, C. A., Mial, S. & Borer, K. T. Food restriction postpones, not prevents, exercise-induced growth in hamsters. *Growth Dev. Aging* 57(3): 193-204 (1993).

80. Duck, F. A. in *Physical Properties of Tissue* (Academic Press, San Diego, 1990).

81. Mercer, C., He, M. Y., Wang, R. & Evans, A. G. Mechanisms governing the inelastic deformation of cortical bone and application to trabecular bone. *Acta Biomater.* 2(1): 59-68 (2006).

82. Vashishth, D., Behiri, J. C. & Bonfield, W. Crack growth resistance in cortical bone: concept of microcrack toughening. *J. Biomech.* 30(8): 763-769 (1997).

83. Akkus, O. & Rimnac, C. M. Cortical bone tissue resists fatigue fracture by deceleration and arrest of microcrack growth. *J. Biomech.* 34(6): 757-764 (2001).

84. Nalla, R. K., Kruzic, J. J. & Ritchie, R. O. On the origin of the toughness of mineralized tissue: microcracking or crack bridging? *Bone* 34(5): 790-798 (2004).

CHAPTER THREE

AGING DECREASED MECHANICAL PROPERTIES OF BONE BY COMPROMISING TISSUE QUALITY, NOT QUANTITY, IN MURINE TIBIAE

ABSTRACT

This chapter addressed the hypothesis that aging results in decreased skeletal integrity not only through reduced bone size, but also through altered composition, increased microdamage, decreased material properties, and decreased adaptation to mechanical loading. A murine aging model was used, examining the tibiae of young, but skeletally mature, male mice (5 months old) and old male mice (19 months old). The effects of aging were assessed on whole-bone and tissue-level mechanical properties (by four point bending), composition (by Raman microspectroscopy), microdamage (by fuchsin staining and histomorphometry), and bone geometric properties (by micro-computed tomography). Additionally, the ability of exercise to modulate those properties was examined in each age group, by subjecting weight and age-matched groups of mice to a short-term exercise program and then conducting the same assays. Compared to young mice, old mice had significantly reduced structural and tissue-level mechanical properties, larger mineral crystals with increased carbonate substitution, and significantly increased microcracking. There were no changes to bone size or shape with aging that would account for the reductions in whole-bone mechanical properties, indicating that the changes in composition, damage, and material properties were the primary source of reduced skeletal integrity. Finally, exercise significantly improved tissue strength and fatigue resistance in young mice without increasing bone size, but had no measured

benefit in old mice. This study demonstrates that aging may decrease skeletal integrity by compromising tissue quality even without reducing bone size.

INTRODUCTION

Skeletal fragility among the elderly is the most significant health problem associated with bone. After middle age, the risk of fracture increases with age and fractures can occur in the absence of a traumatic overload. Nontraumatic fractures are usually associated with osteoporosis, which accounts for 1.5 million fractures and 12-18 billion dollars in direct health care cost each year in the United States [1]. Osteoporosis is attributed to 80-95 percent of all hip and spine fractures in women older than 45 years [2]. In the United States, osteoporosis is a growing problem because of the aging population and is expected to affect estimated 12 million people by 2010 [3].

Osteoporosis is diagnosed in the clinic by low bone mass or occurrence of a nontraumatic fracture. Therefore, bone mass scans are the primary clinical tool for evaluating bone health and estimating fracture risk. Although these scans give insight into the amount of bone tissue present, they provide little information about composition or mechanical integrity of the tissue and are therefore insufficient predictors of fracture risk [4-9]. There is also concern that interventions like antiresorptive drug treatments may compromise tissue quality, despite increasing bone mass, and eventually lead to increased fracture risk [10-12]. While it has been generally accepted that tissue-level factors such as material properties and composition affect skeletal integrity, clinically their contributions have been considered peripheral to bone mass [6].

However, clinical evidence points to an overlooked contribution of tissue quality on fracture risk. For instance, fracture risk increases with age even when risk is adjusted for bone mass, indicating that bone tissue competence is compromised with age [13]. Bone mineralization and carbonate substitution increase with age which may contribute to decreased strength [14]. Also, increases in microdamage and targeted remodeling of that damage may contribute to age-related skeletal fragility [5, 6, 15-17]. Therefore,

diagnosis and treatment of bone fragility could be improved through a better understanding what contributes to "tissue quality" and how these contributions affect skeletal integrity.

In previous work with young adult mice, exercise improved tissue-level strength and resistance to fatigue-induced damage formation without increasing bone mass (Chapter 2). Further, exercise induced compositional changes throughout the mid-diaphysis of tibiae in the absence of significant bone formation or remodeling. The effects of exercise in young mice demonstrated that bone tissue quality may be improved without the processes of modeling or remodeling, a finding that has potential implications for older adults. Exercise in old adults is thought to have limited benefit in decreasing fracture risk because bone's ability to add mass in response to mechanical loading is compromised with age [18-20]. However, if exercise is able to increase tissue-level mechanical integrity in old bones, fracture risk may be decreased without increasing bone mass. For example, fracture risk in elderly women decreases with physical activity even when risk is adjusted for bone mineral density or number of falls [21].

This study examined the effects of aging on skeletal integrity of murine tibiae, testing the hypothesis that changes in tissue-level quality with aging would accompany reductions in overall mechanical competence. A murine aging model was used, employing young skeletally mature mice (19 weeks old) and old mice (19 months old). The effects of aging on the tibiae were examined in terms of whole-bone and tissue-level mechanical properties, bone size and geometric distribution, chemical composition, and microdamage. Additionally, the ability of exercise to modulate those properties was examined in each age group, testing the secondary hypothesis that exercise could improve tissue-level properties in both age groups.

Experimental Design

Two age groups of male C57BL/6 mice were used in this study, young and old, and were approved for use by the University of Michigan Committee on Use and Care of Animals (protocol # 8518). The young age group was previously analyzed (Chapter 2) and consisted of 30 mice that were 19 weeks old at the time of sacrifice. Although called young, at this age, mice are skeletally mature and roughly equivalent to a 20 year old man in development [22-25]. The old age group consisted of 40 mice that were 19 months old at the time of sacrifice, roughly equivalent to a 60 year old man. More mice were used in the old age group because the natural death and data variance were expected to be greater among old mice, but they were not. All mice were obtained five weeks prior to sacrifice and had access to food and water ad libitum. After sacrifice, left and right tibiae were harvested, stripped of soft tissue, and stored in calcium buffered saline (-80 °C) [26].

All tibiae were first analyzed by micro-computed tomography (micro-CT) to determine geometric properties. Bones from half of the mice in each age group were then designated for mechanical testing while bones from the other half were designated for quantification of microdamage. Bones used for microdamage analysis were also used for compositional analysis via Raman microspectroscopy. Within each mouse, a randomly selected tibia was used for the designated assay, while the contralateral tibia was reserved for fatigue experiments.

Micro-Computed Tomography

Tibiae from young mice were imaged with a GE/EVS MS-8 specimen scanner, while tibiae from old mice were scanned with an eXplore Locus SP" scanner (GE Healthcare Pre-clinical Imaging) because the MS-8 scanner was replaced after the young tibiae had already been imaged. A subset of young tibiae were rescanned on the eXplore system to confirm that no significant difference in geometric measurements existed between the two systems. On both systems, specimens were scanned with a voxel size of 25 μm and

then analyzed with MicroView software (General Electric Health Care) and custom written scripts [27, 28]. A 125 μm thick transverse section from a standard location (22% of distance from the tibio-fibular junction to the tibial plateau) was selected for analysis. This mid-diaphyseal site lies in the center of the mechanical testing region and is the same location used for microdamage analysis (see below).

Mechanical Testing

Mechanical properties were determined by monotonic loading of tibiae, using a material testing machine (Admet eXpert 450 Universal Testing Machine) and a custom designed loading fixture to meet ASTM Standard D6272-02 [29] for four point bending. The loading fixture was mounted on a pivot and had cylindrical rollers as loading points to minimize testing errors [30]. Tests were conducted with the medial side of the mid-diaphysis in tension and under position control with a crosshead displacement of 0.025 mm/s until failure. Force and displacement data were recorded and converted to stress and strain using beam bending theory and geometric measurements taken by micro-CT at the fracture site. A MatLab program (The MathWorks, Inc.) was created to perform this transformation and calculate all whole-bone and tissue-level mechanical properties. Post-yield tissue-level properties can only be considered approximate because beam bending theory is invalid after yield.

Quantification of Microdamage

Bones were stained *en bloc* with 1% basic fuchsin in a graded series of ethanol solutions, allowing thorough penetration of stain and dehydration of the bones [31-33]. Staining the whole bone before sectioning ensured that damage produced during processing would not be stained and would therefore be excluded from damage quantification. After staining, the tibiae were embedded in Koldmount (Vernon-Benshoff Company). A transverse cross section was removed from the mid-diaphysis of each bone using a low-speed sectioning saw (South Bay Technology), and polished to a final thickness of 125 μm. The location of this section matched the location used for micro-CT geometric analysis and lies in the center of the mechanical testing region.

Sections were imaged using a Bio-Rad MRC-600 laser scanning confocal microscope with a Nikon 60X oil immersion objective and LaserSharp 2000 acquisition software. Confocal microscopy allowed panning through the depth of the specimen to distinguish damage from native bone structures such as blood vessels, lacunae, and canaliculi [17, 34]. Two types of damage were observed: microcracks and diffuse damage. Microcracks were clear, individually distinguishable, linear cracks, while diffuse damage appeared as a dense collection of indistinguishable tiny cracks. Therefore, microcracks were quantified by number of cracks and cumulative length per section while diffuse damage was quantified by total area in each section. These metrics were divided by cross-sectional area to obtain a normalized measure of damage per unit area.

Raman Microspectroscopy

After sections were examined for microdamage, the same sections were analyzed by Raman microspectroscopy. A line-focused 785 nm laser (Invictus, Kaiser Optical Systems, Inc.) was focused on the specimens through a NIR-optimized 20 × 0.75 NA objective (Fluar Series, Carl Zeiss, Inc.), producing incident laser power of 98 mW distributed over a 100 μm long line. Raman scatter was collected with a 5 min integration time through the objective and focused into an axial-transmissive spectrograph (HoloSpec f/1.8I, Kaiser Optical Systems Inc.) equipped with a 25-μm slit, providing a maximum spectral resolution of 3-4 cm^{-1} [35]. Spectral data analysis was performed with Matlab (Math Works, Inc.) and GRAMS/32 (Galactic Industries). All spectra were preprocessed by removing detector-generated artifacts (spikes) and subtracting the detector dark current. The extraction of Raman spectra was performed by band target entropy minimization (BTEM) [36].

Band areas were determined for select Raman peaks representing specific components of bone mineral (phosphate, 958 cm^{-1}; carbonate, 1070 cm^{-1}) and bone matrix (hydroxyproline, 851 and 873 cm^{-1}; proline, 917 cm^{-1}; amide-I, 1660 cm^{-1}). The following band area ratios were used to characterize the chemical composition of the

bone samples: mineral/matrix ratio (958 / [851+873+917]), carbonate/phosphate ratio (1070 / 958), and collagen cross-linking ratio (1660 / 1690) [37-41]. Mineral/matrix ratio is often defined as the band area ratio of 958/1660 but here the matrix is represented by the summed band areas of the hydroxyproline and proline peaks because the amide-I band area could be altered by changes in cross-linking even if the amount of collagen is unchanged. Lastly, mineral crystallinity was measured as the inverse of the width of the 958 cm^{-1} peak at half of the maximum intensity (1 / FWHM).

Mineral/matrix gives insight into the degree of bone mineralization and carbonate/phosphate ratio is related to the level of carbonate substitution in the apatite lattice [42]. Crysallinity reflects both the level of mineral crystallographic order and average crystal size, with increasing order or size leading to greater crystallinity measurements [43]. Finally, the two peaks at 1660 and 1690 cm^{-1} underlie the amide I band and are indicative of changes in collagen cross-linking, with the area ratio between them corresponding to the non-reducible/reducible cross-link ratio [40]. Therefore, the collagen cross-linking ratio increases with increasing number of non-reducible cross-links.

As previously described (Chapter 2), sixteen spectral lines were collected from each young tibia: four circumferentially-oriented lines incrementing radially through the cortical thickness, collected at each of the four quadrants (anterior, posterior, lateral, medial). For old bones, three circumferentially-oriented lines were used at each quadrant because no radial variance was found in young bones. No significant effect of radial location or anatomical quadrant was found for any Raman metric, so for each metric, the band area ratios were averaged from all locations to obtain an overall measurement for each specimen.

Exercise Protocol

For each age group, weight-matched groups of mice with equal sample sizes were used to evaluate the effects of exercise. Like control mice, exercise mice were obtained five

weeks prior to sacrifice. After two weeks of acclimation, mice in the exercise groups were run on a treadmill (12 m/min, 5 degree incline) 30 minutes a day for 21 consecutive days [44]. The mice were sacrificed a on the 22nd day, making them the same age at sacrifice as control mice. The tibiae were harvested and subjected to the same assays as control tibiae.

Fatigue Protocol

In the young group, the tibia designated for fatigue analysis (see experimental design) were fatigued by mechanical cycling, using the same material tester and loading fixture as mechanical testing. Fatigue loading was normalized for each specimen to generate a peak load each cycle that would produce a peak stress of 95 MPa at the medial surface (the side of tension). The load required to produce 95 MPa was calculated by beam bending theory using the average geometry from the 3mm region between the inner loading points, determined by micro-CT. Fatigue loading was then conducted under load control using a 2Hz haversine waveform for 21,600 cycles. Specimens were kept in a calcium buffered saline bath during testing to avoid dehydration and loss of mineral [26]. After fatigue loading, young tibiae were then stained and analyzed for microdamage and Raman microspectroscopy to evaluate fatigue damage resistance.

The same protocol could not be used on tibiae from old mice because there was so much preexisting damage that a protocol could not be found to generate significantly more damage in the bones without causing fracture. Instead, these bones were mechanically fatigued, as described above, for 21,600 cycles or until failure and cycles to failure were used to judge fatigue resistance. Because of the different testing methods, direct comparisons could not be made about fatigue resistance in old and young bones, but the influence of exercise on fatigue resistance within each age group could be judged separately.

Statistical Analysis

Statistical analyses were performed using SPPS 16. Differences between age, exercise or fatigue groups were tested for significance using Student t-tests, or Mann-Whitney U tests when sample distributions were not normal or had unequal variances. Testing differences in fatigue life in old bones was conducted by Kaplan-Meier survival analysis. For all statistical tests, differences were considered significant for p values less than 0.05.

RESULTS

Mechanical Properties

By visual inspection during testing, old and young tibiae failed by mode I fracture with fracture initiating from the tensile side. Among non-exercised mice, tibiae from old mice compared to young had significantly reduced yield force ($p < 0.001$, Table 3.1), ultimate force ($p < 0.001$), deformation to yield ($p < 0.001$), deformation to failure ($p = 0.005$), work to yield ($p < 0.001$), post-yield work ($p = 0.029$), and work to failure ($p < 0.001$). At the tissue level, the corresponding mechanical properties were also significantly reduced by aging: yield strength ($p = 0.001$, Table 3.1), ultimate strength ($p < 0.001$), strain to yield ($p = 0.029$), strain to failure ($p = 0.026$), resilience ($p < 0.001$), post-yield energy ($p = 0.038$), and toughness ($p < 0.001$). Stiffness and modulus were the only measured mechanical properties that were not significantly different between age groups. The percent changes between age groups in whole bone mechanical properties were well matched with the corresponding changes in tissue-level mechanical properties.

Bone Size and Shape

While there were differences in the average shape of the mid-diaphysis between age groups, especially on the lateral side (Figure 3.1), the bones were similar in size (Table 3.2.). Cortical area and thickness were significantly reduced in old bones ($p = 0.001$ and $p < 0.001$, respectively), but second moment of area about the anterior-posterior axis (I_{AP})

and about the medial-lateral axis (I_{ML}) were not significantly different between age groups. Polar second moment of area (I_{Polar}) and the ratio of I_{ML} to the distance from the centroid to medial side (c_M) were also not significantly altered by aging. The ratio of I_{ML}/c_M is a shape factor that proportionally relates load during mechanical testing or fatigue loading to the maximum tensile stress in the bone.

Chemical Composition

At the mid-diaphysis, tibiae from old mice had significantly greater mineral/matrix ratio (Figure 3.2, $p < 0.001$), carbonate/phosphate ratio ($p = 0.003$), and crystallinity ($p < 0.001$) compared to tibiae from young mice. Cross-linking ratio was not significantly different between age groups.

Microdamage

Tibiae from old mice compared to young mice had significantly greater total crack length per unit bone area ($p = 0.041$) in mid-diaphyseal cross sections. Tibiae from old mice also had marginally significant increases in number of cracks per unit area ($p = 0.051$) and average crack length ($p = 0.059$) over tibiae from young mice. These differences were large, but only marginally significant because of large variance in damage metrics. Control and exercise groups were pooled because exercise had no significant effect on any damage metric in young or old bones (data not shown). After pooling, the age-associated increases in number of cracks and total crack length per unit area were significant, as well as the increase in average crack length (Figure 3.3, $p = 0.003$, 0.001, 0.014, respectively). The increase in average crack length appears to be due to a greater percentage of cracks with lengths over 40 um in old bones compared to young bones (Figure 3.3C). There was no significant difference between age groups in diffuse damage area per unit area before or after pooling (Figure 3.3D).

Effects of Exercise

Exercise in young mice significantly increased mineral/matrix ratio (Figure 3.4, $p = 0.027$) and ultimate strength ($p = 0.050$) and significantly decreased carbonate/phosphate ratio in the tibiae. The only significant effect of exercise in tibiae of old mice was reduced carbonate/phosphate ratio (Figure 3.4, $p = 0.026$).

An important finding from Chapter 2 was that exercise improved fatigue resistance in young tibiae. In nonfatigued young tibiae, control and exercised bones had similar crack length density, diffuse damage density, and collagen cross-linking ratios (Figure 3.5). However, after fatigue, control bones had significantly greater total crack length ($p = 0.040$) and diffuse damage area per unit area ($p = 0.009$) than exercised bones, as well as significantly reduced cross-linking ratio ($p = 0.023$).

In old tibiae, not enough samples survived the fatigue protocol to examine the effects of fatigue on damage or cross-linking. However, fatigue resistance was estimated by observing the number of cycles to failure (Figure 3.6). Exercise had no significant effect on percent of samples surviving the fatigue protocol or on fatigue survival behavior.

DISCUSSION

In this study, reductions in mechanical competence of tibiae by aging were driven by reductions in tissue-level mechanical properties and not by changes in bone size or shape. Every significant reduction in whole-bone mechanical properties was accompanied by a significant reduction in the corresponding tissue-level property (Table 3.1). Further, the percent reduction in tissue-level properties caused by aging was in good agreement with the percent reduction in whole bone properties. For instance, yield force and work to failure were reduced 22% and 45% by aging, respectively, while the corresponding tissue-level properties yield strength and toughness were reduced by 24% and 43%, respectively. This was a consistent trend for all measured mechanical properties (Table 3.1). Every measured mechanical property except for stiffness and modulus

(corresponding structural and tissue-level properties) was reduced by aging, resulting in tibiae that required significantly less force, displacement, and work to cause yield or failure than young, mature tibiae. These reductions in structural properties could potentially decrease the bone's ability to absorb impact energy or tolerate overloading and repetitive physiological loading without sustaining damage or failure, and thereby increase fracture risk.

Further evidence that reductions in tissue-level properties with aging were driving the reductions in structural competence is that there were minimal changes to cross-sectional size and shape that would account for deficient mechanical properties (Figure 3.1). Although cortical area and average cortical thickness were significantly reduced in old tibiae (Table 3.2), there were no significant changes in the bones' geometric resistance to anterior-posterior bending (I_{ML}) or medial-lateral bending (I_{AP}). Additionally, the lack of significant difference between age groups in polar second moment of area (J) illustrates that young and old bones in this study are equally adapted, in terms of geometry, to resist torsion. Perhaps most relevant to this study, the ratio of I_{AP} to c_M (distance from the neutral axis in bending to the periosteal surface on the medial side, the side of tension) was not significantly different between age groups. The assumption in determining c_M was that the neutral axis during medial-lateral bending runs through the geometric centroid of the transverse cross-section. While this assumption may not be correct, error in the location of the neutral axis would likely be similar between age groups because medial-lateral width was similar between groups. The ratio I_{AP}/c_M gives an indication of the peak tensile stress (and strain) that would be reached for any given medial-lateral bending moment. Because bone more easily fails by tension than compression, I_{AP}/c_M indicates the geometric contribution to fracture resistance by medial lateral bending. Therefore, changes to bone size and shape with aging did not significantly contribute to reduced mechanical properties under the mechanical testing regime used in this study.

One potential source of compromised tissue-level mechanical properties in old tibiae was that these bones had an altered mineral composition compared to young tibiae (Figure 3.2). Increased carbonate substitution in bone mineral, indicated by an increased

carbonate/phosphate ratio, is normally associated with more amorphous mineral crystals because the substitution is not stoichiometric [43, 45]. However, in old mice there was an increase in carbonate substitution and mineral crystallinity. The measure of crystallinity used here represents not only crystal perfection but also crystal size and can therefore be increased by greater perfection or greater average size of the mineral crystals [43]. In this experiment, increased crystallinity with age was likely due to increased crystal size because crystal perfection was likely not improved with greater carbonate substitution. The combination of increased mineral/matrix ratio with increased crystallinity also points to enlargement of mineral crystals as increasing mineral/matrix ratio by addition of new small crystals would have decreased crystallinity rather than increased it. Therefore, aging resulted in enlargement of mineral crystals with increased carbonate substitution. Aging had no significant effect on collagen cross-linking ratio, which is an indirect measure of cross-linking by measuring collagen secondary structure [40].

Increased crystal (or grain) size results in decreased strength in many materials because there are fewer grain boundaries to disrupt motion of dislocations [46]. In bone, larger crystals could hinder motion of collagen fibers, potentially decreasing the strain required to cause yield or fracture. Increased mineralization has been associated with decreased tissue strength and ductility [14, 47-49]. The mechanical consequence of increased carbonate substitution is less documented, but has also been associated with decreased mechanical properties [14]. Carbonate substitution in mineral apatite is not stoichiometric and therefore disrupts lattice spacing and mineral uniformity [43, 45, 50]. This disruption could potentially cause weakening or embrittlement of the mineral crystals.

Another potential source of compromised mechanical properties in old tibiae was increased microcracking. Not only were there more microcracks, but also less restricted crack growth and a greater tendency to form microcracks rather than diffuse damage (Figure 3.3). This data indicates that old bones have less resistance to crack propagation than young bones, especially considering that diffuse damage may arise from resistance

to crack propagation [17]. A similar damage pattern occurs in human cortical bone where young bones resist crack propagation and instead form more diffuse damage upon fatigue loading, while old bones form more cracks with greater length but not more diffuse damage[51, 52]. The reduced ability of old bones to resist crack propagation could, in part, be due to increased mineral size hindering motion of collagen fibers.

While diffuse damage and small microcracks are well tolerated in bone and may act as a toughening mechanism [17, 53-57], larger microcracks disrupt the bone matrix and create stress concentrations, potentially contributing to decreased strength and ductility [58-61]. Further, microcracks are more likely to trigger remodeling than diffuse damage [16], which can result in resorptive cavities that further weaken the bone and produce more stress concentrations. New microdamage may form because of increased strain near resorptive cavities, which would trigger further remodeling. This positive feedback cycle may play a central role in bone fragility [5, 6, 17].

Tibiae from old mice were less responsive than tibiae from young mice to the short-term exercise program used in this study. Exercise in young mice resulted in significantly increased ultimate strength and mineralization, with decreased carbonate substitution (Figure 3.4). While exercise also decreased carbonate substitution in old mice, exercise did not result in an improvement in mechanical properties. Perhaps the most important effect of exercise in young mice was increased resistance to fatigue-induced microdamage formation and collagen cross-links reduction (Figure 3.5). This improved fatigue resistance occurred at the tissue level and has been previously discussed in detail (Chapter 2). In old tibiae, there was already so much microdamage that the fatigue protocol could not create significantly more damage without causing failure. However, exercise had no significant effect on fatigue resistance in old tibiae as judged by loading cycles to failure (Figure 3.6), which is consistent with the observation that exercise did not improve mechanical properties in old mice.

The findings of this study suggest that not only do old mice have compromised bone tissue quality compared to young mice, but they are also less able to positively adapt their

existing bone tissue in response to exercise. However, this finding should be considered with the caveat that the exercise program was short, 21 days. Even in young mice, the response may have been greater if the duration of the experiment was increased. Decreased carbonate substitution with exercise occurred in both young and old mice, indicating that perhaps a bone adaptation was beginning in old mice, similar to the one that occurred in young mice. Without further experimentation, it cannot be said conclusively that old mice are less able to adapt tissue quality in response to exercise. All that can be concluded definitively is that at the very least, old mice would require more time for an adaptation to take place.

Conclusion

Reduced mechanical competence of tibiae from old mice compared to young mice was not the result of bone loss, but rather decreased tissue-level mechanical integrity. Increases in microcracking, mineral crystal size, and carbonate substitution likely contributed to decreased tissue-level mechanical properties in old tibiae. Exercise significantly improved tissue strength and fatigue resistance in young mice without increasing bone size, but had no measured benefit in old mice. This study demonstrates that changes to tissue quality can occur in the absence of changes to bone size and can significantly impact the mechanical competence of bone.

Acknowledgements

I would like to thank the co-authors of this work, Kutrus Golcuk, Michael D. Morris, Lisa A. Winkel and David H. Kohn. I would also like to thank Michael Ron and Steven Obreiter for their assistance on this project. This study was funded by DoD/US Army DAMD17-03-1-0556, The University of Michigan Regenerative Sciences Training Grant R90-DK071506, NIH P30-AR46024, NIDCR Training Grant DE007057, an American Association for Dental Research Fellowship, and The University of Michigan School of Dentistry.

Table 3.1. Effects of age on mechanical properties at the whole-bone and tissue levels.

Whole Bone Property				Corresponding Tissue-Level Property			
	Young	Old	Change		Young	Old	Change
Yield Force (N)	19.7 (3.5)	15.4 (2.5)	**-22%**	Yield Stress (MPa)	210 (39)	161 (34)	**-24%**
Ultimate Force (N)	21.1 (3.7)	16.3 (2.5)	**-23%**	Ultimate Stress (MPa)	225 (44)	169 (31)	**-25%**
Deformation to Yield (μm)	218 (50)	149 (33)	**-31%**	Strain to Yield (millistrain)	17.0 (3.2)	12.6 (2.4)	**-26%**
Deformation to Failure (μm)	261 (59)	182 (57)	**-30%**	Strain to Failure (millistrain)	26.7 (4.8)	20.2 (8.3)	**-24%**
Work to Yield (mJ)	2.26 (0.53)	1.27 (0.37)	**-44%**	Resilience (J/m^3)	1.88 (0.46)	1.13 (0.39)	**-40%**
Post-Yield Work (mJ)	2.22 (1.3)	1.19 (1.2)	**-46%**	Post-Yield Energy (J/m^3)	1.85 (1.1)	1.01 (1.0)	**-46%**
Work to Failure (mJ)	4.51 (1.3)	2.46 (1.2)	**-45%**	Toughness (J/m^3)	3.73 (1.1)	2.13 (1.0)	**-43%**
Stiffness (N/mm)	114 (33)	125 (21)	9%	Modulus (GPa)	15.6 (4.5)	15.1 (2.0)	-3%

Values shown are Mean (Standard Deviation)
Bold indicates a significant change between young and old tibiae.

Table 3.2. Effects of age on geometric properties of tibial mid-diaphysis (transverse **cross**-section)

	Young	Old	Change
Cortical Area (mm^2)	0.691 (0.068)	0.638 (0.054)	**-8%**
Avg. Cortical Thickness (mm)	0.204 (0.015)	0.184 (0.010)	**-10%**
I_{AP} (mm^4)	0.0907 (0.015)	0.0941 (0.015)	4%
I_{ML} (mm^4)	0.131 (0.024)	0.120 (0.022)	-8%
Polar Area Moment of Inertia, J (mm^4)	0.222 (0.039)	0.215 (0.036)	-3%
I_{AP} / c_M (mm^3)	0.1536 (0.0192)	0.1540 (0.0191)	0.2%

Values shown are Mean (Standard Deviation)
Bold indicates a significant change between young and old tibiae.

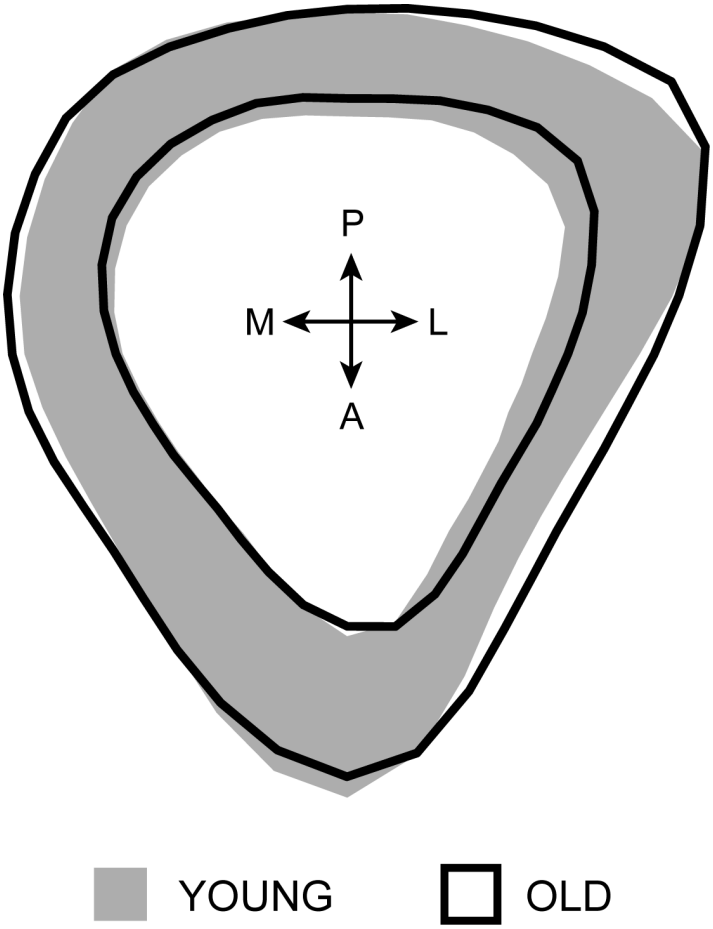

Figure 3.1. Average geometric traces from micro-CT measurements of transverse tibial mid-diaphysis cross-sections. The grey area represents the average size and shape of young bones and is overlaid with black lines representing the inner and outer dimensions of old bones. While the age groups have slightly different shapes, particularly on the lateral side, there are not dramatic decreases in quantity of bone with age.

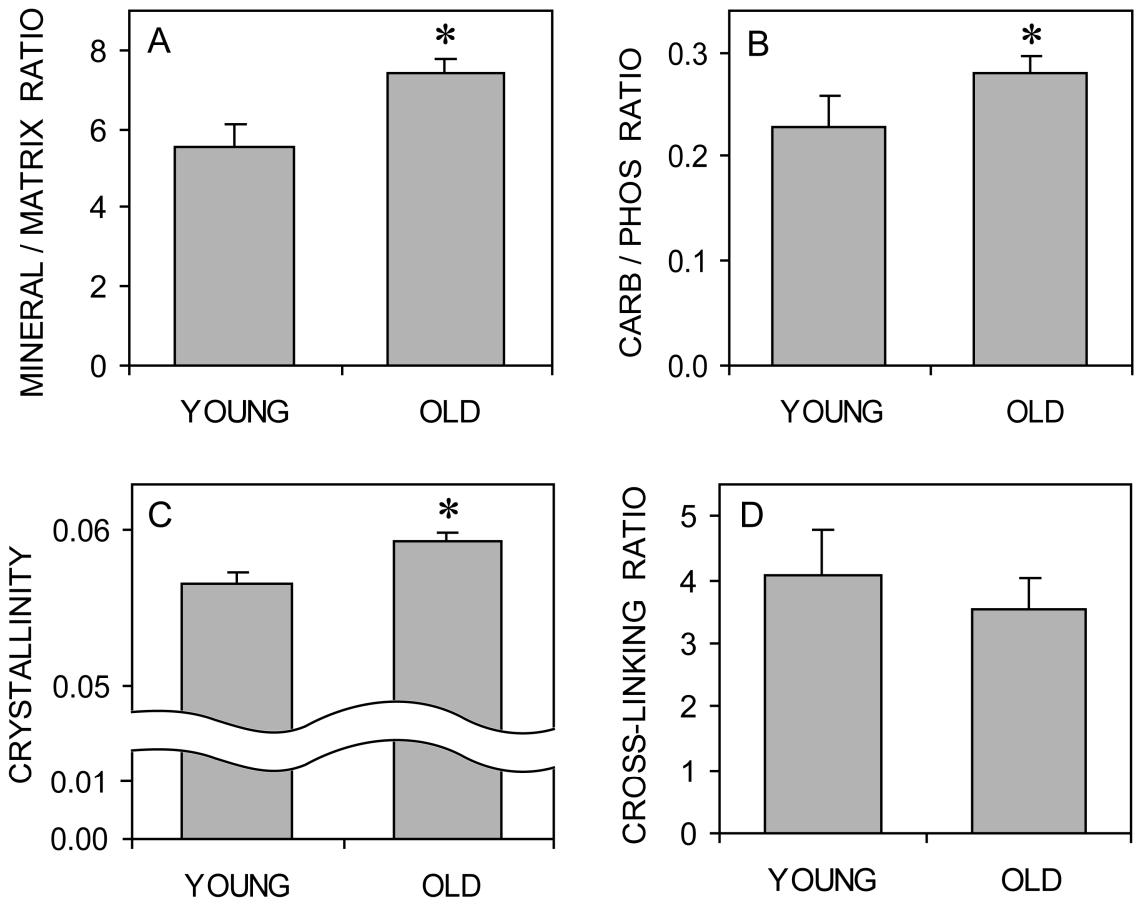

Figure 3.2. Bone composition as measured by Raman microspectroscopy (mean + std. dev.). Tibiae from old mice compared to young had significantly increased mineral/matrix ratio (A), carbonate/phosphate ratio (B), and mineral crystallinity (C). There was no significant effect of age on collagen cross-linking ratio (D). * indicates significant differences between age groups.

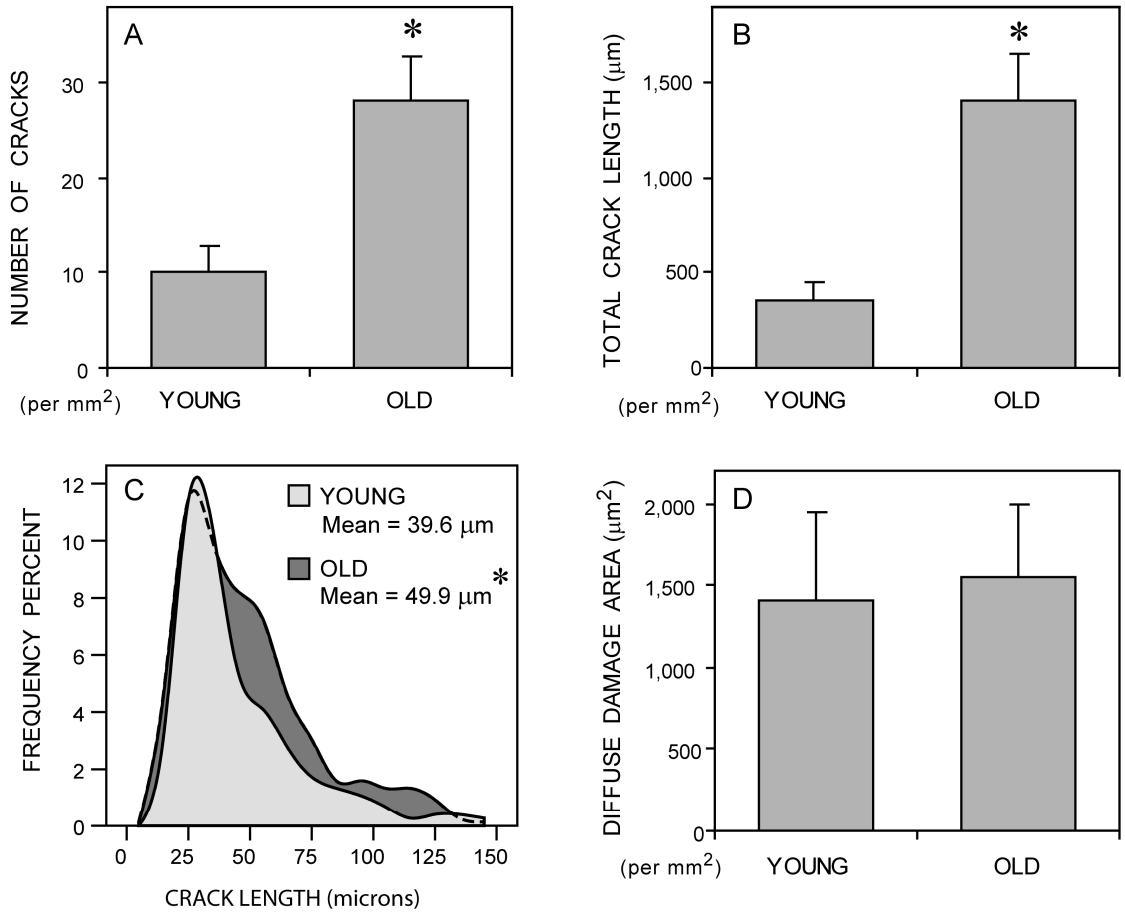

Figure 3.3. Microdamage in transverse cross-sections of tibiae (mean + SEM). Tibiae from old mice compared to young mice had significantly more cracks and significantly greater total crack length per unit area than young tibiae (A, B). Also, the distribution of crack lengths was shifted to longer lengths in old mice compared to young, resulting in significantly greater average crack length in old tibiae (C). There was no significant difference between age groups in diffuse damage area per unit bone area. * indicates significant differences between age groups.

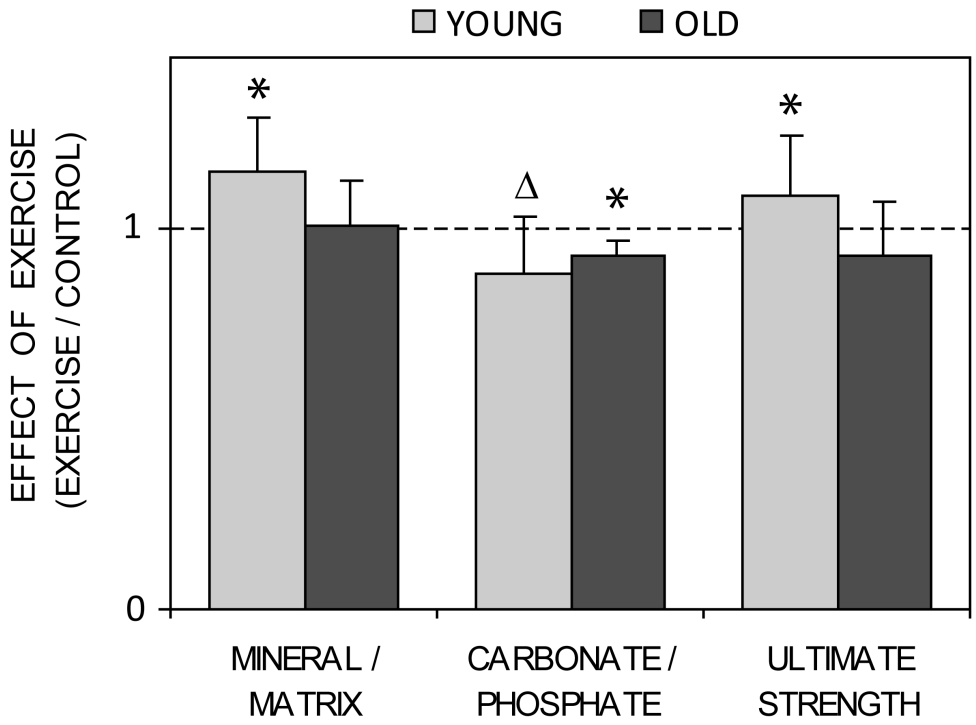

Figure 3.4. Effects of exercise in tibiae from young and old mice (mean + std. dev). In young mice, exercise significantly increased mineral/matrix ratio and ultimate strength and decreased carbonate/phosphate ratio. In old mice, the only significant effect of exercise was decreased carbonate/phosphate ratio. * indicates significant effect of exercise within age group. Δ indicates significant effect of exercise when analyzed with fatigued bones in two-way ANOVA (Chapter 2).

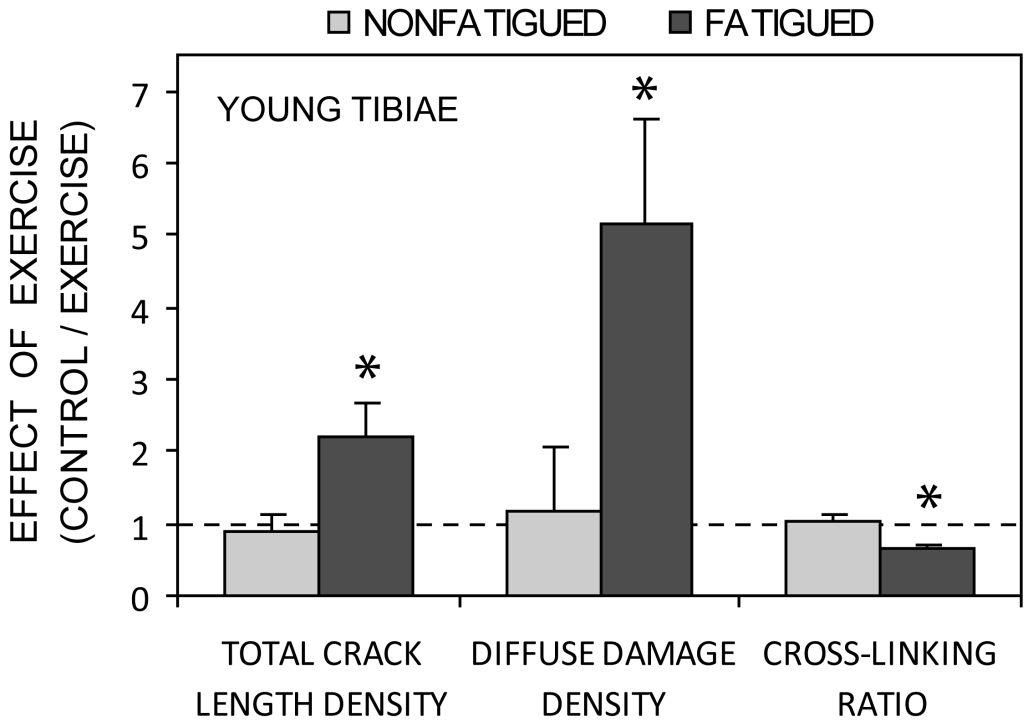

Figure 3.5. Effects of exercise on fatigue resistance in young mice (mean + SEM). Without being subjected to fatigue loading, tibiae from control and exercised mice had similar levels of cracking, diffuse damage, and collagen cross-linking. However, after fatigue loading, control bones had significantly more cracking and diffuse damage than exercised bones and had a significantly reduced cross-linking ratio, indicating that exercise increased resistance to fatigue-induced damage formation and cross-link reduction. ∗ indicates significant difference between control and exercise groups within a fatigue treatment.

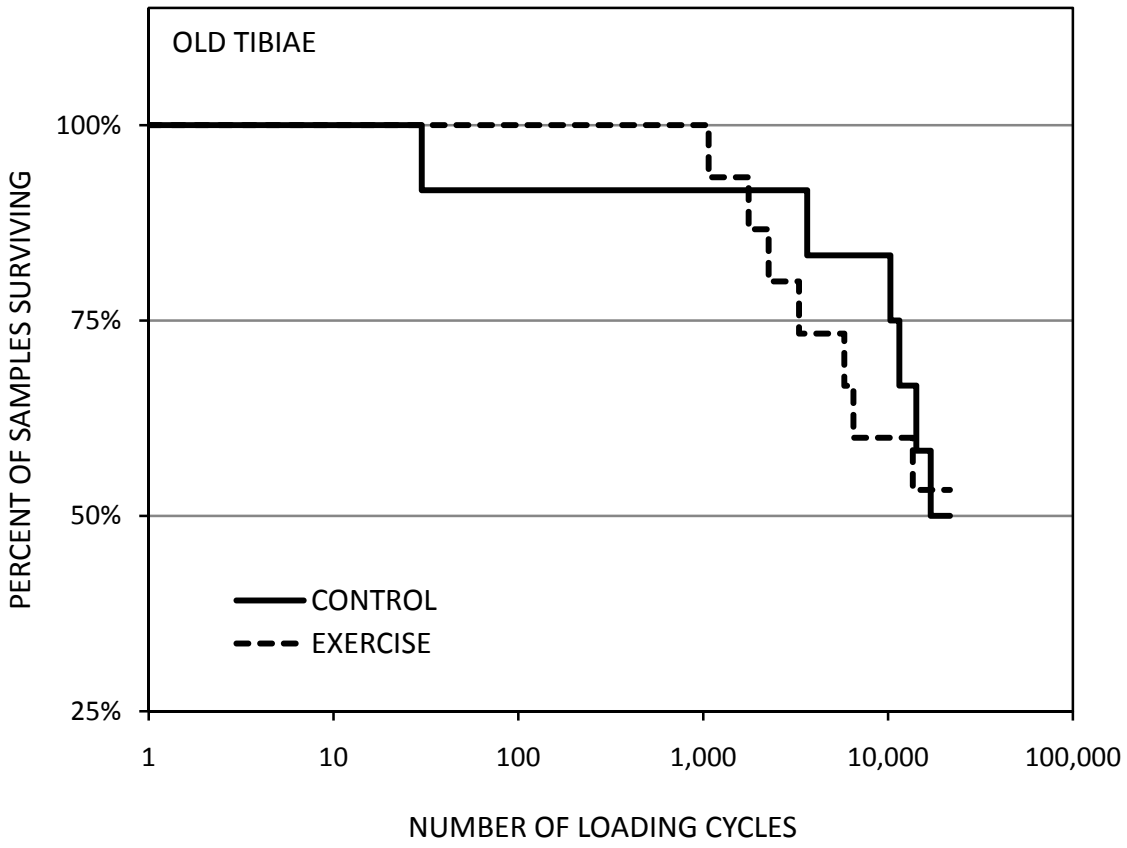

Figure 3.6. Effects of exercise on fatigue resistance in old mice. In old mice, exercise had no significant effect on the number of fatigue loading cycles to cause failure or the percentage of bones surviving the fatigue protocol.

1. United States. Public Health Service. Office of the Surgeon General. Bone health and osteoporosis. (2004).

2. Melton, L. J.,3rd *et al*. Fractures attributable to osteoporosis: report from the National Osteoporosis Foundation. *J. Bone Miner. Res.* 12(1): 16-23 (1997).

3. National Osteoporosis Foundation. America's bone health: The state of osteoporosis and low bone mass in our nation. (2002).

4. Allolio, B. Risk factors for hip fracture not related to bone mass and their therapeutic implications. *Osteoporos. Int.* 9 Suppl 2: S9-S16 (1999).

5. Burr, D. B. *et al*. Bone microdamage and skeletal fragility in osteoporotic and stress fractures. *J. Bone Miner. Res.* 12(1): 6-15 (1997).

6. Heaney, R. P. Is the paradigm shifting? *Bone* 33(4): 457-465 (2003).

7. Marshall, D., Johnell, O. & Wedel, H. Meta-analysis of how well measures of bone mineral density predict occurrence of osteoporotic fractures. *BMJ* 312(7041): 1254-1259 (1996).

8. McCreadie, B. R. & Goldstein, S. A. Biomechanics of fracture: is bone mineral density sufficient to assess risk? *J. Bone Miner. Res.* 15(12): 2305-2308 (2000).

9. Sandor, T., Felsenberg, D. & Brown, E. Comments on the hypotheses underlying fracture risk assessment in osteoporosis as proposed by the World Health Organization. *Calcif. Tissue Int.* 64(3): 267-270 (1999).

10. Grynpas, M. Age and disease-related changes in the mineral of bone. *Calcif. Tissue Int.* 53 Suppl 1: S57-64 (1993).

11. Mashiba, T. *et al*. Suppressed bone turnover by bisphosphonates increases microdamage accumulation and reduces some biomechanical properties in dog rib. *J. Bone Miner. Res.* 15(4): 613-620 (2000).

12. Mashiba, T. *et al*. Effects of suppressed bone turnover by bisphosphonates on microdamage accumulation and biomechanical properties in clinically relevant skeletal sites in beagles. *Bone* 28(5): 524-531 (2001).

13. Hui, S. L., Slemenda, C. W. & Johnston, C. C.,Jr. Age and bone mass as predictors of fracture in a prospective study. *J. Clin. Invest.* 81(6): 1804-1809 (1988).

14. Akkus, O., Adar, F. & Schaffler, M. B. Age-related changes in physicochemical properties of mineral crystals are related to impaired mechanical function of cortical bone. *Bone* 34(3): 443-453 (2004).

15. Burr, D. B. Targeted and nontargeted remodeling. *Bone* 30(1): 2-4 (2002).

16. Bentolila, V. *et al*. Intracortical remodeling in adult rat long bones after fatigue loading. *Bone* 23(3): 275-281 (1998).

17. Sahar, N. D., Hong, S. I. & Kohn, D. H. Micro- and nano-structural analyses of damage in bone. *Micron* 36(7-8): 617-629 (2005).

18. Haapasalo, H. *et al*. Dimensions and estimated mechanical characteristics of the humerus after long-term tennis loading. *J. Bone Miner. Res.* 11(6): 864-872 (1996).

19. Hoshi, A., Watanabe, H., Chiba, M. & Inaba, Y. Effects of exercise at different ages on bone density and mechanical properties of femoral bone of aged mice. *Tohoku J. Exp. Med.* 185(1): 15-24 (1998).

20. Kannus, P. *et al*. Effect of starting age of physical activity on bone mass in the dominant arm of tennis and squash players. *Ann. Intern. Med.* 123(1): 27-31 (1995).

21. Gregg, E. W., Cauley, J. A., Seeley, D. G., Ensrud, K. E. & Bauer, D. C. Physical activity and osteoporotic fracture risk in older women. Study of Osteoporotic Fractures Research Group. *Ann. Intern. Med.* 129(2): 81-88 (1998).

22. Ferguson, V. L., Ayers, R. A., Bateman, T. A. & Simske, S. J. Bone development and age-related bone loss in male C57BL/6J mice. *Bone* 33(3): 387-398 (2003).

23. Somerville, J. M., Aspden, R. M., Armour, K. E., Armour, K. J. & Reid, D. M. Growth of C57BL/6 mice and the material and mechanical properties of cortical bone from the tibia. *Calcif. Tissue Int.* 74(5): 469-475 (2004).

24. Brodt, M. D., Ellis, C. B. & Silva, M. J. Growing C57Bl/6 mice increase whole bone mechanical properties by increasing geometric and material properties. *J. Bone Miner. Res.* 14(12): 2159-2166 (1999).

25. Favus, M. J. *Primer on the Metabolic Bone Diseases and Disorders of Mineral Metabolism, 4th Edition*. (1999).

26. Gustafson, M. B. *et al*. Calcium buffering is required to maintain bone stiffness in saline solution. *J. Biomech.* 29(9): 1191-1194 (1996).

27. Feldkamp, L. A., Goldstein, S. A., Parfitt, A. M., Jesion, G. & Kleerekoper, M. The direct examination of three-dimensional bone architecture in vitro by computed tomography. *J. Bone Miner. Res.* 4(1): 3-11 (1989).

28. Kuhn, J. L., Goldstein, S. A., Feldkamp, L. A., Goulet, R. W. & Jesion, G. Evaluation of a microcomputed tomography system to study trabecular bone structure. *J. Orthop. Res.* 8(6): 833-842 (1990).

29. ASTM International. Standard Test Method for Flexural Properties of Unreinforced and Reinforced Plastics and Electrical Insulating Materials by Four-Point Bending. *D 6272-02* (2002).

30. Hoagland, R. G., Marschall, C. W. & Duckworth, W. H. Reduction of Errors in Ceramic Bend Tests. *J Am Ceram Soc* 59(5-6): 189-192 (1976).

31. Frost, H. M. Presence of microscopic cracks *in vivo* in bone. *Bulletin of the Henry Ford Hospital* 8: 25-35 (1960).

32. Burr, D. B. & Stafford, T. Validity of the bulk-staining technique to separate artifactual from in vivo bone microdamage. *Clin. Orthop. Relat. Res.* (260)(260): 305-308 (1990).

33. Burr, D. B. & Hooser, M. Alterations to the en bloc basic fuchsin staining protocol for the demonstration of microdamage produced in vivo. *Bone* 17(4): 431-433 (1995).

34. Zioupos, P., Currey, J. D. & Sedman, A. J. An examination of the micromechanics of failure of bone and antler by acoustic emission tests and Laser Scanning Confocal Microscopy. *Med. Eng. Phys.* 16(3): 203-212 (1994).

35. Crane, N. J., Popescu, V., Morris, M. D., Steenhuis, P. & Ignelzi, M. A.,Jr. Raman spectroscopic evidence for octacalcium phosphate and other transient mineral species deposited during intramembranous mineralization. *Bone* 39(3): 434-442 (2006).

36. Widjaja, E. *et al*. Band-target entropy minimization (BTEM) applied to hyperspectral Raman image data. *Appl. Spectrosc.* 57(11): 1353-1362 (2003).

37. Timlin, J. A., Carden, A., Morris, M. D., Rajachar, R. M. & Kohn, D. H. Raman spectroscopic imaging markers for fatigue-related microdamage in bovine bone. *Anal. Chem.* 72(10): 2229-2236 (2000).

38. Rajachar, R. M. Effects of age-related ultra-structural level changes in bone on microdamage mechanisms, Ph.D. Dissertation. (2003).

39. Golcuk, K. *et al*. Is photobleaching necessary for Raman imaging of bone tissue using a green laser? *Biochim. Biophys. Acta* (2006).

40. Paschalis, E. P. *et al*. Spectroscopic characterization of collagen cross-links in bone. *J. Bone Miner. Res.* 16(10): 1821-1828 (2001).

41. Carden, A., Rajachar, R. M., Morris, M. D. & Kohn, D. H. Ultrastructural changes accompanying the mechanical deformation of bone tissue: a Raman imaging study. *Calcif. Tissue Int.* 72(2): 166-175 (2003).

42. Awonusi, A., Morris, M. D. & Tecklenburg, M. M. Carbonate assignment and calibration in the Raman spectrum of apatite. *Calcif. Tissue Int.* 81(1): 46-52 (2007).

43. Baig, A. A. *et al*. Relationships among carbonated apatite solubility, crystallite size, and microstrain parameters. *Calcif. Tissue Int.* 64(5): 437-449 (1999).

44. Wallace, J. M. *et al*. Exercise-induced changes in the cortical bone of growing mice are bone- and gender-specific. *Bone* 40(4): 1120-1127 (2007).

45. Dorozhkin, S. V. Calcium orthophosphates. *J. Mater. Sci.* 42(4): 1061-1095 (2007).

46. Callister Jr, W. D. Fundamentals of Materials Science and Engineering: An Integrated Approach. *Fundamentals of Materials Science and Engineering: An Integrated Approach, 2nd Edition, by William D.Callister, Jr.*: 824 (2004).

47. Vose, G. P. & Kubala, A. L. Bone strength—its relationship to x-ray determined ash content. *Human Biology* 31: 261-270 (1959).

48. Hernandez, C. J., Beaupre, G. S., Keller, T. S. & Carter, D. R. The influence of bone volume fraction and ash fraction on bone strength and modulus. *Bone* 29(1): 74-78 (2001).

49. Akhter, M. P. *et al*. Genetic variations in bone density, histomorphometry, and strength in mice. *Calcif. Tissue Int.* 67(4): 337-344 (2000).

50. Sari, Y. W., Soejoko, D. S. & Dahlan, K. Nanostructure in Bone Apatite. *3rd Kuala Lumpur International Conference on Biomedical Engineering 2006*: 118-121 (2007).

51. Diab, T., Condon, K. W., Burr, D. B. & Vashishth, D. Age-related change in the damage morphology of human cortical bone and its role in bone fragility. *Bone* 38(3): 427-431 (2006).

52. Diab, T. & Vashishth, D. Morphology, localization and accumulation of in vivo microdamage in human cortical bone. *Bone* 40(3): 612-618 (2007).

53. Diab, T. & Vashishth, D. Effects of damage morphology on cortical bone fragility. *Bone* 37(1): 96-102 (2005).

54. Sobelman, O. S. *et al*. Do microcracks decrease or increase fatigue resistance in cortical bone? *J. Biomech.* 37(9): 1295-1303 (2004).

55. Vashishth, D., Behiri, J. C. & Bonfield, W. Crack growth resistance in cortical bone: concept of microcrack toughening. *J. Biomech.* 30(8): 763-769 (1997).

56. Vashishth, D., Tanner, K. E. & Bonfield, W. Experimental validation of a microcracking-based toughening mechanism for cortical bone. *J. Biomech.* 36(1): 121-124 (2003).

57. Nalla, R. K., Kruzic, J. J. & Ritchie, R. O. On the origin of the toughness of mineralized tissue: microcracking or crack bridging? *Bone* 34(5): 790-798 (2004).

58. Carter, D. R. & Hayes, W. C. Compact bone fatigue damage: a microscopic examination. *Clin. Orthop. Relat. Res.* (127)(127): 265-274 (1977).

59. Danova, N. A. *et al*. Degradation of bone structural properties by accumulation and coalescence of microcracks. *Bone* 33(2): 197-205 (2003).

60. Norman, T. L., Yeni, Y. N., Brown, C. U. & Wang, Z. Influence of microdamage on fracture toughness of the human femur and tibia. *Bone* 23(3): 303-306 (1998).

61. Reilly, G. C. & Currey, J. D. The effects of damage and microcracking on the impact strength of bone. *J. Biomech.* 33(3): 337-343 (2000).

CHAPTER FOUR

COMPOSITIONAL CHANGES OF BONE MINERAL AND MATRIX HAVE ASSOCIATIONS WITH MECHANICAL PROPERTIES THAT MAY DEPEND ON BONE AGE AND INITIAL COMPOSITION

ABSTRACT

This chapter addressed the hypothesis that tissue-level mechanical properties are related to mineral density and mineral crystal composition as well as the maturity of collagen cross-links. To test this hypothesis, femora from 4, 5, and 19 month old male C57Bl/6 mice were used to establish colocalized correlations between composition and mechanical properties. A 60 μm marker system was used to ensure that compositional measurements (by Raman microspectroscopy) and mechanical measurements (by nanoindentation) were taken at the same location in each bone. Multivariate regression analyses were conducted using Raman metrics as covariates and nanoindentation metrics as dependent variables. The influence of mouse age group on the regressions was also investigated. Compositional measurements were significantly correlated with mechanical properties but in an age dependent manner. For instance, mineralization correlated positively with mechanical properties in bones from young mice (4 and 5 month old) but negatively in bones from old mice (19 month old). Cross-linking ratio was negatively correlated with mechanical properties in bones from young mice but had no significant correlation with mechanical properties in bones from old mice. These results highlight the potential utility of using bone compositional measurements in diagnosing skeletal

fragility but also show the difficulty in making sweeping conclusions about the effects of compositional changes in bone.

INTRODUCTION

There is growing evidence that "tissue quality" and not just quantity plays a significant role in determining the mechanical competence of bone and therefore risk of fracture. Changes to bone mass and risk of falling inadequately predict increased risk of fracture in the elderly and therefore point to reduced material properties in bone contributing to age-related skeletal fragility [1-6]. Similarly, stress fractures and spontaneous fractures in non-elderly individuals often have no clear association with bone mass [7, 8]. Evidence in Chapters 2 and 3 of this thesis suggests that aging and exercise can alter skeletal integrity, not by changing bone mass but by altering bone's chemical composition and material properties, illustrating that tissue quality may be a dynamic contributor to skeletal integrity.

Despite this evidence, clinical diagnosis of bone health is conducted primarily through the use of bone mass scans. Currently there are few alternatives to bone scans in the clinical evaluation of bone, but there are ongoing efforts to develop new techniques for *in vivo* monitoring of composition, material properties, and microdamage [9-15]. However, even if these techniques are successfully developed, there is not a clear understanding of how the properties they measure contribute to skeletal fragility. Therefore, diagnosis and treatment of bone fragility could be improved through a better understanding what contributes to "tissue quality" and how it affects skeletal integrity.

Many investigations have implicated tissue properties, such as composition or the amount and type of microdamage, in contributing to bone's mechanical competence, but the findings of these studies are often conflicting. For instance, formation of microdamage has been associated with both increased and decreased toughness of bone [16-24]. Similarly, increasing levels of mineralization, carbonate substitution, mineral

crystallinity, and collagen cross-linking have also been both positively and negatively associated with mechanical properties and fracture risk [25-32].

One potential source for these conflicting results is that many investigations have used bones from different ages or experimental treatment groups in establishing associations between composition and mechanical properties. Without accounting for age or group, it is possible that measured compositional properties change with age or treatment along with the true, but unmeasured, sources for altered mechanical properties. This problem is compounded when there is a disparity in length scales between measured compositional and mechanical properties. For instance, measurements of ultrastructural composition by spectroscopy, high pressure liquid chromatography (HPLC) or X-ray diffraction may not be predictive of whole bone mechanical properties if there are changes to bone at higher levels of the hierarchical structure. Although, the possibility of confounding variables cannot be eliminated, using closely matched groups and taking measurements at similar locations and length scales could reduce the chance of confounding influences.

Raman microspectroscopy and nanoindentation are techniques that can measure composition and mechanical properties, respectively, at similar length scales. While, Raman microspectroscopy directly measures chemical bonding, it reflects higher order bone composition such as mineralization, average crystal size and uniformity, and collagen organization. With appropriate magnification, Raman measurements represent the average of these properties over a length scale of microns and are appropriately matched in scale to nanoindentation. Besides being matched in scale, nanoindentation measurements can be spatial with previous Raman measurements measurement because Raman microspectroscopy is nondestructive. Nanoindentation has been used on bone to determine effects of tissue maturity or bone structural unit on mechanical properties [33-36]. The traditional nanoindentation metrics, modulus and hardness, reflect pre-yield mechanical properties, but the technique can be extended to characterize viscoelastic properties, resistance to creep, and elastic recovery of work [37-41].

This study tested the hypothesis that tissue-level mechanical properties are related to composition and size of bone mineral crystals as well as maturity of collagen cross-links. Raman microspectroscopy and nanoindentation were used to measure compositional and mechanical properties, respectively, at the same spatial location and with similar depth in femora of mice from three age groups. Regression analysis was used across age groups and within age groups to determine correlations between Raman and nanoindentation metrics as well as the effects of age group on those associations.

MATERIALS AND METHODS

Experimental Design

Right femora from 4, 5, and 19 month old male C57Bl/6 mice were used in this study. The mice were used in previous experiments, in which the tibiae were analyzed (Chapters 2 & 3), and were approved for use by the University of Michigan Committee on Use and Care of Animals (protocol # 8518). All mice were obtained five weeks prior to sacrifice and had access to food and water ad libitum. Based on previous work (Chapters 2 and 3) and other evidence [42-45], 4 month old mice are nearly skeletally mature, 5 month mice appear to have fully developed skeletal integrity, and 19 month old mice have compromised structural and tissue-level mechanical integrity in the tibia.

Five and nineteen month age groups included both non-exercised mice and mice subjected to an exercise program (running on a treadmill, 12 m/min, 5 degree incline, 30 minutes/day) the 21 days prior to sacrifice (Chapter 2 and 3). After sacrifice, femora from all groups were harvested, stripped of soft tissue, and stored in calcium buffered saline (-80 °C) [46]. There were 8 femora from four month old mice (all non-exercised), 13 from five month old mice (6 non-exercised and 7 exercised), and 12 from nineteen month old mice (6 non-exercised and 6 exercised).

Femora were prepared for colocalized analysis by Raman microspectroscopy and nanoindentation by creating a flat smooth surface and stamping a marker system onto that

surface so that Raman and nanoindentation measurements could be taken at the same location. Specimens were first analyzed by Raman microspectroscopy, a nondestructive technique, and then by nanoindentation so that compositional measurements, by Raman analysis, and mechanical properties, by nanoindentation, could be correlated. Between analyses, femora were kept frozen in Ca Buffer (-20 °C).

Sample Preparation

An approximately 10 mm longitudinal section was removed from the mid-diaphysis of the femora using a low-speed sectioning saw (South Bay Technology). This section started near the proximal end of the trochanter and ran 10 mm distally (Figure 4.1). The section was then mounted, posterior side down, to a plastic slide using a viscous cyanoacrylate glue. A custom designed specimen holder was used with a polishing wheel, along with a rigid polishing cloth and a 3 μm diamond suspension (Buehler, Inc.) to create a flat surface on the anterior side of the bone that was parallel to the plastic slide. A soft, low nap polishing cloth was then used with a 0.05 μm alumina suspension (Buehler, Inc.) to increase the smoothness of that surface. In total, a depth of approximately 20-30 μm was removed from the anterior surface of each bone. Finally, the samples were ultrasonically cleaned for 20 seconds in Calcium buffered saline to remove any particles remaining from the polishing process.

After polishing, bones were stamped with a marker by micro-contact printing. The stamp was created using a micro-fabricated polydimethylsiloxane (PDMS) master and custom designed lithographic ink (The Flint Group). A thin layer of the ink was manually rolled onto the surface of the PDMS master and then stamped precisely on the flat, smooth surface of the bones by using a custom built, 3-dimensional micrometer stamping stage. The stamp pattern had two regions of interest, each with a diameter of 60 μm (Figure 4.2). Only one region of interest was used in each sample, but two regions were included in the stamp in case one of the regions covered an area of bone that had micro-cavities from vascularization. This marker served as a guide for co-localizing Raman and nanoindentation measurements (Figure 4.1).

Raman Microspectroscopy

The samples were thawed to room temperature immediately before use, and remained in calcium buffer throughout the analysis. Four Raman spectra were collected within the ink marker of each sample as show in Figure 4.1. At each location, a line-focused 785 nm laser (Invictus, Kaiser Optical Systems, Inc.) was focused on the specimens through a NIR-optimized 60X, 1.0NA water immersion objective (Fluor series, Nikon Inc., Japan). The approximate length of the laser line was 10-20 μm with a depth of field of 2-3 μm. Raman scatter was collected with a 1 min integration time through the objective and focused into an axial-transmissive spectrograph (HoloSpec f/1.8I, Kaiser Optical Systems Inc.) equipped with a 25-μm slit, providing a maximum spectral resolution of 3-4 cm^{-1}. Polarization scramblers (Thor Labs, NJ, USA) were used at the laser exit and at the spectrometer entrance slit to remove orientation effects from Raman spectra [47] and obtain average bulk properties of the tissue. The polarization scramblers effectively removed orientation effects as there were no significant differences between spectra taken in the longitudinal and transverse directions. After the spectra were collected, the samples were kept wet, covered with gauze soaked in Ca buffer and refroze (-20 ˚C).

Spectral data analysis was performed with Matlab (Math Works, Inc.) and GRAMS/32 (Galactic Industries). The spectra were preprocessed to correct curvature, remove detector-generated artifacts (spikes), subtract the detector dark current, and to normalize the spectra to the 959 cm^{-1} band. Peak fitting was performed uniformly on the mineral (799 to 1141 cm^{-1}) and matrix regions (1184 to 1719 cm^{-1}) across all specimens using Razr tool. The extraction of Raman spectra was performed by band target entropy minimization (BTEM) [48].

Band areas were determined for select Raman peaks representing specific components of bone mineral (phosphate, 958 cm^{-1}; carbonate, 1070 cm^{-1}) and bone matrix (hydroxyproline, 851 and 873 cm^{-1}; proline, 917 cm^{-1}; amide-I, 1660 cm^{-1}). The following band area ratios were defined and used to characterize the chemical composition of the bone samples: mineral/matrix ratio (958 / [851+873+917]), carbonate/phosphate ratio (1070 / 958), and collagen cross-linking ratio (1660 / 1690)

[26, 49-52]. Mineral/matrix ratio is often defined as the band area ratio of 958/1660 but here the matrix is represented by the summed band areas of the hydroxyproline and proline peaks because the amide-I band area could be altered by changes in cross-linking even if the amount of collagen is unchanged. Lastly, mineral crystallinity was measured as the inverse of the width of the 958 cm^{-1} peak at half of the maximum intensity (1 / FWHM).

Mineral/matrix gives insight into the degree of bone mineralization and carbonate/phosphate ratio is related to the level of carbonate substitution in the apatite lattice [53]. Crysallinity reflects both the level of mineral crystallographic order and average crystal size, with increasing order or size leading to greater crystallinity measurements [54]. Finally, the two peaks at 1660 and 1690 cm^{-1} underlie the amide I band and are indicative of changes in collagen cross-linking, with the area ratio between them corresponding to the non-reducible/reducible cross-link ratio [26].

Nanoindentation

After Raman spectra were collected, samples were subjected to nanoindentation using a Nanoindenter II equipped with a diamond Berkovich indenting tip and a lock-in amplifier for continuous stiffness measurements (Nano Instruments). Five indents were made within the marker as shown in Figure 4.1. The loading profile at each location consisted of two indenting procedures (Figure 4.3). The first part of the profile was a typical loading/unloading procedure used for determining modulus and hardness [37, 55]. Specifically, it consisted of a loading segment to a depth of 2000 nm, in which the ratio of current loading rate to current load was maintained at 0.05 sec^{-1} to produce an approximately constant strain rate [56]. This indentation depth was matched to the depth of field from the Raman analysis. After the indentation depth was reached, a constant-load hold period of 100 seconds was used to prevent viscoelastic behavior from contributing to the unloading behavior [40]. The samples was then unloaded to 10% of the maximum load and held at constant load for 50 seconds to allow for thermal drift correction and viscoelastic recovery of the sample. Finally, samples were completely

unloaded and kept unloaded for 10 seconds. On each day of analysis, this indentation procedure was also performed on a single-crystal aluminum standard to confirm that measurements were consistent from day to day.

The second part of the indentation procedure consisted of a step load of 60 mN followed by a 100 second constant-load hold period and a complete unloading (Figure 4.3). This part of the indenting profile was included to record creep behavior in the hold period after the step loading. The step load of 60 mN was greater than the load required to reach a depth of 2000 nm in the first segment of the indenting procedure, which insured that the step loading caused new plastic and elastic deformation in each sample.

A Matlab (The Mathworks, Inc.) program was written to analyze the data collected by nanoindentation. For each indentation profile, the first loading/unloading segment was used to calculate modulus and contact hardness by the Oliver-Pharr method [55], using an assumed Poison ratio of 0.3 for bone [35]. Calculation of contact hardness by the Oliver-Pharr method assumes that the contact area between the sample and the indenter tip at maximum load is equivalent to the area of the residual indent after unloading. If this assumption holds, as with brittle materials and metals, then contact hardness is roughly equivalent to conventional measures of hardness and represents resistance to permanent plastic deformation. However, if there is significant elastic recovery upon unloading, as with bone, then the assumption made in the Oliver-Pharr method is violated. Therefore, a correction was applied to account for elastic recovery and transform contact hardness to true hardness:

$$H = \frac{1}{\alpha_1 \left[(\alpha_1 H_C)^{-1/2} - (\alpha_2 E')^{-1/2}\right]^2}$$

where H is true hardness (resistance to plastic deformation), E′ and H_c are the measured plain strain modulus and contact hardness of the sample, respectively, and α_1 and α_2 are constants assumed to be 24.5 and 4.4, respectively for an ideal Berkovich indenter[57].

The first loading/unloading segment was also used to calculate plasticity index, the ratio of plastic work during loading and unloading to the total work to reach peak indentation depth (Figure 4.4). The amount of plastic work is equivalent to the total work minus the work accounted for by elastic recovery of the sample during unloading. Therefore, larger values of plasticity index indicate less elastic recovery and a greater percentage of plastic deformation to elastic deformation.

The creep behavior following step loading was modeled using a combined Maxwell-Voigt model for viscoelasticity and viscoplasticity (Figure 4.5A). The model includes a spring and damper in parallel to model viscoelasticity in series with a spring to model viscoplasticity. The viscoplastic portion of the model is unrealistic for long loading periods because plastic deformation will continue unabated. However, in the time frame of 100 seconds, there was always linear displacement with time at the end of the hold period, making the Maxwell-Voigt model an appropriate choice (Figure 4.5 B & C). The governing equation for creep of a Maxwell-Voigt material by nanoindentation with a conical indenter is

$$h^2(t) = \frac{\pi}{2} P_0 \cot\alpha \left[\frac{1}{E_{parallel}} \left(1 - e^{-t\frac{E_{parallel}}{\eta_{parallel}}} \right) + \frac{1}{\eta_{series}} t \right]$$

where h is the creep displacement after time t, P_0 is the applied load, α is the cone semi-angle, $E_{parallel}$ is the modulus of the parallel spring in the model, and $\eta_{parallel}$ and η_{series} are the viscosities of the parallel and series damper, respectively (Figure 4.5A) [37]. For a Berkovich indenter, the equivalent cone semi-angle is 70.3˚. In this model, h represents the creep displacement after the instantaneous displacement resulting from the step load. The values for modulus and viscosity in were calculated in the Matlab program by fitting the model with load, displacement and time data from the hold period. Even though creep displacement varied greatly between samples (ranging from 300-1600 nm) the model fit creep behavior exceptionally well ($R^2 > 0.999$) for all samples (Figure 4.5 B & C).

Load-displacement and stiffness-displacement (by continuous stiffness measurements) profiles were analyzed to find improper surface contact or micro-failures during indentation. After eliminating 14 problematic indentations, the remaining indentations were averaged in each sample. Although the assumption of sample isotropy is violated for the mechanical calculations, the error in the calculations is likely similar between bones and much less than the variance in calculated properties between bones.

Statistical Analysis

Statistical analyses were performed using SPPS 16. For all statistical tests, $p < 0.05$ was considered significant and $p < 0.1$ was considered marginally significant. The effects of age and exercise on the means of Raman and nanoindentation metrics were evaluated by two-way analyses of variance (ANOVA) with Bonferroni and Holm-Sidak post-hoc tests. Because there was no significant or marginally significant effect of exercise on the means of any metric, exercised groups were not separated from non-exercised groups in the presentation of means in order to improve clarity. However, exercise was still included as a potential factor in model selection for linear regressions (see below).

Bivariate correlations between Raman metrics were analyzed by Pearson correlation coefficients. Partial correlations were also determined for the three Raman metrics of bone's mineral state (mineral/matrix ratio, carbonate/phosphate ratio, and crystallinity) because all three were significantly correlated with each other by bivariate analysis. These partial correlations were determined between two metrics while controlling for the third for all possible combinations.

Linear regressions were conducted using Raman metrics as covariates and nanoindentation metrics as dependent variables. A natural log transformation was applied to creep metrics (displacement, $E_{parallel}$, $\eta_{paralle}$, η_{series}) because they did not follow a normal distribution without the transformation. Raman metrics were centered so that interactions between the metrics could be analyzed with creating a covariance problem. Several different models were considered. First, each covariate was linearly regressed

alone with each dependent variable, across all age groups. Next multivariate linear regressions were conducted using all Raman covariates and step-wise selection with the criteria $p < 0.1$ to include a covariate in the model and $p > 0.11$ to remove a covariate. Age group was also available for step-wise selection into the model as well as the interaction between age and Raman covariates. There was a consistent significant effect of the 19 month age group as main or interactive effect, indicating that the relations in this group were significantly different than the 4 and 5 month age groups. Therefore, the multivariate analysis was repeated separately on 19 month old bones and on 4 and 5 month old bones. In all the models, there were no significant contributions from interactive terms.

The contributions of covariates included in the model were judged by their partial correlation with the dependent variable and the corresponding p-value. Multicovariance was not a problem in any model, as judged by variance inflation factor and condition index. Models fits were not driven by influential points as judged by the Cook's Distance and DFFIT.

RESULTS

Mineral/matrix ratio (min/mat) and crystallinity were significantly greater in the 19 month old murine femora than in the two younger age groups, which had no significant difference in those metrics (Figure 4.6). Collagen cross-linking ratio, was marginally greater in 4 month old femora than in 5 and 19 month old femora, which were not significantly different. There was no significant difference in carbonate/phosphate ratio (carb/phos) between age groups. Hardness was significantly greater in the 5 and 19 month age groups compared to you 4 month group (Table 4.1).

Raman measures of the mineral phase of bone (min/mat, carb/phos, crystallinity) were all significantly and positively correlated (Table 4.2). However, the only significant correlation between any two of these metrics when adjusting for the third was between

min/mat and crystallinity. There was also a marginally significant ($p < 0.1$) positive correlation between carb/phos and collagen cross-linking.

In linear regressions of single Raman metrics with mechanical properties across all age groups, carb/phos was only significantly, and positively, related to plasticity index (Table 4.3). Similarly, plasticity index was the only mechanical property significantly related to min/mat. Crystallinity was significantly, positively correlated with modulus, but no other mechanical properties. In contrast, cross-linking ratio was significantly, negatively correlated with modulus, contact hardness, hardness, and η_{series}, and marginally negatively correlated with $E_{parallel}$ and $\eta_{parallel}$. Cross-linking ratio was also significantly, but positively correlated with plasticity index and creep displacement. The most significant of the univariate regressions, cross-linking ratio and hardness ($R^2 = 0.355$), is illustrated in Figure 4.7.

In multiple linear regressions, the effect of covariates in the 4 and 5 month age groups (young) differed than in the 19 month age group (old). Therefore, these age groups were modeled separately (Table 4.4). These models included only the Raman covariates that significantly improved prediction of the dependent variable ($p < 0.1$). The effect (magnitude and sign) of each covariate within the model is judged by partial correlation.

In multivariate analysis of young bones, min/mat and cross-linking ratio both significantly contributed to the model of modulus (Table 4.4). Crystallinity and carb/phos were excluded from the model because they did not significantly improve the prediction of modulus. Similarly the models for $E_{parallel}$ and $\eta_{parallel}$ also included only min/mat and cross-linking ratio. In contrast, models of contact hardness, hardness, creep displacement, and η_{series}, had only cross-linking ratio as a significant predictor. However in the models of creep displacement and η_{series}, there was a marginal contribution of exercise. Finally, the model of plasticity index had significant contributions of carb/phos and age group (4 vs. 5 month old). Min/mat was correlated with improved mechanical properties for all models in which it was included, while cross-link and carb/phos were

correlated with decreased mechanical properties for all models in which they were included. Crystallinity did not significantly contribute to any model.

In multivariate analysis of old bones (Table 4.4), the only covariate that significantly or marginally contributed to mechanical properties was min/mat. Min/mat was positively associated with plasticity index and negatively associated with contact hardness, hardness, and η_{series}. The differential effect between age groups of Raman metrics on mechanical properties was further investigated on hardness and plasticity index. Increasing min/mat ratio had no significant effect on hardness in either 4 or 5 month old femora, but significantly reduced hardness in old mice (Figure 4.8). In all age groups, plasticity index significantly increased with min/mat with slopes that were not significantly different (Figure 4.9). However, the intercepts of these regressions were offset as min/mat ratio, but not plasticity index, increased with age group, perhaps indicating an umeasured compensatory mechanism.

DISCUSSION

The most consistent trend between measures of composition and mechanical properties across all age groups was that collagen cross-linking ratio was negatively correlated with mechanical properties. For instance, cross-linking ratio explained 36% of the variation in hardness across all age groups (Figure 4.7). Increased cross-linking ratio was also significantly correlated with decreased modulus, elastic recovery (1 - plasticity index), and resistance to viscoplastic creep (η_{series}, Table 4.3). In contrast, characteristics of the mineral phase (min/mat, carb/phos, and crystallinity) had significant correlations with only modulus and elastic recovery when regressed across all age groups.

However, the regressions across all age groups may be misleading because the contributions of compositional changes were different in young adult (4 and 5 month old) and old (19 month) mice. In young mice, which are near skeletal maturity [42-45], cross-linking ratio still had a dominant effect, significantly predicting decreased mechanical properties for all properties except elastic recovery (Table 4.4). The relationships

between mechanical properties and cross-linking ratio within young mice may have been driven by the significant decrease in cross-linking ratio in 5 month old femora compared to 4 month old femora (Figure 4.6), but cross-linking ratio was a stronger predictor than age. Along with the negative contribution of cross-linking ratio, mineral/matrix ratio was significantly and positively correlated with elastic modulus, $E_{parallel}$ and $\eta_{parallel}$ (Table 4.4). The results of multivariate regressions in young bones therefore suggests that in bones nearing skeletal maturity, increased mineralization makes the tissue stiffer and less viscoelastic while increased cross-linking maturity has the opposite effect on those properties and also decreases hardness and resistance to viscoplastic creep.

Cross-linking ratio, which represents the relative amount of mature/immature (or nonreducible/reducible or trivalent/divalent) collagen cross-links, is conventionally thought to increase with tissue maturity, as immature cross-links become mature cross-links, and thereby improve mechanical properties [26, 58]. However, this presumption is most often based on observations from newly formed bone or bone that has been perturbed by chemical treatment, genetic disruption, or enzymatic and dietary interventions. Besides diminishing cross-linking, these interventions may also affect mineralization and collagen organization. In unperturbed adult bone, there has been no demonstrated positive association between maturation of enzymatic cross-linking and mechanical properties [27, 31, 32, 59-64]. On the contrary, increased cross-linking ratio has been associated with osteoporotic fractures and spontaneous fractures in premenopausal women with normal bone mass [7]. Osteoporotic fractures have also been associated with increased total enzymatic cross-linking [65]. A high density of cross-links could reduce collagen's ability to dissipate energy, resulting in increased chance of molecular rupture and reduced toughness of bone [66].

An alternate explanation for the negative impact of increased cross-linking ratio is that an increase in the ratio reflected a reduction in reducible cross-links without changing the number of nonreducible cross-links. For instance, in osteoporotic bone there may be a decrease in reducible cross-links without a change in nonreducible cross-links or collagen concentration [67]. The loss of reducible cross-links could also explain Paschalis's

observation of reduced cross-linking ratio in osteoporotic and spontaneous fractures [7]. If increased cross-links do impart mechanical benefit, it may not matter whether those cross-links are reducible or nonreducible.

A final consideration regarding the negative influence of cross-linking ratio on mechanical properties in young mice is that cross-linking ratio is an indirect measure of cross-linking through its effect on collagen secondary structure. While the 1660/1690 cross-linking ratio has been associated with specific enzymatic cross-links [26], it is still possible that other changes to collagen, such as altered collagen organization or the formation of nonenzymatic cross-links, could affect cross-linking ratio. These changes have also been associated with significantly compromised mechanical properties in bone [27, 32, 59, 61, 62].

While cross-linking ratio dominated compositional correlations with mechanical properties in young bones, only mineral/matrix ratio was significantly or marginally correlated with any mechanical property in old bones. Increased mineral/matrix ratio in this study likely reflected increased bone mineral density through growth of mineral crystals. Even the youngest age groups in this study were nearly skeletal mature and would add mineral primarily by crystal growth (secondary mineralization) rather than nucleation of new mineral crystals (primary mineralization) [68-70]. The strong correlation between mineral/matrix ratio and crystallinity supports this hypothesis. Crystallinity likely reflected the length of mineral crystals more than crystal perfection because there was no significant association between carbonate substitution, which would decrease crystal perfection [54, 71], and crystallinity when controlling for level of mineralization (Table 4.2).

In old bones, increased mineralization was negatively correlated with hardness, elastic recovery and resistance to plastic creep (Table 4.4, Figure 4.8). The reason that mineralization was negatively associated with mechanical properties in old but not young bones could be due to significantly higher mineralization in the old bones (Figure 4.6). There may be a threshold before increased mineralization or crystal size has a negative

impact on tissue mechanics. While increased mineralization can improve the strength and stiffness of poorly mineralized, immature bone [36, 72], further increases in mineralization or crystal size could make bone brittle and weak, possibly by inhibiting sliding of collagen fibers and increasing load transfer to bone defects or by decreasing crystal strength [25, 73-77]. The relation between mineralization and hardness, which represents the bone's resistance to plastic deformation, particularly demonstrates the possibility of a minimum threshold before mineralization negatively impacts mechanical properties (Figure 4.8). For values of mineral/matrix ratio below 10, there is no correlation with hardness, but for values above 10, which only occur in old bones, there is a significant negative association with hardness.

Elastic recovery of work (1 - plasticity index, Figure 4.4) was the exception to the disparity between young and old bones in compositional-mechanical correlations, and was negatively correlated with mineralization across all age groups and all degrees of mineralization (Figure 4.9). However, the reason that mineralization was associated with elastic recovery may have been different in young and old bones. In young bones, mineralization was also significantly associated with increased elastic modulus and viscoelastic modulus (Table 4.4), which could decrease elastic recovery by decreasing the elastic and viscoelastic storage of work. Alternatively, the association between mineralization and plasticity index in young bones may have been dependent on carbonate substitution (Table 4.4), which was highly correlated with mineralization (Table 4.3) and could increase plasticity index by making the bone crystals more amorphous and less tough [25, 54, 71, 78]. In old bones, mineralization was associated with decreased resistance to viscoplastic creep (Table 4.4), which would increase plasticity index by increasing the amount of permanent plastic deformation during the hold period at maximum load (Figure 4.3).

As with any regression analysis, only correlation, and not cause, can be established in this study. While the changes in compositional metrics may responsible for variations in mechanical properties, it is also possible that these Raman metrics are simply altered along with other factors that contribute to mechanical properties. Examples of other

factors that could influence mechanical properties include nonenzymatic cross-linking, collagen organization, concentration of noncollagenous proteins, or amount of microdamage, all of which could vary with tissue age (Chapter 3) [24, 27, 32, 59, 61, 62, 79, 80]. The Raman metrics in this study could therefore represent local tissue age or maturity. However, using genetically similar inbred mice and accounting for age group diminishes this possibility, although there may have been spatial differences in tissue maturity based on the small sampling area in each bone. Even if the compositional measures used here do not represent the cause of altered mechanical properties, they may still have utility as indicator variables for potentially compromised skeletal integrity.

Conclusion

This study demonstrates that the mechanical consequence of compositional changes in bone may depend on the age and initial compositional state of the bone. Counter to conventional wisdom, collagen cross-linking ratio was negatively associated with mechanical competence, a finding consistent with observations of greater cross-linking ratio in bones sustaining osteoporotic or spontaneous fracture [7, 67]. The mechanical correlations with cross-linking were particularly strong in young adult bone. However, in old bones, mineralization, which was significantly higher than in young bones, was the dominant predictor of mechanical competence and was negatively correlated with mechanical properties. These results highlight the potential utility of using bone compositional measurements in diagnosing skeletal fragility but also show the difficulty in making sweeping conclusions about the effects of compositional changes in bone. Much work remains before compositional measurement could effectively be used in clinical diagnosis of skeletal fragility.

Acknowledgements

I would like to acknowledge my co-authors on this work Mekhala Raghavan, Michael D. Morris, and David H. Kohn. I would also like to thank Jonathon Song, Yu-suke Torisawa, and Sheereen Majd for their assistance in making the PDMS stamp and

Rodney Balmer and Seyed Hojjati of Flint Group for making the lithographic ink. This study was funded by DoD/US Army DAMD17-03-1-0556 and The University of Michigan Regenerative Sciences Training Grant R90-DK071506.

Table 4.1. Mechanical properties determined by nanoindentation in each age group.

	4 Months	5 Months	19 Months
Modulus (GPa)	7.09 (1.5)	7.82 (2.2)	8.11 (2.3)
Contact Hardness (GPa)	0.286 (0.088)	0.361 (0.090)	0.365 (0.094)
Hardness (GPa)	0.982 (0.40)	1.38* (0.36)	1.40* (0.45)
Plasticity Index	78.1% (3.1%)	75.6% (2.3%)	76.4% (3.1%)
Creep Displacement (nm)	942 (330)	764 (340)	823 (360)
Creep $E_{Parallel}$ (GPa)	719 (650)	989 (870)	992 (740)
Creep $\eta_{Parallel}$ (GPa-s)	8,833 (6,140)	12,707 (10,200)	12,175 (8,280)
Creep η_{Series} (GPa-s)	12,689 (18,000)	16,763 (13,700)	15,508 (17,900)

Data shown as mean (standard deviation).

* indicates property is marginally greater than in 4 month old group with $p < 0.1$.

Table 4.2. Bivariate and partial correlations coefficients between Raman metrics

	Carbonate/ Phosphate	Crystallinity	Cross-Linking
Mineral/Matrix Ratio	0.595*	0.790*	0.152
Carbonate/Phosphate		0.613*	0.356$^{\Delta}$
Crystallinity			-0.033
Mineral/Matrix Ratio (Controlling for Crystallinity)	0.228		
Mineral/Matrix Ratio (Controlling for Carb./Phos.)		0.669*	
Carbonate/Phosphate (Controlling for Mineral/Matrix)		0.291	

* and $^{\Delta}$ indicate significant ($p < 0.05$) and marginal ($p < 0.1$) correlations.

Table 4.3. Coefficient of determination (R^2) of single covariate regressions across all age groups

	Carbonate/ Phosphate	Crystallinity	Mineral/ Matrix	Cross-linking
Modulus	N.S.	0.139 (+)	N.S.	0.132 (-)
Contact Hardness	N.S.	N.S.	N.S.	0.287 (-)
Hardness	N.S.	N.S.	N.S.	0.355 (-)
Plasticity Index	0.221 (+)	N.S.	0.193 (+)	0.260 (+)
Creep Displacement $^{(ln)}$	N.S.	N.S.	N.S.	0.214 (+)
Creep $E_{parallel}$ $^{(ln)}$	N.S.	N.S.	N.S.	0.101 (-) $^{\Delta}$
Creep $\eta_{parallel}$ $^{(ln)}$	N.S.	N.S.	N.S.	0.108 (-) $^{\Delta}$
Creep η_{series} $^{(ln)}$	N.S.	N.S.	N.S.	0.230 (-)

N.S. indicates regression with covariate was not significant.
$^{\Delta}$ indicates $0.05 < p < 0.10$. All other reported models are significant at $p < 0.05$
+ / - indicates the direction of the relation.
$^{(ln)}$ indicates that the natural log of dependent variable was used in the regression (to satisfy normality assumption)

Table 4.4. Multivariate regressions using all covariates that significantly contribute to the model, separated by age.

		Partial Correlation to Dependent Variable				Overall Model Fit		
	Age	Carbonate/ Phosphate	Mineral/ Matrix	Cross-linking	Group Effect	p	R2	Adjusted R2
Modulus	4-5Months		0.538	-0.650		0.003	0.484	0.426
	19 Months					N.S.		
Contact Hardness	4-5Months			-0.604		0.004	0.365	0.332
	19 Months		-0.531 $^{\Delta}$			0.076	0.282	0.210
Hardness	4-5Months			-0.598		0.004	0.358	0.324
	19 Months		-0.883			0.000	0.779	0.757
Plasticity Index	4-5Months	0.768			A = - 0.542	0.000	0.669	0.632
	19 Months		0.914			0.000	0.835	0.818
Creep Displacement $^{(ln)}$	4-5Months			0.606	E = 0.429 $^{\Delta}$	0.020	0.407	0.328
	19 Months					N.S.		
Creep $E_{Parallel}$ $^{(ln)}$	4-5Months		0.653	-0.609		0.004	0.525	0.462
	19 Months					N.S.		
Creep $\eta_{Parallel}$ $^{(ln)}$	4-5Months		0.656	-0.590		0.004	0.517	0.453
	19 Months					N.S.		
Creep η_{Series} $^{(ln)}$	4-5Months			-0.613	E = -.439 $^{\Delta}$	0.017	0.417	0.339
	19 Months		-0.531 $^{\Delta}$			0.075	0.282	0.211

$^{\Delta}$ indicates significance of partial correlation $0.05 < p < 0.10$. All other partial correlations significant at $p < 0.05$.
N.S. indicates no significant model existed with covariates.
A = Effect of increasing age group, E = Effect of exercise
$^{(ln)}$ indicates that the natural log of dependent variable was used in the regression (to satisfy normality assumption)
Crystallinity was excluded from the table because it did not significantly contribute to any model.

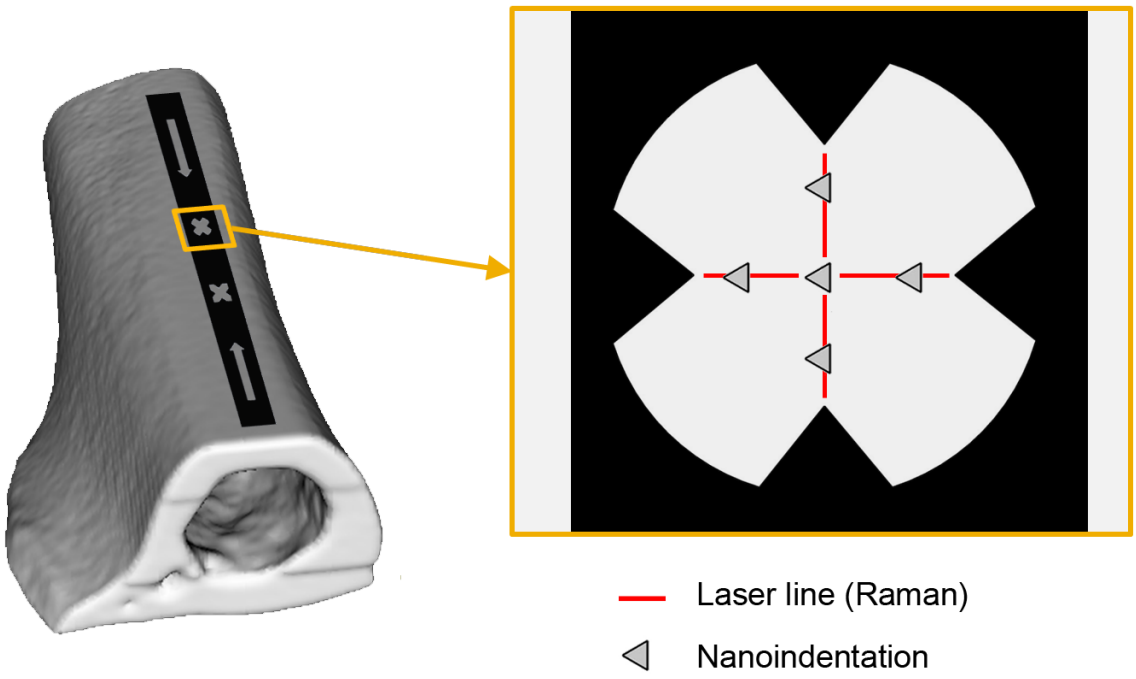

Figure 4.1. Experimental design to co-localize compositional and mechanical properties. After creating a flat, smooth surface on the anterior side of murine femora, a marker was stamped onto that surface. The marker was used as a guide to ensure Raman spectra (4 lines) and nanoindentation measurements (5 indents) were taken at the same location.

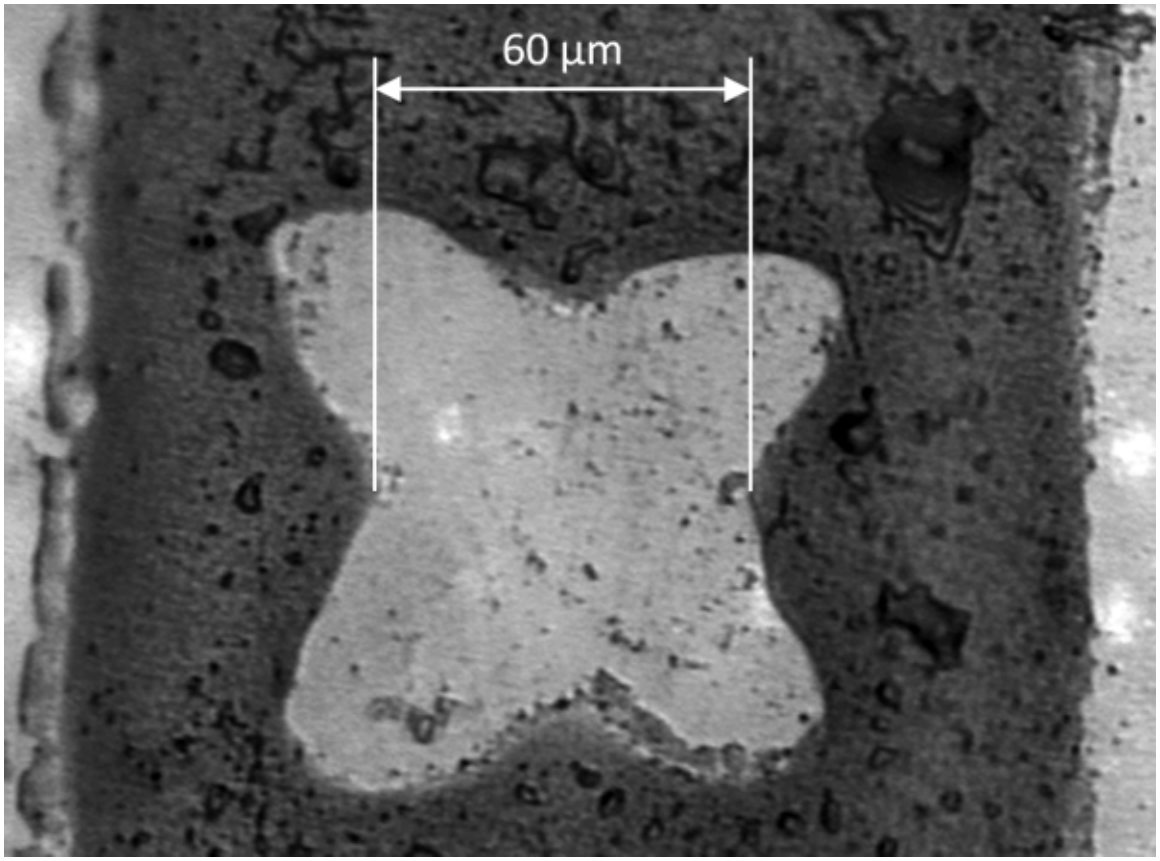

Figure 4.2. 20X optical image of marker used for co-localization of Raman micro-specroscopy and nanoindentation. The surface of the bone within the marker was smooth and flat and untouched by the ink stamp.

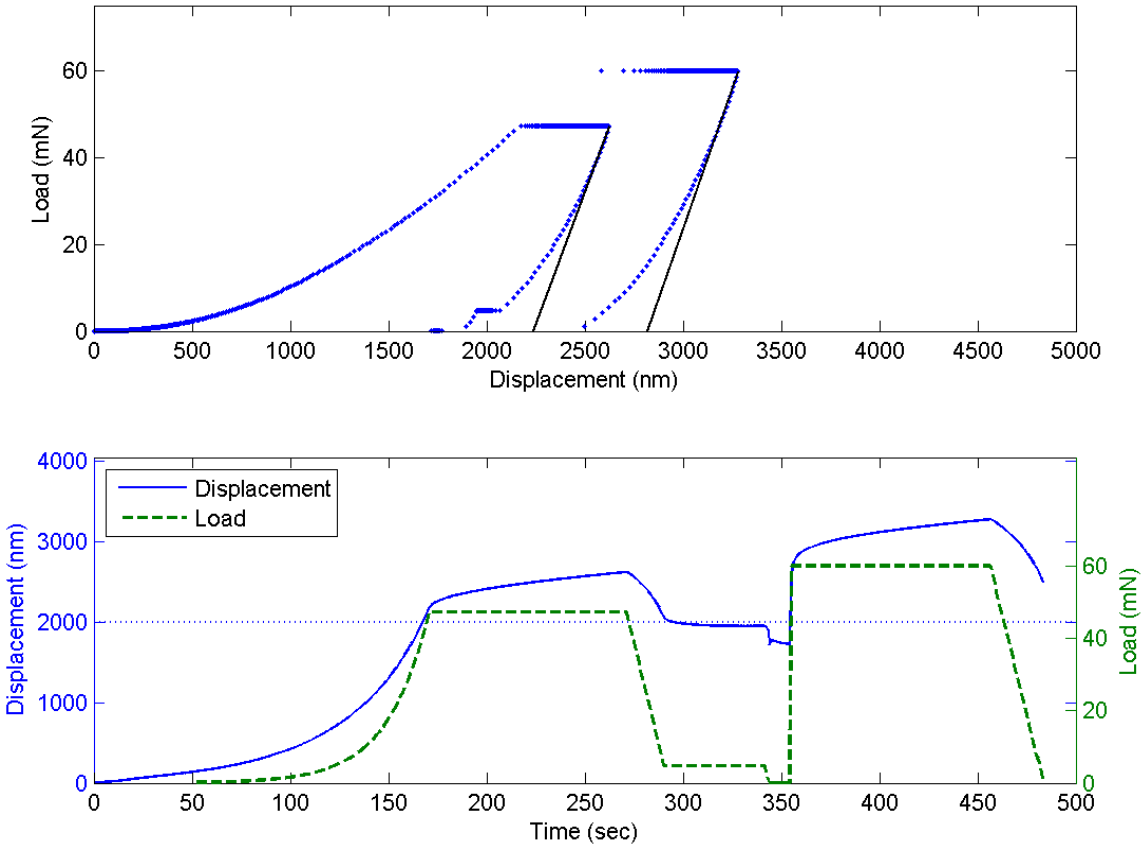

Figure 4.3. Loading profile used for nanoindentation shown as load vs. displacement (top) and load and displacement vs. time (bottom). The first segment of the profile consisted of loading to an indentation depth of 2000 nm, a 100 second hold, and then a complete unloading (with a 50 second hold at 10% of peak load for thermal drift correction). The second segment of the profile proceeded after a 10 second pause and consisted of a 60 mN step load, 100 second hold at maximum load, and a complete unloading. Calculated unloading stiffness for each unloading (black lines) is illustrated on the load-displacement profiles.

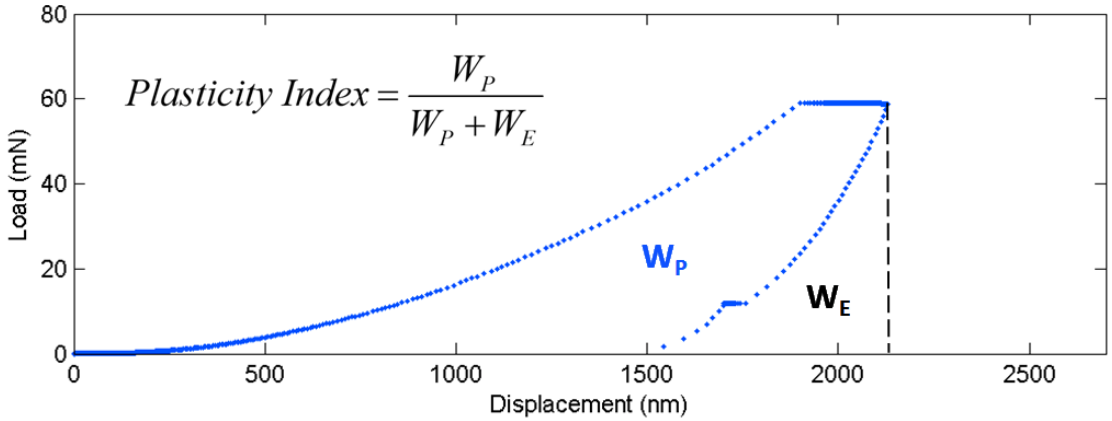

Figure 4.4. Plasticity index was calculated as the percent of total work from the first loading/unloading procedure that was not returned by elastic recovery. A greater plasticity index indicates that there was less elastic recovery.

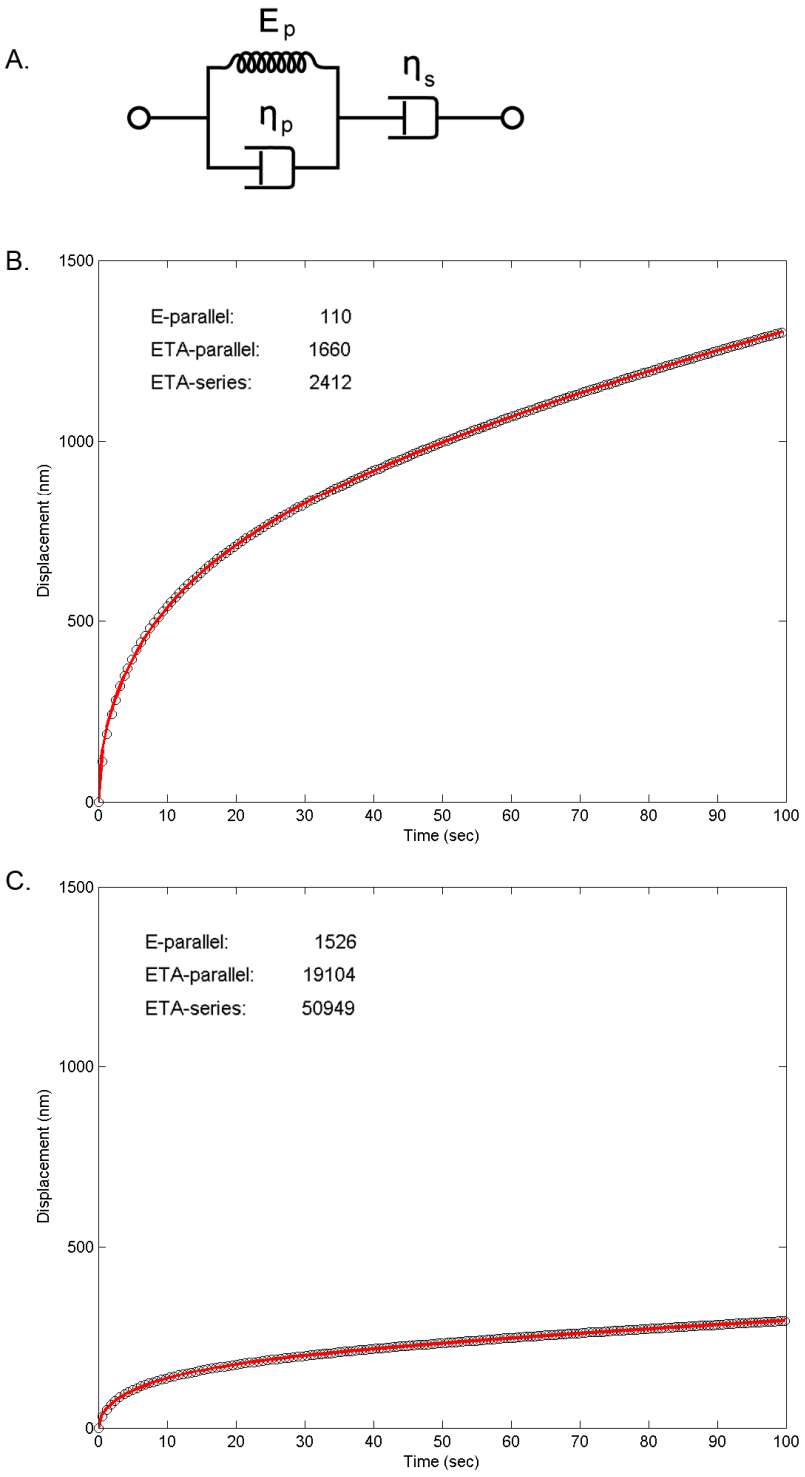

Figure 4.5. Creep behavior after a 60 mN step load was modeled as a combined Maxwell-Voigt model, containing parallel spring and damper elements in series with another damper (A). The model fit the creep behavior well ($R^2 > 0.999$) for all samples, whether there were large or small creep displacements (B & C, respectively). Black circles show measured values and the red line shows the model fitted to that data.

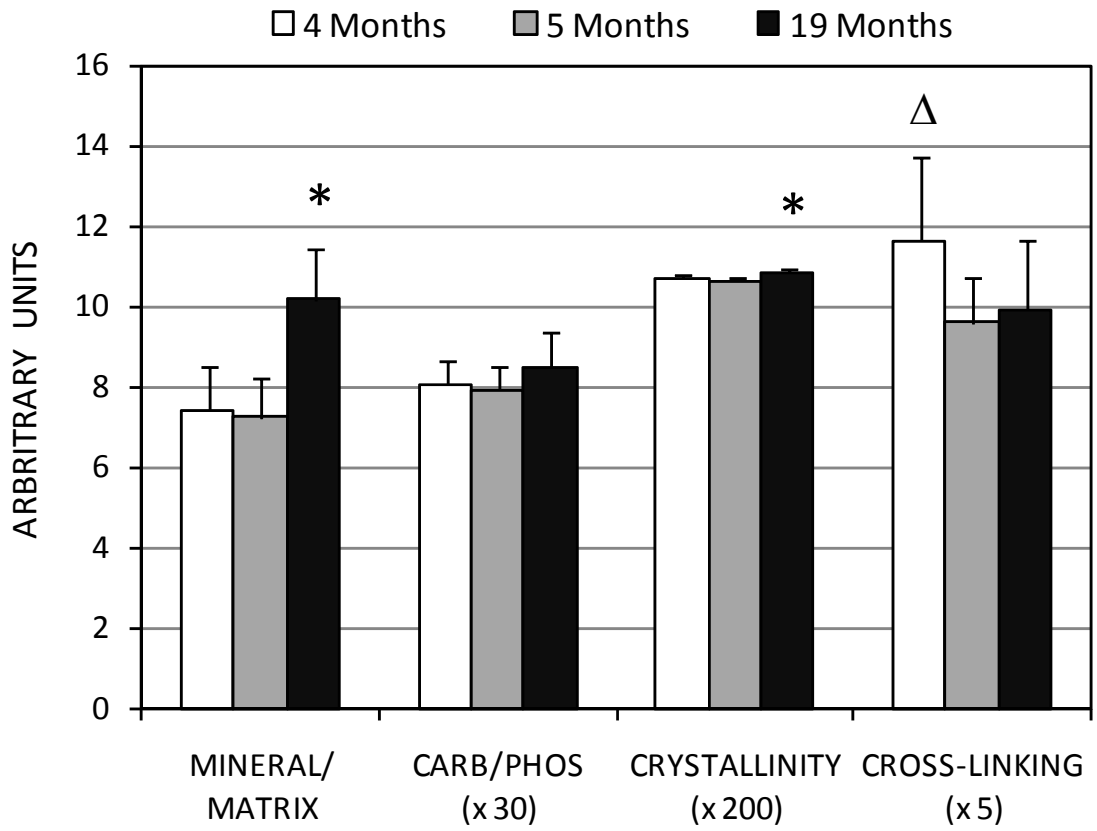

Figure 4.6. Average Raman metrics by age group. Mineral/matrix ratio and crystallinity were significantly greater in 19 month old femora than any other age groups and cross-linking ratio was marginally greater in 4 month old femora than any other age group. There were no significant differences in carbonate/phosphate ratio between groups. * and $^{\Delta}$ indicate that the specified age group was significantly greater ($p < 0.05$) or marginally greater ($p < 0.1$) than all other age groups, respectively.

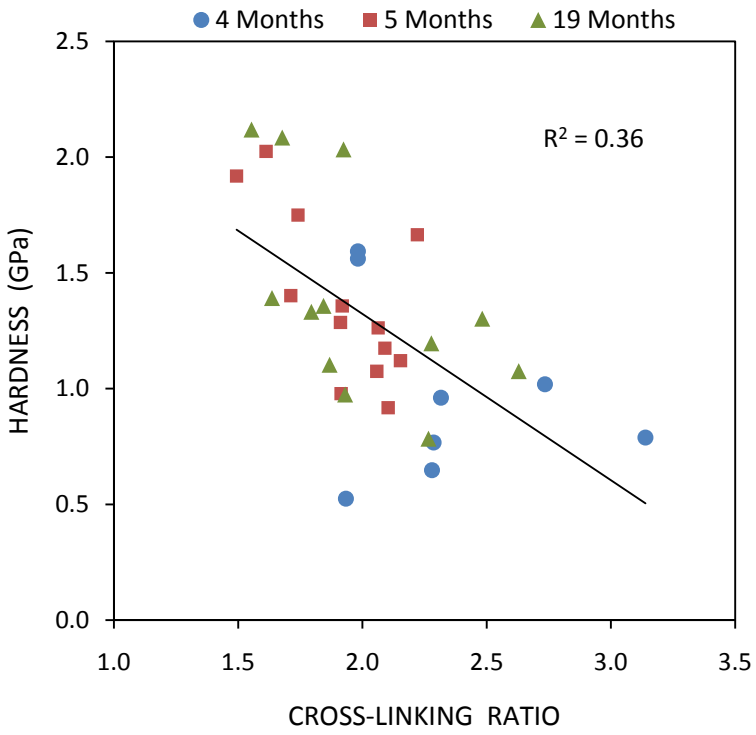

Figure 4.7. Relationship between cross-linking ratio and hardness. There was a significant negative correlation between cross-linking ratio and hardness across all age groups.

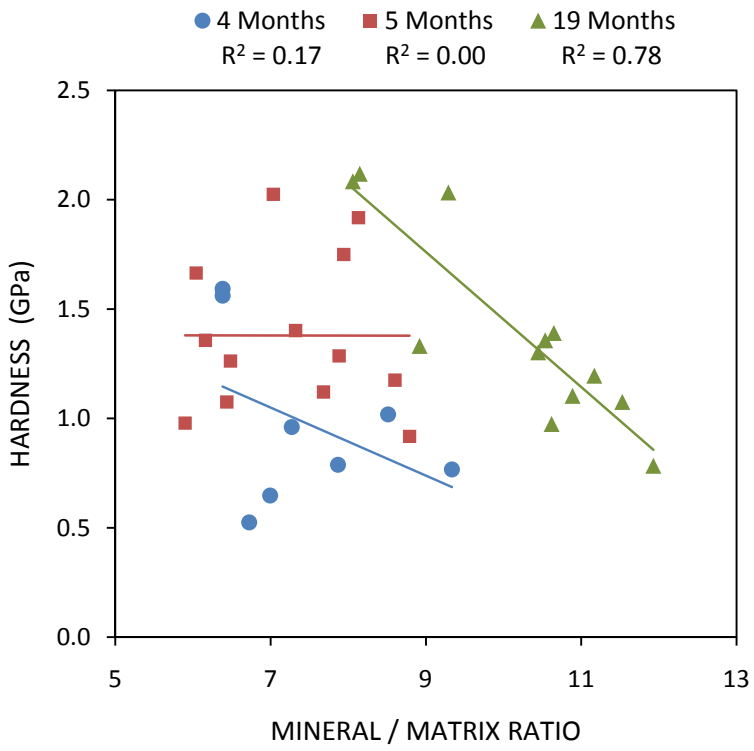

Figure 4.8. Relationship between mineral/matrix ratio and hardness. Mineral/matrix ratio had no significant correlation with hardness in 4 and 5 month old femora, but had a significant negative relationship with hardness in 19 month old femora. The decrease in hardness of 19 month bones appears to occur at values of mineral/matrix ratio that exceed the highest values found in younger bones.

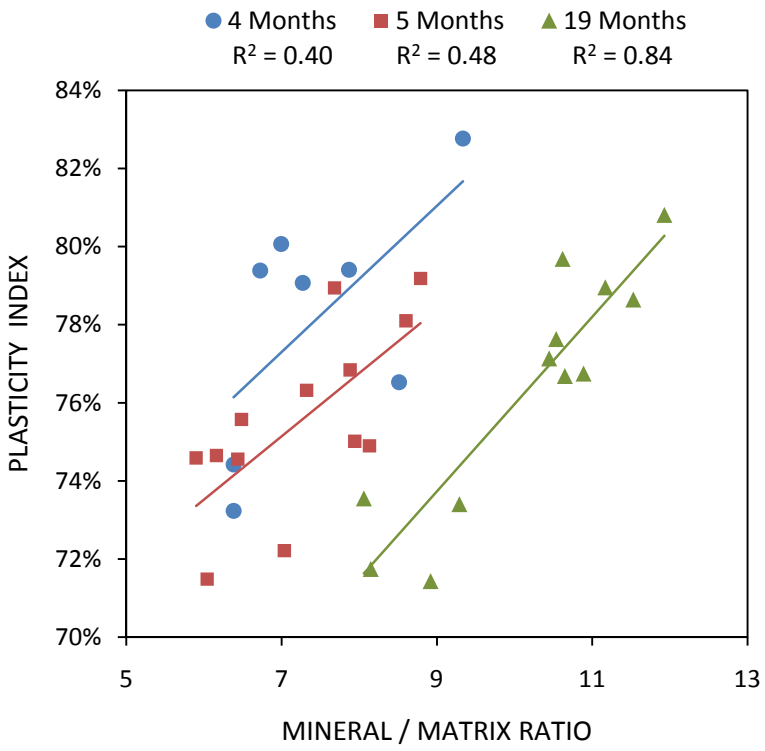

Figure 4.9. Relationship between mineral/matrix ratio and plasticity index. Plasticity index significantly increased with mineral/matrix ratio in all age groups and with slopes that were not significantly different. However, the groups were offset from each other and the range of plasticity indices was similar between age groups even though mineral/matrix ratio was significantly greater in the 19 month age group.

1. Allolio, B. Risk factors for hip fracture not related to bone mass and their therapeutic implications. *Osteoporos. Int.* 9 Suppl 2: S9-S16 (1999).

2. Burr, D. B. *et al*. Bone microdamage and skeletal fragility in osteoporotic and stress fractures. *J. Bone Miner. Res.* 12(1): 6-15 (1997).

3. Heaney, R. P. Is the paradigm shifting? *Bone* 33(4): 457-465 (2003).

4. Marshall, D., Johnell, O. & Wedel, H. Meta-analysis of how well measures of bone mineral density predict occurrence of osteoporotic fractures. *BMJ* 312(7041): 1254-1259 (1996).

5. McCreadie, B. R. & Goldstein, S. A. Biomechanics of fracture: is bone mineral density sufficient to assess risk? *J. Bone Miner. Res.* 15(12): 2305-2308 (2000).

6. Sandor, T., Felsenberg, D. & Brown, E. Comments on the hypotheses underlying fracture risk assessment in osteoporosis as proposed by the World Health Organization. *Calcif. Tissue Int.* 64(3): 267-270 (1999).

7. Paschalis, E. P. *et al*. Bone fragility and collagen cross-links. *J. Bone Miner. Res.* 19(12): 2000-2004 (2004).

8. Burr, D. B. & Milgrom, C. *Musculoskeletal Fatigue and Stress Fractures*. (2001).

9. Hansma, P. K., Turner, P. J. & Fantner, G. E. Bone diagnostic instrument. *Rev. Sci. Instrum.* 77(7): 075105 (2006).

10. Hansma, P. *et al*. The bone diagnostic instrument II: Indentation distance increase. *Rev. Sci. Instrum.* 79(6): 064303 (2008).

11. Schulmerich, M. V., Dooley, K. A., Morris, M. D., Vanasse, T. M. & Goldstein, S. A. Transcutaneous fiber optic Raman spectroscopy of bone using annular illumination and a circular array of collection fibers. *J. Biomed. Opt.* 11(6): 060502 (2006).

12. Schulmerich, M. V. *et al*. Noninvasive Raman tomographic imaging of canine bone tissue. *J. Biomed. Opt.* 13(2): 020506 (2008).

13. Wang, X. *et al*. Detection of trabecular bone microdamage by micro-computed tomography. *J. Biomech.* 40(15): 3397-3403 (2007).

14. Gluer, C. C. Quantitative Ultrasound--it is time to focus research efforts. *Bone* 40(1): 9-13 (2007).

15. Marin, F., Gonzalez-Macias, J., Diez-Perez, A., Palma, S. & Delgado-Rodriguez, M. Relationship between bone quantitative ultrasound and fractures: a meta-analysis. *J. Bone Miner. Res.* 21(7): 1126-1135 (2006).

16. Carter, D. R. & Hayes, W. C. Compact bone fatigue damage--I. Residual strength and stiffness. *J. Biomech.* 10(5-6): 325-337 (1977).

17. Norman, T. L., Yeni, Y. N., Brown, C. U. & Wang, Z. Influence of microdamage on fracture toughness of the human femur and tibia. *Bone* 23(3): 303-306 (1998).

18. Reilly, G. C. & Currey, J. D. The effects of damage and microcracking on the impact strength of bone. *J. Biomech.* 33(3): 337-343 (2000).

19. Danova, N. A. *et al*. Degradation of bone structural properties by accumulation and coalescence of microcracks. *Bone* 33(2): 197-205 (2003).

20. Schaffler, M. B., Choi, K. & Milgrom, C. Aging and matrix microdamage accumulation in human compact bone. *Bone* 17(6): 521-525 (1995).

21. Sobelman, O. S. *et al*. Do microcracks decrease or increase fatigue resistance in cortical bone? *J. Biomech.* 37(9): 1295-1303 (2004).

22. Vashishth, D., Behiri, J. C. & Bonfield, W. Crack growth resistance in cortical bone: concept of microcrack toughening. *J. Biomech.* 30(8): 763-769 (1997).

23. Vashishth, D., Tanner, K. E. & Bonfield, W. Experimental validation of a microcracking-based toughening mechanism for cortical bone. *J. Biomech.* 36(1): 121-124 (2003).

24. Sahar, N. D., Hong, S. I. & Kohn, D. H. Micro- and nano-structural analyses of damage in bone. *Micron* 36(7-8): 617-629 (2005).

25. Akkus, O., Adar, F. & Schaffler, M. B. Age-related changes in physicochemical properties of mineral crystals are related to impaired mechanical function of cortical bone. *Bone* 34(3): 443-453 (2004).

26. Paschalis, E. P. *et al*. Spectroscopic characterization of collagen cross-links in bone. *J. Bone Miner. Res.* 16(10): 1821-1828 (2001).

27. Zioupos, P., Currey, J. D. & Hamer, A. J. The role of collagen in the declining mechanical properties of aging human cortical bone. *J. Biomed. Mater. Res.* 45(2): 108-116 (1999).

28. Ager, J. W., Nalla, R. K., Breeden, K. L. & Ritchie, R. O. Deep-ultraviolet Raman spectroscopy study of the effect of aging on human cortical bone. *J. Biomed. Opt.* 10(3): 034012 (2005 May-Jun).

29. Gordon, K. R., Burns, P. & Keller, G. Experimental changes in mineral content of juvenile mouse femora. *Calcif. Tissue Int.* 51(3): 229-232 (1992).

30. Camacho, N. P. *et al*. The material basis for reduced mechanical properties in oim mice bones. *J. Bone Miner. Res.* 14(2): 264-272 (1999).

31. Burr, D. B. The contribution of the organic matrix to bone's material properties. *Bone* 31(1): 8-11 (2002).

32. Viguet-Carrin, S., Garnero, P. & Delmas, P. D. The role of collagen in bone strength. *Osteoporos. Int.* 17(3): 319-336 (2006).

33. Hengsberger, S., Kulik, A. & Zysset, P. Nanoindentation discriminates the elastic properties of individual human bone lamellae under dry and physiological conditions. *Bone* 30(1): 178-184 (2002).

34. Hengsberger, S., Kulik, A. & Zysset, P. A combined atomic force microscopy and nanoindentation technique to investigate the elastic properties of bone structural units. *Eur. Cell. Mater.* 1: 12-17 (2001).

35. Zysset, P. K., Guo, X. E., Hoffler, C. E., Moore, K. E. & Goldstein, S. A. Elastic modulus and hardness of cortical and trabecular bone lamellae measured by nanoindentation in the human femur. *J. Biomech.* 32(10): 1005-1012 (1999).

36. Busa, B., Miller, L. M., Rubin, C. T., Qin, Y. X. & Judex, S. Rapid establishment of chemical and mechanical properties during lamellar bone formation. *Calcif. Tissue Int.* 77(6): 386-394 (2005).

37. Fisher-Cripps, A. C. in *Nanoindentation* (Springer-Verlag New York, LLC, New York, NY, 2004).

38. Briscoe, B. J., Fiori, L. & Pelillo, E. Nano-indentation of polymeric surfaces. *Journal of Physics D-Applied Physics* 31(19): 2395-2405 (1998).

39. Odegard, G. M., Gates, T. & Herring, H. M. Characterization of viscoelastic properties of polymeric materials through nanoindentation. *Exp. Mech.* 45(2): 130-136 (2005).

40. Fan, Z. F. & Rho, J. Y. Effects of viscoelasticity and time-dependent plasticity on nanoindentation measurements of human cortical bone. *Journal of Biomedical Materials Research Part a* 67A(1): 208-214 (2003).

41. Oyen, M. L. & Cook, R. F. Load-displacement behavior during sharp indentation of viscous-elastic-plastic materials. *J. Mater. Res.* 18(1): 139-150 (2003).

42. Ferguson, V. L., Ayers, R. A., Bateman, T. A. & Simske, S. J. Bone development and age-related bone loss in male C57BL/6J mice. *Bone* 33(3): 387-398 (2003).

43. Somerville, J. M., Aspden, R. M., Armour, K. E., Armour, K. J. & Reid, D. M. Growth of C57BL/6 mice and the material and mechanical properties of cortical bone from the tibia. *Calcif. Tissue Int.* 74(5): 469-475 (2004).

44. Brodt, M. D., Ellis, C. B. & Silva, M. J. Growing C57Bl/6 mice increase whole bone mechanical properties by increasing geometric and material properties. *J. Bone Miner. Res.* 14(12): 2159-2166 (1999).

45. Favus, M. J. *Primer on the Metabolic Bone Diseases and Disorders of Mineral Metabolism, 4th Edition*. (1999).

46. Gustafson, M. B. *et al*. Calcium buffering is required to maintain bone stiffness in saline solution. *J. Biomech.* 29(9): 1191-1194 (1996).

47. Kazanci, M., Roschger, P., Paschalis, E. P., Klaushofer, K. & Fratzl, P. Bone osteonal tissues by Raman spectral mapping: orientation-composition. *J. Struct. Biol.* 156(3): 489-496 (2006).

48. Widjaja, E. *et al*. Band-target entropy minimization (BTEM) applied to hyperspectral Raman image data. *Appl. Spectrosc.* 57(11): 1353-1362 (2003).

49. Timlin, J. A., Carden, A., Morris, M. D., Rajachar, R. M. & Kohn, D. H. Raman spectroscopic imaging markers for fatigue-related microdamage in bovine bone. *Anal. Chem.* 72(10): 2229-2236 (2000).

50. Rajachar, R. M. Effects of age-related ultra-structural level changes in bone on microdamage mechanisms, Ph.D. Dissertation. (2003).

51. Golcuk, K. *et al*. Is photobleaching necessary for Raman imaging of bone tissue using a green laser? *Biochim. Biophys. Acta* (2006).

52. Carden, A., Rajachar, R. M., Morris, M. D. & Kohn, D. H. Ultrastructural changes accompanying the mechanical deformation of bone tissue: a Raman imaging study. *Calcif. Tissue Int.* 72(2): 166-175 (2003).

53. Awonusi, A., Morris, M. D. & Tecklenburg, M. M. Carbonate assignment and calibration in the Raman spectrum of apatite. *Calcif. Tissue Int.* 81(1): 46-52 (2007).

54. Baig, A. A. *et al*. Relationships among carbonated apatite solubility, crystallite size, and microstrain parameters. *Calcif. Tissue Int.* 64(5): 437-449 (1999).

55. Oliver, W. C. & Pharr, G. M. An Improved Technique for Determining Hardness and Elastic-Modulus using Load and Displacement Sensing Indentation Experiments. *J. Mater. Res.* 7(6): 1564-1583 (1992).

56. Oliver, W. C. & Pharr, G. M. Measurement of hardness and elastic modulus by instrumented indentation: Advances in understanding and refinements to methodology. *J. Mater. Res.* 19(1): 3-20 (2004).

57. Oyen, M. L. Nanoindentation hardness of mineralized tissues. *J. Biomech.* 39(14): 2699-2702 (2006).

58. Ahsan, T., Harwood, F., McGowan, K. B., Amiel, D. & Sah, R. L. Kinetics of collagen crosslinking in adult bovine articular cartilage. *Osteoarthritis Cartilage* 13(8): 709-715 (2005).

59. Wang, X. & Puram, S. The toughness of cortical bone and its relationship with age. *Ann. Biomed. Eng.* 32(1): 123-135 (2004).

60. Wang, X., Shen, X., Li, X. & Agrawal, C. M. Age-related changes in the collagen network and toughness of bone. *Bone* 31(1): 1-7 (2002).

61. Hernandez, C. J. *et al*. Trabecular microfracture and the influence of pyridinium and non-enzymatic glycation-mediated collagen cross-links. *Bone* 37(6): 825-832 (2005).

62. Nyman, J. S., Reyes, M. & Wang, X. Effect of ultrastructural changes on the toughness of bone. *Micron* 36(7-8): 566-582 (2005).

63. Siegmund, T., Allen, M. R. & Burr, D. B. Failure of mineralized collagen fibrils: modeling the role of collagen cross-linking. *J. Biomech.* 41(7): 1427-1435 (2008).

64. Bailey, A. J. *et al*. Age-related changes in the biochemical properties of human cancellous bone collagen: relationship to bone strength. *Calcif. Tissue Int.* 65(3): 203-210 (1999).

65. Saito, M., Fujii, K. & Marumo, K. Degree of mineralization-related collagen crosslinking in the femoral neck cancellous bone in cases of hip fracture and controls. *Calcif. Tissue Int.* 79(3): 160-168 (2006).

66. Buehler, M. J. Nature designs tough collagen: explaining the nanostructure of collagen fibrils. *Proc. Natl. Acad. Sci. U. S. A.* 103(33): 12285-12290 (2006).

67. Oxlund, H., Mosekilde, L. & Ortoft, G. Reduced concentration of collagen reducible cross links in human trabecular bone with respect to age and osteoporosis. *Bone* 19(5): 479-484 (1996).

68. Paschalis, E. P. *et al*. FTIR microspectroscopic analysis of human osteonal bone. *Calcif. Tissue Int.* 59(6): 480-487 (1996).

69. Akkus, O., Polyakova-Akkus, A., Adar, F. & Schaffler, M. B. Aging of microstructural compartments in human compact bone. *J. Bone Miner. Res.* 18(6): 1012-1019 (2003).

70. Marotti, G., Favia, A. & Zallone, A. Z. Quantitative analysis on the rate of secondary bone mineralization. *Calcif. Tissue Res.* 10(1): 67-81 (1972).

71. Dorozhkin, S. V. Calcium orthophosphates. *J. Mater. Sci.* 42(4): 1061-1095 (2007).

72. Tanck, E. *et al*. The mechanical consequences of mineralization in embryonic bone. *Bone* 35(1): 186-190 (2004).

73. Vose, G. P. & Kubala, A. L. Bone strength—its relationship to x-ray determined ash content. *Human Biology* 31: 261-270 (1959).

74. Hernandez, C. J., Beaupre, G. S., Keller, T. S. & Carter, D. R. The influence of bone volume fraction and ash fraction on bone strength and modulus. *Bone* 29(1): 74-78 (2001).

75. Akhter, M. P. *et al*. Genetic variations in bone density, histomorphometry, and strength in mice. *Calcif. Tissue Int.* 67(4): 337-344 (2000).

76. Weiner, S. & Traub, W. Crystal size and organization in bone. *Connect. Tissue Res.* 21(1-4): 259-265 (1989).

77. Callister Jr, W. D. Fundamentals of Materials Science and Engineering: An Integrated Approach. *Fundamentals of Materials Science and Engineering: An Integrated Approach, 2nd Edition, by William D.Callister, Jr.*: 824 (2004).

78. Sari, Y. W., Soejoko, D. S. & Dahlan, K. Nanostructure in Bone Apatite. *3rd Kuala Lumpur International Conference on Biomedical Engineering 2006*: 118-121 (2007).

79. Zappone, B., Thurner, P. J., Adams, J., Fantner, G. E. & Hansma, P. K. Effect of Ca2+ ions on the adhesion and mechanical properties of adsorbed layers of human osteopontin. *Biophys. J.* 95(6): 2939-2950 (2008).

80. Diab, T., Condon, K. W., Burr, D. B. & Vashishth, D. Age-related change in the damage morphology of human cortical bone and its role in bone fragility. *Bone* 38(3): 427-431 (2006).

CHAPTER FIVE

CONCLUSIONS AND FUTURE WORK

BONE ADAPTATION AND AGING

Chapters 2 and 3 presented data that challenges the conventional understanding of bone adaptation. It was demonstrated for the first time that external stimuli, in the form of exercise, and aging modulate bone composition and tissue-level mechanical properties, even in the absence of bone formation or remodeling. In young adult mice, a short-term moderate-intensity exercise program significantly increased mineralization and decreased carbonate substitution in pre-existing tissue. These changes were accompanied by significant increases in tissue strength and resistance to fatigue-induced microdamage formation and collagen cross-link reduction. Additionally, there was not a significant bone formation response to exercise as judged by lack of calcein double labeling and lack of significant changes in bone size compared to baseline bones (at the start of exercise).

Traditional belief is that exercise is beneficial for skeletal integrity because the mechanical loading of exercise will stimulate bone formation. However, the findings of Chapter 2 indicate that exercise can impart mechanical benefits to bone by improving tissue quality, and that this benefit may take place without a significant change in bone size. It is possible that the benefits of exercise are often overlooked because bone adaptation is clinically evaluated by bone mass scans. For instance, fracture risk is reduced by exercise in the elderly, even if it is not accompanied by a change in bone mass. This unexplained benefit is typically attributed to a decreased risk of falling, but

adjusting fracture risk for the risk of falling still underestimates the benefit of exercise [1]. This discrepancy is likely due to overlooked changes in tissue quality. Therefore, proper evaluation of bone adaptation to external stimuli – such as exercise, nutrition, disease, and hormone and drug treatments – likely requires more than examining bone mass.

In old mice, exercise did not result in improved tissue-level mechanical properties or fatigue resistance (Chapter 3), but did result in significantly reduced carbonate substitution in mineral crystals. Reduced carbonate substitution was also seen with exercise in young tibiae and may indicate the start of a bone adaptation in old tibiae. In these experiments, a short-term exercise program, 21 days, was employed. Extending the program could possibly allow enough time for a positive bone adaptation to take place in old mice. In young mice, exercise slowed bone growth in the tibiae, which may have also been the result of the short exercise program (Chapter 2). Extending the program to allow for physiological adaptations to the sudden challenge of exercise may restore normal growth patterns or even induce a period of "catch up growth" [2, 3]. However, the possible sources of slowed growth and the potential benefits of an extended program in young and old mice can only be considered speculation without further experimentation (see "Future Studies").

Paralleling the adaption to exercise, reductions in skeletal integrity with aging in the mice seemed to be driven by changes in the quality of preexisting tissue (Chapter 3). Micro-CT analysis of young and old bones indicated that as much as 90% of the bone tissue from the mid-diaphysis of 19 month old tibiae may have already been present at 5 months of age (Figure 5.1). The changes in bone size and shape with aging did not explain the significant reductions in whole-bone mechanical properties and therefore indicate that reduction of tissue-level mechanical properties was the sources of compromised skeletal integrity. The amount of pre-existing tissue may be slightly overestimated because of geometric averaging and because surface resorption and formation could renew some of the preexisting tissue. However, investigation of calcein labeling suggests that there is

little surface remodeling at either age and that there is almost no intracortical remodeling (only one case of remodeling was found in 87 samples).

The lack of bone formation and remodeling, combined with the finding that compositional differences between age groups were ubiquitous throughout the tibial cross-section, indicates that aging of pre-existing bone tissue resulted in altered composition and decreased tissue-level mechanical properties. With aging, mineral crystal size and carbonate substitution were significantly increased, which could reduce tissue strength and toughness by weakening mineral crystals or inhibiting sliding of collagen fibers and increasing load transfer to bone defects [4-9]. There was also a significant increase in microcracking and average crack length in old bones without an increase in diffuse damage, indicating that old tibiae had reduced capacity to dissipate loading energy and prevent crack propagation. Young tibiae had less damage and seemed to preferentially form short cracks and diffuse damage, which are less detrimental to mechanical integrity than long cracks [10]. These changes in composition and microdamage mechanisms with aging likely contributed to the decreased tissue strength, toughness, resilience and ductility observed in old tibiae (Table 5.1). Similar age-related changes in composition and microdamage mechanisms have been observed in human bone [7, 11, 12].

Murine models are a good choice to study aging because mice typically do not have intracortical remodeling, meaning that tissue age is related to mouse age rather than the rate of tissue replacement. Murine aging models may also reflect the effects of suppressed bone turnover in humans, for instance by antiresorptive drug treatments. However, the shortcoming of relating murine models to humans is that murine bone lacks a secondary osteon structure, which could alter fracture mechanics, fatigue resistance, and microdamage formation.

The results of Chapter 2 and 3 not only present new possibilities for the effects of exercise and aging but also point to new adaptation mechanisms in bone. The currently understood adaptation mechanisms in bone require pathway signaling for bone deposition

by osteoblasts or bone resorption by osteoclasts. These mechanisms, which can occur independently or in a coupled action for removal and replacement of tissue, were almost completely absent in exercised young and old murine tibiae. As discussed in Chapter 2, the adaptation in these bones may not have been an active cell-mediated response but rather a physical-chemical response due to exercise altering serum ion concentrations and increasing fluid flow through the bone by mechanical cycling. Alternatively, it may have been an active response mediated by the osteocyte-canaliculi network. This network is exposed to a great surface area in bone and could potentially control ion release to the extracellular matrix or stimulate chemical digestion of local mineral. The possibility of these two mechanisms warrant further investigation and are discussed in "Future Studies."

RELATIONS BETWEEN COMPOSITION AND MECHANICS

Because the results of Chapter 2 and 3 implicated compositional changes in contributing to exercise and age induced-changes in mechanical properties, the work of Chapter 4 sought to establish direct correlations between bone composition and mechanical properties. Table 5.1 provides a summary of the findings in these chapters. In many cases, the suspected causes for altered mechanical properties in Chapters 2 and 3 were supported by evidence in Chapter 4, but there were also new correlations discovered between composition and mechanical properties that were not previously suspected.

For instance, in young mice, it was suspected that increased mineralization and decreased carbonate substitution contributed to increased tissue strength and fatigue resistance in tibiae of exercised mice. By colocalized Raman and nanoindentation measurements in femora of the same mice, increased mineralization was significantly and positively correlated with elastic modulus, viscoelastic modulus, and viscoelastic viscosity (Table 5.1). Also, carbonate substitution was negatively associated with elastic recovery, indicating that increased carbonate substitution resulted in a greater percentage of permanent plastic deformation for any given strain. These findings support the hypothesis that, in young mice, greater mineralization with less carbonate substitution

resulting from exercise contributed to the improved tissue-level mechanical competence of those bones.

The Raman-nanoindentation experiment also revealed a surprising and significant association between collagen cross-linking ratio and mechanical properties in young femora. In these bones, cross-linking ratio was negatively correlated with modulus, hardness, and resistance to viscoelastic deformation and viscoplastic creep. All of these findings are counter to the conventional wisdom that cross-linking imparts mechanical benefit to bone, but there are explanations for this apparent discrepancy, discussed in Chapter 4 and briefly summarized here. First, there is no direct evidence supporting the conventional wisdom that increased cross-linking in adult bone improves mechanical competence [13-21]. Second, increased cross-linking ratio and increased total cross-linking have been implicated with fragility fractures and decreased ability to dissipate loading energy [22, 23]. Finally, because cross-linking ratio is not a direct measurement of the number cross-links, it could be increased by an increase of mature cross-links, a decrease of immature cross-links or by perturbations to collagen organization. At this point it is not clear why cross-linking ratio was negatively associated with mechanical properties because it is not clear what changes in bone were driving changes in cross-linking ratio. Further investigations could reveal the true source of these associations (see "Future Studies"). Regardless of the controlling source of cross-linking ratio, it is still possible that cross-linking ratio could be a useful marker for skeletal fragility if it is consistently associated with reduced mechanical properties.

In old bones, mineralization, which likely reflected average mineral crystal size, was the only measured compositional property that was significantly associated with mechanical properties (Chapter 4, Table 5.1). Whereas mineralization was positively correlated with mechanical properties young bones, in old bones it was negatively correlated with hardness, elastic recovery of work, and resistance to viscoplastic creep. These findings support the hypothesis made in Chapter 3 that increased mineralization with aging contributed to decreased strength, toughness, ductility, and resilience of the bone tissue. The findings also corroborate previous observations that as bone tissue ages it can

become mineralized to such an extent that mechanical properties, in particular ductility, are compromised [4-9].

The Raman-nanoindentation correlations as well as the suspected associations between composition and mechanical properties in Chapters 2 and 3 reveal that the effects of compositional changes were different between age groups (Table 5.1). Increased mineralization improved mechanical competence of young bones but decreased mechanical competence in old bones. Similarly, cross-linking ratio played an important role in mechanical properties of young bones but not old bones. The relations between composition and mechanics may be dependent on tissue age, but a more likely explanation is that there is a nonlinear association between composition and mechanical properties. For instance, Figure 5.2 shows a simplified representation of the potential associations between composition and mechanical competence. In newly formed bone, mechanical competence is rapidly established, possibly by increases in mineralization and cross-link formation [24, 25]. The data in this thesis and other studies [4-6] suggests that increased mineralization in bones nearing skeletal maturity also improves mechanical properties. After skeletal maturity, tissue-level mechanical competence may be fully realized and increasing mineralization or cross-linking may not impart any further benefit. This portion of tissue maturation is represented by the plateau region of Figure 5.2. However, after some threshold is reached, further increases in mineralization and possibly cross-linking will have detrimental effects on mechanical competence. Therefore, as regions of bone tissue age and become heavily mineralized, mechanical competence may be locally compromised. The detrimental effects of excessive mineralization or cross-linking could be due to hindered sliding of collagen fibers and potentially increased load transfer to stress concentrations like microcrack tips [4-9]. In humans, proper bone remodeling may renew tissue to keep average composition in the plateau region. Too much remodeling may result in reduced average mechanical properties in bone by increasing the percentage of immature tissue, while too little remodeling may decrease average mechanical properties by increasing the percentage of tissue that is aged to the point of decreased mechanical competence.

Figure 5.2 is intentionally oversimplified to illustrate the concept that a compositional change could improve mechanical properties up to a point but the decrease mechanical properties if a threshold is exceeded. It is unlikely that both mineralization and cross-linking would scale linearly with tissue age or that their individual contributions to mechanical competence would follow the same pattern. Further, "mechanical competence" is a generic term meant to represent a composite of all mechanical properties that would contribute to fracture resistance. It is unlikely that all mechanical properties would share the same dependence on composition. For instance, Figure 5.3 illustrates that the optimal level of mineralization could be different to maximize strength and toughness. Establishing relationships between composition and mechanical properties is made even more difficult by the possibility that along with a measured change in composition, there may be other changes in composition or structural organization that also affect mechanical properties but are unmeasured.

The findings in the thesis highlight the potential utility of using bone compositional measurements in diagnosing skeletal fragility, but also show the difficulty in making sweeping conclusions about the effects of compositional changes on bone fragility. The Raman-nanoindentation experiment provided corroborating evidence for previously assumed associations between composition and mechanical properties but also raised new questions (Table 5.1). Much work remains before compositional measurement could effectively be used in clinical diagnosis of skeletal fragility (see "Future Studies").

FUTURE STUDIES

Expanding the Exercise Program

The exercise experiments in young and old mice left unresolved questions. In young mice, exercise improved tissue-level mechanical properties and altered mineral composition but slowed growth of the tibiae. As discussed in Chapter 3 and briefly in "Bone Adaptation" of this chapter, the slowed bone growth may be due to a physiological

mechanism to match bone size to body weight, which was significantly reduced by exercise, or to develop a lighter but equally competent bone structure that would be more efficient for exercise. However, it is also possible that slowed growth resulted from inadequate protein or ion supply in the diet or inadequate time for physiological adaptation to exercise. Normal bone growth or even a period of "catch-up growth" could possibly take place if more time was allowed for adaptation to exercise [2, 3].

To determine why bone growth was slowed in young mice and if catch-up growth is possible, the exercise experiment could be repeated with additional groups. Examples of potentially telling experimental groups are listed below. Each exercise group would have a weight- and age-matched control group.

- 3 weeks of exercise (complete, Chapter 2)
- 3 weeks of exercise with weight packs to keep "body weight" constant
- 3 weeks of exercise and a high protein, high Ca^{2+} diet
- 3 weeks of exercise followed by 3 weeks of rest
- 3 weeks of exercise followed by 3 weeks of rest, with high protein/Ca^{2+} diet
- 6 weeks of exercise
- 6 weeks of exercise with a high protein, high Ca^{2+} diet

Once the sources of slowed growth are understood, it would be interesting to use the optimal exercise program and determine how long after cessation of exercise the benefits of exercise are maintained. Mice could be subjected to the exercise program and sacrificed one week, one month, three months, and six months after cessation of exercise. Mechanical, compositional and geometric properties could then be compared to the properties taken immediately after cessation of exercise as well as to age-matched controls. The starting age previously used (16 weeks) is ideal for these experiments because very little bone growth is expected after 19 weeks of age (Figure 5.1).

There were also unanswered questions about exercise in old mice. While exercise in old mice did not improve tissue-level mechanical properties or fatigue resistance as it did in young mice, it significant decreased carbonate substitution in tibiae of both age groups.

Decreased carbonate substitution in old mice may have been the beginning of an exercise-induced tissue adaptation that was not fully realized because of the short experiment duration. Extending the exercise program or including a rest period before sacrifice may allow for the full adaptation to take place. Similarly, allowing more time before sacrifice may allow for further improvements of tissue quality in young mice. Finally, investigating the effects of extended and more strenuous exercise programs in young and old mice may help determine whether old mice require more time or greater mechanical stimulation to adapt to exercise than young mice or whether they are totally unresponsive to exercise.

Investigating How Composition of Pre-Existing Tissue Could be Altered

Short-term exercise in young adult mice altered mineral composition of pre-existing tissue without involving the processes of modeling or remodeling. Currently there is no well-understood mechanism other than modeling or remodeling that could cause these compositional changes. As discussed in Chapter 2, the adaptation in these bones may not have been a cell-mediated response but rather a physical-chemical response due to exercise altering serum ion concentrations and increasing fluid flow through the bone by mechanical cycling. Alternatively, the adaptation may have been a response mediated by the osteocyte-canaliculi network, which is exposed to a tremendous surface area in bone. Osteocytes may have ion channels that could control local release of ions to the extra cellular matrix (ECM) or cause local resorption of the ECM [26-28].

We currently plan to reexamine cross-sections used for Raman microspectroscopy in Chapter 2. Compositional mapping of lacunae and surrounding bone tissue could be conducted by Raman imaging, using a high magnification objective and a motorized microscope stage. The compositional maps could then be examined to determine if mineralization, crystallinity, and carbonate substitution tend to be different in peri-lacunar regions of bone compared to regions further away from osteocytes. If compositional changes were controlled by osteocytes, we would expect to find those alterations occurring specifically around osteocytes in the compositional maps.

Alternatively, if altered serum and fluid flow through bone was responsible for compositional changes, we would expect to find altered composition everywhere in bone.

One shortcoming of this study is that if osteocytes were controlling the compositional adaptation, they may elicit that adaptation not only through the cell membranes but also through the canalicular network, which is ubiquitous throughout bone. If the adaptation took place by this mechanism, it would be difficult to discern whether the adaptation was osteocyte-mediated or due to altered serum flow through the bone. Investigating expression of genes associated with osteocytes, for instance dentin matrix protein 1 (DMP1), by polymerase chain reaction (PCR) may resolve this experimental shortcoming and provide additional information about the response of osteocytes to exercise. These experiments will not answer all questions about how pre-existing bone composition could be altered but may show where changes were taking place and thereby allow better design of future experiments.

An alternate approach would be to address the hypothesis that altered serum ion concentration and fluid flow through the bone caused the altered crystal composition. Bones could be assigned to groups soaked in solutions of varying ion concentrations and either left to soak or mechanically cycled by four-point bending while in solution to produce fluid flow through the bones. In this way, the effects of ion concentration and mechanical loading on mineralization and mineral composition could be determined. One difficulty of this experiment is ensuring that bones do not degrade while they remain unfrozen. Degradation could be reduced by reasonably limiting the length of the experiment and by adding a preservative, for instance sodium azide, to the solutions. A limited amount of degradation may not be detrimental to the experiment because the investigation focuses on the inorganic phase of bone.

Further Investigation of Cross-Linking

Collagen cross-linking ratio was negatively associated with mechanical properties in young adult murine femora (Chapter 4). However, it is unknown whether variations in

cross-linking ratio were due to maturation of cross-links, addition/loss of immature cross-links, or alterations to collagen organization. This uncertainty exists because the cross-linking ratio metric in Raman spectroscopy is a measure of collagen secondary structure, which is inferred to reflect the ratio of mature/immature cross-links. In contrast, high pressure liquid chromatography (HPLC) is a technique that measures the various types of collagen cross-links directly. An appropriate experiment would be to measure changes in cross-linking with age and exercise by HPLC and by Raman spectroscopy. Both techniques could be conducted on the same bones because Raman spectroscopy is nondestructive. Average cross-linking ratio by Raman for each bone could then be correlated to concentrations of the various types of enzymatic and nonenzymatic cross-links, potentially providing insight into what specific changes in cross-linking were driving changes to cross-linking ratio in these bones. The results combined with previous correlations between cross-linking ratio and mechanical properties may then allow inference of the influence of specific types of cross-links or the total concentration of cross-links on mechanical properties. However, the findings of this examination may only apply to the bones used in the study. It may be inappropriate to extend associations between cross-link concentration and cross-linking ratio or mechanical properties to all situations.

Extending the Associations Between Composition and Mechanical Properties

As discussed in Chapter 4 and in "Relations Between Composition and Mechanics" of this chapter, much work remains before compositional markers can be effectively used in clinical evaluations. Establishing relationships between composition and mechanical properties is made difficult by the possibility that along with a measured change in composition, there may be other unmeasured changes in composition or structural organization. A thorough analysis of the relationship between composition and mechanical properties would be an ambitious undertaking and would require matching compositional measurements to mechanical properties throughout length scales and hierarchical structures of bone.

One strategy would be to use micro-machined bone specimens so that multiple assays could be conducted on each bone. The problem with this strategy is that composition and mechanical properties may vary between machined specimens within each bone. However, many assays could be run on a single sample if the assays are designed to be nondestructive. For instance, if a rectangular beam was micro-machined for mechanical testing by four-point bending, it could first be analyzed by Raman microspectroscopy on the four long sides to obtain an average chemical composition. A very thin section from one side could be removed with a microtome for analysis of lamellar organization by optical microscopy. The same section may even be used for examination mineral size, collagen fiber width, or the organization of mineralized collagen fibers by transmission electron microscopy (TEM) or atomic force microscopy (AFM).

After these assays have been conducted and the machined beam has been mechanically tested to failure, the fractured beam could be homogenized and analyzed for content of non-collagenous proteins by western blot. Alternatively, the fractured surfaces could be examined by scanning electron microscopy (SEM) to determine if the fracture occurred by a brittle-type blunt fracture, by lamellar pull-out, or by a staggered cross-lamellar fracture. The type of fracture may be determined by the composition of the bone and may also influence the relationship between composition and measured mechanical properties. If fractured specimens were used for SEM analysis, quantification of non-collagenous proteins could still be conducted on a nearby section. Finally, if relationships were not previously established between cross-linking ratio measured by Raman spectroscopy and cross-linking content measured by HPLC, as described in "Further Investigation of Cross-Linking," analysis of collagen cross-linking could be conducted on a contralateral limb using HPLC.

The power of the described investigation would be the ability to estimate the effect of a compositional metric while controlling for all others. However, this power could only be achieved with large sample sizes. An appropriate sample size may require at least 30 samples per age group plus additional samples for every compositional metric that is to be included in a multivariate model. Although many different ages should be considered

in this study, age should be treated as a discrete variable instead of a continuous variable so that the confounding influence of age can be removed if necessary. Age likely does not have an easily defined influence on the relationship between composition and mechanical properties and therefore cannot easily be accounted for if treated as a continuous covariate. By having discrete age groups, the composition-mechanics relationship can be analyzed within each age group and compared or all groups could be analyzed together with age included as a factor in the model instead of a covariate. With large sample sizes, it may also be possible to model all effects and interactions of age, composition, and mechanics together using structural equation modeling.

SUMMARY

This work provides evidence for shifts in our understanding of bone adaptation and the influence of bone composition on mechanical integrity. It was demonstrated for the first time that aging and external stimuli, in the form of exercise, modulate bone composition, and therefore tissue-level mechanical properties, even in the absence of bone formation or remodeling. These findings not only demonstrate the importance of composition on skeletal integrity but also demonstrate that changes to tissue quality can be overlooked because they may not always be accompanied with detectable changes in bone mass. There is therefore great potential for improving diagnosis and treatment of skeletal fragility by inclusion of markers for tissue quality. However, much work remains before compositional markers could be used in clinical evaluations.

Table 5.1. Suspected sources of altered mechanical properties with exercise and aging (Chapters 2 and 3) and corroborating/conflicting evidence by direct associations of compositional and mechanical measurements (Chapter 4)

	CHAPTERS 2 & 3 (TIBIAE)	CHAPTER 4 (FEMORA)
ASSAYS USED	Whole bone mechanical testing Raman microspectroscopy Microdamage quantification	Colocalized microscopic assays: - Nanoindentation - Raman microspectroscopy
CORRELATING COMPOSITION & MECHANICS	Only by associated changes in group means	Direct correlations between colocalized assays
OBSERVATIONS (YOUNG MICE)	Exercise resulted in: ↑ Strength ↑ Fatigue resistance Suspected causes: **↑ Mineralization** **↓ Carbonate substitution** No significant change: *Cross-linking ratio* Microdamage	**Mineralization:** ↑ Elastic modulus ↑ Viscoelastic modulus ↑ Viscoelastic viscosity **Carbonate substitution:** ↓ Elastic recovery of work *Cross-linking ratio:* ↓ Elastic modulus ↓ Hardness ↓ Viscoelastic modulus ↓ Viscoelastic viscosity ↓ Resistance to plastic creep
OBSERVATIONS (OLD MICE)	Old bones compared to young: ↓ Strength ↓ Toughness ↓ Resilience ↓ Ductility Suspected causes: **↑ Mineralization** ↑ *Carbonate substitution* ↑ Microcracking No significant change: Cross-linking ratio Diffuse damage	**Mineralization:** ↓ Hardness ↓ Elastic recovery of work ↓ Resistance to plastic creep No significant association: *Carbonate substitution* Cross-linking

Bold indicates that a suspected source of altered mechanical properties in Chapter 2 or 3 was corroborated by direct correlations between mechanical properties and composition in Chapter 4. *ITALICS* indicate a lack of corroborating evidence between Chapters 2/3 and 4. Microdamage was not evaluated in Chapter 4 and therefore could not be corroborated or contradicted.

Figure 5.1. Illustration of how little new bone formation occurred between 5 and 19 months of age in murine tibiae. The overall shape shows the average size and shape of the tibial mid-diaphysis (transverse cross-section) at 19 months and the dark grey area shows the bone that was present (by average shape) at 5 months. As little as 10% of the total bone area was formed after 5 months of age (light blue areas). This percentage may be underestimated due to averaging of bone shapes and neglecting surface remodeling.

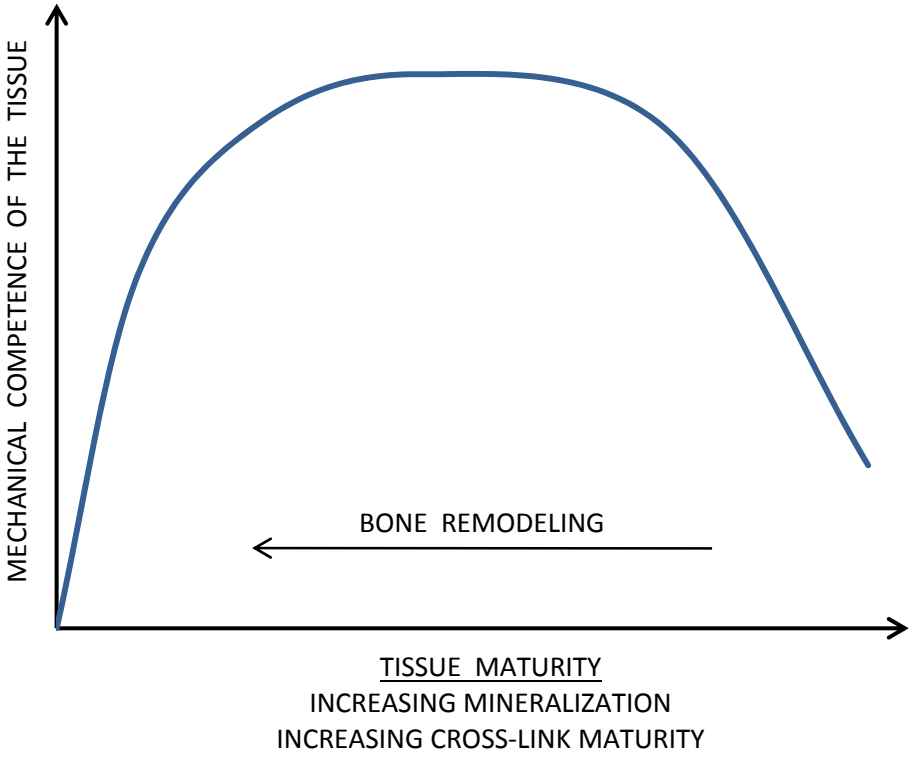

Figure 5.2. Illustration of the potential tri-phase influence of composition on mechanical properties. Increasing mineralization and cross-link formation of immature bone tissue may rapidly establish mechanical competence. Nearing skeletal maturity, increases in mineralization or cross-linking may still improve tissue competence but may reach a point of saturated benefit, represented by the plateau region. Finally, further increases in mineralization or cross-linking beyond a threshold may result in decreases tissue competence. Changes in cross-linking and mineralization are just two examples of potential compositional changes that could occur with increasing tissue maturity. In humans, proper bone remodeling may renew tissue to keep average composition in the plateau region. Lack or excess of remodeling could therefore decrease average mechanical competence.

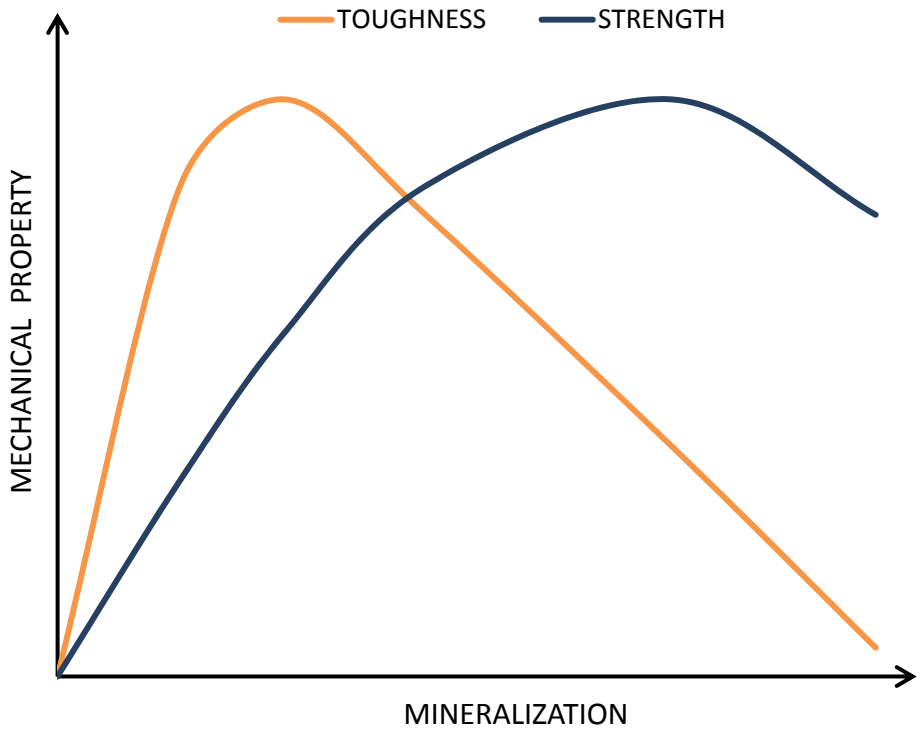

Figure 5.3. Example of difficulty in determining "optimal composition." It is possible that level of mineralization that results in optimal tissue strength may result in less than optimal toughness. This dichotomy may exist for many measures of composition and mechanical properties.

1. Gregg, E. W., Cauley, J. A., Seeley, D. G., Ensrud, K. E. & Bauer, D. C. Physical activity and osteoporotic fracture risk in older women. Study of Osteoporotic Fractures Research Group. *Ann. Intern. Med.* 129(2): 81-88 (1998).

2. Borer, K. T. The effects of exercise on growth. *Sports Med.* 20(6): 375-397 (1995).

3. Boersma, B. & Wit, J. M. Catch-up growth. *Endocr. Rev.* 18(5): 646-661 (1997).

4. Vose, G. P. & Kubala, A. L. Bone strength—its relationship to x-ray determined ash content. *Human Biology* 31: 261-270 (1959).

5. Hernandez, C. J., Beaupre, G. S., Keller, T. S. & Carter, D. R. The influence of bone volume fraction and ash fraction on bone strength and modulus. *Bone* 29(1): 74-78 (2001).

6. Akhter, M. P. *et al*. Genetic variations in bone density, histomorphometry, and strength in mice. *Calcif. Tissue Int.* 67(4): 337-344 (2000).

7. Akkus, O., Adar, F. & Schaffler, M. B. Age-related changes in physicochemical properties of mineral crystals are related to impaired mechanical function of cortical bone. *Bone* 34(3): 443-453 (2004).

8. Weiner, S. & Traub, W. Crystal size and organization in bone. *Connect. Tissue Res.* 21(1-4): 259-265 (1989).

9. Callister Jr, W. D. Fundamentals of Materials Science and Engineering: An Integrated Approach. *Fundamentals of Materials Science and Engineering: An Integrated Approach, 2nd Edition, by William D.Callister, Jr.*: 824 (2004).

10. Diab, T., Condon, K. W., Burr, D. B. & Vashishth, D. Age-related change in the damage morphology of human cortical bone and its role in bone fragility. *Bone* 38(3): 427-431 (2006).

11. Diab, T. & Vashishth, D. Morphology, localization and accumulation of in vivo microdamage in human cortical bone. *Bone* 40(3): 612-618 (2007).

12. Akkus, O., Polyakova-Akkus, A., Adar, F. & Schaffler, M. B. Aging of microstructural compartments in human compact bone. *J. Bone Miner. Res.* 18(6): 1012-1019 (2003).

13. Zioupos, P., Currey, J. D. & Hamer, A. J. The role of collagen in the declining mechanical properties of aging human cortical bone. *J. Biomed. Mater. Res.* 45(2): 108-116 (1999).

14. Wang, X. & Puram, S. The toughness of cortical bone and its relationship with age. *Ann. Biomed. Eng.* 32(1): 123-135 (2004).

15. Viguet-Carrin, S., Garnero, P. & Delmas, P. D. The role of collagen in bone strength. *Osteoporos. Int.* 17(3): 319-336 (2006).

16. Wang, X., Shen, X., Li, X. & Agrawal, C. M. Age-related changes in the collagen network and toughness of bone. *Bone* 31(1): 1-7 (2002).

17. Hernandez, C. J. *et al*. Trabecular microfracture and the influence of pyridinium and non-enzymatic glycation-mediated collagen cross-links. *Bone* 37(6): 825-832 (2005).

18. Nyman, J. S., Reyes, M. & Wang, X. Effect of ultrastructural changes on the toughness of bone. *Micron* 36(7-8): 566-582 (2005).

19. Siegmund, T., Allen, M. R. & Burr, D. B. Failure of mineralized collagen fibrils: modeling the role of collagen cross-linking. *J. Biomech.* 41(7): 1427-1435 (2008).

20. Burr, D. B. The contribution of the organic matrix to bone's material properties. *Bone* 31(1): 8-11 (2002).

21. Bailey, A. J. *et al*. Age-related changes in the biochemical properties of human cancellous bone collagen: relationship to bone strength. *Calcif. Tissue Int.* 65(3): 203-210 (1999).

22. Paschalis, E. P. *et al*. Bone fragility and collagen cross-links. *J. Bone Miner. Res.* 19(12): 2000-2004 (2004).

23. Saito, M., Fujii, K. & Marumo, K. Degree of mineralization-related collagen crosslinking in the femoral neck cancellous bone in cases of hip fracture and controls. *Calcif. Tissue Int.* 79(3): 160-168 (2006).

24. Busa, B., Miller, L. M., Rubin, C. T., Qin, Y. X. & Judex, S. Rapid establishment of chemical and mechanical properties during lamellar bone formation. *Calcif. Tissue Int.* 77(6): 386-394 (2005).

25. Tanck, E. *et al*. The mechanical consequences of mineralization in embryonic bone. *Bone* 35(1): 186-190 (2004).

26. Aarden, E. M., Burger, E. H. & Nijweide, P. J. Function of osteocytes in bone. *J. Cell. Biochem.* 55(3): 287-299 (1994).

27. Cullinane, D. M. The role of osteocytes in bone regulation: mineral homeostasis versus mechanoreception. *J. Musculoskelet. Neuronal Interact.* 2(3): 242-244 (2002).

28. Gluhak-Heinrich, J. *et al*. Mechanical loading stimulates dentin matrix protein 1 (DMP1) expression in osteocytes in vivo. *J. Bone Miner. Res.* 18(5): 807-817 (2003).

APPENDIX A

MICRO- AND NANO-STRUCTURAL ANALYSES OF DAMAGE IN BONE

ABSTRACT

Skeletal fractures represent a significant medical and economic burden for our society. In the US alone, age-related hip, spine, and wrist fractures accounted for more than $17 billion in direct health care costs in 2001. Moreover, skeletal fractures are not limited to the elderly; stress fractures and impact/trauma-related fractures are a significance problem in younger people also. Gaining insight into the mechanisms of fracture and how these mechanisms are modulated by intrinsic as well as extrinsic factors may improve the ability to define fracture risk and develop and assess preventative therapies for skeletal fractures. Insight into failure mechanisms of bone, particularly at the ultrastructural-level, is facilitated by the development of improved means of defining and measuring tissue quality. Included in these means are microscopic and spectroscopic techniques for the direct observation of crack initiation, crack propagation, and fracture behavior. In this review, we discuss microscopic and spectroscopic techniques, including laser scanning confocal microscopy (LSCM), scanning electron microscopy (SEM), transmission electron microscopy (TEM) and Raman spectroscopic imaging for visually observing microdamage in bone, and the current understanding of damage mechanisms derived from these techniques.

Clinical Importance of Damage - Skeletal Fragility

Skeletal fractures represent a significant medical and economic burden for our society (Hui et al., 1988; Burr and Milgrom, 2001; Burr, 1997; Praemer et al., 1999). In the US alone, age-related hip, spine, and wrist fractures accounted for more than $17 billion in direct health care costs in 2001, and this annual cost is rising (National Osteoporosis Foundation 2001). It is estimated that the number of Americans that will have osteoporosis by 2015 could be in excess of 41 million, a third more than the 28 million currently affected by the disease. Moreover, skeletal fractures are not limited to the elderly - stress fractures and impact/trauma-related fractures are a clinically significance problem in younger people also. For example, approximately half a million long distance runners present with stress fractures each year, and over 20% of "competitive" runners incur stress fractures (Burr and Milgrom, 2001; Bennell et al., 1996). A significant percentage of military recruits, particularly females, exhibits stress fractures, and a significantly greater percentage of the military population exhibits stress fractures compared to the general population (Burr and Milgrom, 2001; Jones et al., 1989). It is generally thought that a high incidence of musculoskeletal fatigue loading results in damage accumulation at too high of a rate to be efficiently remodeled, leading to skeletal fracture (Jordaan and Schwellnus, 1994; Beck et al., 2000).

Gaining insight into the underlying mechanisms of fracture and how these mechanisms are modulated by intrinsic (e.g. aging, disease) as well as extrinsic (e.g. mechanical loading) factors may improve the ability to define fracture risk and develop and assess preventative therapies for skeletal fractures. It is generally accepted that age-related fractures result from not only a loss in bone mass, but also because of alterations in tissue quality, such as reduced elasticity of the organic phase resulting from changes in collagen cross-linking, and altered mineral composition and crystal structure (Burr et al., 1997; Rajachar, 2003). Therefore, it is important to also delineate changes in tissue quality and how these changes in tissue ultrastructure affect the mechanistic response of bone to its physical environment. Insight into failure mechanisms of bone, particularly at the

ultrastructural-level, is facilitated by the development of improved means of defining and measuring tissue quality. Included in these means are microscopic and spectroscopic techniques for direct observation of crack initiation, propagation, and fracture behavior.

Microdamage as an Indicator of Skeletal Fragility

Repetitive mechanical loading can lead to ultrastructural-level damage, the most prevalent form being discrete microcracks in the bone extracellular matrix that are easily visible under brightfield light microscopy (Burr and Milgrom, 2001; Burr et al., 1997; Courtney et al., 1996; Currey et al., 1996; Zioupos and Currey, 1998; Schaffler et al., 1995). Even though younger people are more active and subject to repetitive loading of greater magnitude and duration, they typically have a greater physiologic capacity to withstand the functional demands placed on the musculoskeletal system, and microdamage is repaired by remodeling. However, with age and/or pathologic conditions, the compensatory mechanisms needed to maintain the mechanical stability of skeletal tissue become impaired (Birdwood, 1996). As a result, ultrastructural-level damage, which may no longer be repaired as efficiently, can play a role in the etiology of osteoporotic and stress fractures (Burr and Milgrom, 2001; Burr, 1997; Jones et al., 1989; Burr et al., 1997; Schaffler et al., 1995).

There is therefore an inter-relationship between fatigue loading, microdamage accumulation, remodeling, bone matrix repair and fracture (Figure A.1), and should damage processes exceed the local capacity of tissue to remodel (through either true greater net damage or compromised repair), fracture occurs. Remodeling is triggered caused by microdamage accumulation, through cell sensory mechanisms, leading to bone matrix repair. However, sometimes remodeling can also enhance microdamage accumulation or directly lead to fracture upon exceeding a threshold stress. Locally, because there is less bone to sustain loading upon resorption induced by remodeling, strains on the remaining bone would increase, generating even more microdamage, which stimulates another sequence of remodeling and so forth (Burr et al., 1997). Therefore high remodeling as well as microdamage accumulation can lead to fracture.

Distributions of sub-threshold microcracks increase exponentially in number with age (Schaffler et al., 1995). These cracks range in length up to 300 μm and may ultimately contribute to age-related property degradation and fatigue fracture in skeletally mature cortical and trabecular bone (Schaffler et al., 1995). Most microcracks form preferentially at cement lines and inter-lamellar boundaries, where one might expect planes of weakness. Vashishth *et al*. (2000a) provided a detailed account of microcrack formation and contribution towards the propagation of a fracture crack, and showed that the basic fractured element is a mineralized collagen fibril. The processes guiding the location, orientation, size and rate of microdamage accumulation and the relationships between these damage parameters and ultrastructural constituents are therefore important in assessing the competence of skeletal tissues. To better understand these processes, an ability to accurately detect and measure microdamage is essential. In the following sections, we discuss microscopic and spectroscopic techniques, including laser scanning confocal microscopy (LSCM), scanning electron microscopy (SEM), transmission electron microscopy (TEM) and Raman spectroscopic imaging for visually observing microdamage in bone, and the current understanding of damage mechanisms derived from these techniques.

OBSERVATIONS OF MICRODAMAGE AT THE LIGHT AND CONFOCAL MICROSCOPIC LEVELS AND INSIGHT DEVELOPED

Identifying Different Types of Microdamage

The most common technique for viewing microdamage in bone generated *in-vivo* or controlled *in-vitro* testing is optical microscopy. However, sectioning and grinding specimens to make slides suitable for observing microdamage can create artifactual microdamage. Frost (1960) addressed this problem by bulk staining bone with basic fuchsin before sectioning. Fuchsin stains all surfaces of bone, including lacunae, canaliculi, blood vessels, and microdamage. Therefore, damage that existed before processing will be stained, while processing-induced damage will not be. Using this

technique, Frost (1960) was able to show that microdamage does exist *in vivo*, indicating that repetitive physiological loads are sufficient to create small scale damage in bone. Burr and Stafford (1990) later validated this method, finding that the dehydration steps of the staining protocol do not create additional damage, and pre-existing damage can be discriminated from artifactual damage.

Using bulk staining techniques, two main types of damage have been found in bone: microcracks and diffuse microdamage. Microcracks are clear, distinguishable, linear cracks (at least in the plane of the 2D section being viewed), while diffuse damage appears as a cloud of stain with indistinguishable individual features. Since microcracks and other forms of microdamage are 3D entities, but are being viewed in specific 2D planes, explicit identification and quantification are not always straightforward. Burr and Stafford (1990) therefore developed criteria for identifying microcracks. Microcracks have sharp borders surrounded by a halo of stain, are larger than canaliculi and smaller than vascular canals, are stained through the depth of the section, and have well stained edges with less stain in the intervening space.

Although diffuse damage appears as a cloud of stain, it is likely comprised of many tiny cracks, as indicated by higher magnification observations. Diffuse damage may have a fractal nature to it; as magnification and resolution are increased, more and more cracks become visible in the network of cracks that create the damage pattern.

Recently, laser scanning confocal microscopy (LSCM) has been used to view microdamage **(**Fazzalari et al., 1998; Boyce et al., 1998; Rajachar, 2003) (Figure A.2). This technique has two advantages over light microscopy. First, only stained surfaces are imaged, making it easier to separate preexisting damage from processing-induced damage. Second, LSCM creates a thin plane of focus that can be panned up and down through the specimen. Having microstructural information in the third dimension is helpful in better characterizing microdamage and distinguishing it from native features in bone, and also allows for three dimensional reconstruction of images. Using LSCM to characterize different types of damage in three dimensions, microcracks are observed to

be sheet-like and diffuse damage consists of a fine network of smaller cracks ("ultra-microcracks") (Fazzalari et al., 1998; Boyce et al., 1998).

Initiation and Propagation of Microdamage

Using bulk staining techniques, relationships between mechanical history and spatial patterns of damage have been addressed. These different types of damage often appear in specific locations within a bone. In bones subjected to bending, linear microcracks regularly appear in regions subjected to compressive strains, while diffuse microdamage appears in tensile zones (Carter and Hayes, 1977a; Boyce et al.,1998; Reilly and Currey 2000; Rajachar, 2003) (e.g. Figure A.2). "Whispy-appearing" cracks near the neutral axis of specimens fatigued in bending have also been found (Boyce et al., 1998).

Most microdamage is found in interstitial bone (Schaffler et al., 1995; O'Brien et al., 2003). Interstitial bone is older than bone located in osteons, because it was formed prior to the remodeling that created the osteons. It is possible that the older bone is more susceptible to damage (e.g. because of altered mineral and/or collagen). Alternatively, it is possible that this bone contains more damage because it has been subjected to more loading cycles. Although most microdamage initiates in interstitial bone, it seldom crosses cement lines and into osteons, leading to the hypothesis that cement lines arrest crack growth (Norman and Wang, 1997). An exception to this trend is the whispy-appearing cracks, which commonly cross cement lines and propagate into osteons (Boyce et al., 1998).

Micro and ultrastructural features of bone can create stress concentrations that initiate crack formation. Frequently, microcracks initiate at osteocyte lacunae, leading to the hypothesis that lacunae serve as stress concentrations (Reilly, 2000; Martin, et al., 1998). Besides lacunae, vascular canals can also initiate crack formation (Carter and Hayes, 1977a). In addition to stress concentrations, higher mineralization can increase the probability of microcracking. For example, heavily mineralized bone is stiffer than less

mineralized bone, but also more brittle and associated with more microcracks (Sobelman et al., 2004).

Crack growth in bone appears to be self-limiting in tension, but less restricted in compression, indicating strain mode-dependent crack extension (Akkus and Rimnac, 2001; Vashishth et al., 2003; Griffin et al., 1997). Microcracks formed from cyclic tension have decreasing growth rate with increasing length and typically arrest in less than 10,000 cycles (Akkus and Rimnac, 2001). Similarly, crack growth resistance increases with crack extension (Vashishth et al., 2003). Burr et al. (1998) claimed that damage actually accumulates more rapidly in tension than compression, but is limited by slow growth in tension. Collectively, these findings indicate that although microcracks do form under far-field tensile loading, their growth is limited and the cracks remain small. In contrast, microcracks produced in compression tend to be long linear cracks, indicative of more uninhibited growth.

Patterns of diffuse damage can also be explained by these observations. Since microcracks are formed easily in tension, but remain small, a fine network of many tiny cracks is created. In the limit, this network becomes so fine that one crack is indistinguishable from another.

Mechanical Consequences of Microdamage

Based on the mechanical behavior of composites, there is an expected association between microdamage accumulation and mechanical property degradation, in particular modulus degradation. However, the specific relationship between these two indicators of damage is unclear. Surprisingly, Burr et al. (1998) did not detect significant microdamage in specimens fatigued in bending until a 15% reduction in elastic modulus was reached, and tensile damage did not reduce bone's energy-absorbing ability until the elastic modulus was reduced by 20% (Reilly and Currey, 2000). There is debate over whether this finding is universal, or bone and testing condition-specific. It is likely that testing method plays an important role in determining the relationship between damage

accumulation and mechanical property degradation (Zioupos, 1999; Burr et al., 1999). For instance, strain rate has an effect on the amount of damage produced and the degree of modulus degradation, and may be just as important as peak strain in determining how much damage will accumulate (Schaffler et al., 1989). Also, the amount and nature of microdamage may differ between uniaxial tension, uniaxial compression, and bending or between fatigue and monotonic testing. Even within a specified testing mode, subtle differences in experimental conditions could change damage processes. For example, in load-control fatigue, some researchers load to a specified initial stress level, while others load to a specified initial strain, calculated to yield a desired initial stress. Because mineralization and elastic modulus differ from bone to bone, mode of testing is an important consideration (i.e. the relationship between stress and strain differs between bones). Another variable that is important in designing a fatigue test is whether the test is conducted under load control or displacement/strain control. In load control, as microdamage accumulates, elastic modulus slowly decreases. When the modulus degrades, loading to the same stress causes each cycle to have a higher peak strain. The result is that after initial modulus loss, samples fatigued in load control will reach failure more rapidly than those fatigued in displacement or strain control.

Left unchecked, fatigue induced microdamage can accumulate and eventually cause fracture. As microdamage accumulates and coalesces, stiffness, ultimate strength and energy to failure are all eventually compromised, resulting in decreased resistance to fracture (Carter and Hayes, 1977b; Danova et al., 2003). Fatigue damage coupled with a progressive loss of stiffness also leads to reduced tensile strength in bone (Carter and Hayes, 1977b). Microdamage can also decrease fracture toughness (Norman et al., 1998) and mechanical energy-absorbing ability (Reilly and Currey, 2000). However, unlike man-made composites, the ability of bone to adapt and self repair allows for recovery of mechanical properties. For example, rat ulnae fatigued *in vivo* to 40% stiffness loss exhibited significant decreases in ultimate force and toughness, but 14 days of adaptation recovered all mechanical properties and significantly reduced microdamage (Colopy et al., 2004).

Although microdamage has detrimental effects on bone's mechanical properties, under appropriate conditions, it may also have benefit. For example, microdamage may toughen bone, making it harder to fracture from repetitive loading. A network of microcracks has energy absorbing ability which can dissipate stress and slow crack propagation. Fatigue life can therefore be increased by the presence of microcracks (Sobelman et al., 2004). Vashishth et al. (1997) investigated the propagation of a main crack in bone under tensile fatigue and saw an increase in fracture toughness with increased number of microcracks and extension of a main propagating crack. This group later provided more evidence for a microcrack-based toughening mechanism by identifying microcrack patterns in a frontal process zone and wake of a main propagating crack associated with increased crack growth resistance (Vashishth et al., 2003).

The ability of a microcrack to toughen or embrittle bone may depend on whether toughening is caused by intrinsic properties like microdamage or by extrinsic means, specifically crack bridging. Crack bridging is the formation of unbroken regions of bone in the wake of a crack. These bridges span the crack and prevent it from opening further. It has been argued that this mechanism is the dominant toughening mechanism in bone (Nalla et al., 2004). It may seem confusing that some work has found benefit from microdamage while others show negative effects. One explanation could be the amount of damage that is allowed to accumulate before evaluating mechanical properties. If microdamage does have the ultrastructural benefit of improving mechanical properties such as toughness, it will only be beneficial up to some critical threshold of accumulation. For example, although microcracking can increase fatigue life, cracks exceeding a critical length will grow and ultimately cause failure of the bone (Sobelman et al., 2004). Another consideration is the way in which mechanical properties are tested (i.e. whether properties are derived from monotonic or cyclic testing). The physiological analogue of monotonic testing is a traumatic overload, while fatigue is similar to repetitive loading that occurs during walking, running or various other activities. A controlled amount of damage may help prevent further damage accumulation during normal activity which, in turn, precludes microdamage from reaching a critical level and

causing failure. However, the same amount of microdamage may make the bone more susceptible to fracture by a single traumatic event.

Fracture of bone can therefore occur by one of four mechanisms: traumatic overload (which may or may not be dependent on present microdamage), failure of the ultrastructural toughening mechanism(s), failure of remodeling to prevent a critical amount of microdamage from accumulating, and/or physiological loading so intense that remodeling and toughening cannot prevent accumulation of microdamage.

In summary, microdamage and mechanical properties in bone are generally known to be intertwined, but their specific relationship is not fully understood. The type of microdamage and the way in which it was produced (e.g. *in vivo* vs. *in vitro*, uniaxial loading vs. bending, monotonic loading vs. fatigue) will likely change the correlation between damage and mechanical properties. Much remains unclear at this point, but several conclusions are apparent. Microdamage can occur *in vivo* from physiological loads. Run away extension of microdamage is prevented by a toughening mechanism in which the microdamage can absorb energy from loading. In healthy bone, accumulation of microdamage will initiate remodeling, reducing the amount of damage remaining. Small amounts of microdamage are likely to be stable and not compromise function of bone. To better identify relations between damage, mechanical properties and remodeling, better techniques are needed to detect, monitor and visualize damage, and also relate compositional changes to mechanical and morphological changes.

MICRODAMAGE ANALYSIS USING SCANNING ELECTRON MICROSCOPY

Bone has a hierarchical composite architecture with various arrangements of material structures at a wide range of length scales that work in concert to perform diverse mechanical, biological and chemical functions (Rho et al., 1998). In order to assess bone architecture, microdamage accumulation and fracture mechanisms, direct observation using various microscopic techniques is necessary. Scanning electron microscopy (SEM) is effective for the analysis of hierarchical composite structure and surface topography

induced by microdamage accumulation and fracture because of its high resolution and large depth of field (Hong et al., 1996; Hong and Suryanarayana, 2001; Lee and Hong, 2003). One of the most powerful characteristics of SEM is a great depth of field at all magnifications, which renders the area above and below the focal plane to appear in focus. The depth of field for SEM is 100-500 times greater than the light microscope (Goldstein et al., 1981) and a three-dimensional appearance of the specimen image can be obtained. SEM has been used extensively to study the damage accumulation and fracture behavior of bone (Braidotti et al., 2000; Hiller et al, 2003; Nalla et al., 2003; Schaffler et al., 1994). Ultrastructural level damage in bone which cannot be observed at the light microscopic level can be observed using SEM (Schaffler et al., 1994).

Microdamage in bone can be observed using SEM with or without basic fuchsin staining (Schaffler et al., 1994). Most bone tissue is riddled with voids, in the form of blood channels, erosion cavities, osteocyte lacunae and canaliculi (Currey, 2003), which may act as potential stress concentrators. The extent to which these stress concentrators increase the likelihood of bone microdamage and fracture is difficult to determine, because the fracture mechanics properties of bone are still not well understood. The arrangement and orientation of these voids in the architecture of bone is complex and these voids in many ways can act as crack deflectors or barriers to crack propagation.

SEM observation of human bone (Vashishth et al., 2000b) indicates that microcracks associated with longitudinally oriented osteons are present in individual lamellae (e.g. Figure A.3a). In this figure, longitudinal microcracks are marked with arrowheads and the main crack is marked with "MC". The failure of longitudinally oriented osteons in human bone was observed to have two important features (Vashishth et al., 2000b). First, easier microcrack formation and damage localization occur within an osteon due to weak inter-lamellar bonding. Second, formation of microcracks occurs at the osteon-matrix interface in the presence of less mineralized cement lines. Crack deflection due to stress concentration effects of Volkmann's canals (e.g. Figure A.3b) reduces energy available at the crack tip for extension, and a higher load is required to produce further crack propagation. In the presence of microcracks oriented unfavorably with respect to the

main crack, damage is localized and limited, resulting in the deceleration of the main crack propagation (Sobelman et al., 2004; Vashishth et al., 2000b).

Recently Nalla et al. (2003) examined how a propagating crack interacts with the bone microstructure to provide a mechanistic understanding of fracture using SEM. They suggested that crack bridging by collagen fibers (e.g. Figure A.4), as well as microcracks, contribute to the fracture toughness of bone. Microcracks preferentially form around osteons, leading to matrix debonding or osteon pullout (Nalla et al., 2004). Crack bridging, conversely, involves the formation of unbroken regions that span the crack in the wake of the crack tip and act to resist crack opening. Bridging may occur by unbroken individual collagen fibers and "uncracked ligaments" (Nalla et al., 2004).

SEM is effective in studying the fracture surface morphology of bone because of the ability to view images in three-dimensions. The most frequently observed features on the fracture surface of lamellar bones are inter-lamellar delamination and layered morphology (e.g. Figure A.5a), protruded fiber bundles (e.g. Fig 5b), and osteon pull-out (e.g. Figure A.6) (Braidotti et al, 2000; Weiner et al., 1999; Hiller et al., 2003; Vashishth et al., 2000b). These features observed on the fracture surface reflect the cracking behavior of bone. Inter-lamellar delamination and layer morphology can be associated with the microcracks at the inter-lamellar interfaces and the protruded fiber bundles can be linked to crack bridging by uncracked ligaments and/or collagen fibers. Osteon pull-out is thought to result from shear microcracks along the inter-lamellar interface or cement lines and subsequent osteonal crack bridging (Hiller et al., 2003). It is therefore clear that detailed crack initiation and crack propagation mechanisms can be deduced from careful analyses of the fractography of bones via SEM.

TEM Analyses of Fatigue-Damage in Bone

Bone is one of the few tissues with density high enough to be imaged with transmission electron microscopy (TEM) without staining. TEM is useful in examining the morphological and crystalline arrangement of mineral apatites and crystal-collagen interactions.

TEM analyses of collagen fibrils and apatite crystals in fatigue-damaged bone are limited. Recently, collagen fibrils and apatite crystals in fatigued and non-fatigued murine femora were examined for the ultrastructural damage using high resolution transmission electron microscopy (HRTEM) (Hong et al., 2005; Hong and Kohn, 2005). The longitudinally sectioned non-fatigued femora (Figure A.7a) displayed well-aligned and uniformly distributed collagen fibrils mostly parallel to the bone axis (indicated by an arrow). In the fatigue-damaged femora (Figure A.7b), the aligned arrangement of collagen fibrils appeared to be impaired and loosened. The damage is manifested by non-uniformly distributed and shorter collagen fibrils, which may have resulted from rearrangement and fragmentation of collagen fibrils in reaction to the applied load. At a higher magnification, HRTEM images of the non-fatigued femora displayed tablet-like crystals with lattice fringes (Hong and Kohn, 2005). In the fatigue-damaged femora, crystalline lattice fringes were much less frequently observed and small pieces of particles adjacent to each other were observed (Figure A.8, indicated by arrows). Hong (2005) suggested, based on HRTEM images and the presence of diffuse halos in the diffraction patterns that some apatite crystals were broken into small pieces and a fraction of crystalline mineral apatites became amorphous during fatigue. The observation of amorphization represents morphological validation of Raman spectroscopic findings, in which altered Raman signatures at the tips of microcracks were interpreted as evidence of fatigue-induced amorphization (Timlin et al., 2000)

The load-carrying capacity of mineral apatites deteriorates following amorphization, and fragmentation, which are likely to trigger the overall fatigue-induced microdamage and microcracks of bones. More detailed analyses using TEM are needed to understand nanostructural damage accumulation mechanisms and their effect on macroscopic failure and bone remodeling.

TEM Analyses of Osteoporotic Bone

Differences between normal and osteoporotic trabecular bone include lower bone mineral density and trabecular volume, and thinner trabecular struts in osteoporotic bone (Rubin et al., 2003). Relatively few studies, however, have analyzed ultrastructural differences between normal and osteoporotic bone, and the ultrastructural changes in collagen in osteoporotic bone are still under debate. For example, an irregular and random arrangement of collagen fibrils has been noted in osteoporotic bone, compared to the parallel and well-aligned array of fibrils in normal bone (Kafantari et al., 2000). The diameter of collagen fibrils decreases in both trabecular and cortical bone of ovariectomized rats, a finding attributed to defective cross-linking (Kafantari et al., 2000). The reduced diameter and irregular fibril array, along with altered cross linking may deteriorate the strength of osteoporotic bone. In other studies, however, no appreciable difference in the size, shape and distribution of collagen fibrils between normal and osteoporotic trabecular bone was noted in either rats (Rohanizadeh et al., 2000).or humans (Rubin et al., 2003). The differences in collagen morphology found in different investigations may be due to changes in collagen that occur upon demineralization and whether fibrils were being analyzed as an isolated matrix phase or as part of a collagen/mineral aggregate.

Regarding the mineral phase of bone, even though many investigators have examined mineral apatites using TEM, there is no consensus about crystallite size in bone. Moreover, there is also a lack of knowledge about the structure of diseased bone, such as osteoporotic bone. For example, three distinct views on the size of osteoporotic bone crystals have been presented: the osteoporotic crystals are either smaller (Grynpas and

Holmyard, 1988), of the same size (Rohanizadeh et al., 2000; Rubin et al., 2003; Simmons et al., 1988) or, larger than those in normal bone (Boskey, 1990; Chatterji et al., 1981).

TEM micrographs of the cross-section of mineral/collagen fibril conglomerates demonstrated no appreciable difference in the size, shape and distribution of apatite between normal and osteoporotic trabecular bone in humans (Rubin et al., 2003) or rats (Rohanizadeh et al., 2000). (e.g. Figure A.9). Plate-like and tablet-like crystals with their long axes aligned with the long-axis (c-axis) of fibrils were observed in both normal and osteoporotic trabecular bone (Rubin et al., 2003). The length and width of apatite crystals in human osteoporotic trabecular bone in longitudinal section fibrils were 49.8 ± 10.4 and 7.1 ± 1.7 nm, respectively, compared with 50.7 ± 9.1 and 7.7 ± 1.5 nm in normal bone, supporting no significant difference in length and morphology of apatite crystals between normal and osteoporotic bones. Rubin et al. (2003) therefore suggested that the chief mechanism underlying the lower bone mineral density in osteoporotic bone is a reduction in trabecular volume, rather than a deterioration of the bone crystals at the nanoscale.

It requires caution, however, to interpret data on the size of apatite crystals in osteoporotic bone, because it is difficult to separate effects of age from effects of the disease itself. In addition, a more important feature than the size of apatite crystals in osteoporotic bone may be the local volume density of apatite crystals, which has not been given much attention. Further work directed at analysis of the local volume density of apatite crystals and the relationship between alterations in collagen fibrils and apatite crystals using TEM is needed for a better understanding of osteoporosis and other bone diseases.

Compositional Parameters Affecting Bone Quality

In engineering composite materials, it is well-known that composition has a significant influence on mechanical properties as well as on the spatial and temporal progression of damage accumulation (Matthews and Rawlings, 1994). By analogy, bone may be viewed as a composite (at multiple levels of hierarchy), and its composition as well as architecture (e.g. mineral crystallite size, shape, orientation and specific mineral to mineral and mineral to matrix ratios; collagen fiber organization and orientation; bonding between the mineral and collagen phases, among other parameters) also dictate mechanical performance (Carter and Hayes, 1977a,b; Grynpas and Holmyard, 1988; Currey et al., 1996; Martin et al., 1998; Rho et al., 1998). The compositional and ultrastructural parameters of bone modulate whole bone properties and also play an important role in determining mechanisms of fatigue-induced microdamage (Carter and Hayes, 1977a,b; Grynpas and Holmyard, 1988; Currey et al., 1996; Martin et al., 1998; Rho et al., 1998). These parameters also change with age and are therefore likely contributors to age-related skeletal fragility, which may be reflected first in an increase in local damage and, upon continued growth, a decrease in global mechanical properties (Ruff and Hayes, 1984; Boyde et al., 1993). For example, mineral crystallinity, orientation, and impurity substitution increase with age (Camacho et al., 1999). These age-related changes in mineral are also accompanied by an increase in organic phase (i.e. collagen) compaction (Grynpas, 1993). Less rigorously defined, however, are specific associations between local microdamage and local composition of the surrounding tissue matrix. Toward this end, investigators have started to use spectroscopic techniques, primarily fourier transform infrared spectroscopy (FTIR) and Raman spectroscopy, to relate mechanical history, spatial state of damage and local bone chemistry.

Vibrational Spectroscopy and Imaging

Bone mineral spectra observed as Raman-shifted scatter from near-infrared excitation will be found around 850-860 nm, while the infrared absorption spectra will be found

around 10-11 μm. Since lateral resolution in optical microscopic imaging is limited by diffraction to about half the observation wavelength, spatial resolution for mineral content is at least 10X better with Raman spectroscopy than with IR spectroscopy, because of the much shorter wavelengths involved in Raman spectroscopy. Spatial resolution is especially important in the imaging of any boundary – such as around an osteon, a cement line or the edge of a crack or fracture, where poor resolution from IR imaging can blur important detail. High resolution (< 1 μm) Raman imaging is possible, even with a dry microscope objective.

In bone mineral, there are several slightly different phosphate moieties, depending on the substitution of the matrix near the phosphate. Each different moiety gives rise to a slightly different frequency for the same phosphate vibration. This is why each phosphate band can usually be resolved into two or more components by multivariate analysis techniques. The situation is similar for the matrix bands.

Spectroscopy of Bone

There is a reasonably large literature on vibrational spectroscopy of bone (Carden and Morris, 2000; Penel et al., 1998). The major Raman band assignments for bone (Table A.1) include vibrational modes for phosphate, carbonate and mono-hydrogen phosphate. The important matrix bands are mostly markers for the collagen backbone (amide I, 1660 cm^{-1}; methylene (CH_2) wag, 1450 cm^{-1}; amide III, 1260 cm^{-1}). A point Raman spectrum of bone (Figure A.10) also shows the phosphate (PO_4^{-3}) symmetric stretch (ν_1, ca. 960 cm^{-1}), B-type carbonate (CO_3^{-2}) symmetric stretch (ca. 1070 cm^{-1}) and amide I envelope (ca. 1660-1670 cm^{-1}).

The positions, intensities and widths of PO_4^{-3} and CO_3^{-2} bands change in response to the local perturbations to the crystal structure caused by the local ion composition; therefore, vibrational spectroscopy is a sensitive probe of the changes in the environment of the molecule. The band positions, intensities and shapes can be shown to report on the state of maturation as well as on abnormal composition resulting from genetic defects or

disease. Vibrational spectroscopy therefore allows convenient measurement of mineral/matrix ratios, as well as alterations in mineral content associated with aging and/or mechanical deformation.

Chemical Changes Associated with Damage and Deformation in Bone

A Raman image of a small region of bovine femoral cortical bone that had been loaded in fatigue, stained en-bloc with basic fuchsin and histologically analyzed for microdamage shows spectra despite the presence of basic fuchsin, a stain that has appreciable fluorescence in the visible wavelengths (Figure A.11b). An unusually high frequency component to the phosphate ν_1 band (963 cm^{-1}), corresponding to uncarbonated apatite, appears in the region of microcracks (Timlin, et al., 2000). The high-frequency component was not seen in undamaged areas (Fig 11a). This data did not determine whether the altered phosphate chemistry was a cause or result of the microdamage, but did provide evidence that compositional changes are associated with regions of damage.

Following the observation of an association between local chemical changes and local microfractures, the hypothesis that mechanical loading leads to these chemical changes was addressed by performing experiments in which bones were loaded and spectra were collected in near real-time. Under compressive loading that ranged up to 1% strain, a change in the PO_4^{3-} peak center of gravity was observed (Morris et al., 2001). A smaller and more transient change was observed in the carbonate bands. A considerable shift in the amide I band was observed (Morris et al.,2001), confirming that the matrix is also influenced by mechanical load. The fact that these changes in mineral and matrix were observed as functions of increasing stress and strain indicates that loading drives the chemical shifts, not that local deformation preferentially occurs at sites of altered chemistry.

Recent indentation experiments also provide convincing evidence that stress causes mineral phase changes (Carden et al., 2003). Cylindrical indents of 100–400 μm depth and 500 μm diameter were made in bovine cortical tissue using pressures of 0.4-1.4 GPa

for 10 sec. New mineral factors were observed within the indents, up to the walls. Within 20 μm of the walls, but not in the center of the indents, we observed rupture of collagen cross-links as high frequency shoulders on the collagen amide I envelope. Collectively, this data supports stress-induced crystal structure changes in bone mineral as a mechanism of ultrastructural response to loading.

Similar phenomena were observed in 4 month old mouse femora subjected to bending (Morris et al., 2002). Factor analysis of 4 month old specimens revealed only one type of mineral present, a carbonated hydroxyapatite-like mineral. However, when the same specimens were loaded and re-imaged,they showed two distinct mineral species: a carbonated HAP-like mineral and an uncarbonated mineral with a high-frequency phosphate component. This two-component composition was observed in all 4 month fractured specimens near the site of fracture, while the control specimens showed only one mineral component. These results were consistent with the hypothesis that the stress leading to fracture caused a phase transformation within the bone mineral lattice which was easily found using Raman imaging. Interestingly and importantly, this effect was not observed in older (18 month) tissue. Factor analysis of images of control and fractured femurs in this age group showed only one mineral component occurring in both fractured and unfractured bone. It is therefore possible that there are age-related differences in the mineral's response to stress. Older mineral tends to have more uniform crystallite sizes (Rey et al., 1991; Paschalis et al.,1997); this may affect its reaction to applied load.

SUMMARY

Gaining insight into the mechanisms of fracture and how these mechanisms are modulated by intrinsic (e.g. aging and disease) and extrinsic (e.g. mechanical loading) factors may improve the ability to define fracture risk and develop and assess preventative therapies for skeletal fractures. Insight into failure mechanisms of bone, particularly at the ultrastructural-level, is facilitated by the development of improved means of defining and measuring tissue quality. In particular, high resolution microscopy, including scanning and transmission electron microscopies, and

spectroscopic imaging techniques (FTIR and Raman) allow for a direct observation of crack initiation and growth, and are valuable for deciphering incipient mechanisms of failure. Collectively, the information gained from these techniques can compliment mechanical and histological assays leading to a more complete understanding of fragility.

Acknowledgements

I would like to acknowledge my coauthors Sun-Ig Hong and David H. Kohn. The authors were supported by the US Department of Defense/Department of the Army DAMD17-03-1-0556 (DHK) and the Korea Research Foundation (2004-D00318).

Table A.1. Raman Band Assignments and Positions

Band Assignment	Position, cm^{-1}
P-O ν_2	422-454
P-O ν_4	578-617
P-O ν_1	957-962
Mono-hydrogen phosphate ν_1	1010
Carbonate ν_1	1065-1071
Amide III	1243-1269
CH_2 wag	1447-1452
Amide I	1660-1671

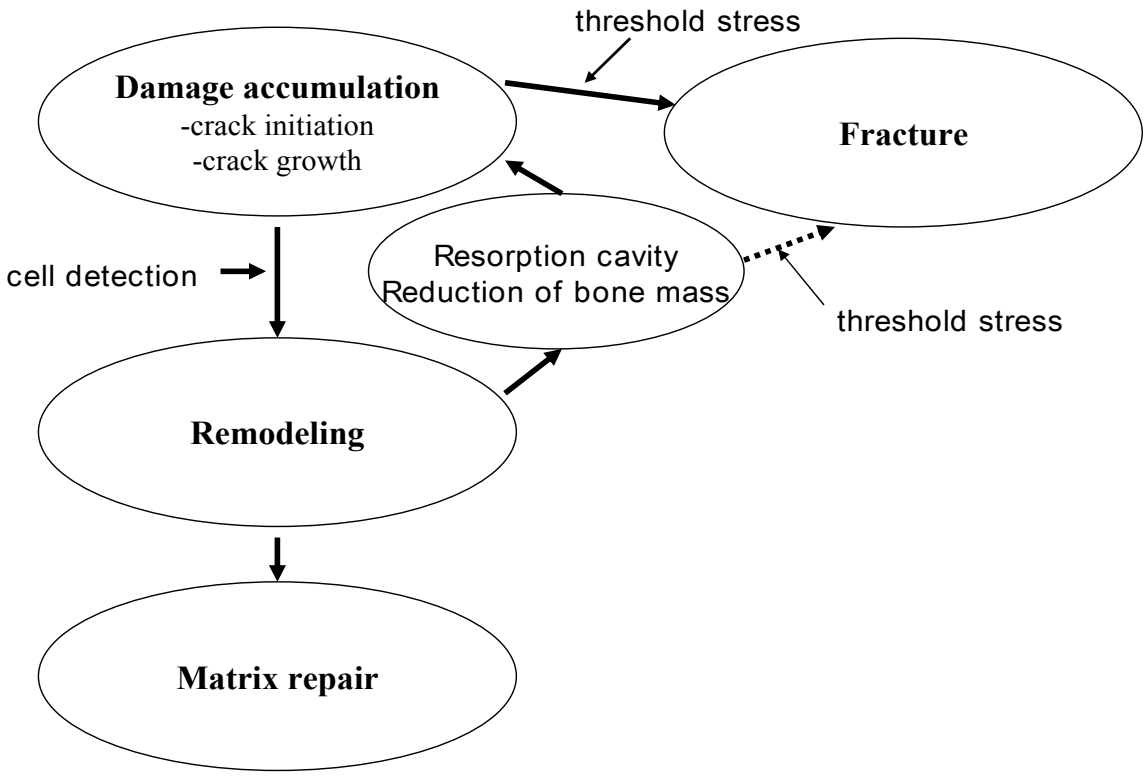

Figure A.1. Schematic of relationship between microdamage, bone remodeling and fracture. Microdamage accumulation can provide a stimulus for intracortical bone remodeling and matrix repair or, beyond a certain threshold, damage exceeds repair and fracture occurs.

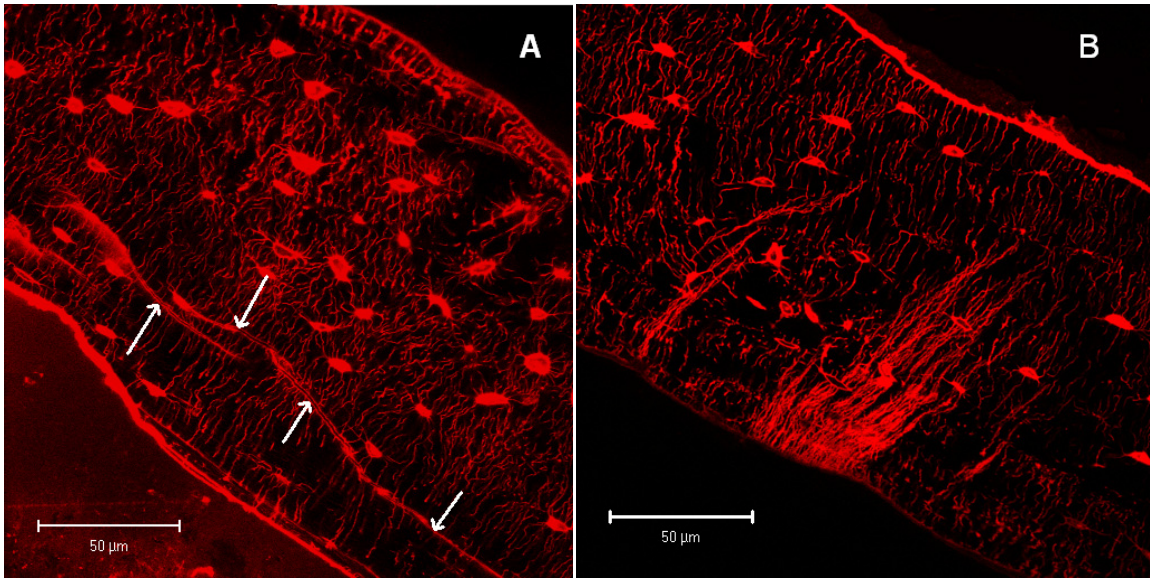

Figure A.2. Laser scanning confocal microscope images of murine cortical bone subjected to fatigue under four point bending. In the compressive region **(A)**, long linear microcracks are present (indicated by arrows). In the tensile region **(B)**, there is a cloudy network of tiny cracks that is classified as diffuse damage (60X).

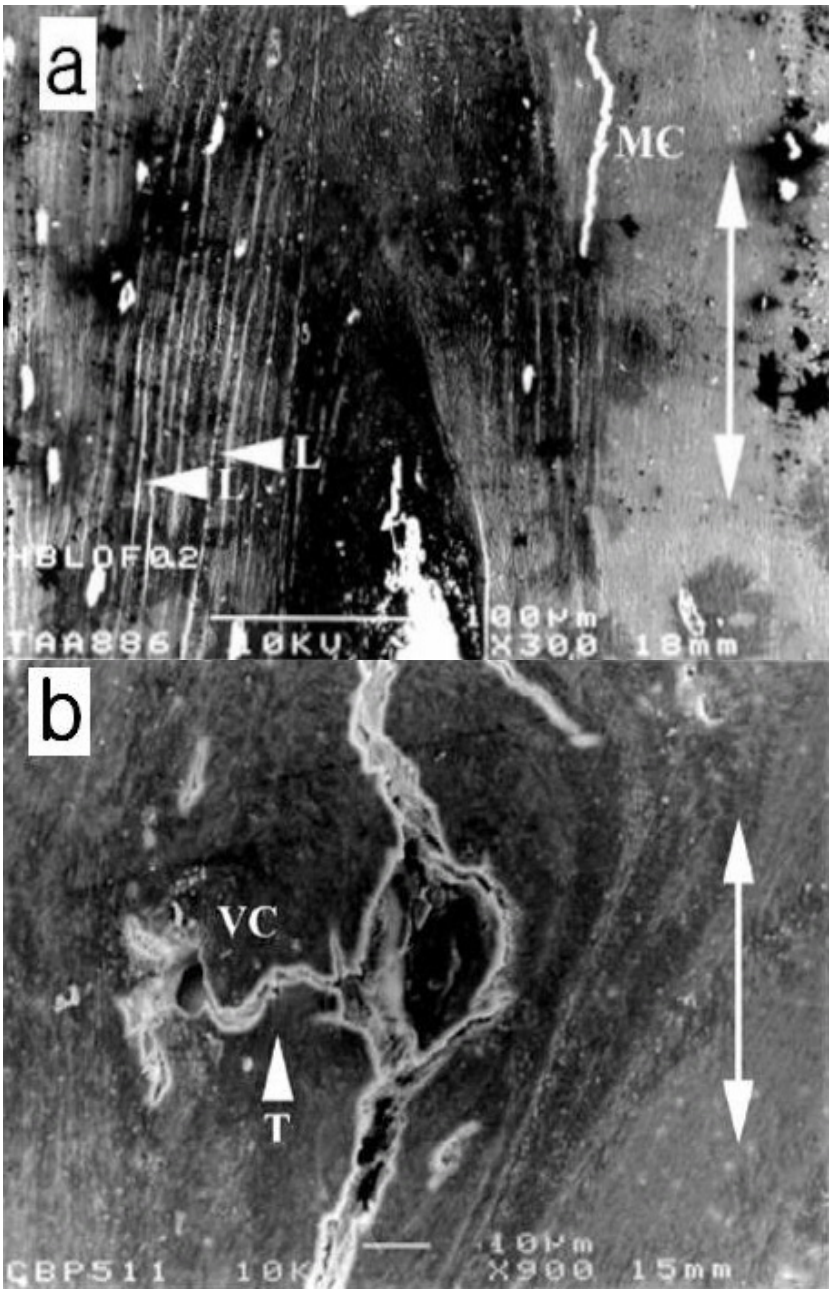

Figure A.3. (a) Failure of longitudinally oriented osteons in human bone. Arrowheads in this micrograph indicate longitudinal microcracks (represented by the letter 'L'); **(b)** Micrographs demonstrating the presence of stress concentration effects of Volkmann's canals in bovine bone. A transverse microcrack (indicated by an arrowhead and represented by the letter 'T') can be seen connecting the main crack and the Volkmann's canal (VC). In the micrographs, the line with arrowheads at both ends indicates the longitudinal axis of the long bone and the direction in which the main crack (MC) propagated. From Vashishth, et al., 2000b, with permission.

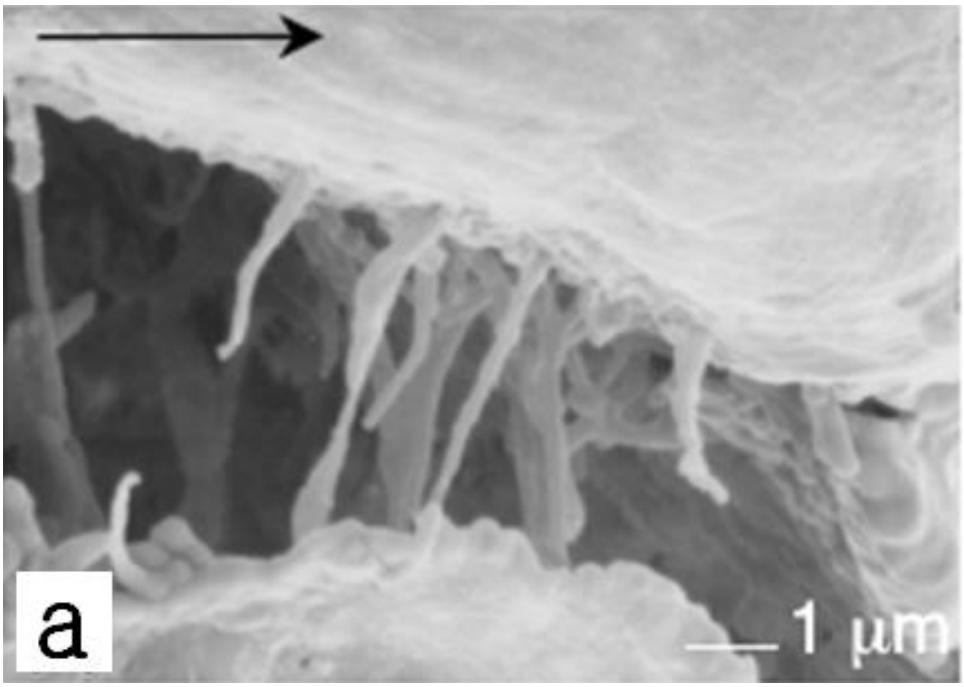

Figure A.4. Scanning electron micrographs of crack bridging by collagen fibers in human cortical bone. The direction of crack propagation is indicated by a black arrow at the top. From Nalla, et al., 2003, with copyright permission from Nature (http://www.nature.com/).

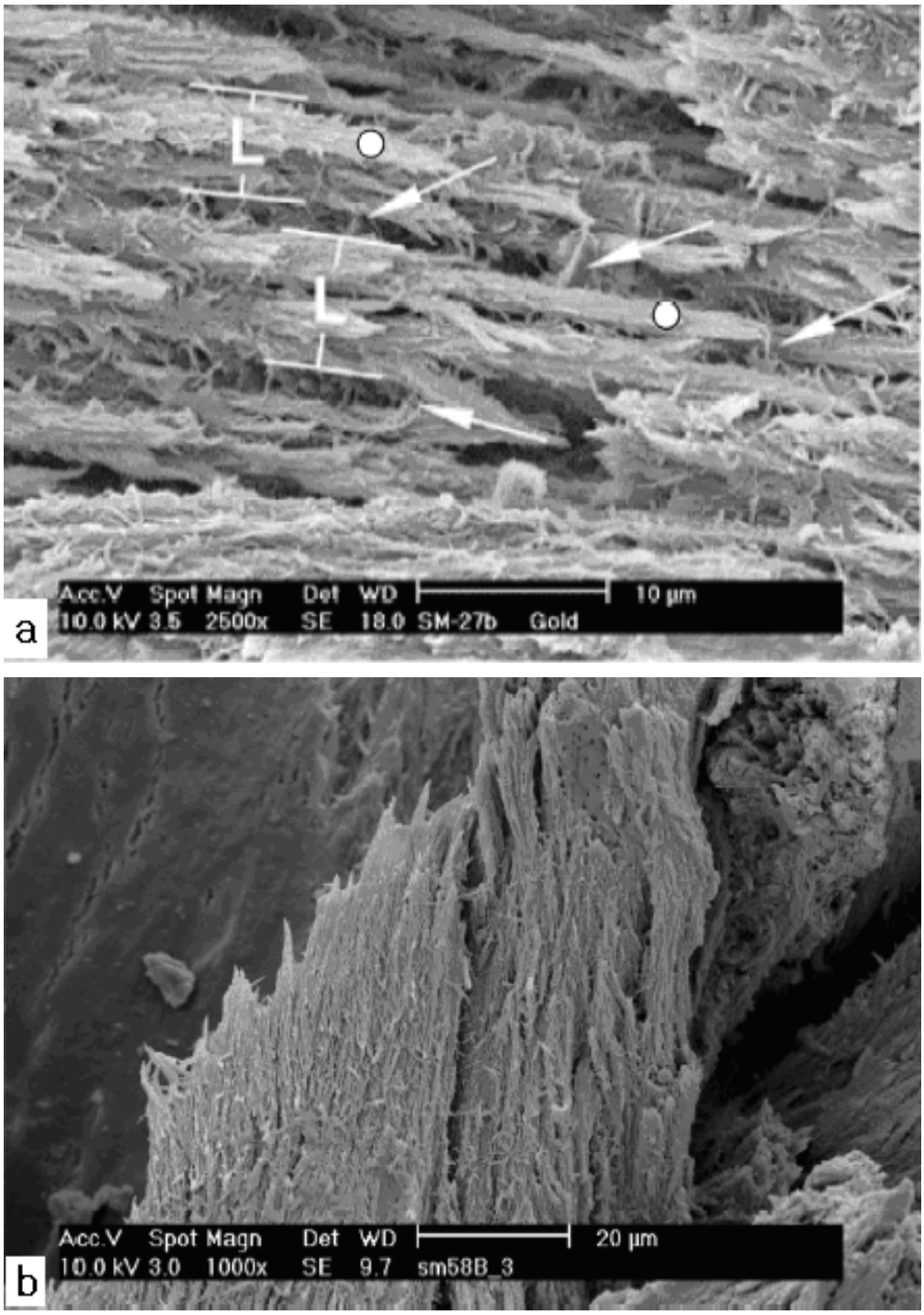

Figure A.5. Details of failure surfaces of bovine subchondral bone: **(a)** intra-lamellar fiber bundles (dots) belonging to a set of separated lamellae (*L*), connected by short inter-lamellar fibers (arrows), and; **(b)** pulled-out fiber bundles belonging to a set of undivided lamellae. From Braidotti, et al., 2000, with permission.

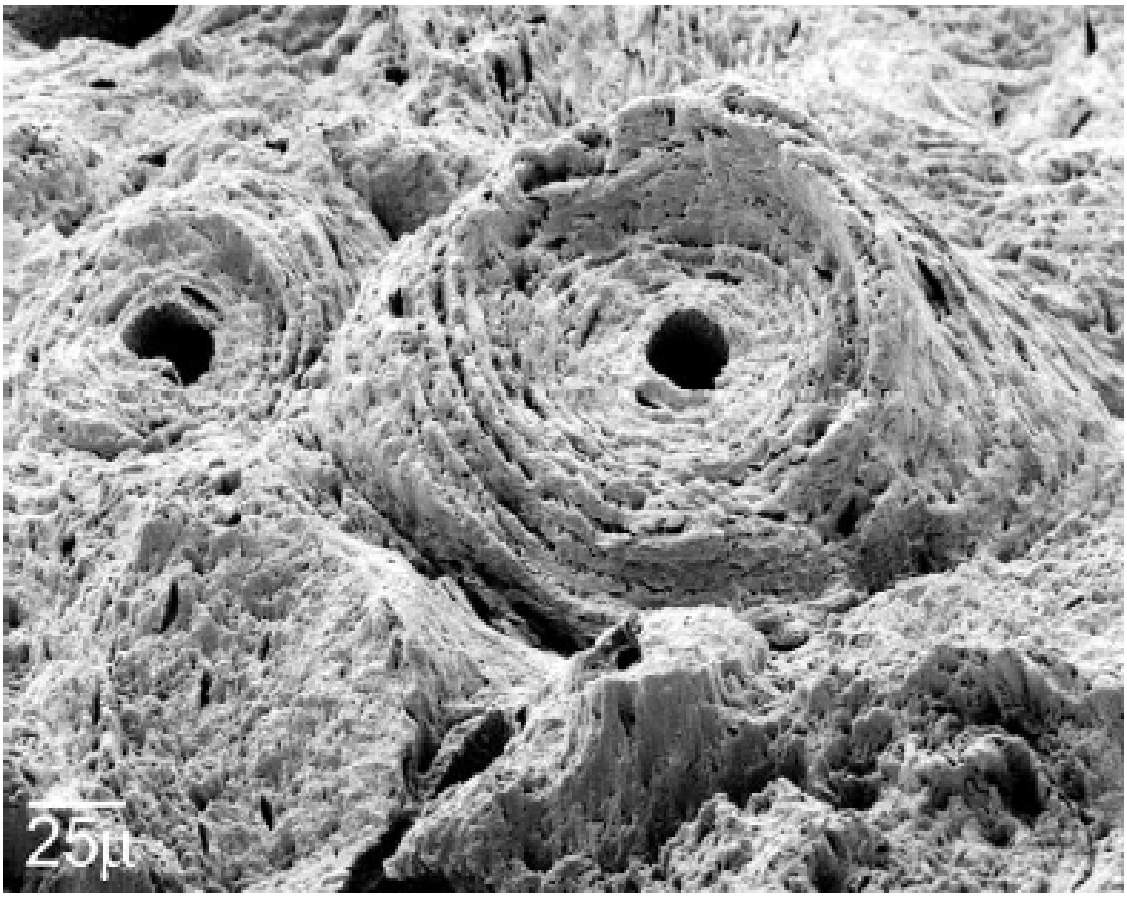

Figure A.6. Scanning electron micrograph of an osteon on the transverse fracture surface of a cyclically loaded dorsal specimen. Disruption of interlamellar and cement line interfaces reveals concentric lamellae and the outer osteon boundary of ‘‘pulled out’’ osteons. From Hiller, et al., 2003, with permission.

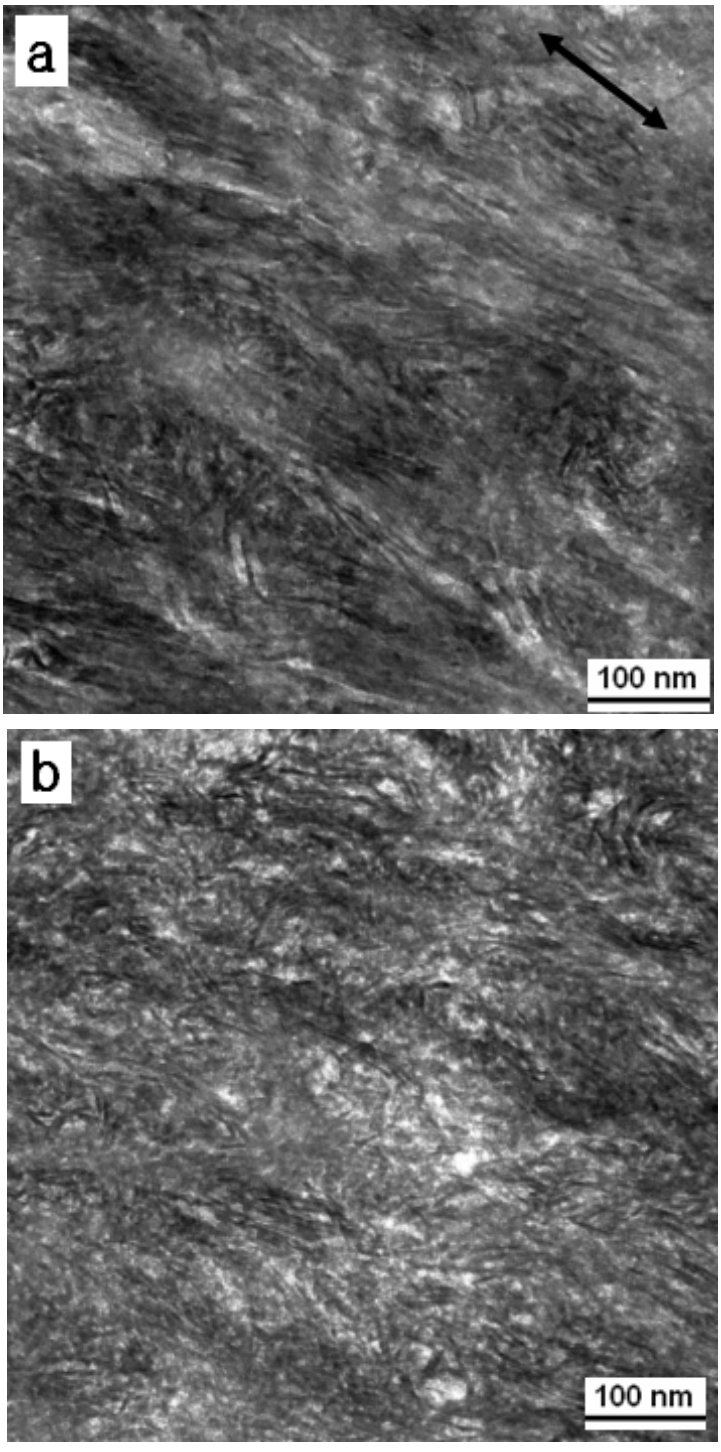

Figure A.7. Ultrastructure of murine lamellar bone before **(a)** and after **(b)** fatigue. The non-fatigued femora displayed well-aligned and uniformly distributed collagen fibrils mostly parallel to the bone axis (indicated by an arrow). In the fatigue-damaged femora, the aligned arrangement of collagen fibrils appeared to be impaired and loosened.

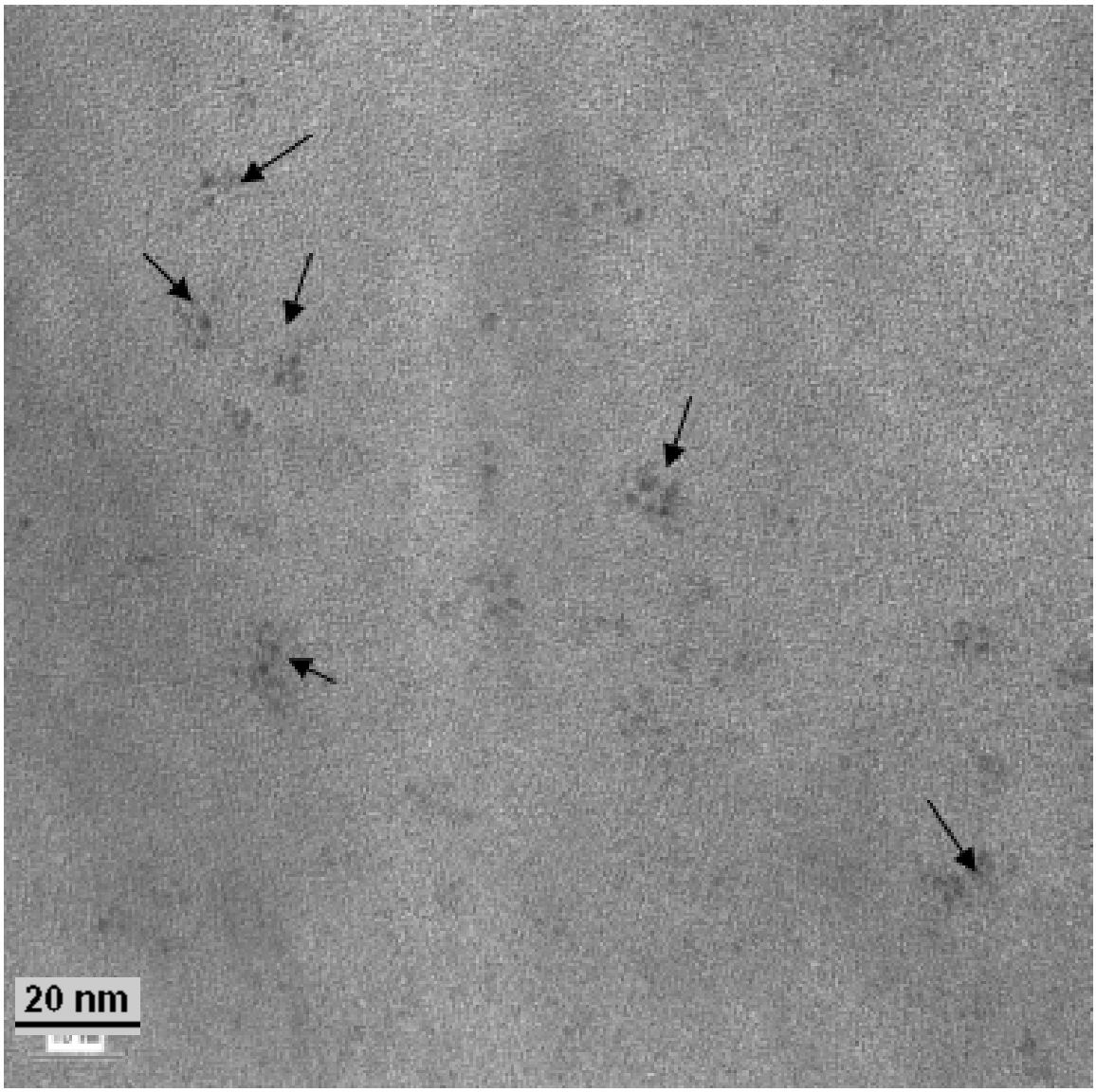

Figure A.8. High resolution transmission electron microscopic (HRTEM) images of fatigued murine lamellar bone at a high magnification. Small pieces of particles adjacent to each other and some featureless amorphous regions were observed.

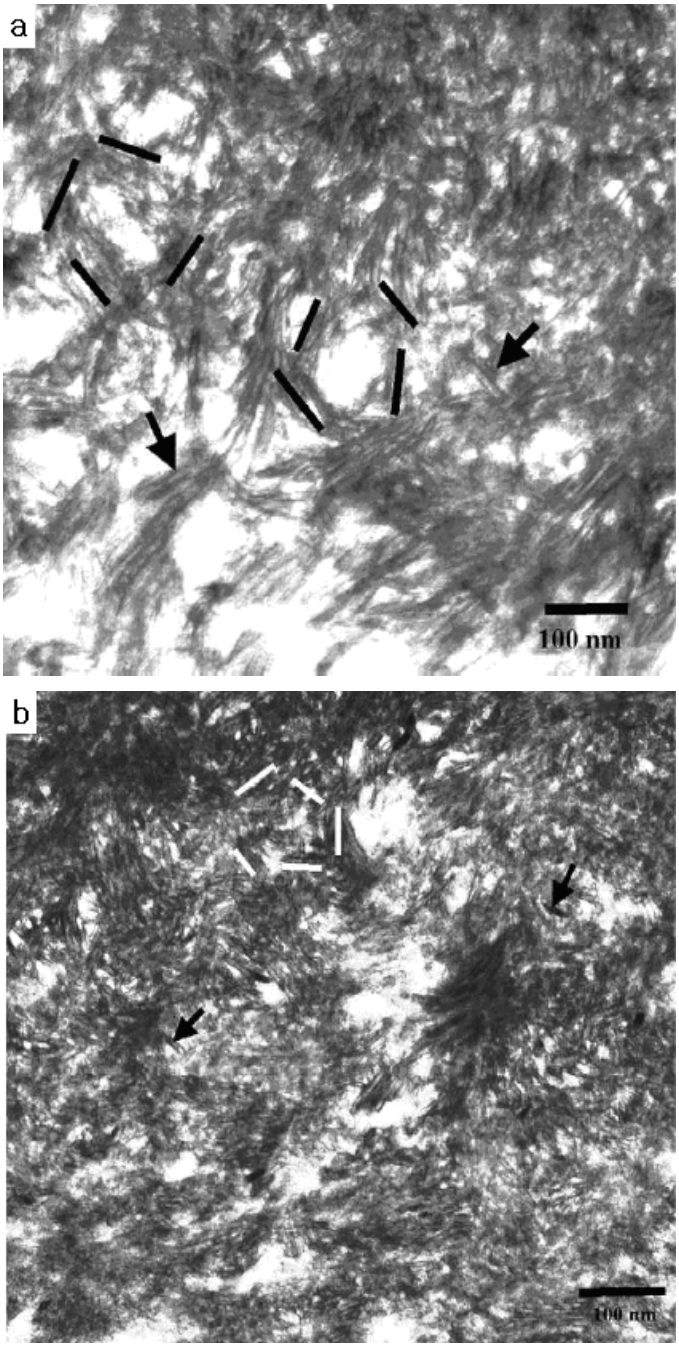

Figure A.9. TEM micrographs of the cross-section of mineral/collagen fibril aggregates in normal **(a)** and osteoporotic **(b)** human trabecular bone. Distinct individual hydroxyapatite crystals are seen within the mineral/collagen aggregates as tablet-like (plates on edge) shapes (arrows). Crystal organization in fibrils displayed more of a random undulated arrangement, with localized areas demonstrating circular oriented patterns of only tablet-like crystals patterns (bars indicate orientation of the crystal at that particular location). The orientation of the tablet-like crystals distinctively changes within a 100–200-nm-diam area. From Rubin, et al., 2003, with permission.

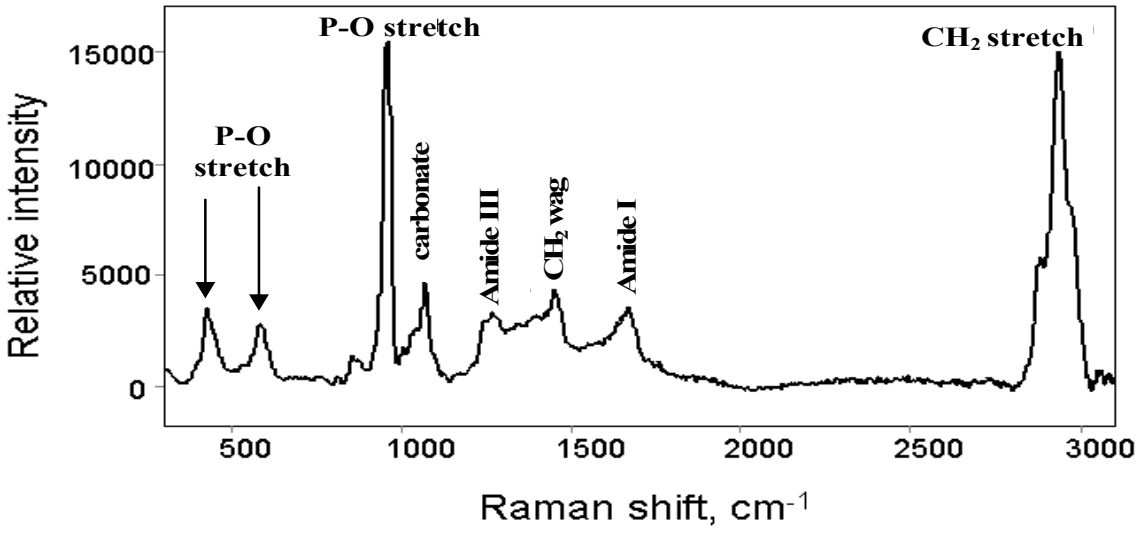

Figure A.10. Raman spectrum of bovine cortical bone taken on a near-IR optimized system, identifying mineral matrix bands of importance, Courtesy Kaiser Optical Systems, Inc., Ann Arbor, Michigan, USA.

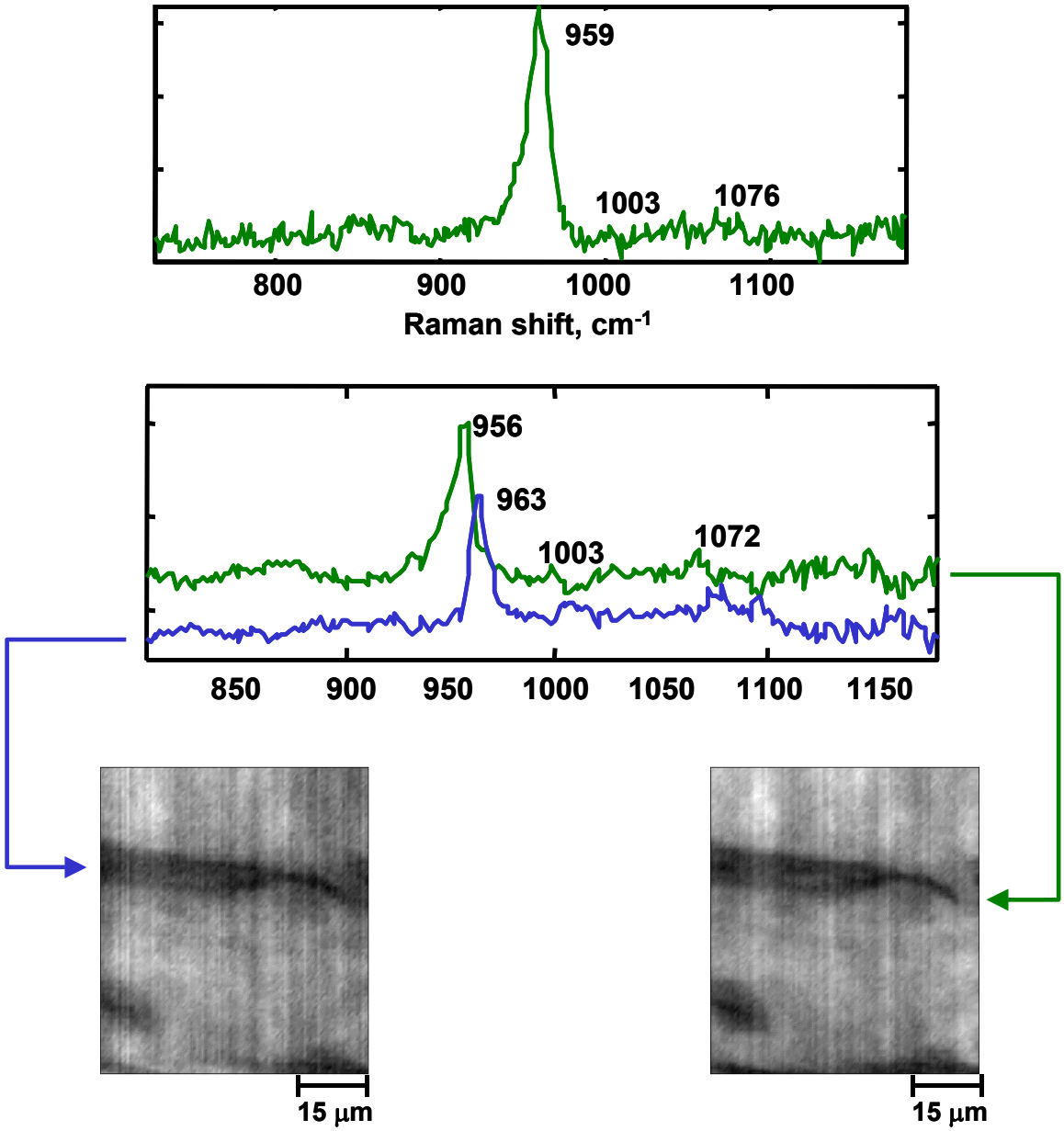

Figure A.11. Raman Spectra for undamaged **(a, top)** and damaged (microcracked) regions **(b, bottom)** of bovine cortical bone. Factor analysis revealed an additional high frequency phosphate species in cracked regions. Score images reveal the spatial distribution of these two mineral factors. From Timlin, et al., 2000, with permission.

Akkus, O., Rimnac, C.M., 2001. Cortical bone tissue resists fatigue fracture by deceleration and arrest of microcrack growth. Journal of Biomechanics 34, 757-764.

Beck, T.J., Ruff, C.B., Shaffer, R.A., 2000. Stress fracture in military recruits: gender differences in muscle and bone susceptibility factors. Bone 27, 437-444.

Bennell, K.L., Malcolm, S.A., Thomas, S.A., 1996. Risk factors for stress fractures in track and field athletes: a twelve month prospective study. American Journal of Sports Medicine 24, 810-818, 1996.

Birdwood, G.,1996. Understanding Osteoporosis and its Treatment. A Guide for Physicians and their Patients, Pearl River, New York.

Boyce, T.M., Fyhrie, D.P., Glotkowski, M.C., Radin, E.L., Schaffler, M.B., 1998. Damage type and strain mode associations in human compact bone bending fatigue. Journal of Orthopaedic Research 16, 322-329.

Boyde, A., Elliott, C., Jones, S.J., 1993. Stereology and histogram analysis of backscattered electron images: age changes in bone. Bone 14, 205-210.

Braidotti, P., Bemporad, E., D'Alessio, T., Sciuto, S.A., Stagni, L., 2000. Tensile experiments and SEM fractography on bovine subchondral bone. Journal of Biomechanics 33, 1153-1157.

Boskey, A.L., 1990. Bone mineral and matrix: are they altered in osteoporosis? Orthopaedic Clinics of North America 21, 19-29.

Burr, D.B.,1997. Bone, exercise and stress fractures. Exercise Science and Sports Review 25: 171-194.

Burr, D.B., Milgrom, C. (Eds.), 2001. Musculoskeletal Fatigue and Stress Fractures. CRC Press, Boca Raton, FL.

Burr, D.B., Stafford, T., 1990. Validity of the bulk-staining technique to separate artifactual from in vivo bone microdamage. Clinical Orthopaedics and.Related Research 260, 305-308.

Burr, D., Forwood, M., Fyhrie, D., Martin, R., Schaffler, M., Turner, C., 1997. Bone microdamage and skeletal fragility in osteoporotic and stress fractures. *Journal of Bone and Mineral Research* 12, 6-15.

Burr, D.B., Turner, C.H., Naick, P., Forwood, M.R., Ambrosius, W., Hasan, M.S., Pidaparti, R., 1998. Does microdamage accumulation affect the mechanical properties of bone? Journal of Biomechanics 31, 337-345.

Burr, D.B., Turner, C., Forwood, M.R., Pidaparti R., 1999. Quantification of bone damage and crack morphology and its effect on skeletal fragility: response to Zioupos. Journal of Biomechanics 32, 213-215.

Camacho, N.J., Rinnerthaler, S., Paschalis, E.P., Mendelsohn, R., Boskey, A.L., Fratzl, P., 1999. Complementary information on bone ultrastructure from scanning small angle x-ray and Fourier transform infrared microspectroscopy, Bone 25, 287-293.

Carden, A., Morris, M.D. 2000. Application of vibrational spectroscopy to the study of mineralized tissues. *Journal of Biomedical Optics* 5, 259-268.

Carden, A., Morris, M.D., Rajachar, R.M., Kohn, D.H., 2003. Ultrastructural changes in the mechanical deformation of bone tissue: a raman imaging study, Calcified Tissue International 72, 166-175.

Carter, D.R., Hayes, W.C., 1977a. Compact bone fatigue damage: a microscopic examination. Clinical Orthopaedics and.Related Research 127, 265-274.

Carter, D.R., Hayes, W.C., 1977b. Compact bone fatigue damage--I. Residual strength and stiffness. Journal of Biomechanics 10, 325-337.

Chatterji, S., Wall, J. C., Jefferey, J. W., 1981. Age related changes in the orientation and particle size of the mineral phase in human cortical bone. Calcified Tissue International 33, 567-574.

Colopy, S.A., Benz-Dean, J., Barrett, J.G., Sample, S.J., Lu, Y., Danova, N.A., Kalscheur, V.L., Vanderby, R., Jr, Markel, M.D., Muir, P., 2004. Response of the osteocyte syncytium adjacent to and distant from linear microcracks during adaptation to cyclic fatigue loading. Bone 35, 881-891.

Courtney, A.C., Hayes, W.C., Gibson, L.J.,1996. Age-related differences in post-yield damage in human cortical bone. experiment and model. Journal of Biomechanics 29, 257-260.

Currey, J. D., 2003. The many adaptations of bone. Journal of Biomechanics 36, 1487-1495.

Currey, J.D., Brear, K., Zioupos, P., 1996. The effects of ageing and changes in mineral content in degrading the toughness of human femora. Journal of Biomechanics 29, 257-260.

Danova, N.A., Colopy, S.A., Radtke, C.L., Kalscheur, V.L., Markel, M.D., Vanderby, R., McCabe, R.P., Escarcega, A.J., Muir, P., 2003. Degradation of bone structural properties by accumulation and coalescence of microcracks. Bone 33, 197-205.

de Carmejane, O., Morris, M.D., Davis, M.K., Stixrude, L., Tecklenburg, M., Rajachar, R.M., Kohn, D.H., 2005. Bone chemical structure response to mechanical stress studied by high pressure raman spectroscopy. Calcified Tissue International 76, 207-213.

Fazzalari, N.L., Forwood, M.R., Manthey, B.A., Smith, K., Kolesik, P., 1998. Three-dimensional confocal images of microdamage in cancellous bone. Bone 23, 373-378.

Frost, H.M., 1960. Presence of microscopic cracks in vivo in bone. Bulletin of the Henry Ford Hospital 8, 25-35.

Goldstein, J.I., Newbury D.E., Echlin, P., Joy, D.C., Fiori, C., Lifshin, E., 1981. Scanning Electron Microscopy and X-ray Microanalysis, Plenum Press, New York.

Griffin, L.V., Gibeling, J.C., Martin, R.B., Gibson, V.A., Stover, S.M., 1997. Model of flexural fatigue damage accumulation for cortical bone. Journal of Orthopaedic Research 15, 607-614.

Grynpas, M., 1993. Age and disease-related changes in post-yield damage in human cortical bone. *Calcified Tissue International* 53, S57-S64.

Grynpas, M.D., Holmyard, D., 1988. Changes in quality of bone mineral on aging and in disease. Scanning Microscopy 2, 1045-1054.

Hiller, L.P., Stover, S.M., Gibson, V.A., Gibeling, J.C., Prater, C.S., Hazelwood, S.J., Yeh, O.C., Martin, R.B., 2003. Osteon pullout in the equine third metacarpal bone: effects of ex-vivo fatigue. Journal of Orthopaedic Research 21, 481-488.

Hong, S.I., Gray, G.T., Wang, Z., 1996. Microstructure and stress-strain response of Al-Mg-Si alloy composites reinforced with 15 % Al2O3. Materials Science and Engineering 221, 38-47.

Hong, S.I., Suryanarayana, C., 2001. Is ductilization of intermetallic compounds by nanostructure processing a possibility? Materials Transactions 42, 502-508.

Hong, S.I., Kohn, D.H., 2005. Nanostructural analysis of murine femoral trabecular bone, in review.

Hong, S.I., Hong, S.K., Kohn, D.H., 2005. Fatigue induced damage of mineral apatites in murine femoral bone, in review.

Hui, S., Slemenda, C., Johnston, C.,1988. Age and bone mass as predictors of fracture in a prospective study. Journal of Clinical Investigation 81, 1804-1809.

Jones, B.H., Harris, J.M., Vinh, T.N., Rubin, C., 1989. Exercise-induced stress fractures and stress reactions of bone: epidemiology, etiology and classification, *Exercise Sport Science Reviews* 17: 379-422.

Jordaan, G., Schwellnus, M.P, 1994. The incidence of overuse injuries in military recruits during basic military training. Military Medicine 159, 421-426.

Kafantari, H., Kounadi, E., Fatouros, M., Milonakis., M., Tzaphlidou, M., 2000. Structural alterations in rat skin and bone collagen fibrils induced by ovariectomy. Bone 26, 349-353.

Lee, K.H., Hong, S.I., 2003. Interfacial and twin boundary structures of nanostructured filamentary composites. Journal of Materials Research 18, 2194-2202.

Martin, R.B., Burr, D.B., Sharkey, N.A., 1998. Skeletal Tissue Mechanics, Springer Verlag, New York.

Matthews, F., Rawlings, R., 1994. Composite Materials: Engineering and Science, Chapman and Hall, New York.

Morris, M.D., Carden, A., Rajachar, R.M., Kohn, D.H., 2001. Bone microstructure deformation observed by raman microscopy. In: Biomedical Diagnostic, Guidance, and Surgical-Assist Systems III, T Vo-Dinh, et al., Eds, Society for Optical Instrumentation and Engineering (SPIE) Press, Vol 4254, Bellingham, WA, 81-89;
Morris, M.D., Carden, A., Rajachar, R.M., Kohn, D.H.,2002. Effects of applied load on bone tissue as observed by Raman spectroscopy, In: *Biomedical Vibrational Spectroscopy II*, A Mahadevan-Jansen, et al., Eds, Society for Optical Instrumentation and Engineering (SPIE) Press, Vol 4614, Bellingham, WA, 47-54.

Nalla, R.K., Kinney J.H., Ritchie, R.O., 2003. Mechanistic fracture criteria for the failure of human cortical bone. Nature Materials, 2, 164-168.

Nalla, R.K., Kruzic, J.J., Ritchie, R.O., 2004. On the origin of the toughness of mineralized tissue: microcracking or crack bridging? Bone 34, 790-798.

National Osteoporosis Foundation, Annual Report, 2001 (http://www.nof.org).

Norman, T.L., Wang, Z., 1997. Microdamage of human cortical bone: incidence and morphology in long bones. Bone 20, 375-379.

Norman, T.L., Yeni, Y.N., Brown, C.U., Wang, Z., 1998. Influence of microdamage on fracture toughness of the human femur and tibia. Bone 23, 303-306.

O'Brien, F.J., Taylor, D., Lee, T.C., 2003. Microcrack accumulation at different intervals during fatigue testing of compact bone. Journal of Biomechanics 36, 973-980.

Paschalis, E.P., Betts, F., DiCarlo, E., Mendelsohn, R., Boskey, A.L., 1997. FTIR microspectroscopic analysis of normal human cortical and trabecular bone. *Calcified Tissue International* 61, 480-486.

Penel, G., Leroy, G,, Rey, C., Bres, E., 1998. MicroRaman spectral study of the PO_4 and CO_3 vibrational modes in synthetic and biological apatites. *Calcified Tissue International* 63, 475-481.

Praemer, A., Furner, S., Rice, D.P., 1999. Musculoskeletal Conditions in the United States, American Academy of Orthopaedic Surgeons, Rosemont, IL.

Rajachar, R.M., 2003. Effects of age-related ultrastructural level changes in bone on microdamage mechanism, Ph.D. Thesis, University of Michigan.

Reilly, G.C., 2000. Observations of microdamage around osteocyte lacunae in bone. Journal of Biomechanics 33, 1131-1134.

Reilly, G.C., Currey, J.D., 2000. The effects of damage and microcracking on the impact strength of bone. Journal of Biomechanics 33, 337-343.

Rey, C., Renugopalakrishnan, Collins, B., Glimcher, M.J., 1991. Fourier transform infrared spectroscopic study of the carbonate ions in bone mineral during aging, *Calcified Tissue International* 251-258.

Rho, J.-Y., Kuhn-Spearing L., Zioupos P., 1998. Mechanical properties and the hierarchial structure of bone. Medical Engineering and Physics 20, 92-102.

Rohanizadeh, R., LeGeros, R.Z., Bohie, S., Pilet, P., Barbier, A., Daculsi, G., 2000. Ultrastructural properties of bone mineral of control and tiludronate-treated osteoporotic rat, Calcified Tissue International 67, 330-336.

Rubin, M.A., Jasiuk, I., Taylor, J., Rubin, J., Ganey, T., Apkarian, R.P., 2003. TEM analysis of the nanostructure of normal and osteoporotic human trabecular bone. Bone 33, 270-282.

Ruff, C.B., Hayes, W.C., 1984. Age changes in geometry and mineral content of the lower limb bones, *Annals of Biomedical Engineering* 12, 573-584.

Schaffler, M.B., Choi, K., Milgrom, C., 1995. Aging and matrix microdamage accumulation in human compact bone. Bone 17, 521-525.

Schaffler, M.B., Pitchford, W.C., Choi, K., Riddle, J.M., 1994. Examination of compact bone microdamage using back-scattered electron microscopy. Bone 15, 483-488.

Schaffler, M.B., Radin, E.L., Burr, D.B., 1989. Mechanical and morphological effects of strain rate on fatigue of compact bone. Bone 10, 207-214.

Simmons Jr., E.D., Pritzker, K.P.H., Gryanpas, M.D., 1991. Age-related changes in human femoral cortex. Journal of Orthopaedic Research 9, 155-167.

Sobelman, O.S., Gibeling, J.C., Stover, S.M., Hazelwood, S.J., Yeh, O.C., Shelton, D.R., Martin, R.B., 2004. Do microcracks decrease or increase fatigue resistance in cortical bone? Journal of Biomechanics 37, 1295-1303.

Timlin, J.A., Carden, A., Morris, M.D., Rajachar, R.M., Kohn, D.H., 2000. Raman spectroscopic markers for fatigue-related bovine bone microdamage. Analytical Chemistry 72, 2229-2236.

Vashishth, D., Behiri, J.C., Bonfield, W., 1997. Crack growth resistance in cortical bone: concept of microcrack toughening. Journal of Biomechanics 30, 763-769.

Vashishth, D., Koontz, J., Qiu, S.J., Lundin-Cannon, D., Yeni, Y.N., Schaffler, M.B., Fyhrie, D.P., 2000a. In vivo diffuse damage in human vertebral trabecular bone, Bone 26, 147-152.

Vashishth, D., Tanner, K.E., Bonfield, W., 2000b. Contribution, development and morphology of microcracking in cortical bone during crack propagation. Journal of Biomechanics 33, 1169-1174.

Vashishth, D., Tanner, K.E., Bonfield, W., 2003. Experimental validation of a microcracking-based toughening mechanism for cortical bone. Journal of Biomechanics 36, 121-124.

Weiner, S., Traub, W., Wagner, H.D., 1999. Lamellar bone: structure-function relations, Journal of Structural Biology 126, 241-255.

Yan. J., Clifton, K.B., Mecholsky Jr., J.J., Reep, R.J., 2005. Fracture toughness of manatee rib and bovine femur using a chevron-notched beam test, Journal of Biomechanics, 38, in press.

Zioupos, P., 1999. On microcracks, microcracking, in-vivo, in vitro, in-situ and other issues. Journal of Biomechanics 32, 209-11, 213-59.

Zioupos, P., Currey, J.D., 1998. Changes in the stiffness, strength and toughness of human cortical bone with age. Bone 22, 57-66.

APPEDNIX B

VALIDATION OF A PORTABLE DEVICE FOR INSTRUMENTED INDENTATION

ABSTRACT

Instrumented indentation testing, particularly nanoindentation, has gained interest as a material testing method. Unlike conventional indentation, instrumented indentation allows for calculation of elastic modulus (along with hardness) and analysis of force-displacement curves from loading and unloading. While the utility of these devices is proven, their applications could be greatly expanded. This paper presents a new device for instrumented indentation that is portable (and can be hand-held during operation), rapidly runs tests, and requires no specific sample preparation other than a creating smooth surface. The instrument was validated by testing material samples with known material properties and regressing the measured properties against the specified properties. Significant correlations were found between measured modulus and specified modulus, measured hardness and specified hardness, and measured hardness and specified ultimate tensile strength. An experiment was also conducted testing the mechanical properties of human dentin and comparing the findings to previous results obtained by nanoindentation of the same samples. The instrument's measurements were in good agreement with the nanoindentation measurements. Finally, the ability of the device to measure nonconventional metrics, such as energy dissipation, and the utility of those metrics are demonstrated. Development of this instrument presents new

possibilities for easily, rapidly and nondestructively measuring an array of mechanical properties in the field.

INTRODUCTION

Indentation testing to determine the hardness of materials has a long history. Conventional indentation tests include the Brinell, Rockwell, and Vickers hardness tests. These tests involve indenting at a fixed load and then examining the diameter or depth of the indentation. The development of sophisticated techniques for determining mechanical parameters from force and displacement data has led to instrumented indentation machines, particularly nanoindentation testers [1, 2]. Instrumented indentation allows for determination of elastic modulus and hardness, as well as analysis of force-displacement curves recorded during tests. Use of nanoindentation testers is becoming more common and finding many applications as illustrated in the special issue on indentation. One current limitation is that these devices are not portable and require a rigid frame and rigid specimen mounting to enable accurate measurements.

There are commercially available portable hardness testers. In particular there are many rebound testers such as the TH130 and TH150 pocket-size hardness testers from Corvib and many ultrasonic hardness testers, such as the High Resolution SH-21 Portable Hardness Tester from Micro Photonics Inc. However, these devices can only measure hardness. To the best of our knowledge there exists no portable device for instrumented indentation. Thus, while there have been portable hardness testing devices and devices that measure parameters other than hardness, we are aware of no prior devices that combine the ability to be portable with the ability to measure a wide variety of parameters based on indentation of a probe into a sample.

In this paper, we validate a new instrument for a portable instrumented indentation testing system that is based on a device designed to test mechanical properties of bone through skin and soft tissue [3, 4]. This system does not require rigid mounting of the test specimen or device because it contains a reference probe that rests on the surface of the

material being tested and provides a reference for measuring the distance that a test probe indents into the material. It can then measure complete force vs. displacement curves during one or multiple indentation cycles where the force is the force that the instrument supplies during the indentation cycle(s). In this paper, we validate the device by measuring mechanical properties of some common metals and polymers, and developing correlations between the measured properties and known mechanical properties. We further test the device by examining location dependence of modulus and hardness in human dentin and comparing the results with findings previously obtained by nanoindentation [5].

MATERIALS AND METHODS

The Portable Instrumented Indenter (PII)

We used the Osteoprobe II™ Bone Diagnostic Instrument [4], which is an improved version of the Osteoprobe I™ Bone Diagnostic Instrument [3], as a prototype Portable Instrumented Indenter (PII). The primary improvements are a new control system, which can collect and quantitatively analyze force vs. distance curves (Figure B.1) and the substitution of a voice-coil-based force generator for the solenoid force generator used in the Osteoprobe I (Figure B.2). The control system, written in Labview™, supplies a modified triangular wave to the force generator for the primary loading cycles used in measurements. The modified triangular wave consists of 1/3 of a cycle of linear increase, followed by 1/3 of a cycle hold at maximum current, and then 1/3 of a cycle of linear decrease. A typical total cycle time is 500 msec. The purpose of the hold at maximum current is to monitor creep effects and to minimize the effect of the remaining creep during the linear decrease. This type of hold at the maximum load is used in Instrumented Indentation Analysis, pioneered by Oliver and Pharr(*3*) for getting valid retraction slopes for determining elastic modulus. Typically, for nanoindentation, the hold time and the unloading times are much longer than we use (and the indentations are much less deep). We have found that, for the PII, what really counts in getting a valid retraction slope is the ratio of the unloading time to the hold time. We have found that

the cycle described above gives valid retraction slopes comparable to those found with longer hold times (up to a minute) and correspondingly slower unloading.

We used the PII with the same type of test probe and reference probe that we use for penetrating soft tissue to measure bone properties (Figure B.2). This consists of a 22 gauge hypodermic needle, which serves as a reference probe that rests on the surface of the material under test and a test probe that indents the material under test. The test probe is a hardened steel rod that is 1.6 mm in diameter on the end that sticks to the magnet at the bottom of the shaft of the device (Figure B.2). The other end of the test probe is 375 microns in diameter (to fit through the needle) and is beveled to a cone with a 90^{o} total included angle and then rounded to an approximate radius of 2.5 microns. This type of reference probe and test probe were developed to penetrate soft tissue and measure bone properties [4]. Thus they were optimized to be as small in diameter as possible and to be consistent with measuring properties of a tissue with an elastic modulus of order 10 GPa.

Testing material samples

Nineteen materials with known mechanical properties from manufacturer specifications and material databases [6-8] were selected for analysis (Table B.1). Ten samples were aluminum and copper alloys and nine samples were plastic. Testing these plastics and metal alloys allowed validation of the PII across a wide range of material properties. For the metal samples, the surface layer was ground off with a grinding wheel and then lightly polished (300 grit sand paper) to remove any surface effects from fabrication or oxidation.

The automated test protocol consisted of loading pre-cycles followed by the main loading cycles (20 cycles at 2 Hz, as described above, with peak load of 5 N). The purpose of the pre-cycles is to establish a good zero reference for indentation distance measurements. The pre-cycles are modified trapezoidal waves similar to the primary cycles mentioned above. Unlike the primary cycles, which are of constant amplitude, the pre-cycles have gradually increasing load amplitudes typically starting at 0.1 N and increasing on the

order of 0.1 N after each cycle. The maximum force during the pre-cycles is monitored. When the maximum force reaches a preset threshold value, typically about 1 N, the reference position for indentation distance measurements is set at the distance where the preset threshold force was reached.

This reference position is used to compute modulus and hardness by the Oliver and Pharr method [1, 2] as if it were the contact point. Since the reference position is, however, inside the material being tested, modulus and hardness are overestimated. This is corrected by measuring a known standard, polymethylmethacrylate (PMMA), with the same loading tip and protocol, then dividing the results on the tested material by the results on the standard, and finally multiplying these normalized results by the known values of the PMMA standard (E = 4.483 GPa, H = 292 MPa, determined by nanoindentation).

In testing each material, first five indentation tests were conducted on the PMMA standard. Then five indents were made on each sample and the mechanical properties were calculated. Because the indenting tip was made of hardened steel, it was replaced after testing each metal sample to avoid dulling. Once the measured mechanical properties were normalized to the PMMA standard, they were averaged for each material sample. These means were then linearly regressed (SPSS) against expected values from the material specifications. For the metal samples, the hardness reported in specifications was converted to SI units using hardness conversion tables [9]. Conversion of hardness number into SI units was not possible for plastics, so they were reported on their original scale.

A new metric, mean energy dissipation, was calculated as the mean energy of hysteresis loops above a threshold force of 2 N from loading cycles 3-19. Because these cycles produce very little additional plastic deformation, the hysteresis energy of these loading and unloading cycles represents true energy dissipation and not failure of the material. Mean energy dissipation is reported without units, because the measured values were normalized to the mean energy dissipation measured on the PMMA standard with the

same testing probe, just as in the modulus and hardness calculations. However, unlike modulus and hardness, mean energy dissipation could not be scaled to meaningful units because the true energy dissipation of our standard was not known.

Comparing analysis of human dentin with previous nanoindentation results

Previously, nanoindentation was used to determine effect of radial location on modulus and hardness of dentin in human teeth [5]. Nanoindentation tests were performed on the root portion of adult human molars. Teeth were embedded in PMMA and cross-sectioned, coronally, into 3-mm sections using a low-speed diamond saw. Sections were polished to 0.05 μm with alumina paste and ultrasonically cleaned in deionized water for 10 minutes to remove any smear layer or residual polishing compound.

A Nanoscope III AFM (Digital Instruments, Santa Barbara, CA) was modified using a picoindentation apparatus (Hysitron, Minneapolis, MN). The picoindentation apparatus used the scanning software and control of the AFM, but instead of an optically reflective cantilever, a piezoelectric head was used along with a diamond tip. For each tooth section, indentations were made at 12 locations within the dentin. In each of 4 quadrants (facial, lingual, mesial, distal), measurements were made at 3 radial locations (near the pulp, near the dentin-cementum junction (DCJ), and mid-way between). At each of these locations, 3 indentations were made on areas that were visually determined to be smooth. Indentations were made by applying a 2500 μN load using a triangular waveform at a load rate of 1667 μN/sec, which plastically indented the tissue to a depth of 650-800 nm. As each indentation was generated, force-depth data was collected, and hardness and Young's modulus were calculated [1].

This experiment was repeated using the BDI on the same samples, taking one measurement at the three radial locations within each quadrant. Because, no effect of quadrant was found on modulus or hardness by the BDI or picoindenter, measurements were pooled by raidial location. The effects of radial location (near pulp, middle, near

DCJ) were then determined by independent sample t-tests for both the picoindenter data and BDI data. Differences were considered significant for $p < 0.05$.

RESULTS

Elastic modulus

Measured modulus of elasticity from the material samples was significantly correlated ($p < 0.001$, $R^2 = 0.960$) with the known tensile modulus of elasticity from their specifications (Figure B.3). However, the strength of this regression was largely driven by the cluster of metal data points at high modulus values. When metals and plastics were regressed separately, a significant relationship still existed between specified modulus and measured modulus for plastics ($p < 0.001$, $R^2 = 0.858$), but not for metals ($p = 0.145$, $R^2 = 0.246$). Additionally, the range of values measured for plastics is in the same range as the material specifications, approximately 0.5 - 4.5 GPa. In contrast, the measured values of modulus for metals are less than the values from material specifications (20-50% of specified values).

Hardness

For metals, a significant relationship exists between measured hardness and hardness from material specifications (Figure B.4, $p = 0.025$, $R^2 = 0.536$), and the measured values of hardness are in the same range of values as the material specifications (0.8 – 1.8 GPa). For plastics, materials with hardness specified on the Shore D scale were regressed separately from those reported on the Rockwell M scale because these scales cover different ranges of hardness. Regression of measured hardness was significant with Rockwell M hardness ($p = 0.029$, $R^2 = 0.942$) and marginally significant with Shore D hardness ($p = 0.081$, $R^2 = 0.692$).

To regress all materials together, measured hardness was regressed against specified ultimate tensile strength (Figure B.5), as there is an expected relationship between

hardness and ultimate strength. The regression was significant ($p < 0.001$) with an R^2 value of 0.954.

Energy dissipation

Izod impact energy was specified for six of the materials, all plastics. Mean energy dissipation had a significant relation with Izod impact energy (Figure B.6, $p = 0.002$, $R^2 = 0.923$). Although this regression appears to be forced by one point (Teflon, impact energy = 1.38 J/cm), it is still marginally significant with that point removed ($p = 0.082$, $R^2 = 0.689$).

Hardness and modulus of human dentin

Previously, a location dependence of modulus and hardness within dentin was found by nanoindentation of human tooth cross-sections (Figure. B.7). Elastic modulus was significantly greater in the middle of the dentin and near the dentin-cementum junction (DCJ) than near the pulp. There was a trend of increasing hardness from near the pulp to the middle of the dentin to near the DCJ, but only the difference from near the pulp to near the DCJ was significant.

Similar results were found when this experiment was repeated using the PII. Again, elastic modulus and hardness were significantly greater in the middle of the dentin and near the DCJ than near the pulp. Additionally, hardness in the middle of the dentin was significantly greater than near the pulp and significantly less than near the DCJ. In other words, there was a significant increase in hardness with each radial step outwards from the pulp. This trend was present in the nanoindentation measurements, but not significant.

DISCUSSION

Measurements of hardness by the Portable Instrumented Indenter correlated well with specified hardness for plastics and metals (Figure B.4). The material samples cover a broad range of hardness and were originally specified on four different scales of hardness (Table I). For the metal samples, the range of hardness values matched the material specifications. Conversion of hardness to SI units could not be done for plastics, but there were still good correlations between measured hardness and Shore D and Rockwell M hardness numbers. Additionally, the regression between measured hardness and specified ultimate tensile strength was excellent for plastics and metals (Figure B.5). Together, this data demonstrates that the PII was able to accurately calculate hardness across two orders of magnitude even though it was optimized for testing soft materials.

The PII also measured elastic modulus of plastics accurately (Figure B.3). The regression between measured modulus and tensile modulus from specification was significant and the values were in the same range. The device did not perform as well on the metals. The measured values of modulus ranged from 10-40 GPa but the metals should have moduli between 70-120 GPa. This error may be due to the design and optimization of the PII system for testing bone, which has a modulus of 4-15 GPa. The PII had a hardened steel indenting tip on a 375 micron diameter shaft of hardened steel shaft. While this is sufficiently stiff for testing bone, the shaft and tip may significantly deform when indenting on metals. There are also errors in correcting for system compliance, which includes the 22 gauge needle as part of the mechanical path. Error in system compliance also becomes a greater problem when testing stiffer materials.

All of these problems can be fixed by modifying the device as a material testing instrument instead of an *in vivo* tissue diagnostic instrument, as shown in Figure B.8. If the necessity to penetrate soft tissue with minimum discomfort is lifted then the reference probe and test probe could be made of much larger diameter to stiffen them. The reference probe could terminate with a tripod that rests on the surface. A tripod reference would limit displacement into the material surface, as may have occurred with original the needle-like reference probe, and unload the material immediately surrounding the

indented area. If the necessity to have sterile, disposable probe assemblies is lifted then the test probe could be tipped with a precisely ground diamond. A diamond tip would require less frequent replacement or maintenance, allowing for thorough characterization of the contact area function and eliminating the need for normalizing the data to a PMMA standard. These modifications could decrease the errors in calculating modulus of metals and further improve hardness and modulus measurement in both soft and hard materials.

A possible reason why the PII could accurately measure hardness but not modulus in metals is that hardness is only a function of load and indentation area (determined from the indentation depth), while modulus depends on indentation area and unloading stiffness. Correcting for system compliance on this device seems to affect calculation of unloading stiffness more than indentation area. Therefore, accurate measurement of modulus may be more sensitive to errors in system compliance. Moduli in the range for which the system was designed were accurately measured by the device (Figure B.3, plastics). In this range the compliance corrections do not dominate the measured values. As materials become stiffer, the compliance corrections dominate the measured values and it becomes more difficult to recover materials parameters. Making simple modifications to the device, as mentioned above, along with testing and optimizing the device on stiff materials could make it more accurate for testing stiff materials.

Besides determining conventional indentation measurements, like modulus and hardness, the PII offers the ability to analyze load-displacement curves and effects of rapid, repeated loading and unloading. New metrics may be derived, such as mean energy dissipation. Mean energy dissipation was significantly correlated with Izod impact strength (Figure B.6). This correlation is meaningful because both metrics reflect a material's ability to absorb energy, which can shield a material from strain and potentially protect it from failing. Mean energy dissipation is an example of the power of instrumented indentation. Analyzing load-displacement curves allows for determination of new, meaningful metrics. There are many examples of nonconventional measurement in nanoindentation [10-15] and it is likely that additional meaningful metrics will be developed in the future. The PII can currently measure the increase in indentation

distance with each cycle, loss modulus, and other characteristics of viscoelastic behavior. These metrics have proven useful in testing human tissues [4].

The location dependence of hardness and modulus in dentin previously found by nanoindentation were confirmed with the PII. Furthermore, the PII found significant differences in hardness that were suspected (because of trends in the means) but not significant by nanoindentation. The PII could find these differences because there was less variance in the PII measurements than the nanoindentation measurements. Decreased variability in PII measurements may have been due to the larger indenting tip increasing sampling area for each indent and the greater indentation depth reducing sensitivity to surface roughness. The human dentin study demonstrates that the PII is a suitable device for experimental studies of mechanical properties.

The data presented here demonstrates the potential for the PII as a portable device for instrumented indentation. It may be handheld, runs tests rapidly, and does not require a rigid frame or rigid specimen mounting. It presents new possibilities for nondestructively measuring mechanical properties in the field. In this paper, the PII was used on materials with properties within and outside its designed operating range. Although some problems were found testing materials with high elastic modulus, simple design modifications and proper calibration would likely allow the PII to take accurate measurements in those materials as well. Besides measuring modulus and hardness, the PII may be useful in predicting ultimate strength and ability to absorb impact energy. As with other instrumented indentation devices, it may be possible to obtain other useful metrics as the full load and displacement data are available for analysis.

Table B.1. Material standards tested and their mechanical properties from specifications.

Material	Tensile Modulus of Elasticity (GPa)	Hardness	Ultimate Tensile Strength (MPa)
Aluminum 1100-H14	69	32 Brinell *	124
Aluminum 2011-T3	70	95 Brinell *	379
Aluminum 2024-T4	73	120 Brinell *	448
Aluminum 6061-T651	69	95 Brinell *	310
Aluminum 7075-T651	71	150 Brinell *	572
Copper UNS C11000, H04	124	60 Rockwell B	379
Brass UNS C36000, H02	97	78 Rockwell B	400
Bronze UNS C65500, H02	103	85 Rockwell B	538
Bronze UNS C93200, Cast	100	65 Brinell *	241
Bronze UNS C95400, Cast	110	83 Rockwell B	621
Teflon™, virgin	0.55	50 Shore D	27
High-density polyethylene	1.4	70 Shore D	32
UHMW polyethylene	0.69	66 Shore D	40
PVC - Type I, Grade 1	3.2	89 Shore D	58
Polyoxymethylene (Delrin™)	2.8	85 Shore D	66
Polycarbonate (Lexan™ 9034)	2.4	75 Rockwell M	66
PMMA (Lucite L™)	3.8	100 Rockwell M	75
PMMA (Plaskolite Optix™)	3.4	93 Rockwell M	76
Nylon 6,6	2.9	85 Rockwell M	79

* 500 kg load, 10 mm ball

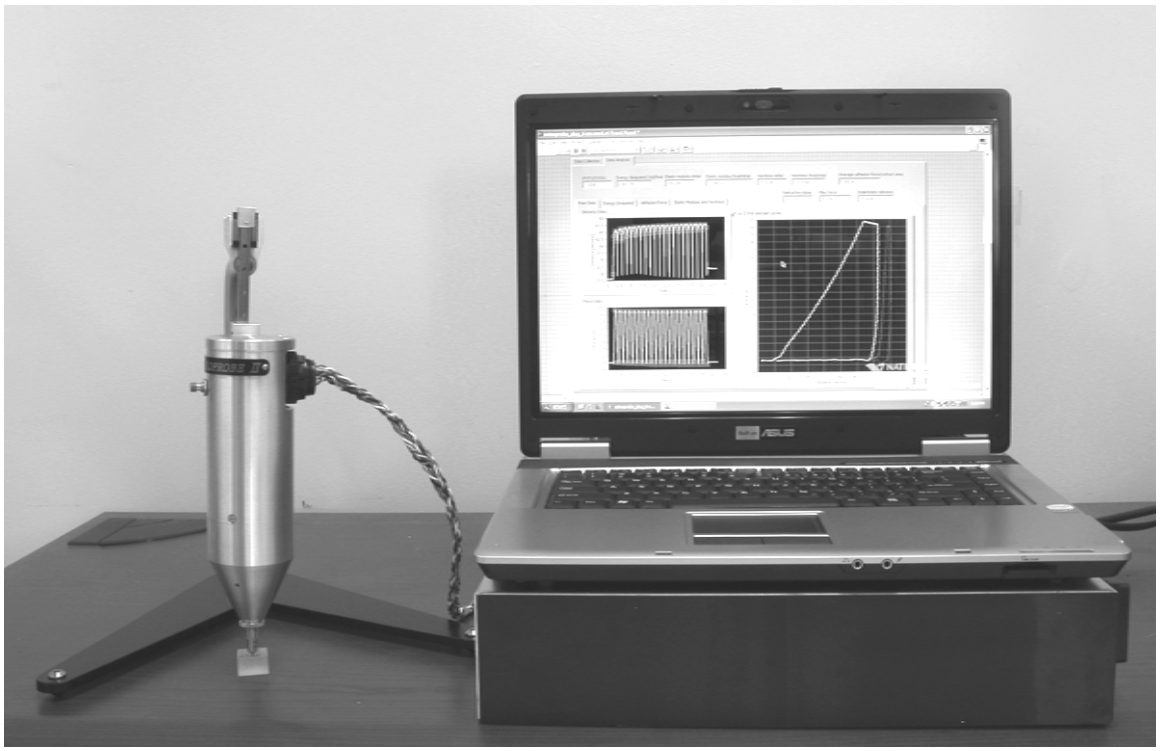

Figure B.1. The Portable Instrumented Indenter consists of a measurement head, an electronics box, and a laptop computer. The electronics box sits under the laptop computer and contains drive electronics for the force generator in the head as well as readout electronics for the force and distance transducers. The laptop computer runs a custom LABVIEW™ program to cycle the current to the force generator and thus move the test probe relative to the reference probe and collect force and distance data.

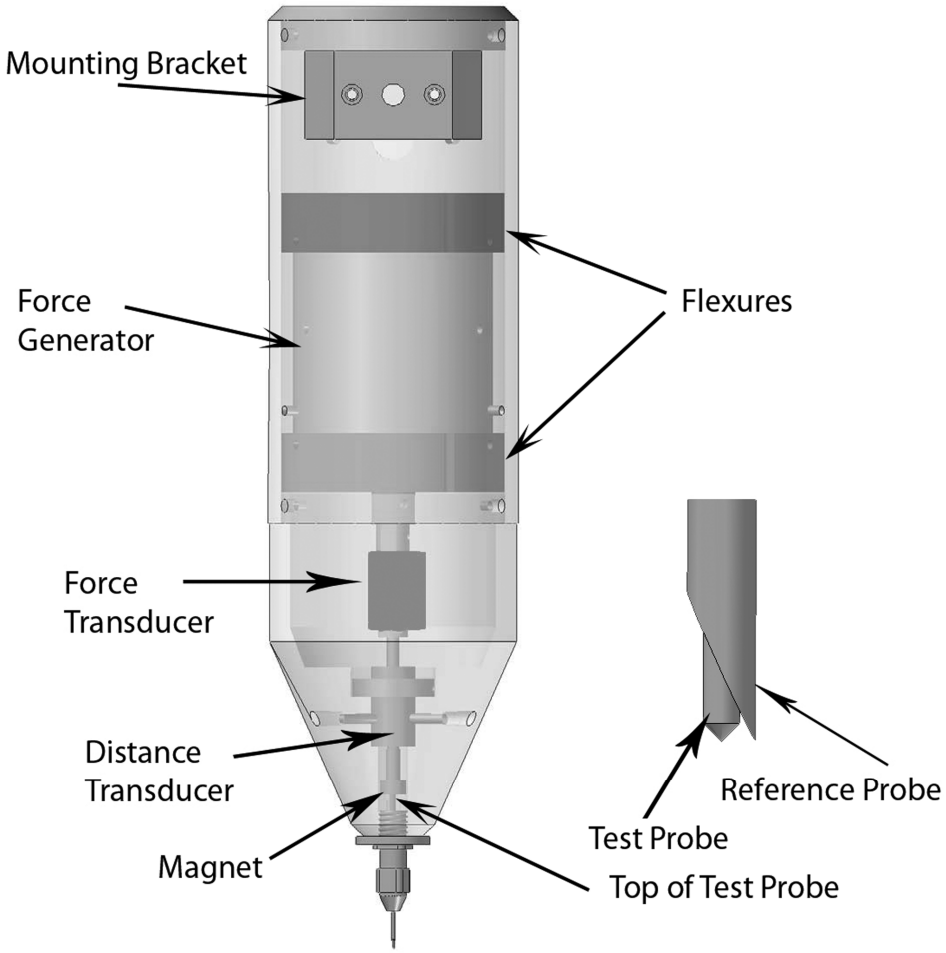

Figure B.2. The Portable Instrumented Indenter uses a force generator to move a test probe relative to a reference probe. The force is monitored by a force transducer. The distance that the test probe moves relative to the reference probe is monitored with a distance transducer. The test probe, which is a ferromagnetic steel alloy, is attached to a magnet in the body of the instrument. The reference probe, which is a modified hypodermic needle, is attached to the body of the instrument with a Luer fitting.

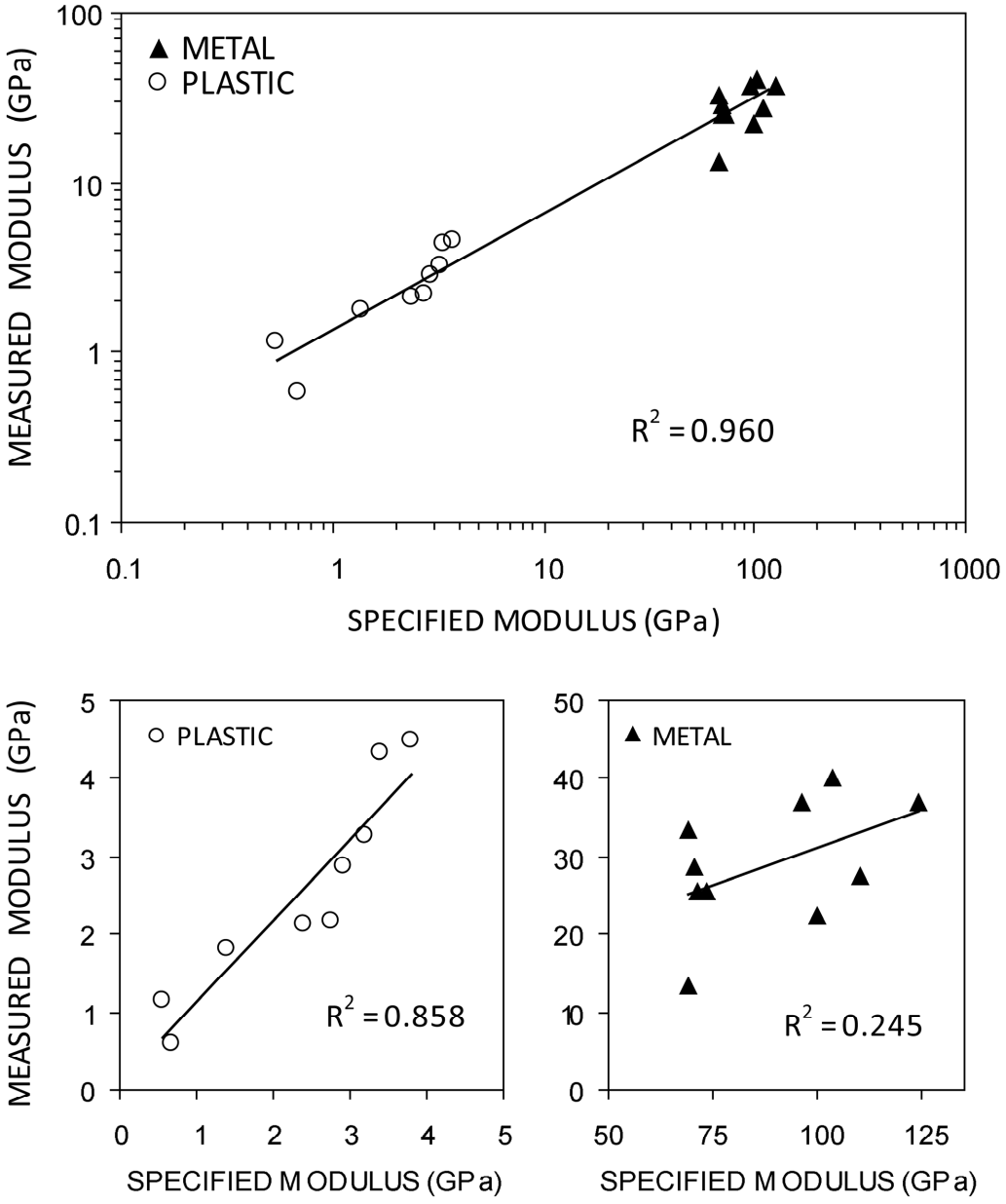

Figure B.3. Over all materials, the regression between tensile elastic modulus and measured modulus by indentation is significant, but has a slope of 0.3. The measurement of low values of modulus (plastics) is accurate, but the accuracy and strength of the regression is reduced for stiffer materials (metals).

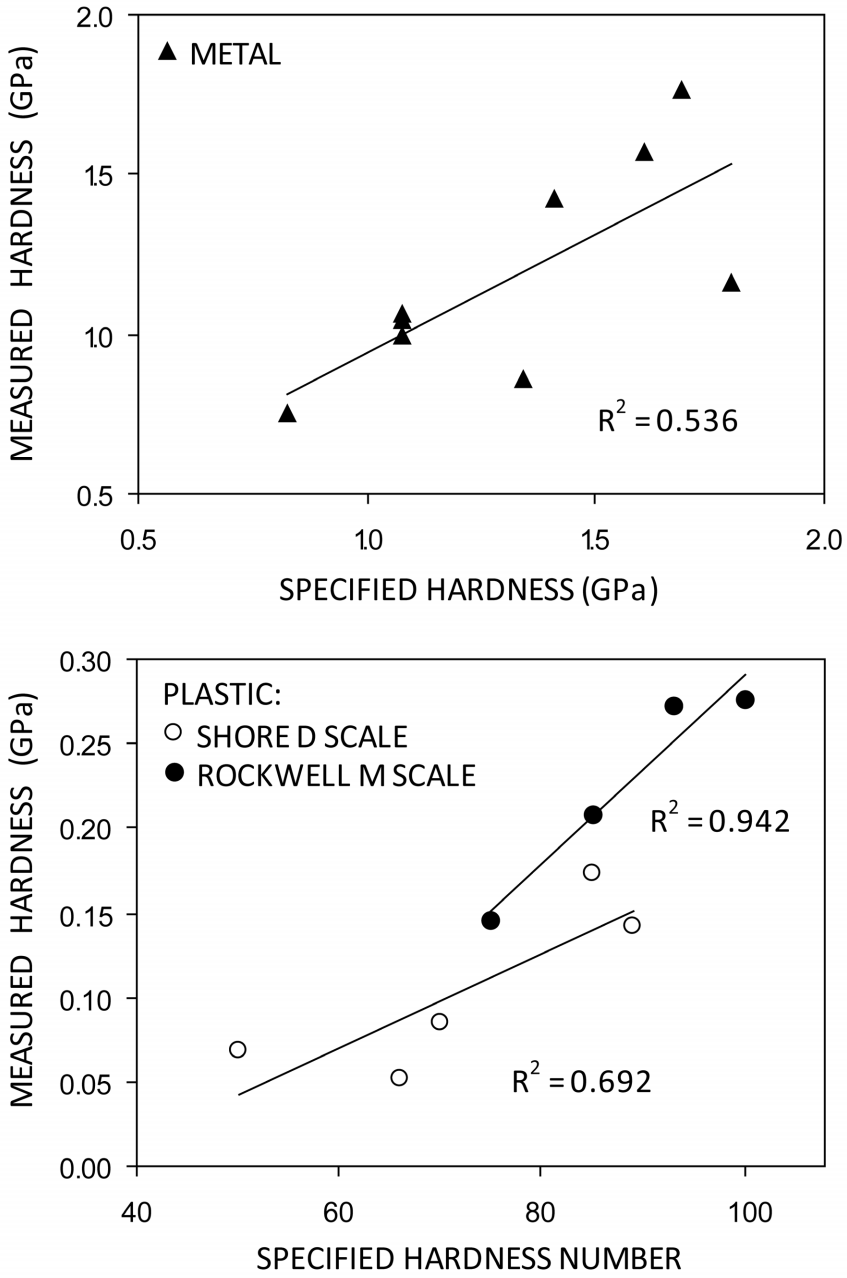

Figure B.4. For metals, hardness is measured well. The regression is strong and the range of values is similar. For plastics, hardness values from material specifications could not be converted to SI units and are therefore shown on their original scales. The measured hardness correlates well with materials measured on the Shore D and Rockwell M hardness scales.

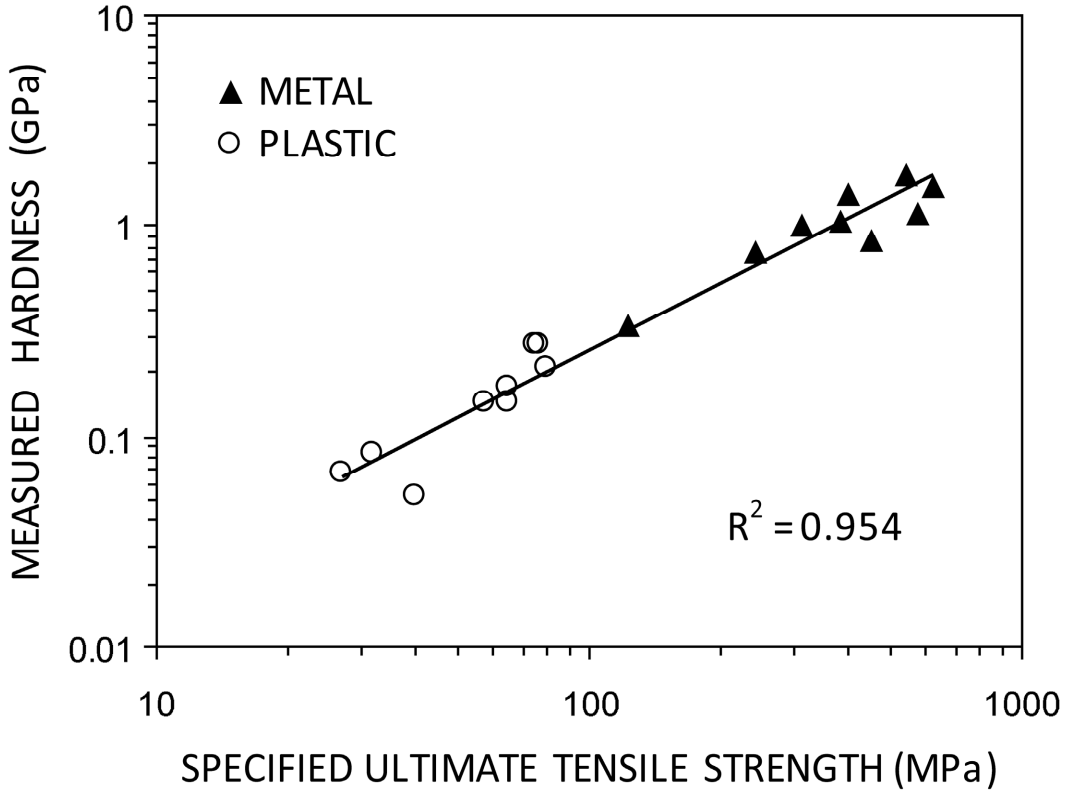

Figure B.5. Measured hardness is significantly correlates with ultimate tensile strength. The regression is strong and continuous through plastics and metals.

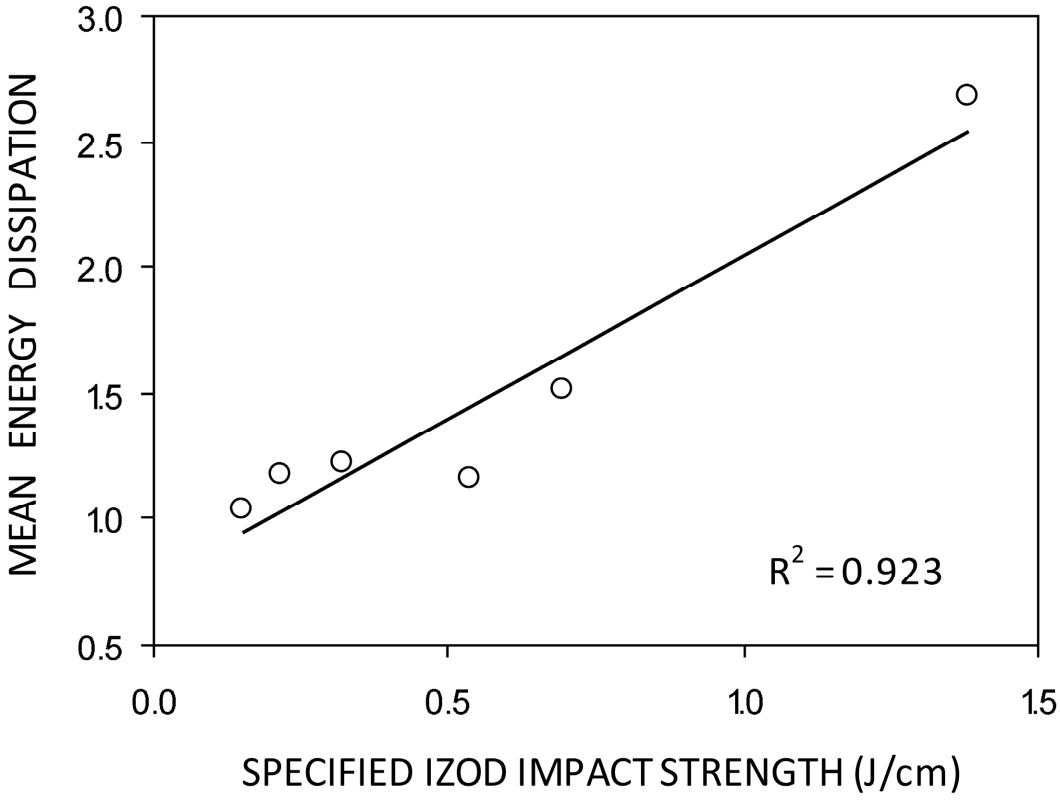

Figure B.6. Mean energy dissipation is significantly correlated with Izod impact energy in plastics.

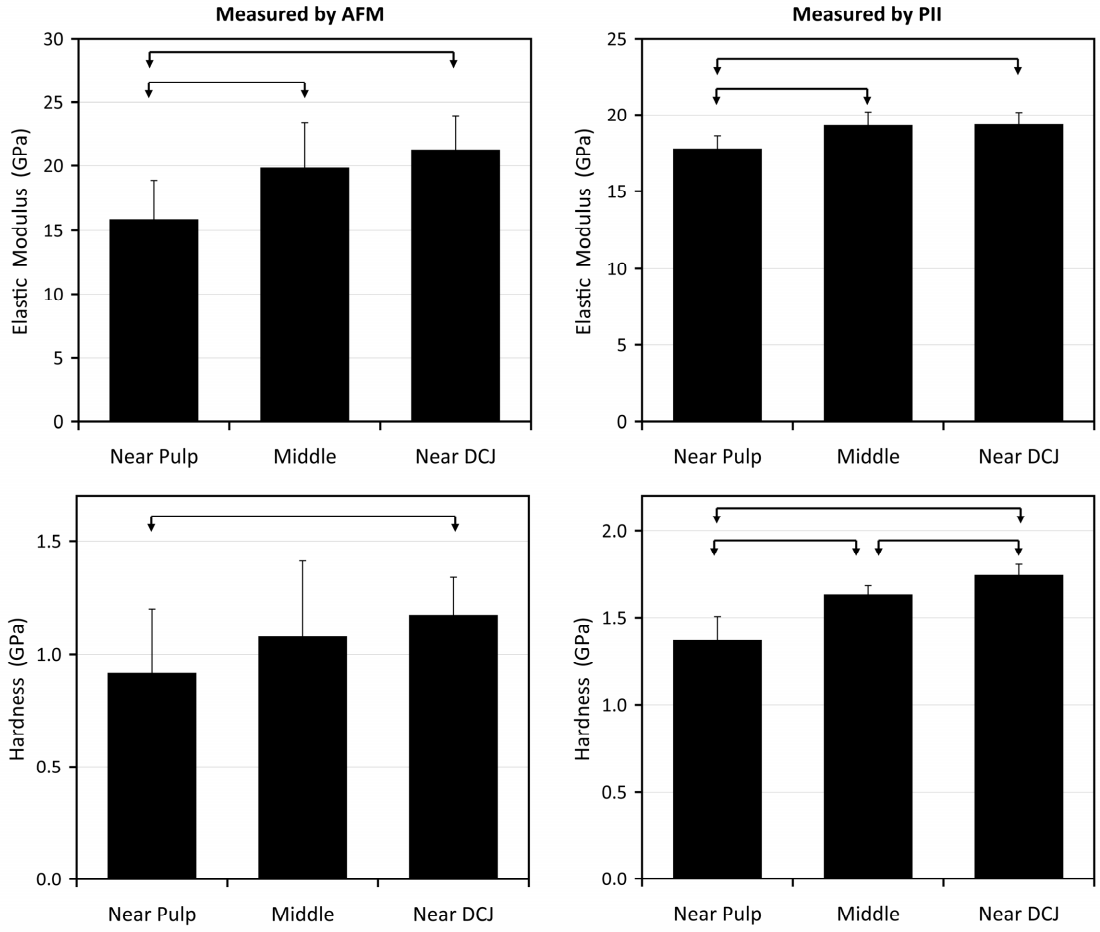

Figure. B.7. Previously dependence of modulus and hardness on radial location within human dentin was measured by nanoindentation. Reevaluating those samples with the PII found the same location dependence. Trends in hardness that were not significant by nanoindentation were significant by PII because of reduced variance (error bars show standard deviation). Arrows indicate significant differences between groups ($p < 0.05$).

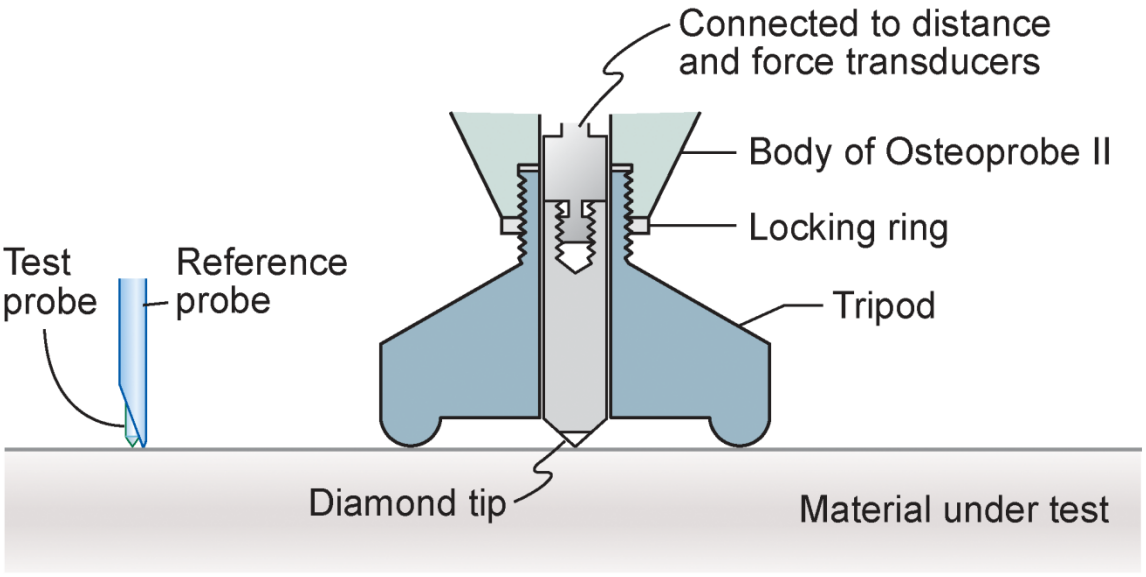

Figure B.8. The PII could be improved as a material tester with some simple modifications. The needle-like reference probe could be replaced by a tripod configuration so that the material surrounding the test area is unloaded. The device could further be improved by using a diamond tip probe attached to a rigid shaft. This shaft could have a greater diameter the previous test probe to make it more rigid. These changes would make the device more suitable for testing materials with high modulus.

1. OLIVER, W. C. & PHARR, G. M. An Improved Technique for Determining Hardness and Elastic-Modulus using Load and Displacement Sensing Indentation Experiments. *J. Mater. Res.* 7(6): 1564-1583 (1992).

2. Oliver, W. C. & Pharr, G. M. Measurement of hardness and elastic modulus by instrumented indentation: Advances in understanding and refinements to methodology. *J. Mater. Res.* 19(1): 3-20 (2004).

3. Hansma, P. K., Turner, P. J. & Fantner, G. E. Bone diagnostic instrument. *Rev. Sci. Instrum.* 77(7): 075105 (2006).

4. Hansma, P. *et al*. The bone diagnostic instrument II: Indentation distance increase. *Rev. Sci. Instrum.* 79(6): 064303 (2008).

5. Tsai, S., Rutherford, R. B., Clarkson, B. H. & Koh, D. H. *Atomic Force Microscopy to Quantify Local Mechanical Properties of Tissue* Proceedings of the Materials Research Society Symposium Ser. 550, Materials Research Society, Warrendale, PA, 1999., Warrendale, PA, 1999).

6. American Society for Metals. in *Metals Handbook* (American Society for Metals, Metals Park, OH, 1979).

7. Holt, J. M., Mindlin, H. & Ho, C. Y. Structural Alloys Handbook. (1996).

8. www.matweb.com.

9. Hoyt, S. L. in *Metal Data* (Reinhold Publishing Corporation, New York, 1952).

10. Fan, Z. F. & Rho, J. Y. Effects of viscoelasticity and time-dependent plasticity on nanoindentation measurements of human cortical bone. *Journal of Biomedical Materials Research Part a* 67A(1): 208-214 (2003).

11. He, L. H. & Swain, M. V. Energy absorption characterization of human enamel using nanoindentation. *Journal of Biomedical Materials Research Part a* 81A(2): 484-492 (2007).

12. Odegard, G. M., Gates, T. & Herring, H. M. Characterization of viscoelastic properties of polymeric materials through nanoindentation. *Exp. Mech.* 45(2): 130-136 (2005).

13. Oyen, M. L. & Cook, R. F. Load-displacement behavior during sharp indentation of viscous-elastic-plastic materials. *J. Mater. Res.* 18(1): 139-150 (2003).

14. Leyland, A. & Matthews, A. On the significance of the H/E ratio in wear control: a nanocomposite coating approach to optimised tribological behaviour. *Wear* 246(1-2): 1-11 (2000).

15. Briscoe, B. J., Fiori, L. & Pelillo, E. Nano-indentation of polymeric surfaces. *Journal of Physics D-Applied Physics* 31(19): 2395-2405 (1998).

APPENDIX C

PROTOCOL FOR MECHANICAL TESTING OF TIBIAE

OVERVIEW

Mechanical testing of murine tibiae is conducted by loading the tibiae under four point bending until failure. Whole-bone mechanical properties are then calculated using a custom written Matlab program. The program also calculates tissue-level mechanical properties by using geometric data from micro-computed tomography (micro-CT) scans of the tibiae to perform estimated transformation of load and displacement to stress and strain by beam bending theory. The process consists of:

- Micro-CT scanning of tibiae
  Protocol previously existed – Orthopedic Research Lab (ORL)
- Four point bend testing
  Protocol previously existed – Biomimetics and Biomechanics Lab
- Microview (micro-CT analysis tool) orientation of scanned tibiae and selection of fracture site region
  Protocol described below
- Calculate geometric properties (by ORL unix scripts) of selected region
  Protocol described below
- Run Matlab program to calculate mechanical properties from testing and geometric data
  Matlab program code shown below

When running the Matlab program, the data files for mechanical testing (.raw), geometric properties (.csv), and geometric traces (.geo) must all be in the same directory. The program will allow you to select the point of failure and two points of the loading slope to define the stiffness and elastic modulus (by linear interpretation of all data points between selected points). All other operations are preformed automatically. The program then outputs a file of mechanical data and a figure showing the load-displacement and estimated stress-strain curves (see Figure C.1 for an example).

- Open file in the old version of MicroView (1.1.15)
    - 0 brings up the axes labels
- Record Bone HU in Excel Sheet - "Plugins" → "Image Information" → check "Bone HU"
- Make sure measurements are in pixels - "Plugins" → "Microview Options" → "Misc" → "Use Measure Unit (mm)" is unchecked.
- Is the bone inverted (proximal should be up)? Enter this in Excel Sheet.
- Scan up/down the bone to a far proximal region. The bone should look like this:

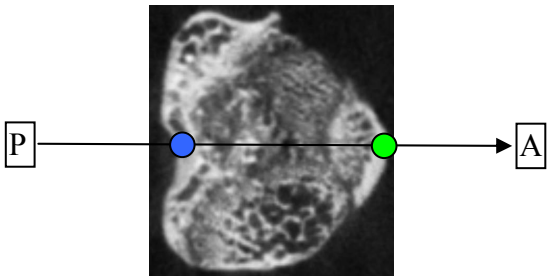

- Put the cursor on the concave notch and hit "1". A **blue** ball should appear.
- Put the cursor on the concave notch and hit "2". A **green** ball should appear. Do this until the newly formed line is oriented parallel to the medial and lateral sides of the bone.
- Hit "i" and "k" to remove y and z axes. Click (with the center button) on the edge of the "j" plane until the border turns red.
- Rotate the plane (while clicking on the edge) and laterally move the plane (while clicking on the plane itself with the middle button) until the plane cuts the green and blue balls in half. The green ball should be on the "new" +X (right) and the blue ball on the "new" –X (left). Use the small images on the right to make sure that the green dot is facing right.
    - This is true whether or not the bone is inverted.
- Hit "F4", click "activate" and hit "5".
- Save as "#_lt_rot.vff"

- Close file

- Open "#_lt_rot.vff." The bone should be oriented with the anterior side to the right (as above).
- Make sure measurements are in pixels - "Plugins" → "Microview Options" → "Misc" → "Use Measure Unit (mm)" is unchecked.
- Scan the bone to find location where the tibia and fibula are first fully joined by bone. Record this location in the Excel Sheet. This will then calculate the next 2 locations you need to mark on the bone.
- Hit F4 and click "Activate."
    - If you forget to activate, the line the connects the blue and green dots in the following 2 steps will be black instead of pink.
- Scan the bone to find the "Distal Alignment" value that is obtained from the Excel sheet. Place the cursor over the most medial part of bone and hit "1" (a large **blue** sphere should appear).
    - Medial will be up if the bone is inverted, down if not.
- Scan the bone to find "Proximal Alignment" value that is obtained from the Excel sheet. Place the cursor over the most medial part of bone and hit "2" (a large **green** sphere should appear).
- Hit "i" and "k" to remove two of the y and z planes
- Move the "j" plane (middle click in plane) until it cuts the **green** sphere in half
- Hit "3" on the "j" plane until a perfect cross is made (click toward the posterior side of the bone) with the j-plane cutting the horizontal part of the cross in half (all 3 spheres on the horizontal part should be sliced in half by the j-plane).
    - This step is the same whether inverted or not.
- Hit "4" to save the image once you are satisfied, save as "#_LT_ rot.vff"
- Close file

- Open "#_LT_rot.vff"
- If things are done properly, the bone should appear with anterior to the left:

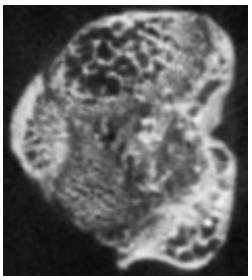

- Now we are trying to remove excess black space from the file to make the file smaller.
- Move the i, j and k planes around until the bone just disappears on each of the axes.
- Put the cursor at the point where the 3 planes come together and hit "7" to form one corner of the region of interest
- Move each plane to the other side of the bone until the bone just disappears.
- Put the cursor at the point where the 3 planes come together and hit "8" to form the second corner of the region of interest - a yellow region of interest box should appear around the bone.
- To ensure you have the bone completely in the region of interest, hit "r", the go to "Plugins" → "Display Isosurface" (or push F6). Change the "Volume Resize Factor" to 1 and lower the threshold to about 1250. Hit "Show" and a 3-D image of the bone should appear. Ensure that the entire bone lies within the yellow region of interest
- Go to "File" → "Save Cropped Region" and save as "#_LT_rot.vff" (replacing the old file you just made a few steps earlier)
- Close file

Convert vff file to be analyzed to 8 bit vff file:

- 4 files required: vff16to8_scale.exe.stackdump
  cygwin1.dll
  vff16to8_scale.exe
  Runme.bat
- Copy these files to the local directory. Right click to edit Runme.bat into this form:
  vff16to8_scale ***sample#_slicename***.vff ***sample#_slicename***_8bit.vff -500 ***1.5*Bone HU***
  stop
- Save and close Runme.bat, then double click the icon to run it.
- This will create a 8.bit file in the local directory named *sample#_slicename_8bit.vff*

Use SSH to connect or Orthopaedic Research Lab (ORL) server
We use the Prozac server: prozac.orl.med.umich.edu
Enter username and password

Open the file transfer window and upload the 8 bit file
Return to the SSH Shell window
Convert the vff file to an ORL file using the vfftoorl command:

prozac% **vfftoorl *sample#_slicename*_8bit.vff *sample#_slicename*.orl 25**

25 is for the voxel size used during the scan.
Next threshold the file to determine what is bone using *thresh-mct*

prozac% **thresh-mct**

Input filename of image to be threshold: ***sample#_slicename*.orl**

Input name for output thresholded file: ***sample#_slicename*.thresh**

The dimensions of the image are:
nx = 94
ny = 70
nz = 125
Enter limits for thresholding (xlims,ylims,zlims): **/**

Input Threshold Estimate, Spread, and Confidence # (defaults = 80,20,2): **100,20,2**

Input % of max-min diff for threshold (default=60): **/**

Enter # of thresh levels allowed (/=50): **/**

The dimensions of the thresholded image will be:
NX = 94 ; NXSIZE = 2350
NY = 70 ; NYSIZE = 1750
NZ = 125 ; NZSIZE = 3125
writing out header (180)...

Reading in data...

Now performing thresholding of data...
Average Threshold is 134 Determined From 14043

Writing out thresholded data...

Total time to threshold image: 1.00 seconds.

Finally run the geometry program, *markgeoplus*

prozac% **markgeoplus**

Enter thresholded image file name: ***sample#_slicename*.thresh**

Enter output file name: ***sample#_slicename*.geo**

Header information for file:

Dimension of image: 94 70 125

Enter zlow and zhigh (default = 1,nz): */*

Enter z-increment (default = 1): */*

Choose side & orientation of specimen scanned:
 0 = Right Side, Anterior Towards Source
 1 = Left Side, Anterior Towards Source
-1 = Left Side, Posterior Towards Source,
Enter Choice (default=0): **Enter *1* for left side or *0* for right side**

Enter threshold level (default=1): */*

Filter image (y=1, n=0; def=0): **1**

Starting analysis to determine the Geometric Parameters...

Reading in data...

Analyzing planes...

Finished finding Geometric parameters...

Now Doing Stats...

Doing regression...

Writing results...

Option: Write centroidal data to file (1=Y,0=N; def=1): **1**

Enter centroidal output file name: ***sample#_slicename*.cent**

Option: Write results data to csv file (1=Y,0=N; def=1): **1**

Enter results csv output file name: ***sample#_slicename.csv***

Enter in specimen number: ***sample#_slicename***

5 new files have now been created: *sample#_slicename*.orl
sample#_slicename.thresh
sample#_slicename.geo
sample#_slicename.cent
sample#_slicename.csv

Transfer these files back to the local computer and then delete them from the server.

```
function [ ]  = mechanics();

% Written by Michael Ron and Nadder Sahar
% University of Michigan, Ann Arbor, MI 48109
% February 15, 2005
%
%Updated 5/8/06 by Joey Wallace to incorporate new method of obtaining
% geomemtric properties from the geo output file from the uCT.

% This program assumes that specimen names are written as "#_RT" or
"#_LT".
% It reads raw mechanical data from a file named "specimen
name_fracture.raw"
% It reads moment of inertia from a file "specimen name_fracture.csv"
% It reads outer fiber length from a file "specimen name_fracture.geo"
%
%
% The program adjusts for system compliance and then uses beam bending
% theory to convert force-displacement data to theoretical stress-
strain
% values.  Mechanical properties are calculated in both domains and
output
% to a file "specimen name_mechanics.csv".  It also outputs a figure
% showing the load-displacement and stress-strain curves with
significant
% points marked.

%close all figure windows and clears all variables
close all
clear all

%*****************\TESTING CONFIGURATION/*************************
%
%       Adjust these values to match the system setup
%
a = 3.01;            %distance between outer and inner load points (mm)
```

```
L = 9.15;            %span between bottom load points (mm)
compliance = 2.299;  %system compliance (microns/N)
%*****************************************************************

%input bone number
number = input('Bone Number: ','s');
letter = input('Right (r) or Left (l) Tibia: ','s');
if letter ~= 'r' && letter ~= 'l'
        error('Please enter an acceptable response of r or l')
end
if letter == 'r'
    letter = 'RT';
end
if letter == 'l'
    letter = 'LT';
end

%Read in raw mechanical testing data
imported_data = csvread([number '_' letter '_fracture.raw'], 12,0);
load = imported_data (:,1);          %in N
position = imported_data (:,5);      %in mm
position = position * 10^3;          %in microns

%Read in MOI from microCT CSV output
CTdata = csvread([number '_' letter '_fracture.csv'], 0,2);
I = CTdata (2);             %Moment of Inertia (mm^4)

% Read in distance from neutral axis to outer most point on medial side
(270
% degrees, side of tension) from microCT GEO output
GEOdata = csvread([number '_' letter '_fracture.geo'],
39,0,[39,0,74,6]);
angle = GEOdata (:,1);          %in degrees
%convert angles to radians
angle_radians = angle.*pi./180;       %in radians
outer_fiber = GEOdata (:,4);          %in mm

%Convert the raw geometric data from angle and radius to x and y
```

```
outer_fiber_x = outer_fiber.*sin(angle_radians);
outer_fiber_y = outer_fiber.*cos(angle_radians);
%Calculate extreme fiber in the medial direction
c = abs(min(outer_fiber_x));          %in mm
c = c * 1000;                         %in microns

%Plot raw data (withot compliance compensation) and choose failure
point
figure (1)
plot (position,load)
xlabel ('Displacement (microns)')
ylabel ('Force (N)')
title ('Pick failure point:')
[x,y]=ginput(1);
hold on
plot(x,y,'ro')

%Find the failure point index
i=1;
while position(i) < x
    i=i+1;
end

%Truncate the data at the failure point
position = position(1:i);
load = load(1:i);

%Adjust position for compliance and set starting position equal to 0.
displacement = position - load*compliance;
displacement = displacement - displacement(1);

%converts the corrected load/displacement data to stress/strain
stress = (load*a*c) / (2*I) * 10^-3;             %MPa
strain = (6*c*displacement) / (a*(3*L - 4*a));   %microstrain

%FAILURE POINT DATA
i = length(load);
fail_load = load(i);
```

```
disp_to_fail = displacement(i);
fail_stress = stress(i);
strain_to_fail = strain(i);

%ULTIMATE LOAD POINT DATA
[ultimate_load,i] = max(load);
disp_to_ult = displacement(i);
ultimate_stress = stress(i);
strain_to_ult = strain(i);
ultimate_index = i;

%Plot the adjusted stress-strain curve and pick points to define
modulus
figure(2)
plot(strain,stress)
axis xy
xlabel('Strain (microstrain)')
ylabel('Stress (MPa)')
title('Pick points to define modulus:')
[x,y] = ginput(2);
hold on
plot(x,y,'ro')

if x(2) < x(1)
    error ('The 2nd selected point must have a larger strain than the
1st selected point')
end


%Create stress and strain vectors spanning region for modulus
determination
i=1;
while x(1) > strain(i)
    i = i+1;
end
linear_strain(1) = strain(i);
linear_stress(1) = stress(i);
```

```
j=2;
while x(2) > strain(i)
    linear_strain(j) = strain(i);
    linear_stress(j) = stress(i);
    i = i+1;
    j = j+1;
end

plot(linear_strain,linear_stress,'r')

%Determine modulus by linear regression of selected points
coeff = polyfit(linear_strain,linear_stress,1);
slope = coeff(1);
modulus = slope * 10^3;                                  % GPa
stiffness = modulus*12*I / (a^2 * (3*L -4*a)) * 10^3;    % N/mm

%Plot linear regression on top of selected region
hold on
linear_stress = slope*linear_strain + coeff(2);
plot(linear_strain,linear_stress,'g')

% Create line with a .2% offset (2000 microstrain)
y_int = coeff(2)-slope*2000;        %y intercept
y_offset = slope*strain + y_int;    %y coordinates of offest line


%Find indeces where the line crosses the x-axis and the stres-strain
curve.
%Then truncates offset line between those points
for j = 1 : length(y_offset)
    if y_offset(j) <= 0
        i=j+1;
    end
    if y_offset(j) >= stress(j)
        break
    end
end
x_offset = strain(i:j);
```

```
y_offset = y_offset(i:j);
plot(x_offset,y_offset, 'k')


%YIELD POINT DATA
if j > ultimate_index
    j=ultimate_index;
end
yield_load = load(j);
disp_to_yield = displacement(j);
yield_stress = stress(j);
strain_to_yield = strain(j);
yield_index = j;

%Get postyield deformation/strain
postyield_disp = disp_to_fail - disp_to_yield;
postyield_strain = strain_to_fail - strain_to_yield;


%**********************************************************************
%Find pre and post yield energies and toughnesses
%Divide curves up into pre- and post-yield regions.
strain1 = strain(1:yield_index);
stress1 = stress(1:yield_index);
load1 = load(1:yield_index);
displacement1 = displacement(1:yield_index);

%Calculate areas under curves
preyield_toughness = trapz(strain1,stress1) / 10^6;            % In MPa
total_toughness = trapz(strain,stress) / 10^6;
postyield_toughness = total_toughness - preyield_toughness;

preyield_work = trapz(displacement1,load1) / 10^3;             % In mJ
total_work = trapz(displacement,load) / 10^3;
postyield_work = total_work - preyield_work;


%**********************************************************************
```

```
%Plot final graphs of stress/strain
figure(3)

%Stress-strain plot
subplot(2,1,1)
plot(strain,stress)
axis xy
xlabel('Strain (microstrain)')
ylabel('Stress (MPa)')
hold on
plot(linear_strain,linear_stress,'r')
plot(x_offset,y_offset, 'k')
plot(strain_to_yield, yield_stress, 'k+', strain_to_ult,
ultimate_stress, 'k+', ...
     strain_to_fail, fail_stress, 'k+')

%Load-displacement plot
subplot(2,1,2)
plot(displacement,load)
axis xy
xlabel('Displacement (microns)')
ylabel('Force (N)')
hold on
plot(disp_to_yield, yield_load, 'k+', disp_to_ult, ultimate_load, 'k+',
...
     disp_to_fail, fail_load, 'k+')

specimen_name = [number '_' letter];


%**************************** OUTPUT *********************************

% Saves an image of figure 3 (sumary of mechanical properties)
print ('-dpng', specimen_name)

% Writes values for mechanical properties to a csv file
results = [specimen_name ',' num2str(yield_stress) ','
num2str(ultimate_stress) ',' ...
```

```
        num2str(fail_stress) ',' num2str(strain_to_yield) ','
num2str(strain_to_ult) ',' ...
        num2str(strain_to_fail) ',' num2str(postyield_strain) ','
num2str(yield_load) ',' ...
        num2str(ultimate_load) ',' num2str(fail_load) ','
num2str(disp_to_yield) ',' ...
        num2str(disp_to_ult) ',' num2str(disp_to_fail) ','
num2str(postyield_disp) ',' ...
        num2str(modulus) ',' num2str(stiffness) ','
num2str(preyield_work) ',' ...
        num2str(postyield_work) ',' num2str(total_work) ','
num2str(preyield_toughness)',' ...
        num2str(postyield_toughness) ',' num2str(total_toughness)];

dlmwrite([specimen_name '_mechanics.csv'], results, '')
```

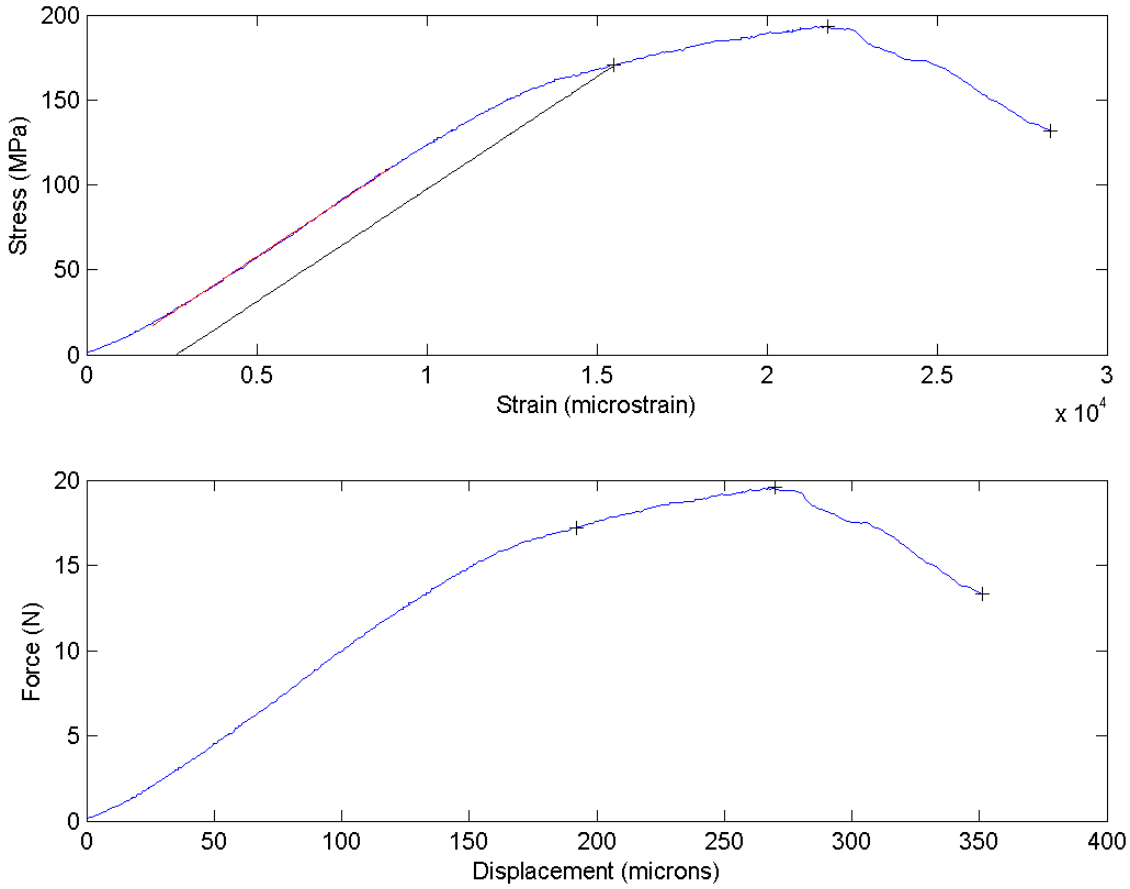

Figure C.1. Example of force-displacement and estimated stress-strain curves from a four point bend test of a tibia. This graph is automatically produced by the Matlab program. The points of yield, ultimate force/stress, and failure are indicated on the graphs and output to a file. The program also calculates stiffness/modulus, and pre-yield, post-yield and total work/toughness.

APPENDIX D

PROTOCOL FOR STAINING & QUANTIFICATION OF MICRODAMAGE

STAINING DAMAGE *EN BLOC*

This protocol is for murine bone and was developed using tibia. It is based on the protocol by D.B. Burr & M. Hooser (Bone 1995). If larger bones or more dense bones are used, staining and infiltration times must be increased. Also, for larger bones, the bone should be sectioned into a smaller segment prior to starting this protocol.

Supplies

3 large amber jars with screw tops
Stir rods
2 dram amber vials (2 per bone)
Breakaway plastic embedding cubes
Basic Fuchsin from JT Baker
Clear-Rite 3
KoldMount liquid monomer
KoldMount powder

Prepare Staining Solutions

Make solutions in glass jars with lids. Keep lid on to prevent evaporation and leave on the stir plate for at least several hours because fuchsin does not easily dissolve in ethanol. Fuchsin dissolves more easily in water (i.e. the 80% and 90% solutions will dissolve more easily than the 100% solution).

Make these three solutions ahead of time in amber jars to minimize light exposure. The solutions have a shelf life of 1-2 months if kept in the fridge. These volumes are good for 7-10 bones – adjust as needed:

- 1% Basic Fuchsin in **80%** EtOH

Basic Fuchsin	1.0 g
Ethanol	80 ml
Distilled water	20 ml

- 1% Basic Fuchsin in **90%** EtOH

Basic Fuchsin	1.0 g
Ethanol	90 ml
Distilled water	10 ml

- 1% Basic Fuchsin in **100%** EtOH

Basic Fuchsin	1.0 g
Ethanol	100 ml

Staining/Dehydration

Staining in graded ethanol solutions serves to both stain and dehydrate the bones.
Put each bone in a 2 dram amber vial and label carefully.
To prepare the bones, store in 70% ethanol overnight.

Staining procedure:

- Fill vials about 2/3 full with staining solution
- Allow 1 hour of stain time per step

- Stain under vacuum (~19 psi), room temperature
- Vacuum pipet old solution and refill vial with new solution
- If the staining procedure must be interrupted, the bones can be held indefinitely in the current ethanol concentration without stain
- Bones should be stained according to the following schedule (6 hours total):
    - 2 changes of **80%** solution
    - 2 changes of **90%** solution
    - 2 changes of **100%** solution

After staining, wash bones in 100% ethanol.
Transfer bones into clean vials and store in 100% ethanol overnight to clear excess stain and to complete dehydration.

Infiltration, Embedding, and Sectioning

Clear the bone:

- Replace ethanol in vial with Clear-Rite 3
- Keep under vacuum and room temperature
- Allow bone to be cleared for 2-4 hours

Infiltration:

- Infiltrate under vacuum and room temperature
- Fill vials with KoldMount liquid monomer
- Infiltrate for 3 days, changing solution every day

Embed

- Stand tibia straight up in the corner of a plastic embedding cube. Position the tibia so that the curve of the tibia is towards the inside.
- Glue the distal end to the bottom of the cube and the proximal end to the side.
- **The rest of the embedding process must be done under a fume hood**

- In separate falcon tubes measure out 2 parts KoldMount powder and 1 part liquid monomer. Mix the two and stir thoroughly.
- Wait until the solution starts to thicken (a couple minutes) and then pour into the molds.
- Let sit for at least an hour

Section/Polish (~150 microns thick)

- Break plastic blocks out of the molds
- Mark the location for sectioning on the block. It is easiest to measure this distance from the distal end of the bone since it should be flush with the bottom of the block.
- Cut a section roughly 120-150 microns thick. This corresponds to roughly one full turn of the micrometer
- Glue section to a microscope slide. Label the backside of the slide using labeling tape.
- Polish the slide using 1200 or 3200 grit sandpaper under water. When finished the polished plastic should be smooth and clear. It should have a final thickness of 90-125 microns.
- When polishing, try to ensure that the section has uniform thickness.

QUANTIFYING MICRODAMAGE WITH LASER SCANNING CONFOCAL MICROSCOPY

Slide preparation

- Mount a coverslip on the specimen using a small amount of immersion oil
    - The coverslip should be 125-170 microns thick.
    - The refractive index of the coverslip and immersion oil should be matched as closely as possible (likely n=1.518).
    - Try to minimize the amount of oil used to mount the cover slip.
- Place the slide in the microscope so that the side with specimen faces the objective.

- When using an immersion objective, use the same immersion oil that was used for mounting the coverslip.

Image Collection

- Start with a 10X objective and use the eyepiece.
- Once the bone is in focus, rotate the slide so that the anterior direction faces 180 degrees (left).
- Switch the capture method to the computer. Start a continuous capture and manually adjust the focus to point of greatest excitation.
- Adjust the iris, gain, and, offset until bone features (canaliculi, osteocytes, cracks, etc.) become clear with little background.
- Capture an image of the entire bone cross section. It may be necessary to take 2 or 3 images to cover the whole bone area.
- Switch to a 60X objective and pan the entire bone area for microcracks and diffuse damage.
    - Microcracks are typically longer and larger than canaliculi and smaller than blood vessels. Often they can be seen as a halo around a dark area (the actual crack). It is helpful to pan the focus up and down through the section to distinguish cracks from other features.
    - Diffuse damage appears as an undistinguishable, cloudy area of stain.
- Capture images from any areas that contains microdamage. Using image analysis software measure crack lengths and diffuse damage areas.
- Calculate the following properties:
    - crack number = number of cracks in the cross section
    - total crack length = total length of all cracks
    - average crack length = total crack length / crack number
    - crack # density = number of cracks / cross sectional area of the section
    - crack density = crack length / cross sectional area of the section
    - damage area = total diffuse damage area
    - diffuse damage density = damage area / cross sectional area of the section

APPENDIX E

RAMAN - NANOINDENTATION PROTOCOL

SECTIONING AND POLISHING

1. Thaw bone
2. Remove 10 mm longitudinal section from the mid-diaphysis of the femurs using a low-speed sectioning saw. This section should start near the proximal end of the trochanter and run 10 mm distally
3. Flush marrow (use pipe cleaner)
4. Glue sample, posterior side down, to a plastic slide using a viscous cyanoacrylate glue
5. After 10 minutes, rewet sample with Ca buffer
6. Attach sample/plastic slide to the specimen holder using adhesive tab
7. With specimen holder and polishing wheel, polish sample with a rigid polishing cloth and a 3 μm diamond suspension (Buehler, Inc.) to create a flat surface on the anterior side of the bone that was parallel to the plastic slide
8. Next use a soft, low nap polishing cloth with a 0.05 μm alumina suspension (Buehler, Inc.) to increase the smoothness of that surface. In total, a depth of approximately 20-30 μm was removed from the anterior surface of each bone
9. Ultrasonically clean for ~ 20 sec in beaker. Immediately transfer samples to a beaker of clean Ca buffer
10. Put beaker on ice

STAMPING

1. Check PDMS stamp under microscope – should be clean, no ink residue
2. Attach stamp to glass slide with double sided tape
3. Roll out ***small*** amount of ink on glass using rough ink roller
4. Prepare bone for stamping
    a. Gently dry surface
    b. Clear surface with compressed air
    c. Put two fine ink marks in line with desired stamp location (to help guide stamping)
5. Roll smooth roller on glass to cover with thin layer of ink
6. Roll inked roller over stamp
7. Check stamp on microscope for proper inking:
    a. Full coverage of pattern
    b. No ink in wells
    c. Ink should not be withdrawing/pooling due to surface tension
8. Use tape to remove ink from above and below pattern so that stamp can be seen through during alignment
9. Place stamp/slide and bone sample in stamping device
10. Bring stamp close to bone surface and align the stamp pattern with ink marks
11. Stamp bone by briefly pressing stamp holder down to bone, then releasing
12. Remove bone, check pattern under microscope. If pattern is not acceptable, immediately remove with water and kimwipe. *Let ink dry for at least 2 hours.*
13. If stamping another bone, check stamp for ink in well. If cleaning is necessary, wet with 100% ethanol and gently wipe with kimwipe. Wash with plenty of water and dry.

Two important considerations:

- Maintenance of sample
  - Keep hydrated in Ca Buffer
  - Minimize thawed time
  - Do not rapidly change temperature (i.e. putting a room temp water on a cold sample or cold water on a room temp sample)
- Maintenance of stamp
  - Do not rub surface
  - Never apply alcohol to the bone

1. Thaw samples
   - Allow samples to completely thaw at *room temperature*.
   - Only thaw as many samples as you need at a time.

2. Chose one of the two markers to use.

Considerations in choosing marker:

- The quality of the marker
  - Which marker is more clear and appropriately shaped?
  - There should be no ink or pen markings inside the marker.
- The quality of the bone surface within the markers
  - Smoothly polished and flat

- No major defects, holes

Take a picture of the marker to be used. Filename should have the specimen number in it.

3. Collect Raman spectra:
   - Use a polarization scrambler
   - Use the 60X water immersion objective
   - Sample should be submerged in Ca Buffer
   - Take Spectra and name as follows:

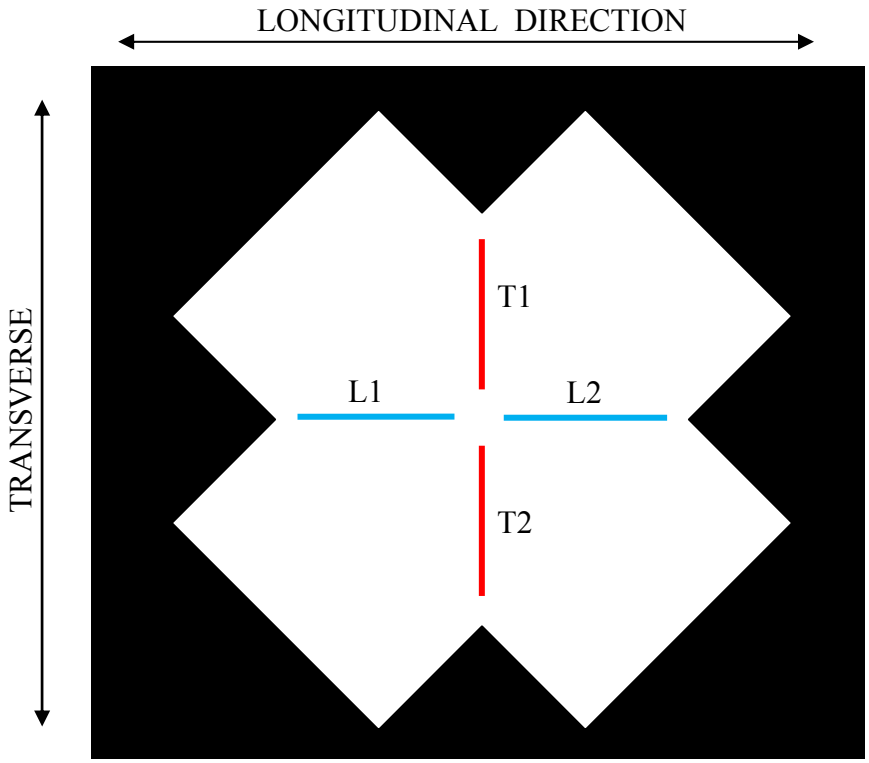

   - Label the spectra as follows:
     Specimen#_Line#
     Example: 54RF_L1

4. Refreeze samples
    - Keep sample wet with Ca buffer
    - Wet gauze in Ca buffer and place over sample
    - Freeze in -20 C freezer

```
function indent_analysis()

clear all
close all


%******* Default variables ****************************************
% These are the default variables and correction factors for
calculating
% modulus and hardness with a berkovich tip indenter.
% These values should not need changing except for the nu_sample.
% MAKE SURE THE POISSON RATIO IS APPROPRIATE FOR YOUR TEST SAMPLE

global epsilon beta_factor E_tip nu_tip nu_sample percent
epsilon = 0.75;      % Shape factor for calculating sink-in
                     % (0.75 is standard for a Berkovich tip)
beta_factor = 1.034; % Fudge factor for (1.034 standard for Berkovich
tip)
E_tip = 1141;        % Elastic modulus of diamond tip (1141 GPa
standard)
nu_tip = 0.07;       % Poisson Ratio of the diamond tip (0.25 standard)
nu_sample = 0.3;     % Assumed Poisson Ratio for sample (0.3 is common
for bone)
percent = 0.9;       % Percent of unloading curve to fit

%*****************************************************************

%input experiment series identifier
name = input('Base name of series to analyze: ','s');
disp(' ')

%Find all indent files that belong to the series
d = dir([name '.*']);


% Setup header row for output file
results = ['Sample, Indent Name, Indent Number, Indent Loading, '...
'Modulus (GPa), Contact Hardness (GPa), True Hardness (GPa), '...
'Max Load (mN), Displacement at Peak Load (nm), '...
'Creep Displacement (nm), Maximum Displacement (nm), '...
'Creep Modulus - Parallel (GPa), Creep Viscosity - Parallel (GPa-s),
'...
'Creep Viscosity - Series (GPa-s), Time Constant (s), ' ...
'Work to reach depth, Total Work, Plasticity Index,' ...
'Unloading Stiffness (mN/nm), Contact Area (um^2), '...
'alpha (unloading power law), m (unloading power law), Residual Depth
(nm), '...
'R-squared of Unloading Curve Fit, R-sqaured of Creep Fit'];


% Run analysis program for each indent within the series.
% The analysis program is called by "nano_anlysis" below
```

```
for i=1:length(d)
    clear sample extension data header
    [dummy1 dummy2 extension dummy3] = fileparts(d(i).name);
    sample = name(4:length(name));  % Truncate 'TDS' from indent name
    extension = extension(2:4);
    disp(['Working on ' name '.' extension '...'])
    header = [sample ', ' name '.' extension ', ' extension(3) ', '];
    header = strvcat(header, [sample ', ' name '.' extension ', '
extension(3) ', ']);
    data = nano_analysis(name,extension);
    header_data = strcat(header, data);
    results = strvcat(results, header_data);
end

disp('Done!')

dlmwrite([name '_analysis.csv'], results, '')




%-------------------------------------------------------------------------
% Area function for indenting tip
% The constants for this function are determined from tip calibration.
% They should be checked for each tip and rechecked over time.

function A = area_function(h)

C0 = 24.5;
C1 = 424.56;
C2 = 0.0067577;
C3 = 0.044573;
C4 = 0.020239;
C5 = 0.027849;
C6 = 0.013737;
C7 = 0.011224;
C8 = 0.0060482;

A = C0*h^2 + C1*h^1 + C2*h^(1/2) + C3*h^(1/4) + C4*h^(1/8) + ...
    C5*h^(1/16) + C6*h^(1/32) + C7*h^(1/64) + C8*h^(1/128);

%-------------------------------------------------------------------------




%-------------------------------------------------------------------------
% Power law function for fitting unloading curves
% Normal form is P = alpha*(h - h_final)^m
% Rearranged and set C = alpha^1/m for easier numeric solving of
equation

function h = unloading_model(Beta,P)

C = Beta(1);
```

```
m = Beta(2);
h_final = Beta(3);

h = 1/C * P .^ (1/m) + h_final;
%-------------------------------------------------------------------------




%-------------------------------------------------------------------------
% Model for creep during hold after step load.

function displacement = maxwell_voigt_model(Beta,X)

% Combined Maxwell-Voigt model for creep displacement.
% Model starts after instantaneous dispcalement from step load.
% The model is comprised of a spring and dashpot in parrallel with a
% another dashpot in series to model steady-state creep.

% Equivalent cone semi-angle of Berkovich indenter
alpha = deg2rad(70.3);

Ep = Beta(1);       % Elastic modulus of parallel spring (GPa)
ETAp = Beta(2);     % Viscosisty of parallel dashpot (GPa-s)
ETAs = Beta(3);     % Viscosisty of series dashpot (GPa-s)
P0 = X(:,1);        % Max load (mN)
t = X(:,2);         % time (sec)

% disp_squared = displacement of model (10^-12 m^2)
disp_squared =  pi()/2*P0*cot(alpha) .* ((1 - exp(-t*Ep/ETAp))./Ep +
t./ETAs);

% displacement in nanometers
displacement = disp_squared .^0.5 * 10^3;
%-------------------------------------------------------------------------




%*************************************************************************
%*************************************************************************
%*************************************************************************
%-------------------------------------------------------------------------
function text_output = nano_analysis(name,indent_number)
% Main analysis program (calls previously defined functions)

global epsilon beta_factor E_tip nu_tip nu_sample percent

% Set whether figures will be visible on screen
visibility = 'off';

%Read in load-displacement data
```

```
imported_data = csvread([name '.' indent_number], 1,0);
subfile = imported_data(:,1);        % segment of indent profile
disp = imported_data(:,3);           % Displacement (nm)
load  = imported_data(:,4);          % Load (mN)
time = imported_data(:,5);           % Time (seconds)
stiff = imported_data(:,6);          % Material stiffness (N/m)


% ********************************************************************
% Find break points between loading, hold, and unloading
% Assumes the following subfiles
%  1 = Approach
%  2 = Loading
%  3 = Hold at max
%  4 = Unloading
%  5 = Hold near bottom for thermal drift correction
%  6 = Complete unloading
%  7 = Short hold while unloaded
%  8 = Step Loading
%  9 = Hold after step loading
% 10 = Complete Unloading


% Find start of loading segment
i = 1;
while(subfile(i) <= 1)
    i = i+1;
end
start2 = i;

% Find start of hold segment
i = 1;
while(subfile(i) <= 2)
    i = i+1;
end
start3 = i;

% Find end of hold segment
while(subfile(i) == 3)
    i = i+1;
end
end3 = i-1;

% Find end of first unloading segment
while(subfile(i) == 4)
    i = i+1;
end
end4 = i-1;


% Find end of complete unloading
while(subfile(i) <= 6)
    i = i+1;
end
end6 = i-1;

% Find end of hold after complete unloading
```

```
while(subfile(i) <= 7)
    i = i+1;
end
end7 = i-1;

% Find start of hold after step loading
while(subfile(i) < 9)
    i = i+1;
end
start9 = i;

% Find end of hold after step loading
while(subfile(i) == 9)
    i = i+1;
end
end9 = i-1;

% Find end of 2nd unloading
end10 = length(subfile);

%**************************************************************************



%**************************************************************************
% Create a figure showing L vs d, L vs t, and d vs t
figure(1)
set(gcf,'Visible',visibility)

% First plot showing load vs displacement
subplot(211)
plot (disp,load,'.')
xlabel ('Displacement (nm)')
ylabel ('Load (mN)')
% Ensure y-axis starts at 0
%V = axis;
%V(3) = 0;
axis([0 5000 0 75])
title(['Indent ' name '.' indent_number])

% Second plot shows load vs time AND displacement vs time
subplot(212)
[AX,H1,H2] = plotyy(time,disp,time,load);

% Set limits of displacement y-axis and line properties
V = axis(AX(1));
V = [V(1), V(2), 0, 1.5*disp(start9)];
axis(AX(1), V)
ylabel(AX(1),'Displacement (nm)')
set(H1,'LineWidth', 1)
XL = xlim;

% Add horizontal line at disp = 2000 nm (the desired depth of
indentation)
line(XL,[2000 2000], 'Color','b', 'LineStyle',':', 'LineWidth',1)
```

```
% Set limits of load y-axis and line properties
V(4) = 1.5*load(start9);
axis(AX(2), V)
ylabel(AX(2),'Load (mN)')
set(H2,'LineStyle','--','LineWidth',1.5)
xlabel('Time (sec)')

% Add legend and save the figure as a png image
legend([H1 H2],'Displacement','Load','Location','NorthWest')

%**********************************************************************



%**********************************************************************
% Determine unloading stiffness for both unloadings
% Percent defines the percentage of the unloading curve to fit and is
% defined with global variables near the beginning of the program.


% Fit unloading curve 1
%----------------------------------------------------------------------

% Define the portion of the unloading curve to fit.
% The first point is defined as the point of maximum displacement
% (not the start of unloading) to account for any "nose" during
unloading.
[h_max i_start] = max(disp(end3:end4));
i_start = end3 + i_start - 1;
i_end = ceil((end4-i_start)*percent) + end3;

unloading_d = disp(i_start:i_end);
unloading_P = load(i_start:i_end);

% Initial guess for power law fitting parameters: [alpha, m, h_final]
Beta0 = [0.002 1.6 disp(end6)];

% Fit unloading curve to power law function defined in "unloading
model"
[betas residuals] = nlinfit(unloading_P, unloading_d, @unloading_model,
Beta0);

C = betas(1);
m1 = betas(2);
h_final1 = betas(3);
alpha1 = C^m1;

% Calculate R-sqaured value from residuals
SSE = residuals' * residuals;
SST = (unloading_P - mean(unloading_P))' * (unloading_P -
mean(unloading_P));
R2_unload1 = 1 - SSE/SST;

% Determine unloading stiffness by using the derivative of the
% power law function
%d_max = unloading_model(betas, max(unloading_P));
```

```
S1 = m1*alpha1*(h_max - h_final1)^(m1-1);

% Add line showing unloadins stiffness to the load-displacement plots
subplot(211)
hold on
d0 = unloading_d(1) - unloading_P(1)/S1;
line([d0 unloading_d(1)],[0 unloading_P(1)], 'Color','k',
'LineStyle','-', 'LineWidth',1)


% Fit unloading curve 2
%--------------------------------------------------------------------

% Define the portion of the unloading curve to fit.
% The first point is defined as the point of maximum displacement
% (not the start of unloading) to account for any "nose" during
unloading.
% Fit to "perecent*0.9" to match unloading curve 1, which only
% unloads to 90%.
[h_max i_start] = max(disp(end9:end10));
i_start = i_start + end9 - 1;
i_end = ceil((end10-i_start)*percent*0.9) + end9;

unloading_d = disp(i_start:i_end);
unloading_P = load(i_start:i_end);

% Initial guess for power law fitting parameters: [alpha, m, h_final]
Beta0 = [0.002 1.6 disp(end10)];

% Fit unloading curve to power law function defined in "unloading
model"
[betas residuals] = nlinfit(unloading_P, unloading_d, @unloading_model,
Beta0);

C = betas(1);
m2= betas(2);
h_final2 = betas(3);
alpha2 = C^m2;

% Calculate R-sqaured value from residuals
SSE = residuals' * residuals;
SST = (unloading_P - mean(unloading_P))' * (unloading_P -
mean(unloading_P));
R2_unload2 = 1 - SSE/SST;

% Determine unloading stiffness by using the derivative of the
% power law function
%d_max = unloading_model(betas, max(unloading_P));
S2 = m2*alpha2*(h_max - h_final2)^(m2-1);

% Add line showing unloadins stiffness to the load-displacement plots
subplot(211)
hold on
d0 = unloading_d(1) - unloading_P(1)/S2;
line([d0 unloading_d(1)],[0 unloading_P(1)], 'Color','k',
'LineStyle','-', 'LineWidth',1)
hold off
```

```
% Save an image of the load-displacement figures
saveas(gcf, ['L_D ' name '_' indent_number], 'png')



%*********************************************************************
% Determine elastic modulus and contact hardness

% Indent 1
hc1 = disp(end3+1) - epsilon * load(end3+1)/S1;     %Contact depth (nm)
Ac1 = area_function(hc1) * (10^-9)^2;               %Contact area (m^2)
Hc1 = load(end3+1)*10^-3 / Ac1;                     %Contact hardness
(Pa)
Hc1 = Hc1 * 10^-9;                                  %Contact hardness
(GPa)
Eeff1 = (S1*10^6)*pi^0.5 / (2*beta_factor*Ac1^0.5); %Effective modulus
(combined tip and sample)
Eeff1 = Eeff1 * 10^-9;                              %Effective modulus
in GPa
E1_plane = (Eeff1^-1 - (1 - nu_tip^2)/E_tip)^-1;   %Plane strain
elastic modulus of the sample
E1 = E1_plane * (1 - nu_sample^2);                  %Elastic moduls of
the sample

% Indent 2
hc2 = disp(end9+1) - epsilon * load(end9+1)/S2;     %Contact depth (nm)
Ac2 = area_function(hc2) * (10^-9)^2;               %Contact area (m^2)
Hc2 = load(end9+1)*10^-3 / Ac2;                     %Contact hardness
(Pa)
Hc2 = Hc2 * 10^-9;                                  %Contact hardness
(GPa)
Eeff2 = (S2*10^6)*pi^0.5 / (2*beta_factor*Ac2^0.5); %Effective modulus
(combined tip and sample)
Eeff2 = Eeff2 * 10^-9;                              %Effective modulus
in GPa
E2_plane = (Eeff2^-1 - (1 - nu_tip^2)/E_tip)^-1;    %Plane strain
elastic modulus of the sample
E2 = E2_plane * (1 - nu_sample^2);                  %Elastic moduls of
the sample


% Calculate true hardness based on work by ML Oyen, 2006, J of
Biomechanics
a1 = 24.5;
a2 = 4.4;

H1 = 1/a1 * ( (a1*Hc1)^-0.5 - (a2*E1_plane)^-0.5 ) ^ -2;
H2 = 1/a1 * ( (a1*Hc2)^-0.5 - (a2*E2_plane)^-0.5 ) ^ -2;




%*********************************************************************
% Model creep during two holds at maximum load
```

```
%---- Analyze viscosity during 2nd hold segment ----------------------

clear residuals SSE SST Beta0 Pmax
time_9 = time(start9:end9) - time(start9);
disp_9 = disp(start9:end9) - disp(start9);

%Initial guess for fit optimization (Ep = 15 GPa, ETAp = 30,000 GPa S,
ETAs)
Beta0 = [15 3000 5000];

%Create X array for input into function  Y = f(Betas, X)
Pmax = load(start9);
X2 = [Pmax*ones(length(time_9),1) time_9];

%Nonlinear regression of the voigt model with X and outcome =
displacement
% Beta 1 = modulus (GPa)
% Beta 2 = viscosity (GPa-s)
% residuals = residuals of fit
[creep_betas2 residuals] = nlinfit(X2, disp_9, @maxwell_voigt_model,
Beta0);

E_parallel2 = creep_betas2(1);
Eta_parallel2 = creep_betas2(2);
Eta_series2 = creep_betas2(3);
time_constant2 = Eta_parallel2 / E_parallel2;

%Calculate R-squared of the fit
SSE = residuals' * residuals;
SST = (disp_9 - mean(disp_9))' * (disp_9 - mean(disp_9));
R2_creep2 = 1 - SSE/SST;


%---------- Plot fit of model against data ----------------------------
figure(3)
set(gcf,'Visible',visibility)

plot(time_9, disp_9, 'ko')
axis([0 100 0 1500]);
hold on
fitted2 = maxwell_voigt_model(creep_betas2, X2);
h = plot(time_9,fitted2,'r-');
set(h,'LineWidth',2)
title(['Indent ' name '.' indent_number])
xlabel ('Time (sec)')
ylabel ('Displacement (nm)')
hold off
text(5,1400,['E-parallel:                ' int2str(E_parallel2)])
text(5,1325,['ETA-parallel:          ' int2str(Eta_parallel2)])
text(5,1250,['Time Constant:          ' int2str(time_constant2)])
text(5,1175,['ETA-series:         ' int2str(Eta_series2)])

%Save the figure as a PNG
saveas(gcf, ['Creep ' name '_' indent_number], 'png')
%*****************************************************************
```

```
%*********************************************************************
%Calculate Energies of indentation

%Total energy spent on indentation
total_energy1 = trapz(disp(1:end3),load(1:end3));

%Energy to reach indentation depth
depth_energy1 = trapz(disp(1:start3-1),load(1:start3-1));

%Elastic Energy
elastic_energy1 = -1*trapz(disp(end3+1:end6),load(end3+1:end6));

%Plastic Energy
plastic_energy1 = total_energy1 - elastic_energy1;

%Percent unrecoverable energy (plasticity index)
plasticity1 = plastic_energy1 / total_energy1;



%Indent 2

%Total energy spent on indentation
total_energy2 = trapz(disp(end7:end9),load(end7:end9));

%Energy to reach indentation depth
depth_energy2 = trapz(disp(end6:start9),load(end6:start9));

%Elastic Energy
elastic_energy2 = -1*trapz(disp(end9+1:end10),load(end9+1:end10));

%Plastic Energy
plastic_energy2 = total_energy2 - elastic_energy2;

%Percent unrecoverable energy (plasticity index)
plasticity2 = plastic_energy2 / total_energy2;

%*********************************************************************


output1 = [E1, Hc1, H1, ...
    load(start3), disp(start3-1), disp(end3)-disp(start3-1),
max(disp(end3:end4)), ...
    -1, -1, -1, -1, ...
    depth_energy1, total_energy1, plasticity1, ...
    S1, Ac1*10^12, alpha1, m1, h_final1, R2_unload1, -1];

%Initiate text_output1 variable and designate sub-indent type
text_output1 = 'Normal';

for i=1:length(output1)
    if output1(i) == -1
        text_output1 = [text_output1 ', '];
    else
        text_output1 = [text_output1 ', ' num2str(output1(i))];
```

```
    end
end

output2 = [E2, Hc2, H2, ...
    load(start9), disp(start9-1), disp(end9)-disp(start9-1), max(disp),
...
    E_parallel2, Eta_parallel2, Eta_series2, time_constant2, ...
    depth_energy2, total_energy2, plasticity2, ...
    S2, Ac2*10^12, alpha2, m2, h_final2, R2_unload2, R2_creep2];

%Initiate text_output2 variable and designate indent type
text_output2 = 'Step';

for i=1:length(output2)
    text_output2 = [text_output2 ', ' num2str(output2(i))];
end

text_output = strvcat(text_output1, text_output2);




%**********************************************************************
% Creat figures of stiffness vs. displacement or time to diagnose
% "events" such as microfailures or bad contact

figure(4)
set(gcf,'Visible',visibility)

stiff = stiff/1000;             %Convert stiffness from N/m to kN/m

subplot(221)
plot(disp(start2:end3),stiff(start2:end3))
title('First Loading & Hold')
xlabel('Displacement (nm)')
ylabel('Stiffness (kN/m)')

subplot(222)
plot(disp(end3:end4),stiff(end3:end4))
title('First Unloading')
xlabel('Displacement (nm)')
ylabel('Stiffness (kN/m)')

subplot(223)
plot(time(start9:end9),stiff(start9:end9))
title('Hold After Step Load')
xlabel('Time (sec)')
ylabel('Stiffness (kN/m)')
axis tight

subplot(224)
plot(disp(end9:end10),stiff(end9:end10))
title('Second Unloading')
xlabel('Displacement (nm)')
ylabel('Stiffness (kN/m)')
```

```
%Save the figure as a PNG
saveas(gcf, ['Stiff ' name '_' indent_number], 'png')
```

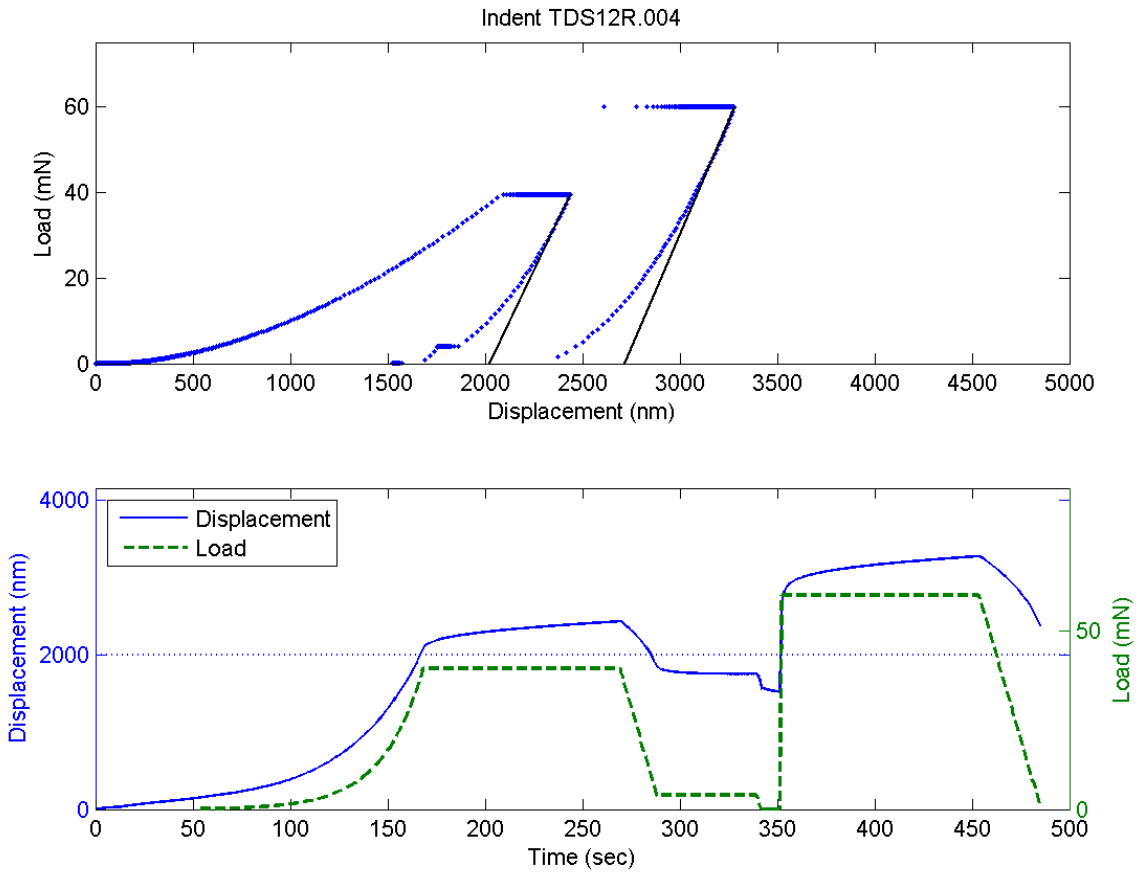

Figure E.1. Load, displacement, and time data from a nanoindentation test. This figure is automatically output by the custom-written Matlab program.

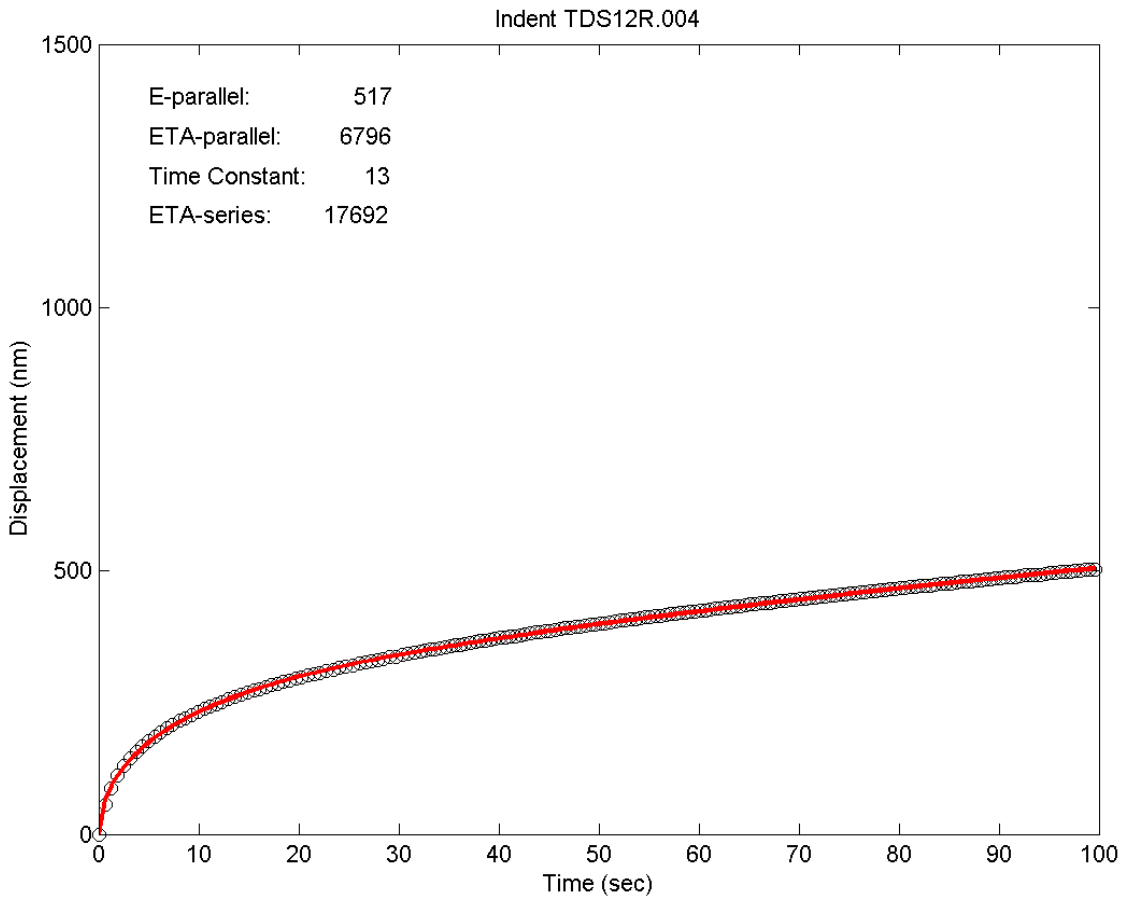

Figure E.2. Creep displacement after a step load with nanoindentation and the model fit of the creep data. This figure is automatically output by the custom-written Matlab program.

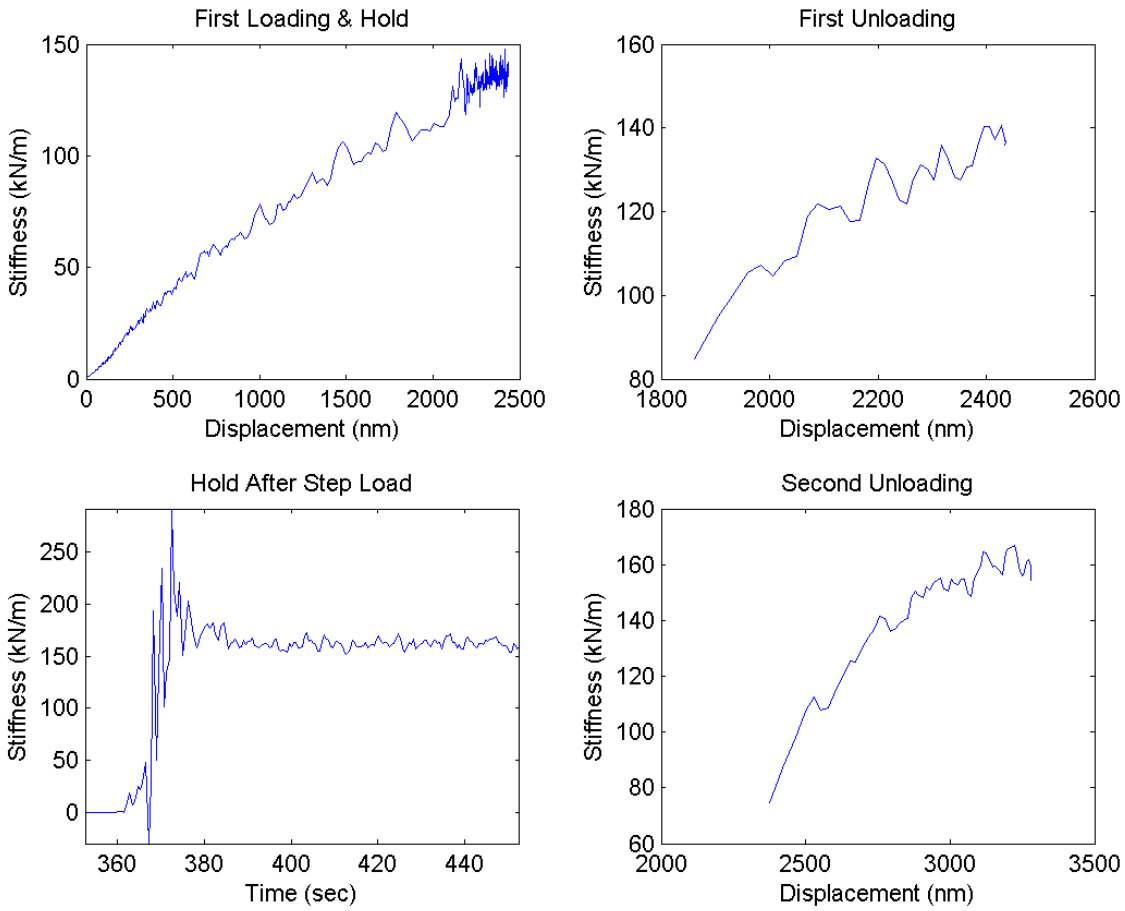

Figure E.3. Stiffness determined by the continuous stiffness method of nanoindentation. The stiffness is plotted during loading and unloading periods to diagnose cases of improper contact mechanics or micro-failures. This figure is automatically output by the custom-written Matlab program.

Sample	Indent Name	Indent Number	Indent Loading	Modulus (GPa)	Contact Hardness (GPa)	True Hardness (GPa)	Max Load (mN)	Displace-ment at Peak Load (nm)	Creep Displace-ment (nm)	Max Displace-ment (nm)	Creep Modulus - Parallel (GPa)	Creep Viscosity - Parallel (GPa-s)
12R	TDS12R.001	1	Normal	7.200	0.320	1.161	30.89	1877	354	2232		
12R	TDS12R.001	1	Step	5.569	0.284	1.172	59.96	2650	712	3363	389	5209
12R	TDS12R.002	2	Normal	7.159	0.352	1.403	37.29	1993	374	2368		
12R	TDS12R.002	2	Step	5.858	0.302	1.261	59.96	2586	678	3266	487	6651
12R	TDS12R.003	3	Normal	7.374	0.361	1.431	38.42	2015	358	2373		
12R	TDS12R.003	3	Step	6.029	0.310	1.294	59.97	2564	655	3221	495	6207
12R	TDS12R.004	4	Normal	7.096	0.354	1.433	39.52	2064	371	2436		
12R	TDS12R.004	4	Step	5.866	0.298	1.231	59.96	2610	667	3279	517	6796

Creep Viscosity - Series (GPa-s)	Time Constant (s)	Work to reach depth	Total Work	Plasticity Index	Unloading Stiffness (mN/nm)	Contact Area (um^2)	alpha (unload-ing power law fit)	m (unload-ing power law fit)	Residual Depth (nm)	R-squared of Unload-ing Curve Fit	R-sqaured of Creep Fit
		19458	30371	76%	0.0900	96.4	1.49E-05	2.20	1485	0.994	
16967	13	45949	77740	72%	0.1032	211.3	0.000149	1.85	2301	0.988	0.9996
		25236	39168	75%	0.0938	105.9	2.76E-05	2.10	1542	0.993	
17434	14	41401	71947	70%	0.1053	198.6	0.00011	1.89	2200	0.991	0.9998
		26598	40340	74%	0.0969	106.5	9.30E-06	2.24	1491	0.989	
18065	13	41325	71434	70%	0.1069	193.3	9.28E-05	1.92	2157	0.991	0.9997
		27833	42477	74%	0.0954	111.6	9.70E-06	2.23	1521	0.994	
17692	13	42421	72638	70%	0.1060	200.9	5.79E-05	1.97	2175	0.990	0.9998

Figure E.4. Output of mechanical properties determined for a set of nanoindentation tests. The custom-written Matlab program outputs this data to a .CSV file.

APPENDIX F

PAPERS AND PRESENTATIONS

Publications:

Sahar, ND, K Golcuk, MD. Morris, DH Kohn, Exercise Increased Tissue Strength and Skeletal Fatigue Resistance by Ubiquitously Altering Mineral Composition in Murine Tibiae (in process)

McElderry, JD,ND Sahar, DH Kohn, MMJ Tecklenburg, MD Morris, Validation of Raman spectroscopic bone mineral crystallinity metrics (in process)

Raghavan, M, ND Sahar, DH Kohn, MD Morris, Equilibration of Cortical Bone Tissue with Deuterium Oxide Causes Loss of Mineral and Matrix Orientation: A Quantitative Raman Spectroscopic Study of a Model System for Collagen Disruption, *Bone* (submitted 2009)

Kohn, DH, ND Sahar, JM Wallace, K Golcuk, MD. Morris, Exercise Alters Mineral and Matrix Composition in the Absence of Adding New Bone, *Cells, Tissues, Organs* (in press)

Hansma P, et al., The Bone Diagnostic Instrument II: Indentation Distance Increase, *Review of Scientific Instrumentation* 79(6), 064303 (2008)

Raghavan, M, MD Morris, ND Sahar, DH Kohn, Polarized Raman Spectroscopy: Application to Bone Biomechanics, *Proceedings of SPIE* 6853, 68530W (2008)

Golcuk, K, et al., Rapid Raman Spectroscopy of Musculoskeletal Tissue Using a Visible Laser and an Electron-Multiplying CCD (EMCCD) Detector, *Proceedings of SPIE* 6093, 609314 (2006)

Kohn, DH, ND Sahar, SI Hong, K Golcuk, MD. Morris, Local Mineral and Matrix Changes Associated with Bone Adaptation and Microdamage, *Proceedings of the Materials Research Society*, (2005)

Callender AF, et al., Dynamic Mechanical Testing System for Raman Microscopy of Bone Tissue Specimens, *Vibrational Spectroscopy* 38, 101-105 (2005)

Golcuk, K. *et al*. Is photobleaching necessary for Raman imaging of bone tissue using a green laser? *Biochim. Biophys. Acta* (2006)

Sahar, N. D., Hong, S. I. & Kohn, D. H. Micro- and nano-structural analyses of damage in bone. *Micron* 36, 617-629 (2005).

Presentations:

Sahar ND, K Golcuk, MD Morris, DH Kohn, Bone Composition as the Primary Mechanism for Increased Skeletal Fragility and Decreased Adaptation in Old Mice, *Annual Meeting of the Orthopaedic Research Society,* San Francisco, CA, February 2008.

Sahar, ND, et al., "Effects of Exercise and Age on Bone Tissue Quality," *Midwest Tissue Engineering Consortium*, Ann Arbor, MI, April, 2007

Golcuk, K., et al., "Raman Mircrospectroscopic Study of Compositional Changes in Microdamaged Bone," *Annual Meeting of the Orthopaedic Research Society,* San Diego, CA, February 2007.

Sahar, ND, et al., "Exercise Increases Pre-Yield Mechanical Properties and Damage Resistance in Murine Tibiae," *Midwest Biomedical Engineering Conference,* Ann Arbor, MI, March 2006.

Sahar, ND, et al., "Effects of Exercise on Bone Quality as Shown by Raman Microspectroscopy," *Annual Meeting of the Orthopaedic Research Society,* Chicago, IL, February 2006.

Sahar, ND, et al., "Exercise Increases Pre-Yield Mechanical Properties and Damage Resistance in Murine Tibiae," *Annual Meeting of the Orthopaedic Research Society,* Chicago, IL, February 2006.